ALMA MATER STUDIORUM
UNIVERSITÀ DI BOLOGNA

DOTTORATO DI RICERCA IN

FISICA

Ciclo 37

Settore Concorsuale: 02/B1 - FISICA SPERIMENTALE DELLA MATERIA

Settore Scientifico Disciplinare: FIS/03 - FISICA DELLA MATERIA

2D-HYBRID PEROVSKITE THIN FILMS FOR HIGH ENERGY RADIATION DETECTION

Presentata da: Lorenzo Margotti

Coordinatore Dottorato

Prof. Alessandro Gabrielli

Supervisore

Prof. Beatrice Fraboni

Co-supervisore

Dott. Andrea Ciavatti

Esame finale anno 2025

ABSTRACT

Detection of high energy radiation has always been a hard task to be faced. The physics of interaction between matter and radiation constitutes the basis of dosimetry and related devices. Analyses on materials, architectures and electronic readout systems are mandatory for precise and accurate detection of the absorbed dose. Among the former, one of the notable breakthroughs is to be found in hybrid metal-halide perovskites, that have emerged as promising for radiation detection due to their unique chemical and optoelectronic properties.

This class of materials, consisting of alternating organic and inorganic layers, exhibits semiconducting features with tuneable bandgaps, excellent charge-transport and scintillation properties and high radiation hardness, making them suitable as active layers for dosimetry devices. Furthermore, the high atomic number facilitates detection of high-energy photons and particles, allowing for specific applications such as medical and space-related to be targeted directly.

Recent research has highlighted two-dimensional (2D) perovskites as valid alternative to the well-established 3D counterpart: reasons are to be found in higher stability and remarkably lower dark current, that lead to long-term performance and durability. On top of that, perovskite-based radiation detectors are fabricated from solution-processing techniques, which are cost-effective and allow for scalability to large-area devices.

In this work, we chose PEA_2PbBr_4 2D-perovskite as active material in the form of polycrystalline thin films for direct detection of high energy ionizing radiation. We investigated physical and chemical properties of the material including charge-carriers mobility, lifetime, response time, photovoltage with specific techniques and designed and fabricated devices to be employed for medical and space-related applications. We tested these devices response under X- and γ-rays, under high energy protons and alpha particles. We realized the first flexible dosimeter for real-time monitoring of clinically relevant proton beam and radiotracer extravasation. We demonstrated alpha particles spectroscopy power of thin films, that is of huge interest for medical applications as it directly conveys towards neutron detection. Lasty, space-related applications are targeted as a perovskite-based dosimeter is implemented to be sent to the International Space Station for dedicated tests with the crew onboard.

INDEX

PREFACE

Note: the ensuing written composition is intended to be an approachable guide to whom is interested in direct radiation detectors based on a specific 2D perovskite material. As it aims to highlight the core features of radiation sources and the reason why perovskites have been widely employed as detectors, a compromise is reached between technical language and clarity. References will be of advanced support all long.

The compelling need for cost-effective, high-precision dosimeters has significantly driven research and development efforts toward novel materials aimed at enhancing the overall quality of radiation detection systems. Personal dosimetry, a critical area of this research, has stringent requirements including mechanical flexibility, high stability, low cost, and reliability. These requirements underscore the necessity of studying material properties, as they directly impact the performance and efficacy of dosimetric devices.

This study focuses on the use of 2D perovskite PEA_2PbBr_4 as a core material in the form of a thin film. The research investigates its physical properties and performance under various high-energy radiation environments. The choice of PEA_2PbBr_4 is based on its previously explored features[1], which suggest its potential for reliable device fabrication and performance.

The primary objectives of this work are twofold:

1. To deeply analyse the material features of PEA_2PbBr_4 with the aim of enhancing its performance and providing accurate interpretations of the recorded data.
2. To develop dosimeters incorporating this material that can be integrated into read-out electronic systems, facilitating high-energy radiation detection and monitoring in both technical and clinical contexts.

By addressing these goals, the study aims to contribute to the advancement of personal dosimetry through improved material performance and practical application in radiation detection systems.

The workflow starts with gathering the required knowledge in the field of radiation sources, interaction mechanisms with matter and goes straightforward to the well-established detection techniques. This is intended to underscore the key elements to be considered when fabricating and characterising novel devices. First paragraph briefly covers radiation types and the physics behind signal production and recording; it finally extends it all to applied dosimetry, that is technological transfer to clinically relevant devices. Limitations of state-of-the-art RTSD devices are explained [2] and desired achievements clearly described.

Secondly, metal halide perovskites (MHPs) are presented as a novel class of materials suitable for radiation detection [3]. Although widely employed in solar cells, main topic is high-energy related: for this reason, we outline their major features of interest in matter of radiation absorption and signal recording. Physical and chemical properties are highlighted and described in detail, as their understanding is crucial for the following optoelectronic analyses. Specifically, a comparison between 3D and 2D structures is reported as the differences lead to completely separated fields of interest: 3D perovskites account for high response, 2D on their side are more stable and exhibit lower dark current.

Subsection 1.3 is an extension of this preface, as it goes further with this research targets and goals, together with the needs and challenges to be faced for dosimeters realization.

The second chapter is fully centered on laboratory-scale techniques for fabrication and analysis. It is divided in two specific subsections which distinguish between *how to make a device* and *which analytical tool to be chosen to check material properties and performance*. In order to give the reader clear understanding of mechanisms and the possibility to have them reproduced, accurate description of instruments working principle and set-ups is accounted for. Specifically, we report a step-by-step lithography procedure for substrate patterning and a list of radiation measurement systems that allow for tests under UV light, X-rays and alpha particles.

Results and achievements are reported in Chapter 3 and divided between novel discoveries on material properties and case studies of fabricated devices in relevant medical and space-related applications.

Material features have been investigated at the university of Bologna; extensive analyses have been conducted that demonstrate the high performance of PEA_2PbBr_4 thin films as radiation detectors.

We report the first evidence of 2D perovskite response in form of photovoltage and photocurrent generation when illuminating far from the electric field up to 1cm distance. Attribution of this effect are still uncertain and under investigation.

Furthermore, we demonstrate 2D perovskite thin film response under alpha particles down to single pulse and compare it with its single crystal counterpart. This is crucial for future applications in the field of neutron detection. Measurements have been conducted in the laboratories of the University of Surrey, Guildford, UK, under the supervision of prof. Paul J. Sellin.

Measurements under high energy protons are also presented in collaboration with TIFPA centre, Trento, and LABEC, Firenze.

Published works include:

- proton beam monitoring of 2D perovskite films onto interdigitated multipixel arrays, with which a clear gaussian-shaped profile has been extracted and accurate dose analyses have been performed [4].
- Y-rays monitoring from radiotracer injection and extravasation; setup resembling a human phantom [5].

Finally, the ongoing IRIS project is intended to provide portable dosimeters for the astronauts to be worn during 2025 mission on ISS, with the intent of real-time monitoring radiation environment inside ISS Columbus modulus.

1. INTRODUCTION

1.1 BASICS OF RADIATION: PRINCIPLES AND DETECTION METHODS

As primary target of this contribution is ionizing radiation detection, the following will be centered on high-energy radiation only, ranging from a few tens of keV for photons up to hundreds of MeV for protons. Analyses under visible light will be nevertheless present in the work as they constitute basic investigation of perovskite-based devices performance.

1.1.1 RADIATION MATTER INTERACTION

The detection of ionizing radiation relies on the conversion interaction effects of radiation itself into measurable electronic signals [6]. As a product of such interactions, these signals are generated by high-energy particles interacting with the absorbing material within the detector and transferring energy to it; this produces observable outcomes in the form of ionization or excitation. As the design, prototyping, and operational principles of radiation detectors are intrinsically linked to the *nature* and *energy* of the particles being detected, a comprehensive investigation into the underlying interaction mechanisms is imperative. Specifically, the ways in which high-energy particles trigger physical and chemical processes within the detector's components must be thoroughly understood prior to devices fabrication [7].

Before discussing the relevant physical quantities and establishing the key performance metrics -or figures of merit- required for the successful fabrication of these devices, it is essential to first develop a deep and systematic understanding of these interaction mechanisms. Such an acknowledgement provides the foundation for optimizing detector design and ensuring devices responsivity to the specific types of radiation they are meant to detect. In the following, primary distinction is made between *charged* and *uncharged* ionizing radiation. Reason is to be found in the different interaction mechanisms that lead to different outputs as reported in Fig. 1 below: with the advent of nuclear medicine and radiation therapies, the need for exact penetration behaviour needs to be carefully acknowledged.

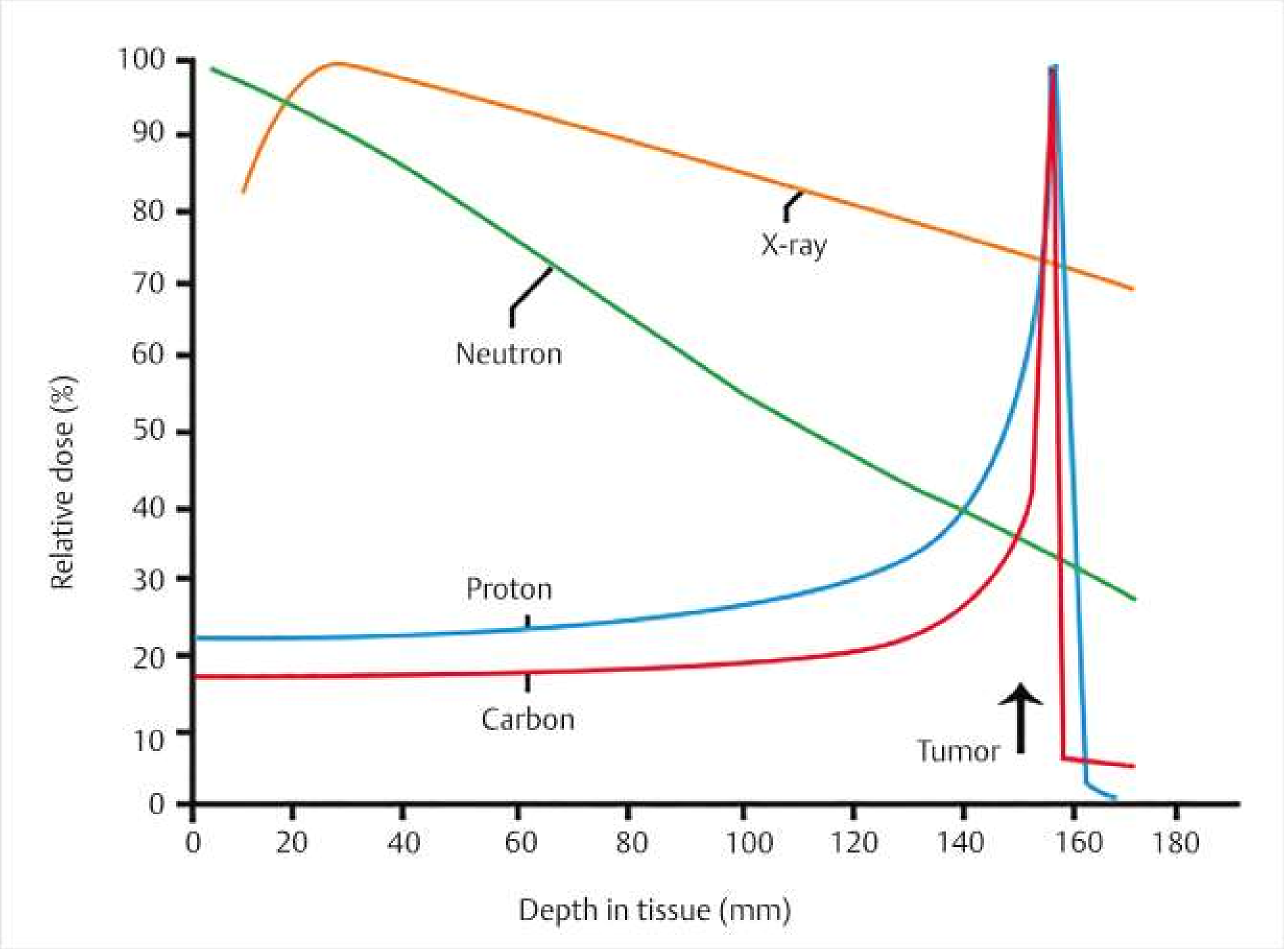

Figure 1 Energy loss of particles in the form of relative dose as function of distance from impinging surface in human tissues. Heavily charged particles such as protons or ions penetrate up to specific finite distance and their energy loss exhibits a peak after which the particle is completely absorbed. That peak -Bragg peak- is of high interest for hadron therapy as it is tuned to target the active tumor regions. Photons and neutrons interact differently, as they can pass through without getting absorbed; their effects are measured through secondary products [8].

Another important distinction must be made between heavily charged particles (in this context: particles with a mass M exceeding the electron mass *m* such as alpha particles or protons) *and* beta particles/fast electrons as they exhibit different energy loss mechanism and penetration depth. For the same reasons, photons (such as X-rays or gamma rays) and neutrons must be treated separately. Although X-rays can ionize matter directly though photoelectric effect, high energy photons and neutrons do not ionize matter directly. Instead, they interact indirectly through specific processes that lead to the creation of secondary charged particles that carry out the ionization process [9].

The interaction of both heavily charged particles and photons with matter can result into the generation of secondary electrons. As these byproducts can vary significantly in energy and behavior, they may contribute additional ionization and energy deposition within the material. We will explore the role and implications of these secondary electrons in greater detail later on, as they play a crucial role in the overall energy transfer and ionization process during particle detection.

1.1.1.1 Charged Particles

Alpha particles, protons, heavy ions

As a direct consequence of Coulombic interactions with the coulombic field that is intrinsic in the atomic structure of absorbing media, charged particles progressively lose energy. This energy transfer occurs in the form of electronic excitation or atomic ionization as the particle interacts with the electrons and nuclei of target materials. The rate at which this energy is dissipated along the particle's path is described by the linear stopping power, expressed as

$$S = -\frac{dE}{dx},$$

where dE/dx represents the energy loss per unit path length: it essentially quantifies how much energy a charged particle loses while travelling through specific elements or compounds.

The stopping power S is influenced by several factors, including the nature and energy of the particle and the density of the material through which it travels. A well-established analytical model that describes this relationship is the Bethe-Bloch equation[10], which is here reported with the assumption of non-relativistic charged particles. This equation can be written as:

$$-\frac{dE}{dx} = [4\pi e^4 \frac{z^2}{(v^2 m_0)} NZ \ln\left(\frac{2m_0 v^2}{I}\right) - B]$$

where:

- m_0 is the electron mass,
- v is the velocity of the particle,
- z is the charge of the particle (in units of elementary charge),
- N is the number density of the target atoms,
- Z is the atomic number of the target material,
- I is the average ionization potential of the target material,
- B accounts for corrections at higher energies.

Notably, key parameters affecting the energy loss of a charged particle are its velocity (v), charge (ze), and the atomic number (Z) of the medium. As the particle moves through the material, it continuously loses energy, and the energy loss increases as the particle slows down. This phenomenon reaches a peak at a specific point in the particle's path, which corresponds to the highest rate of energy deposition -this peak is known as the Bragg peak [11].

The energy loss-distance behavior describes how energy dissipation varies as a function of a particle's position within a material. At first, the particle experiences moderate energy loss, but as it decelerates, the rate of energy release increases significantly, culminating in a peaked value just before the particle stops. This abrupt loss arises from the particle’s decreasing velocity, which enhances the effectiveness of its electric field in interacting with the surrounding atoms.

In the case of particle beams, this effect creates a precisely defined region where the maximum energy deposition occurs. This is of crucial importance in cancer treatment technologies that make use of protons for target therapies.

Another contribution that affects detectors precision is to be found in particles straggling, that refers to the statistical variation in the path length or energy loss of particles as they travel through a material [12].

- Range Straggling: it refers to the variation in the distance travelled by charged particles (such as alpha particles or protons) before they come to rest in a material. Due to random interactions with atomic nuclei and electrons in the material, not all particles of the same energy will travel the exact same distance, leading to a spread in their ranges.
- Energy Straggling: This pertains to the fluctuations in the amount of energy a charged particle loses as it passes through matter. Even though the average energy loss can be described by models like the Bethe-Bloch equation, individual particles lose energy in discrete interactions, leading to variations in their energy loss over a given path length.

It is important to emphasize that the focus of this work is on thin-film devices, which requires special consideration of the interaction dynamics of charged particles with the thin, active material layers. Unlike bulk materials, where total absorption of heavily charged particles is a common scenario, thin films typically allow only partial absorption due to their limited thickness. As a result, the concept of energy loss must be extended to account for scenarios where charged particles traverse the material without being fully stopped.

In these cases, the energy loss per unit path length, defined by the linear stopping power of eq. 1.1, must be averaged over the particle's energy as it travels through the absorber layer. Let t represent the thickness of the absorber and $\left(-\frac{dE}{dx}\right)_{avg}$ denote the stopping power averaged over the particle's energy while within the layer; then, the energy deposition can be estimated from

$$\Delta E = -\left(\frac{dE}{dx}\right)_{avg} t.$$

For thin films, where the energy loss is relatively small, the stopping power may remain approximately constant and can be reasonably approximated by its value at the incident particle energy.

However, as the absorber thickness increases, the problem becomes significantly more complex. The stopping power becomes highly dependent on the particle's energy evolution throughout its path, which is no longer constant. This introduces a challenge in accurately estimating both the stopping power and the total energy loss over the particle's trajectory.

To address this, an integrative approach is required that involves combining an energy-dependent stopping power function with the material's density and thickness to calculate the precise energy loss as the particle passes through the absorber. Such complexity implies that a-priori simulations are essential to obtain accurate predictions of the particle's energy before and after it traverses the thin film. These simulations should consider both the material properties and the energy loss function over the particle's full energy range, enabling the determination of precise energy values after the particle has crossed the target layer. It is assumed, for the purposes of this analysis, that the particle's track remains linear throughout the interaction process, a simplification that holds in cases where scattering or deflection effects are minimal.

Fast electrons

When compared with heavy charged particles, fast electrons lose their energy at a lower rate and follow a much more tortuous path through absorbing materials.

Large deviations in the electron path are now possible because its mass is equal to that of the orbital electrons with which it is interacting, and a much larger fraction of its energy can be lost in a single encounter. In addition, electron-nuclear interactions, which can abruptly change the electron direction, sometimes occur. Moreover, electrons also differ from heavy charged particles as energy may be lost by radiative processes as well as by coulomb interactions. These radiative losses take the form of bremsstrahlung or electromagnetic radiation, which can emanate from any position along the electron track. From classical theory, any charge must radiate energy when accelerated, and the deflections of the electron in its interactions with the absorber correspond to such acceleration.

This leads to changes in the definition of specific energy loss, which need to account for the abovementioned phenomena’ contribution. Interested readers can refer to [9] for analytical expressions.

1.1.1.2 Uncharged Particles

High Energy Photons

Photons interact with matter via a range of mechanisms, which can be classified according to the type of target and the effect of the interaction on the photon (absorption or scattering). At energies beyond the ultraviolet range, the dominant processes are photoelectric absorption, Compton scattering, and pair production. As illustrated in Figure 2, photoabsorption constitutes the largest contribution to the total cross section at low photon energies, pair production is the most frequent interaction at high energies, and Compton scattering dominates in the intermediate energy range [14].

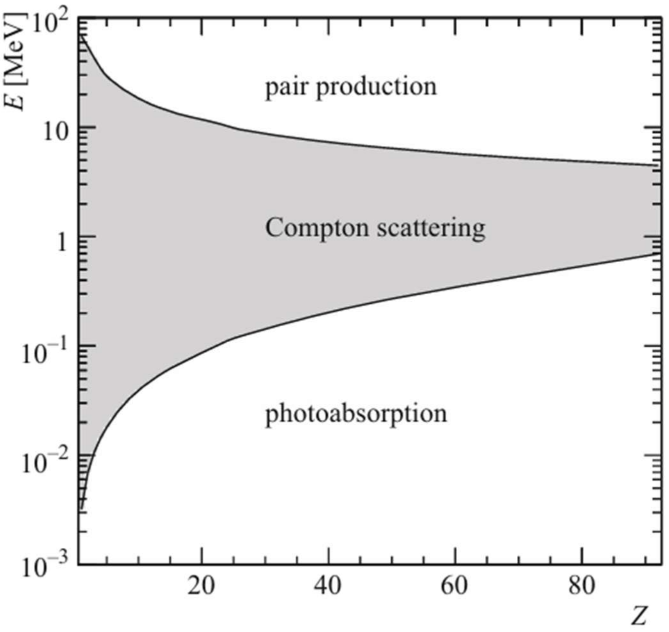

Figure 2 The lower curve shows, as a function of the atomic number Z of the target material, the photon energy E below which photoelectric absorption is the most probable interaction mechanism, while the upper curve shows the energy above which pair production is the most important process. The shaded region between the two curves corresponds to the domain where Compton scattering dominates. The cross sections are taken from the NIST XCOMdatabase [15].

- **Photoelectric effect**

In the photoelectric effect, a photon is completely absorbed by an atom, resulting in the ejection of a photoelectron from one of the atom's bound shells. The energy of the ejected photoelectron is given by:

$$E_{photoelectron} = E_{\gamma} - E_b$$

where Eγ is the energy of the incident photon, and Eb is the binding energy of the electron in its original shell. For gamma rays of sufficient energy, the most probable origin of the photoelectron is the K-shell, due to its tightly bound electrons.

As the photoelectron is ejected, the atom becomes ionized, leaving a vacancy. This vacancy is then filled by a free electron from the medium or by electronic rearrangement from other atomic shells, leading to the emission of characteristic X-rays. Alternatively, the energy may be released through the emission of an Auger electron. The energy of the Auger electron, if emitted, can be expressed as:

$$E_{Auger} = E_{vacancy} - E_{rearr}$$

For high-Z materials, such as lead, the probability of photoelectric absorption increases significantly. The dependence of the photoelectric absorption cross-section σ_{pe} on the photon energy Eγ and atomic number Z can be approximated as:

$$\sigma_{pe} \propto \frac{Z^n}{E_{\gamma}^3}$$

where the exponent n typically ranges between 4 and 5 in the gamma-ray energy region of interest. Notably, this strong dependence on Z makes high-Z materials ideal for gamma-ray detection and shielding.

The cross-section exhibits sharp discontinuities, known as absorption edges, at photon energies that correspond to the binding energies of electrons in various atomic shells, particularly the K-edge. When the photon energy exceeds the binding energy of a shell, the probability of photoelectric interaction jumps abruptly. For instance, if *Eγ>EK-binding* at the K-edge, the interaction probability increases sharply, but if *Eγ<EK-binding* , the interaction becomes energetically impossible, causing the probability to drop. These edges are a key feature in gamma-ray detection materials, such as sodium iodide (NaI) [16].

- **Compton scattering**

Compton scattering refers to the collision of a photon with a weakly bound electron, whereby the photon transfers part of its energy to the electron and is deflected with respect to its original direction of propagation. We assume in the following that the target electron is free and initially at rest, which is a good approximation if the photon energy E is large compared to the electron's binding energy. Due to conservation of energy and momentum, the photon energy E after the collision and the scattering angle θ of the photon are then related by:

$$E' = \frac{mc^2}{1 - \cos\theta + (1/u)},$$

Where $u = \frac{E}{mc^2}$ is the photon energy (before the collision) in units of the electron rest energy.

The kinetic energy $T = E - E'$ imparted to the electron is largest for a head on collision(θ=π) and the energy spectrum of the recoil electrons consequently exhibits a cut-off (Compton edge) at:

$$T_{max} = E(\frac{2u}{1+2u})$$

- **Pair production**

For photon energies exceeding 2mc^2 the incident photon is completely absorbed, resulting in the creation of an electron-positron pair whose total energy equals the photon energy E. To conserve momentum, this process must occur in the presence of an electric field, typically that of a nucleus or atomic electrons. In the case of pair production near atomic electrons, kinematic constraints impose a higher energy threshold, specifically *E>4mc^2*.

At high photon energies, the electron-positron pair is preferentially emitted in the forward direction. The absorption coefficient due to pair production can be approximated as:

$$\mu = N\sigma^{pair\ production} = \frac{7}{9 * X_0}$$

where N is the number of atoms per unit volume, σpair production is the pair production cross section, and X0 is the radiation length, a material-dependent parameter that characterizes the distance over which a high-energy electron loses significant energy due to bremsstrahlung.

Photons attenuation in matter is governed by an exponential relationship between the intensity of the incident gamma radiation and the thickness of the absorber. The attenuation coefficient μ quantifies the fraction of gamma rays absorbed or scattered per unit thickness of material. The transmitted intensity $I(t)$ after passing through an absorber of thickness t is given by the equation:

$$I(t) = I_0 e^{-\mu t}$$

where I_0 is the initial gamma-ray intensity, μ is the linear attenuation coefficient, and t is the thickness of the absorber. This equation assumes monoenergetic gamma rays and narrow-beam geometry, where scattering outside the detector is neglected.

In practical applications, however, scattered radiation from interactions such as Compton scattering can re-enter the detector, effectively increasing the measured intensity. This is known as the buildup effect, which modifies the simple exponential attenuation formula. To account for this, a buildup factor $B(t)$ is introduced, which adjusts for the scattered radiation that contributes to the overall detector response. The revised intensity equation incorporating buildup is:

$$I(t) = I_0 B(t) e^{-\mu}$$

Here, $B(t)$ is a function of the material, photon energy, and absorber thickness, typically greater than 1, especially for thicker absorbers where scattering becomes more significant. The buildup factor corrects for secondary radiation and ensures more accurate predictions of gamma-ray transmission through materials.

Neutrons

Like high-energy photons, neutrons carry no charge and therefore cannot interact in matter by means of the coulomb force: they may travel through long distance up to centimeters of matter without any type of interaction and thus can be totally invisible to a detector of common size.

Primary mean of interaction is with atomic nuclei. As a result, the neutrons may either totally disappear and be replaced by secondary radiations in the form of heavily charged particle, or else the energy or direction is changed significantly. These former particles may be produced either as a result of neutron-induced nuclear reactions or they may be the nuclei of the absorbing material itself, which have gained energy as a result of neutron collisions. Most neutron detectors utilize some type of conversion of the incident neutron into secondary charged particles, which can then be detected directly. The relative probabilities of the various types of neutron interactions change dramatically with neutron energy. In this context, we will examine the distinct interaction properties of slow neutrons (those with energies below 0.5 eV) and fast neutrons (those with energies above 0.5 eV). This threshold is chosen because it marks a significant change in how neutrons interact with matter, particularly in terms of absorption and scattering processes, and serves as a useful reference point for studying neutron behavior.

- **Slow neutrons:** (energies below 0.5 eV), often referred to as thermal neutrons, interact primarily through neutron capture or absorption reactions. As they move at relatively low speeds, slow neutrons have a high probability of being absorbed by nuclei. A prominent example is the boron-10 neutron capture reaction [17]:

  $$^{10}B + thermal\ neutron\ \rightarrow [^{11}B]* \rightarrow \alpha + ^{7}Li + 2.31MeV$$

  In this process, the neutron is absorbed by the boron nucleus, releasing an alpha particle and a lithium nucleus. Similarly, slow neutrons can also induce reactions in other isotopes, such as cadmium or helium-3, with cross sections that peak at low energies. This makes thermal neutrons particularly efficient in nuclear reactions, causing isotopes to become unstable and emit secondary particles.

- **Fast neutrons:** with energies typically above 0.5 eV and up to several MeV, interact mainly through elastic scattering with nuclei. The most common target nuclei for fast neutron interactions are light nuclei, such as hydrogen. In an elastic scattering event, the fast neutron transfers part of its energy to the nucleus, causing the nucleus to recoil. The amount of energy transferred depends on the mass of the target nucleus and the incident neutron energy. The recoil energy E_r is given by:

  $$E_r = \frac{2A}{(1+A)^2} E_n$$

  where *A* is the mass number of the target nucleus and En is the neutron's energy. For hydrogen (*A*=1), the neutron can transfer a significant portion of its energy, while for heavier nuclei, the recoil energy is much lower. This process results in the slowing down of the neutron, eventually reaching thermal energies. Fast neutrons also contribute to inelastic scattering, causing the target nucleus to become excited and emit gamma radiation as it returns to its ground state. However, the cross section for such interactions is lower than that for thermal neutron absorption.

1.1.2 RADIATION DETECTORS

As previously mentioned in sec. 1.1.1, the only way radiation detection is achieved consists in exploitation, quantification and analysis of its effects on target media. This clearly states the need for an integrated system that includes both an active material to manifest radiation effects *and* readout electronics whose yield is sufficiently performing. Prior to the definition of detector types, it is important to highlight the differences in working principles of the current state-of-the-art technologies, as well as their advantages and limitations. As this document focuses on solid state radiation detectors, a large part of the following will target their properties and requirements extensively. Before this, a brief introduction to other detection mechanisms is provided as it underscores the key features of interest to be found in perovskite-based devices described later.

1.1.2.1 Indirect detectors

This class of detectors relies on intermediate processes that account for radiation absorption, generation of energy in different forms and energy conversion to measurable electronic signals. They require a medium whose interaction with the radiation of interest produces secondary products in the form of photons or heavily charged particles that are easily collected afterwards through specific electronics. Among them, two main types of indirect detectors exist: ***gas-filled*** *and* ***scintillators.*** A scheme of the operational working principle of the two types is reported below.

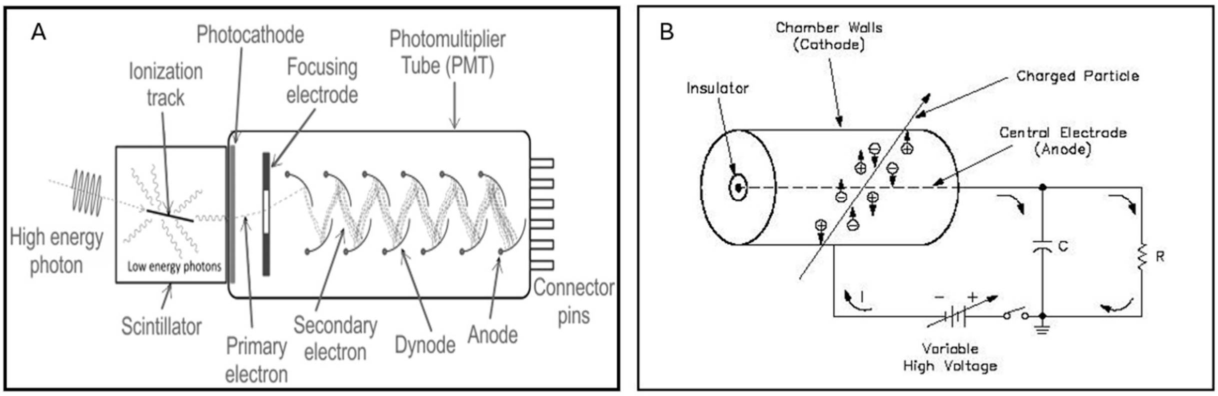

Figure 3 Scheme of a standard scintillation device (A) and a commonly set gas-filled detection system (B). Main components of scintillating detectors are a scintillating material and a photomultiplier tube, that is composed of metal dynodes whose aim is amplification of photons[18]. Gas-filled detectors rely on generating ionization products due to radiation particles interacting with the gas molecules. Collection is performed through the application of an electric field between anode and cathode, connected via external circuit [19].

GAS-FILLED DETECTORS

These systems exploit ionization of gas molecules produced by incoming high-energy radiation that is to be detected. Their basic working principle relies on a gas-filled chamber in which an electric field is applied by mean of two metal electrodes – typically employed gases belong to the 18th group (Ar, Xe). When ionizing radiation passes through the gas, ionization occurs, and free electrons plus positive ions are generated. These are collected by the electrodes in the form of electrical pulses that can be measured and analysed.

Gas-filled detectors behaviour strongly depend on multiple factors: nature and energy of the incoming particles, type and pressure of gas, intensity of applied electric field. Tuning these parameters offer different operational modalities, the most relevant ones are reported below.

- **Ionization chambers:** the electric field is low enough that only the primary ion pairs generated by the radiation are collected, resulting in a current that is directly proportional to the number of ion pairs formed. This mode is highly reliable for measuring high radiation doses due to its stable response -for this reason, this is widely employed as a calibration metric for high energy proton beams in hadron therapy facilities. Nevertheless, its sensitivity to low radiation levels is limited.

- **Proportional counters:** they operate at higher electric fields, allowing for the amplification of the initial ionization through a process called gas multiplication. Here, the free electrons gain enough energy to ionize additional gas molecules, leading to a cascade of ionization events. The resulting signal is larger and remains proportional to the energy of the incident particle, making proportional counters suitable for spectroscopy applications and distinguishing between different types of radiation.

- **Geiger-Muller**: they function at even higher electric fields, through which the initial ionization triggers a full avalanche of ionization throughout the gas, irrespective of the energy of the incoming particle. This results in a uniform, large pulse for every ionizing event, thus providing excellent sensitivity for particle counting but no information about the energy of the incident radiation.

Gas-filled detectors are widely used in radiation protection, medical physics, nuclear research, and environmental monitoring. Their simple construction, cost-effectiveness, and ability to detect a broad range of radiation types make them versatile instruments in a variety of applications. However, factors such as gas purity, pressure, and the geometry of the detector significantly affect their performance, and they may be prone to saturation at high radiation levels due to space charge effects.

SCINTILLATORS

These systems account for the deploy of thin layers of materials that emit lower-frequency light after high-energy radiation absorption. When charged particles or ionizing photons interact with a scintillating material, atomic or molecular excitations occur within the material itself; relaxation of these excited states produces energy release in the form of visible or ultraviolet light. This low-energy radiation is easily converted and collected through photomultiplier tubes or photodiodes, through which an electrical signal is produced that can be quantified and analysed.

A plethora of materials exhibit scintillation properties, ranging from organic compounds (e.g. plastic scintillators) to inorganic crystals such as sodium iodide (NaI(Tl)) or the commercially standard bismuth germanate (BGO). Key parameters to be taken into account are

- **Light yield**, that is the number of photons produced per unit of absorbed energy. State-of-the-art devices produce up to $4x10^4$ photons per MeV [20].
- **Energy resolution,** that is intrinsically related to both the material’s light output and the light collection system’s efficiency. NaI(Tl), for instance, has an energy resolution of approximately 6–7% at 662 keV (from a ^{137}Cs gamma source), while BGO has a poorer resolution, typically around 10–12% at the same energy [21].
- **Decay time**, as this gives quantitative values of time-response of the devices. Standard decay times reach limit values down to nanosecond-scale [22].

Main advantage of scintillation-based radiation detection is to be found in their high sensitivity, broad detection range and versatility, as they can be used for gamma-ray, X-rays, beta-particles detection. Their applicability ranges from medical imaging (PET) to high-energy physics experiment. Limitations of these devices are to be found in their low radiation hardness and their need for complex optoelectronic systems to be integrated for efficient light collection.

It is important to mention that perovskite material have been reported to exhibit incredible light yield: as their emitted-photons energy is tunable, they constitute valid alternative to solid state scintillators. As this is beyond the scope of the present work, we direct interested readers to the relevant references for further information [23], [24], [25], [26]

1.1.2.2 Direct detectors

Direct Ionizing radiation interaction with semiconductor materials produces the creation of electron-hole pairs that can be detected as an electric signal. The average energy needed to create an electron-hole pair depends on the absorbing semiconductor. For most inorganic semiconductor it is given by the empirical Klein's rule [27]:

$$W^{0}{}_{\pm} \sim 2.2E_g + E_{phonon}$$

Where E_g is the band gap energy of the semiconductor and E_{Phonon} is a phonon energy term. In silicon and germanium, the energy required to create an electron-hole pair is 3.69 and 2.62 eV respectively. Notably, these values are incredibly small compared to the one of traditional gas detectors (like Geiger counter) which is about 50 eV.

Another example is amorphous selenium (αSe) [28], for which the ionization energy follows:

$$W_{\pm} \sim W_{\pm}^{0} + \frac{B(E)}{F^{n}}$$

This presents a weak dependence on the photon energy through the term $B(E)$, a constant that decreases with the increase of the radiation energy. F is the external electric field applied to extract the charges and n varies between 0.7 and 1. $W_{\pm}^{0}$ for selenium is expected to be around 5 eV. $W\pm$ can reach 45 eV at the operating bias conditions.

The number of free charge carriers created inside the semiconductor can be calculated by:

$$N = \frac{\Delta E}{W_{\pm}}$$

where ΔE is the energy deposited in the active material.

As the choice of active materials is primary core of devices fabrication, we list here the properties of interest to be accounted for. On top of these, it is necessary to mention that interface effects between the semiconductor and its neighboring layers -substrates or charge-collecting layers- plays crucial role in charge carriers' generation and collection efficiency.

- **High stopping power.** Most of the incident ionizing radiation should be absorbed within a practical semiconductor layer thickness. That means the interaction between the absorber and the radiation is strong enough to stop most of the radiation inside the detector with minimal radiation losses. At fixed radiation, the detector absorption depends on the attenuation coefficient of the semiconductor used and on its thickness.

- **High intrinsic sensitivity.** Sensitivity is defined as the total charge collected by the detector for a unit of radiation exposure. This quantity is representative of the whole detection process. The generation of charges inside the semiconductor depends on the absorbed energy and the ionization energy of the material ($W\pm$). The collected charges are only the ones able to reach the electrodes, therefore sensitivity also accounts for charge transport in the semiconducting layer. The theoretical sensitivity (S) can be defined as:
$$S = S_0 * \alpha * n * \epsilon_{cc}$$
where S_0 is a constant that depends on the incident photon energy. α is the attenuated fraction, *n* is the number of electron-hole pairs generated by each single photon and ϵ_{cc} is the charge collection efficiency representing the fraction of charges collected. Usually, the sensitivity is reported per unit of area. 200 μm thick α-Se and 300 μm CZT have sensitivity, for 20 keV photons, of 24 μC Gy^{-1} cm^{-2} and 255 μC Gy^{-1} cm^{-2} respectively [29], [30].

- **Proportionality with absorbed energy.** The output signal in a direct detector is an electrical current that is proportional to the charges collected. To have the higher output signal possible the bulk recombination of electrons and holes generated by the incoming radiation must be the minimum.

- **Low density of defects.** There should be minimum deep trapping of holes and electrons. When an external electric field is applied the drift length of electrons and holes is equal to $D = \mu\tau F$; where μ is the mobility, τ is the charges lifetime and F the electric field. In order for the carriers to reach the electrodes and generate the output signal, the drift length should be higher than the distance between the electrodes. Semiconductors with high mobility (intuitively the velocity of charge carriers inside the material) and high lifetime (average time after which the charge carriers become useless for conduction) are desired.

- **Structural confinement.** Diffusion of charge carrier should be negligible with respect to the drift. Charges can diffuse in unwanted directions due for example to a concentration gradient. However, this effect should be minimum to ensure in a pixelated detector good spatial resolution.

- **High band gap.** The dark current (I_{dark}) in the detector should be as small as possible. When a potential difference is applied to a semiconductor a current is measured even when no radiation is present. This current is called dark current. In semiconductors, the thermal energy is sufficient to excite some electrons, following the Boltzmann distribution, in the conduction band generating free charges that can move generating a base current. The dark current is a source of noise, with high dark current is impossible to detect the small fluxes of ionizing radiations. The dark current mainly depends on the band gap of the material. The smaller the band gap the higher are the free charges thermally excited. The presence of trap states can also increase the dark current. Kabir and Kasap report an ideal dark current density of 0.1 nA/cm; commercially available detectors exhibit dark current density below 50 nA/cm^{-2} [31], [32]

- **Low limit of detection (LoD)**. The LoD corresponds to the lowest detectable absorbed energy per unit time, and it defines applicability of target detector. For medical diagnostics, a limit of detection below 5.5 μGy s^{-1} is desired. For CT scans pulses below 1 μGy s^{-1} are used [33].

- **Fast time-response.** This is also feature of crucial importance when evaluating the application of a detector. The current pulse generated inside the semiconductor is characterized by a rise and fall times. Both should be as lower as possible if the application employs a train of radiation pulses. As time-response is dependent on the nature and energy of the incoming radiation, precise values can be extracted for state-of-the-art devices.

- **Radiation hardness.** The detector should be radiation hard, meaning that the properties of the semiconducting material should not change during and after the ionizing radiation exposure. The high energy of ionizing radiation can cause damage to the semiconducting material creating defects and trap states. Defects induced by the radiation can degrade the performance of the detector.

- **Uniformity.** The properties of the material must be uniform all over the active area of the detector. This guarantees that radiation is coherently absorbed, and no form factors are required for precise post-processing.

Notably, two points in the above list are in contrast. The band gap choice is a trade-off between the intrinsic sensitivity and the dark current value. For low and stable dark current, a high band gap semiconductor is desired; but the higher the band gap is, the lower the number of electron-hole pairs generated by the incoming radiation is. To overcome the problem of high dark current, a common strategy for direct detectors adopts a *p-n* junction to reduce the dark current. It consists of a highly doped p region in contact with a highly doped n layer. A charge depleted region occurs at the interface of the n- and p-type regions. This region, depleted from the charges, is created as a result of both electrons diffusion from the n-type material into the p-type one and holes diffusion from p-type to n-type material. Therefore concentration-driven diffusion is responsible for the existence of a space charge region. This region is composed of two zones: a first zone made of filled electron acceptor sites not compensated by holes and a second zone made of positively charged empty donor sites not compensated by electrons. The space charge creates an electrical field that reduces further diffusion. At equilibrium, the field is strong enough to prevent additional net diffusion across the junction, a steady state charge distribution is obtained. Therefore, the depletion region acts like a high resistivity parallel plate ionization chamber, making it feasible to use a diode junction for radiation detection. Due to the electric field created inside the semiconductor, electron-hole pairs produced within the depletion region migrate out and their motion gives rise to an electrical signal. For this reason, the depletion region represents the sensitive volume of the semiconductor detectors. The performance of the junction is improved by applying a reverse bias, meaning the n-type region is connected to the high potential output and the p-type region is connected to the low potential output of an external generator. As the reverse bias increase, both the width of the depletion region and the electric field increase thus leading to better performance. In modern detectors an intrinsic semiconductor layer is interposed between the p and n regions, creating a p-i-n photodiode. The intrinsic layer acts as the absorbing region while the p and n layers act as the charge extraction and transport layers.

1.1.2.3 Detection modes

The operational principles of solid-state detectors can be modified, and their properties fine-tuned depending on the required types of measurement and intended application. Specifically, radiation detection is thought to yield two primary outcomes: signals in the form of electrical current or energy-resolved counts. In current mode, the total charge generated within the semiconductor material is integrated over time, producing an electrical current that reflects the average rate of charge deposition. This is of high effectiveness when the rate of incoming ionizing particles is high and individual events -each ionizing particle interacting with the active material releasing energy is called event- cannot be easily distinguished.

Conversely, a detector operating in pulse mode measures the charge deposited by a single radiation event. Unlike current mode, this is possible because the detector’s response time is typically longer than the time between successive events, even in relatively high-flux conditions. As the charge collected per event is proportional to the energy deposited by the radiation, it is possible to perform energy-resolved measurements. This capability leads to the technique known as charge spectroscopy, where the energy of the incident radiation can be determined by analysing the charge from individual events. Charge spectroscopy is crucial in various scientific fields, such as nuclear physics, medical imaging, and environmental monitoring, where precise energy measurements are necessary for identifying radiation types and understanding particle interactions.

The working principles described above are sketched below for a perovskite-based device.

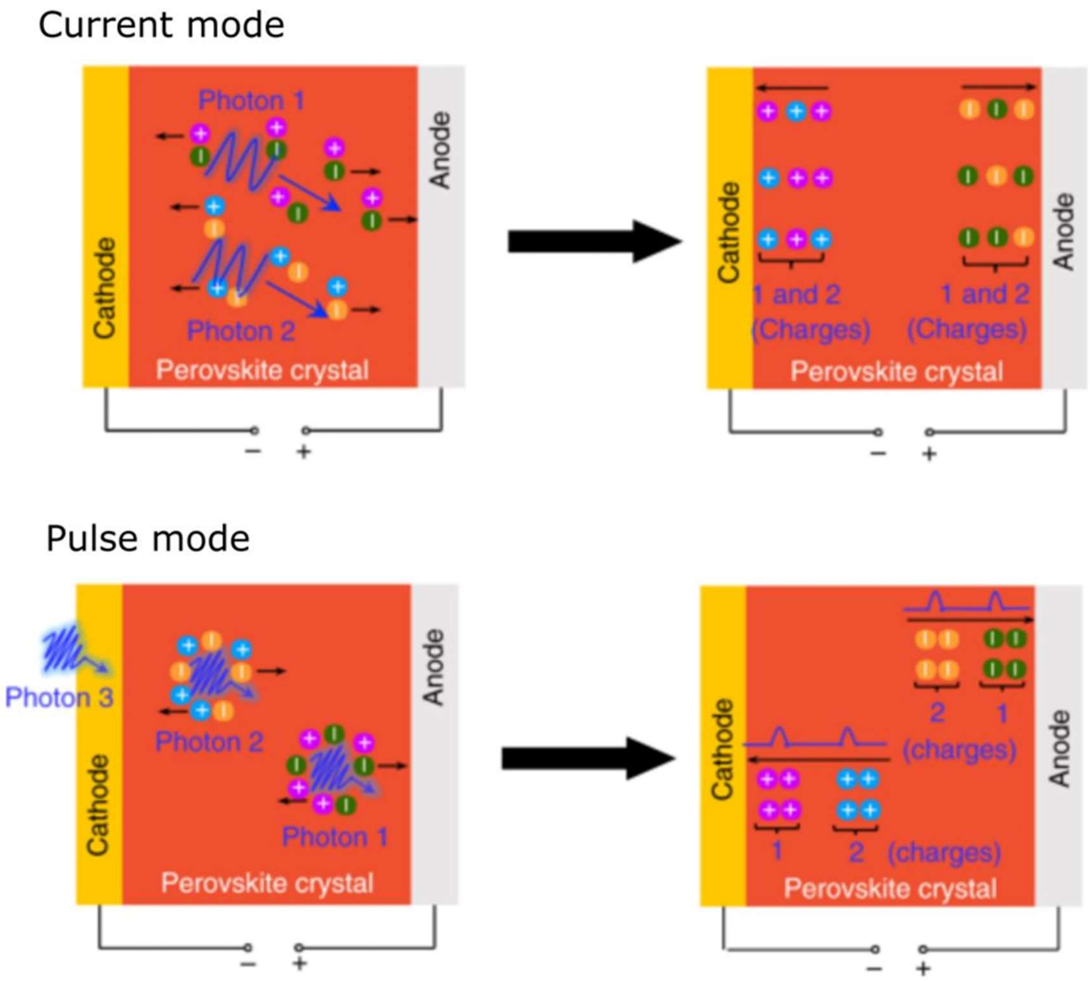

Figure 4 Current and pulse mode. In current mode the detector collects the charges independently of the single-events. Outcomes are in the form of integrated charge as function of time, that is time-dependent generated current. In pulse mode the charge generated from every single event is collected is separate times creating current pulses to be processed and converted into counts per energy [3].

1.1.3 DOSIMETRY

Dosimetry is the measurement, calculation, and assessment of ionizing radiation doses absorbed by matter, particularly biological tissue. When ionizing radiation interacts with matter, it can eject electrons from atoms, producing ion pairs. This process disrupts atomic and molecular structures, thus leading to chemical reactions that can alter or damage cellular components, including DNA. The resulting damage can induce cellular dysfunction, mutations, apoptosis, or carcinogenesis, depending on dose and radiation type.

Because of their importance in personnel protection at radiation-producing facilities and in the medical applications of radiation, the concepts of radiation exposure and dose play prominent roles in radiation measurements. In the following sections, we introduce the fundamental concepts that underlie the quantities and units of importance in this area; then, dedicated applications are listed. Finally, a brief overview of state-of-the-art devices employed for medical imaging and environmental safety is provided.

1.1.3.1 Quantities of Interest

In dosimetry, three key quantities are fundamental to understanding and quantifying radiation interactions with matter: absorbed dose, dose rate, and fluence.

1. Absorbed dose (D) is the amount of energy deposited by ionizing radiation per unit mass of the material. It is expressed in Grays (Gy), where 1 Gy equals 1 joule of radiation energy absorbed per kilogram of material. For example, if a tissue absorbs 2 joules of energy from radiation and weighs 1 kg, the absorbed dose is 2 Gy. Absorbed dose is crucial in both radiation therapy, where precise doses are delivered to tumors, and radiation protection, where exposure limits are monitored.
2. Dose rate refers to the rate at which the absorbed dose is delivered over time, typically in Gy per second (Gy/s) or per hour (Gy/h). This quantity is critical in applications like radiation therapy, where not just the total dose but the speed of delivery can impact biological effects. For example, a high dose rate may cause different tissue responses compared to the same dose delivered slowly. In a clinical context, balancing dose rate is vital to minimize damage to healthy tissue while maximizing the effect on tumors.
3. Fluence (Φ) represents the number of particles (photons, electrons, neutrons, etc.) passing through a given area, often measured in particles per square centimeter (cm^2). The fluence helps determine how many radiation particles interact with the material, which, when combined with the particles' energy, allows for the calculation of the absorbed dose. For instance, in neutron dosimetry, a fluence of neutrons can help estimate how much energy they transfer to the tissue, based on their interactions.

These quantities are interrelated: the fluence and energy of radiation particles determine the absorbed dose, while the dose rate affects how rapidly this energy is delivered. Understanding these parameters is essential in fields such as medical imaging, radiation therapy, nuclear safety, and space exploration, where precise control and measurement of radiation exposure are critical for both effective treatment and protection against harmful radiation effects.

1.1.3.2 Real-life applications

With the advent of radiation-based technologies, the need for precise dosimeters that quantify absorbed dose has become impelling. The following briefly gathers radiation technologies and hazardous environments to be provided radiation detection systems; the latter will be extensively discussed in sec. 1.1.3.3.

- **Radiation Therapy in Oncology**: Dosimetry is critical in calculating and verifying the absorbed dose delivered to cancerous tissues during radiation therapy. Precision in dose delivery is necessary to maximize tumor eradication while minimizing damage to surrounding healthy tissues. Devices such as ionization chambers, thermoluminescent dosimeters (TLDs), and semiconductor detectors are used to monitor dose rates and ensure treatment effectiveness.

- **Radiation Protection and Monitoring in Nuclear Facilities**: Workers in nuclear power plants and research reactors require continuous monitoring to prevent overexposure to ionizing radiation. Dosimetry systems, such as personal dosimeters (e.g., film badges, electronic personal dosimeters), measure cumulative radiation exposure over time to ensure compliance with safety standards set by regulatory authorities.

- **Environmental Monitoring of Radiation Levels**: Dosimetry devices are used to monitor natural and artificial radiation in the environment, particularly near nuclear sites, laboratories, or areas affected by radiation accidents (e.g., Chernobyl or Fukushima). Geiger-Müller counters, scintillation detectors, and environmental dosimeters are used to track radiation levels and ensure public safety.

- **Space Missions and Astronaut Safety**: In space, astronauts are exposed to high levels of cosmic radiation, which can lead to long-term health risks. Dosimetry devices are deployed on spacecraft and within habitats to measure radiation exposure from cosmic rays, solar particles, and other sources. Solid-state dosimeters and tissue-equivalent proportional counters are commonly used for these purposes.

- **Industrial Radiography and Non-Destructive Testing (NDT)**: In industries such as aerospace and civil engineering, dosimetry is used to monitor radiation exposure during X-ray or gamma-ray imaging for the inspection of materials and structures. Dosimetry systems ensure that the operators and surrounding environment remain safe while providing precise control over the radiation used for imaging.

- **Medical Imaging**: Diagnostic techniques such as computed tomography (CT), positron emission tomography (PET), and X-ray imaging require dosimetry to measure patient exposure and optimize the trade-off between image quality and radiation dose. This ensures diagnostic efficacy while adhering to radiation safety standards.

- **Brachytherapy**: In this form of internal radiation therapy, small radioactive sources are implanted near or inside the tumor. Dosimetry ensures that the dose delivered from the implanted source is within the therapeutic range while sparing adjacent healthy tissues. In vivo dosimetry and radiochromic films are commonly used for dose verification.

- **Radiopharmaceuticals and Nuclear Medicine**: When radioactive substances are administered to patients for diagnostic or therapeutic purposes, such as in PET or radioiodine therapy, dosimetry devices are used to calculate the dose absorbed by various organs, ensuring that the therapeutic benefit is maximized, and potential side effects are minimized.

- **Airline and Aviation Industry**: Pilots and crew members are exposed to higher levels of cosmic radiation due to the altitude of flights. Dosimetry is used to track cumulative exposure, particularly for those on long-haul international flights, ensuring that doses remain within permissible limits established by aviation safety authorities.

- **Radiation Accident Response and Contamination Assessment**: In the event of a radiation accident or leakage, portable dosimetry systems are used for the rapid assessment of radiation levels, contamination, and the distribution of radioactive materials. These devices help guide evacuation protocols and cleanup operations, ensuring minimal radiation exposure to emergency responders and the public.

1.1.3.3 State of the art of dosimetry

- **Silicon-Based Semiconductor Dosimeters (Si-Diodes)**: These dosimeters use silicon diodes to measure ionizing radiation with high sensitivity and fast response times. They are widely used in real-time dosimetry, especially in radiation therapy and intraoperative radiotherapy (IORT) due to their compact size, energy dependence, and suitability for precise dose measurements [34], [35].

- **Metal-Oxide-Semiconductor Field-Effect Transistor (MOSFET) Dosimeters**: MOSFET dosimeters leverage the radiation-sensitive properties of MOS capacitors to provide highly accurate, dose-rate-independent measurements. They are popular in medical physics and in vivo dosimetry for their ease of calibration and small size, making them suitable for precise placement in body cavities during radiotherapy [36], [37].

- **Optically Stimulated Luminescence Dosimeters (OSLDs)**: OSLDs, based on materials like Al_2O_3, measure radiation exposure through light emitted when the detector is stimulated by a light source after radiation exposure. These devices are used in personnel monitoring, environmental dosimetry, and medical applications. OSLDs offer advantages such as reusable detectors, high sensitivity, and long-term stability [38].

- **Thermoluminescent Dosimeters (TLDs)**: TLDs, typically made of LiF or $CaSO_4$, are highly sensitive to radiation and provide precise, cumulative dose measurements. After exposure, the dosimeter is heated, causing it to emit light proportional to the absorbed dose. TLDs are commonly used in radiation therapy, radiation protection, and personal dosimetry due to their reliability and ability to measure a wide range of doses [39].

- **Radiochromic Film Dosimeters**: These dosimeters consist of polymer-based films that change color in response to radiation, providing a visual indication of the absorbed dose. Used extensively in radiation therapy QA (quality assurance) and 2D dose mapping, radiochromic films such as Gafchromic™ films are valued for their high spatial resolution, dose range, and tissue-equivalent properties [40], [41].

- **Diamond Detectors**: Leveraging the radiation-sensitive properties of synthetic diamond crystals, diamond dosimeters offer exceptional tissue equivalence and radiation hardness. They are increasingly used in proton therapy and hadron therapy, where precision dosimetry in high-energy particle beams is crucial for patient treatment accuracy [42], [43].

- **Fiber Optic Dosimeters (FODs)**: FODs use radiation-sensitive materials embedded in optical fibers to detect changes in the optical properties of the fibers under radiation exposure. These dosimeters are valuable in remote sensing and in vivo dosimetry, especially in harsh environments such as space and nuclear reactors, where other dosimeters might fail due to high radiation levels [44].

- **Plastic Scintillator Dosimeters**: These dosimeters are based on organic scintillators that emit visible light when exposed to ionizing radiation. The emitted light is collected and analyzed to determine the absorbed dose. Plastic scintillator dosimeters are used in real-time monitoring, radiation therapy, and high-energy physics experiments due to their fast response and relatively low cost [45].

- **Active Personal Dosimeters (APDs)**: These digital dosimeters provide real-time monitoring and alarm capabilities for occupational exposure. APDs, such as E-Perm® or Instadose™, combine radiation detection with wireless data transmission and dose-tracking software, making them ideal for use in nuclear facilities, medical imaging, and radiation emergency response [46].

- **Ionization Chambers**: While traditional, modern ionization chambers have seen significant advancements in terms of digital readouts, miniaturization, and accuracy. These dosimeters are widely used for absolute dose measurements in calibration labs, radiation therapy, and environmental monitoring. Their reliability, wide energy range, and stability make them a cornerstone of radiation dosimetry [47].

Major advantages include compactness, reusability, and the ability to provide accurate dose measurements across a wide energy range. However, some dosimeters face limitations, such as energy dependence (e.g., Si-diodes), dose saturation (e.g., TLDs), or complex readout systems (e.g., FODs). On top of that, major challenge to be faced is the high fabrication cost and the need for active materials to be easily processed and scaled to large area devices. An additional requirement is operational reliability in radiation harsh environments like high intensity beam for medical therapy or space applications.

To enhance their performance, improvements in energy independence, response time, and spatial resolution are needed, alongside advancements in material science, miniaturization and data integration for real-time monitoring in radiation environments.

1.2 METAL HALIDE PEROVSKITES FOR RADIATION DETECTION

Research and development efforts toward next-generation materials for the detection of high-energy radiation have been intensified in recent years. The majority of ongoing efforts are geared toward improving the manufacturability and sensitivity of the detection elements and systems. This is why the development and/or discovery of materials that combine key functionalities with inexpensive manufacturing has become a hot area of research.

Metal halide perovskites (MHPs) have emerged as a prime candidate semiconductor technology for application in third and fourth generation photovoltaics while simultaneously making significant strides in other areas of optoelectronics [48], [49], [50]. Photodetectors are one of the latest additions in an expanding list of applications of this high-performing family of materials[51]. The extensive range of possible inorganic and hybrid perovskites coupled with their processing versatility and ability to convert external stimuli into measurable optoelectronic signals makes them potential active sensors even for the high-energy domain of the electromagnetic spectrum[52], [53], [54], [55], [56].

Key to this is the presence of heavy elements as their internal core, that also grants large, high-quality crystals and polycrystalline layers, thus making them one of the most promising emerging X-ray and γ-ray detector technologies. In this chapter, the fundamental principles of high-energy radiation detection through perovskites are reviewed starting from their internal structure and optoelectronic properties. To guide the readers towards the target application of this work -that is 2D layered perovskite thin films- an extensive paragraph is dedicated to the impact of dimensionality on MHP performance[57], [58], [59], [60]. This straightforwardly leads to the main reason behind the choice of PEA_2PbBr_4 as active layer for high energy radiation detection. Finally, emphasis is put on recent progress in the emerging field of metal halide perovskite-based X-ray, γ-ray, protons and neutrons detection. In this last section a distinction is made between high-performance devices in the form of single crystal and highly applicable thin film structures. This is intended to give the reader an overview of the power of the latter in matter of immediate impact on the improvement of modern healthcare systems.

1.2.1 STRUCTURE AND FEATURES

Perovskites encompass a large family of materials, usually described by the general chemical formula ABX_3. The first perovskite structure material was the calcium titanium oxide mineral ($CaTiO_3$), discovered by Gustav Rose in 1839, and named after the Russian mineralogist Lev Perovski[61]. Perovskites are divided into subgroups depending on their chemical composition and structure. This is often translated into the words “different dimensionality”, on which we will come up later as this will be key for understanding performance metrics. In traditionally called three dimensional (3D) ABX_3 perovskites, the B-site element is octahedrally coordinated in a BX_6 configuration. The A component is situated within the cuboctahedral cavity formed by nearest-neighbor X atoms in an AX_{12} polyhedron. Perovskites can also exist in a layered form, often termed 2D, with the ABX_3 structure separated by thin sheets of spacer material. Synthetic versions of perovskite materials involving organic as well as inorganic cations have also been developed and exploited for a range of applications (Figure 5).

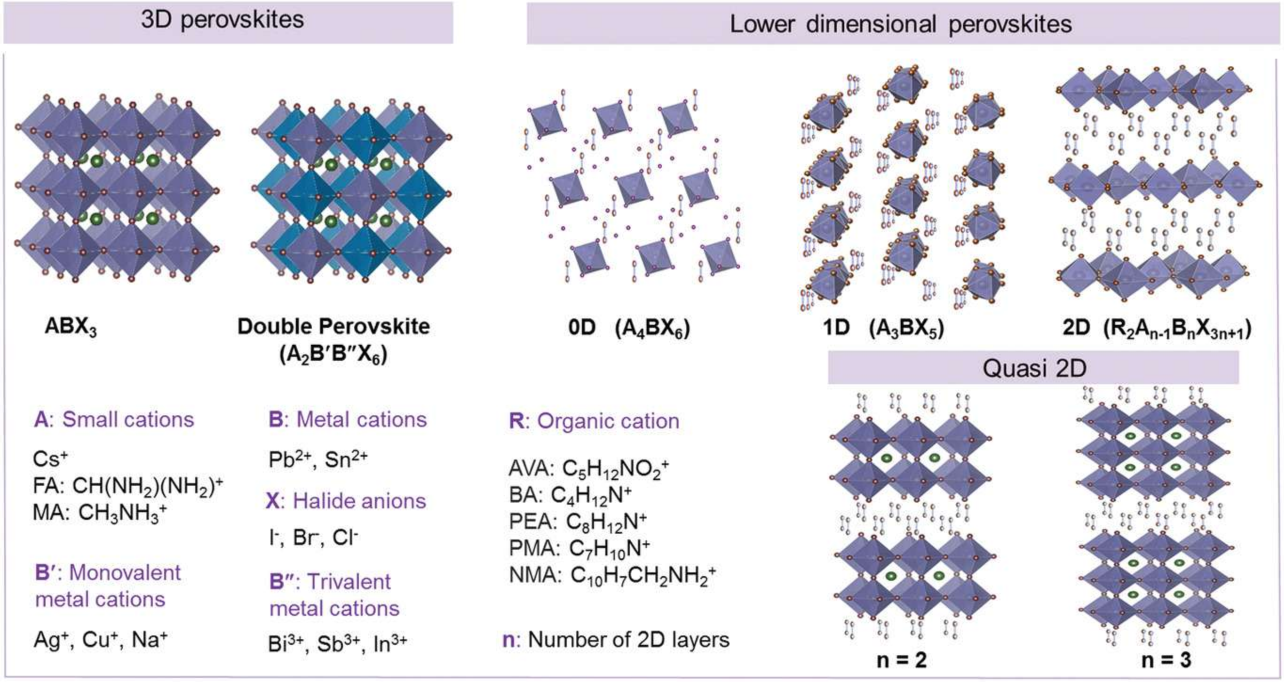

Figure 5 Schematic representation of the structures of 3D (simple and double), 0D, 1D, 2D, and quasi-2D perovskites. Also shown are some examples of commonly used metal and organic cations[3] .

The structure of 3D perovskite can be described by the cubic contractual formula of $A^{+1}M^{+2}(X^{-1})_3$, where each A (an organic group or an inorganic cation) has twelve neighboring X (halide atoms), and each M (a metal cation) connects with six adjacent X through ionic bonds. When a suitable organic molecule is employed as the A cation (e.g., MA$^+$ (methylammonium): $CH_3NH_3^+$ or FA$^+$ (formamidinium):$CH(NH_2)_2^+$), the resulting material is an inorganic–organic hybrid metal halide perovskite (MHP) (Figure 5). On the other hand, if the A cation is an inorganic atom, such as cesium (Cs$^+$), the resulting compound is an inorganic MHP.

The tolerance factor (t), a parameter first introduced from Goldschmidt in 1926, is often used to predict the stability of the perovskite lattice based on the ionic radii (r) of A (r_A), B (r_B), and X (r_X), and is given as[62], [63]:

$$t = \frac{r_A + r_x}{\left[\sqrt{2}(r_B + r_X)\right]}$$

For a perfectly cubic perovskite lattice, t is close to 1[64]. Empirically, the majority of MHPs synthesized to date form in the range $0.81 \leq t \leq 1.0$. Hexagonal structures are typically formed when $t > 1$, and non-perovskite structures are formed when $t \leq 0.8$[65]. Besides t, the octahedral factor (μ), i.e., the ratio of the ionic radius of B site to the A site, provides a measure of the octahedral stability of the perovskite and is usually found in the range of $0.44 \leq \mu \leq 0.9$[66]. The combination of those two factors defines the important parameter space for perovskite formability and stability.

1.2.2 PARAMETERS OF INTEREST FOR RADIATION DETECTION

This paragraph gathers and reviews structural and optoelectronic properties of MHPs that make them suitable for radiation detection. The elements here listed are to be coupled with ideal devices main features listed in sec. 1.1.3. We will go deep into specific requirements of perovskite-based devices later this chapter.

Table 1 summarizes the points listed below.

- **High Atomic Number, Material Density, and Stopping Power**

The high-Z atoms (like Pb, Cs, and Br) that are incorporated into MHPs have large atomic numbers, which lead to strong interactions with high-energy photons. According to the relationship Z^4/AE^3, where Z is the atomic number, A is atomic mass, and E is photon energy, the probability of absorbing X-rays or γ-rays increases significantly with higher Z values. This absorption occurs because photons interact more readily with the tightly bound inner electrons of heavy atoms, leading to more efficient energy transfer.

Additionally, the high density of MHPs (~4 g/cm^3) means that a larger number of these high-Z atoms are packed into a given volume, increasing the likelihood of photon interaction. This high material density and the presence of heavy atoms together contribute to their high stopping power, which is the material's ability to attenuate or block high-energy radiation.

- **Optimal Charge Transport**

The large mobility-lifetime ($\mu_{e/h} \times \tau$) products in MHPs are mainly due to their favorable electronic structure. In perovskites like $MAPbI_3$, the conduction and valence bands are composed primarily of the s and p orbitals of Pb^{2+} and the p orbitals of halide ions (e.g., I^-)[67]. These orbitals hybridize in such a way that it reduces the formation of deep electronic traps. Shallow traps dominate instead, which means that charge carriers (electrons and holes) are less likely to be trapped and recombined prematurely[68].

Moreover, MHPs exhibit long carrier diffusion lengths and low non-radiative recombination rates[69]. This is partially due to strong spin-orbit coupling from the heavy Pb^{2+} cations, which further influences the band structure, leading to smaller band gaps and reducing the likelihood of deep trap formation. These factors, in turn, contribute to long carrier lifetimes (τ) and high mobility (μ), allowing the charges to travel further and more efficiently within the material before being collected at the electrodes.

- **Low Charge Trap Density and Defect Tolerance**

One of the most unique properties of MHPs is their exceptional defect tolerance[70]. In many semiconductors, defects (e.g., vacancies, interstitials) create deep traps that cause charge carriers to recombine non-radiatively, leading to performance losses. However, in perovskites, the nature of the bonding between Pb^{2+} and the halide ions (e.g., I^-, Br^-) leads to shallow traps instead of deep ones. This means that even if there are defects, charge carriers can still move relatively freely without being permanently trapped.

Additionally, the high dielectric constant of MHPs helps to screen charge carriers from these defects. The strong polarizability of Pb^{2+} results in a high Born effective charge, which reduces the electrostatic interactions between charge carriers and charged defects. This makes it harder for defects to capture charge carriers, further enhancing charge transport.

- **Wide Band Gap Tunability**

The band gap of MHPs can be easily tuned by adjusting the composition of the material, especially the halide components (e.g., I, Br, or Cl). By mixing or substituting different halides or cations (e.g., replacing MA^+ with FA^+ or Cs^+), the band gap can be precisely controlled to span different parts of the electromagnetic spectrum[71]. For example, $MAPbI_3$ has a band gap around 1.55 eV, making it suitable for absorbing visible light, but by modifying the halides, the band gap can be shifted to allow absorption from visible light up to hard X-rays.

This tunability is highly advantageous for radiation detection, as it allows MHPs to be optimized for detecting different types of radiation across a broad energy spectrum[72].

- **Fast Response Times**

The fast response times of MHPs, typically in the hundreds of nanosecond range[73], can be attributed to the high mobility and low trap density discussed earlier. The rapid transport of charge carriers (electrons and holes) through the material allows for quick generation and collection of signals in response to radiation.

Additionally, the combination of large $\mu_{e/h} \times \tau$ products and low recombination rates ensures that once carriers are generated, they can be quickly collected without being lost to non-radiative processes. This is crucial for applications like medical imaging, where fast detection speeds are essential.

- **Processing Flexibility and Cost-Effectiveness**

The chemical composition and crystal structure of MHPs allow them to be processed at low temperatures, typically around 100–150°C, using relatively simple solution-based or vapor-phase methods[74], [75]. Unlike traditional semiconductor materials such as silicon or CdTe, which require high-vacuum and high-temperature processes, perovskites can be deposited in thin films through methods like spin-coating or vapor deposition, making the fabrication process cheaper and more scalable.

The flexibility in processing also means that MHPs can be applied to a variety of substrates, including flexible or curved surfaces, which opens up new possibilities for detector designs that are lightweight, flexible, and adaptable to various form factors.

- **High Dielectric Constant**

The high dielectric constant of MHPs (especially Pb-based perovskites) is another contributing factor to their superior performance as radiation detectors. A high dielectric constant means that the material can better screen electrostatic interactions between charge carriers and defects, reducing the likelihood of carriers being captured by traps. This is particularly important for maintaining high charge-carrier mobilities and minimizing losses due to recombination.

The high dielectric constant is primarily due to the strong polarizability of the Pb^{2+} ions and their bonding with halides, which increases the material's ability to dissipate localized charge, enhancing the overall efficiency of the detector[76].

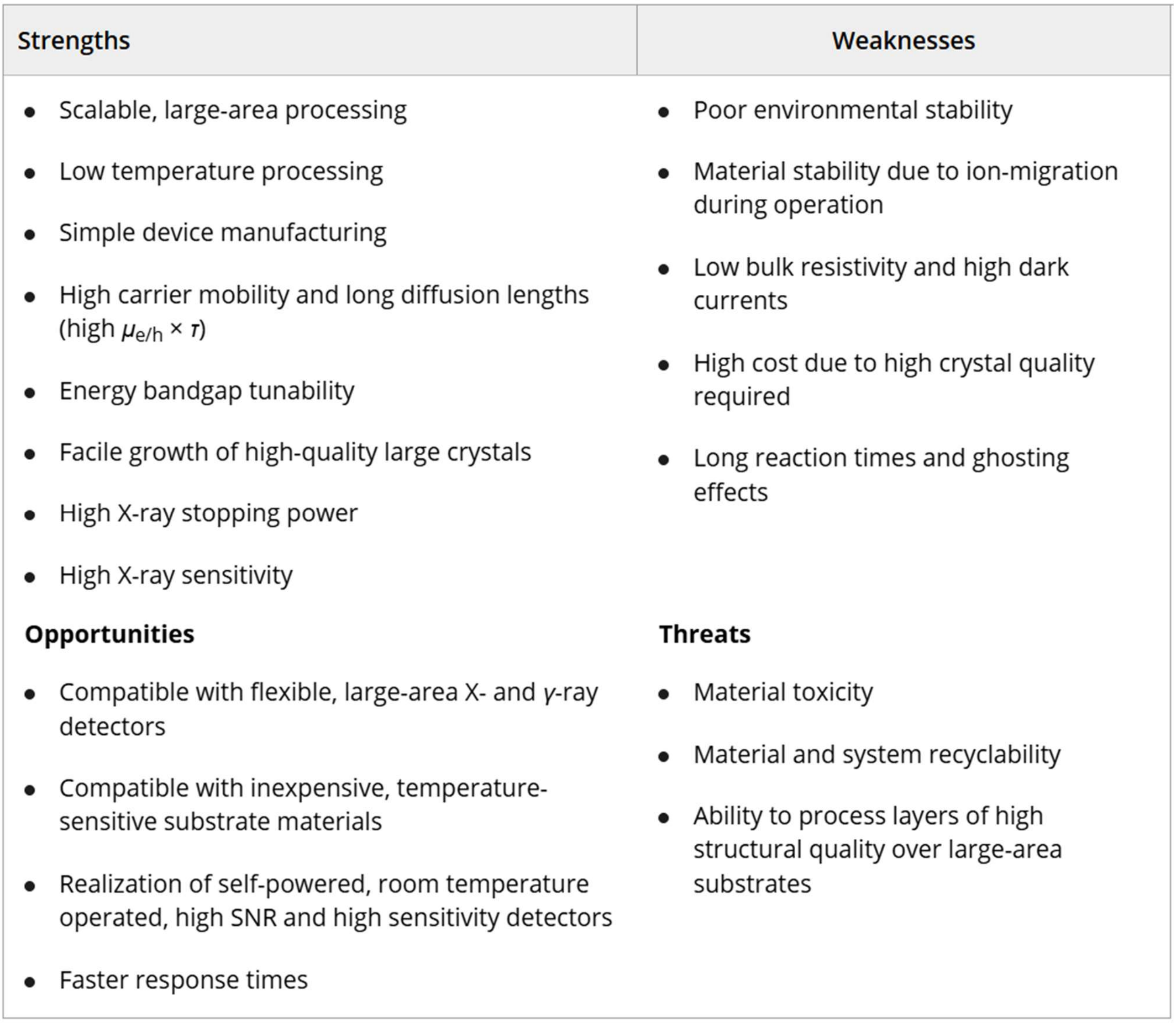

Strengths	Weaknesses
• Scalable, large-area processing • Low temperature processing • Simple device manufacturing • High carrier mobility and long diffusion lengths (high $\mu_{e/h} \times \tau$) • Energy bandgap tunability • Facile growth of high-quality large crystals • High X-ray stopping power • High X-ray sensitivity	• Poor environmental stability • Material stability due to ion-migration during operation • Low bulk resistivity and high dark currents • High cost due to high crystal quality required • Long reaction times and ghosting effects
Opportunities	**Threats**
• Compatible with flexible, large-area X- and γ-ray detectors • Compatible with inexpensive, temperature-sensitive substrate materials • Realization of self-powered, room temperature operated, high SNR and high sensitivity detectors • Faster response times	• Material toxicity • Material and system recyclability • Ability to process layers of high structural quality over large-area substrates

Table 1 Strengths, weaknesses, opportunities, and threats (SWOT) analysis from a material point of view for metal halide perovskite-based X-ray and γ-ray detector technologies[3].

However, in the case of most studied MHPs, the reliance on toxic elements, such as Pb, represents a significant environmental challenge that would need to be addressed before commercial deployment.

1.2.3 IMPACT OF DIMENSIONALITY

As previously mentioned, MHPs have outstanding optoelectronic properties, namely high charge-carrier mobilities, long diffusion lengths, tunable band gaps, long charge carrier lifetimes, high defect tolerance and high absorption coefficients. This has been key in enabling MHP thin films to be grown by simple solution- and vapor-based methods at low temperatures (typically at 100–150 °C) while achieving high efficiencies surpassing those of other thin film and multicrystalline silicon solar cells[77], [78], [79].

To a large extent, the beneficial properties of the MHPs can be attributed to the presence of Pb (and in analogous form Sn in Sn-based perovskites). However, when it comes to actual applicability and required outcomes, dimensionality results to be a key factor that directly impacts their electronic structure, excitonic behavior, dielectric properties, and overall optoelectronic performance. In 3D MHPs, the extended crystal structure provides a highly delocalized electronic band structure, where charge carriers (electrons and holes) experience relatively weak Coulomb interactions[80]. This is due to efficient dielectric screening provided by the bulk perovskite material, which results in low exciton binding energies, typically on the order of 10-50 meV[81]. Such low exciton binding energies facilitate free charge carrier generation upon photoexcitation, making 3D perovskites particularly well-suited for photovoltaic applications, where efficient charge separation and transport are critical. The high charge carrier mobility in 3D perovskites is further supported by their high dielectric constants, which suppress carrier scattering from charged defects, resulting in long diffusion lengths and low non-radiative recombination rates.

As the dimensionality is reduced from 3D to 2D or quasi-2D perovskites, significant quantum confinement effects emerge, dramatically altering their electronic and optical properties[82]. In 2D and quasi-2D perovskites, the spatial restriction of charge carriers to fewer degrees of freedom increases their localization, leading to stronger Coulomb interactions between electrons and holes. This confinement, combined with reduced dielectric screening, results in significantly higher exciton binding energies, often exceeding 200 meV[83], [84]. As a result, excitonic effects dominate the optical and electronic behavior in these lower-dimensional systems. The increased exciton binding energy not only enhances exciton stability but also shifts the absorption edge to higher energies, resulting in a blue-shifted bandgap compared to their 3D counterparts[85].

Furthermore, the dielectric contrast between the inorganic perovskite layers (which exhibit high dielectric constants) and the organic spacers or ligands (which possess much lower dielectric constants) in quasi-2D and 2D perovskites leads to a pronounced polarization effect. This polarization gives rise to the so-called "image charge effect," where the effective Coulomb potential between electron-hole pairs is enhanced, further increasing exciton binding energy and reducing the screening of charge carriers[86], [87]. This effect also enhances the radiative recombination efficiency in 2D perovskites, making them ideal candidates for light-emitting applications, such as light-emitting diodes (LEDs) and lasers, where strong exciton emission is desirable[88], [89].

Additionally, the reduced dimensionality impacts the charge transport properties in MHPs. In 2D and quasi-2D perovskites, the presence of insulating organic spacers between perovskite layers introduces a barrier to out-of-plane charge transport, leading to anisotropic charge carrier mobility[90]. While in-plane mobility can remain relatively high due to the inorganic nature of the perovskite layers, out-of-plane transport is hindered by the organic spacer layers, resulting in increased resistance and reduced carrier mobility in the perpendicular direction. This anisotropy in charge transport is a trade-off that must be considered when optimizing these materials for specific applications[91].

Moreover, reduced-dimensional MHPs exhibit enhanced environmental stability compared to their 3D counterparts. In 3D perovskites, the extended crystal structure can be more prone to degradation from moisture, oxygen, and thermal stress. In contrast, the organic spacers in 2D and quasi-2D perovskites often serve as protective barriers, improving the material's resistance to environmental degradation[92]. This enhanced stability makes lower-dimensional perovskites attractive for applications requiring long-term stability, such as in outdoor photovoltaics or display technologies.

Finally, the flexibility in tuning the dimensionality of perovskites allows for a wide range of electronic and optical properties[93]. By controlling the number of perovskite layers in quasi-2D systems (often denoted as (n = 1, 2, 3, ...), where n represents the number of perovskite layers), it is possible to engineer the degree of quantum confinement, exciton binding energy, and dielectric screening[94], [95]. For instance, higher values of n lead to properties closer to those of 3D perovskites (lower exciton binding energy, narrower bandgap), while lower values of n increase confinement effects and excitonic behavior. This tunability makes quasi-2D perovskites highly versatile materials for a range of optoelectronic applications, including photovoltaics, LEDs, lasers, and photodetectors.

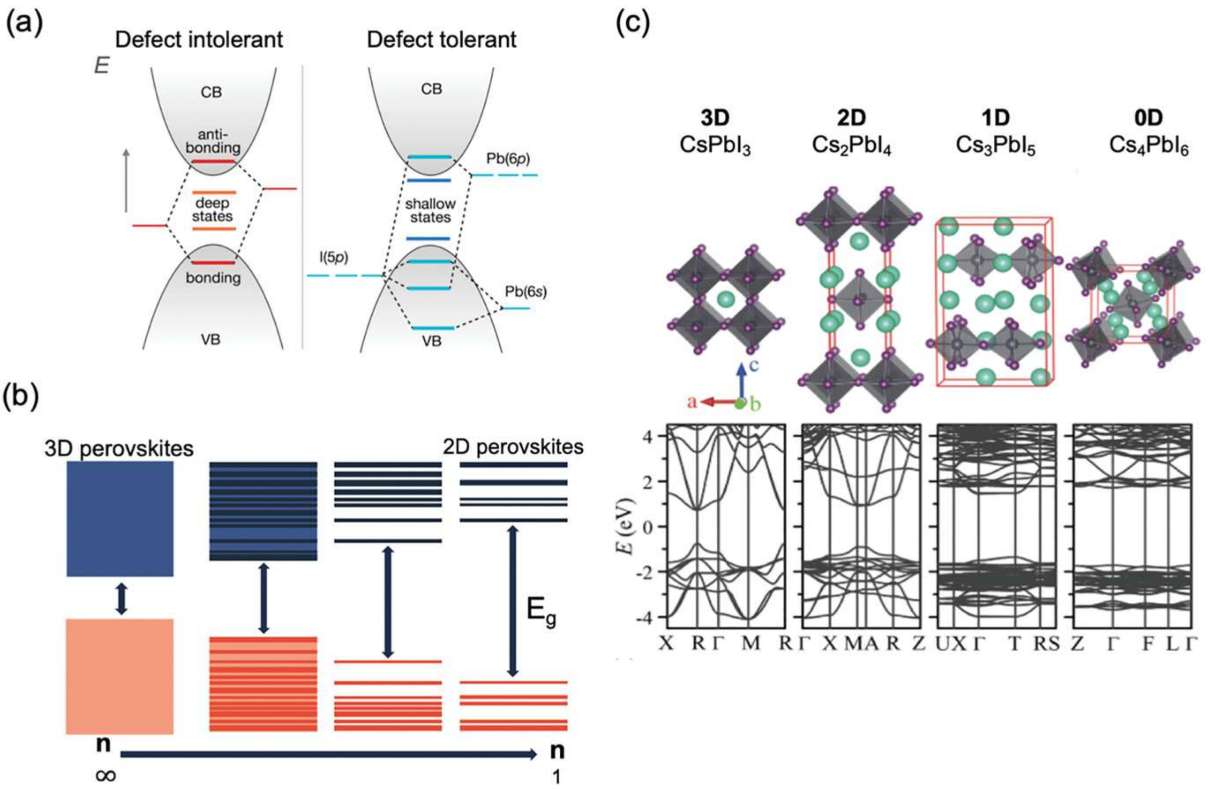

Figure 6 Comparison of the electronic structure of defect sensitive (left) and defect tolerant (right) materials. Illustration of the effect of structural dimensionality on the b) band gap and c) electronic structure and band dispersion[59].

1.2.4 2D LAYERED PEROVSKITES

Pure 2D layered halide perovskites consist of a single monolayer of inorganic corner-sharing lead-halide octahedra, with organic ligands situated both above and below the monolayer. In contrast, quasi-2D perovskites contain *n* inorganic monolayers sandwiched between organic ligands. By increasing the value of *n* from 1 to ∞, the structural dimensionality of the perovskite transitions from 2D to 3D. This transition allows for tuning of the band gap, exciton binding energy, and both thermal and environmental stability across a broad range. Adjusting the dimensionality from pure 3D to quasi-2D and then to 2D can be achieved by altering the ratio of long and short A-site cations, as the longer A-site cations serve as the ligands that sandwich the inorganic layers.

One of the most widely explored classes of 2D or quasi-2D halide perovskites is the Ruddlesden–Popper (RP) family of perovskites (Figure 7a) [59]. The general chemical formula is $R_2A_{n-1}Pb_nX_{3n+1}$, where R is the bulky monovalent organic cation that sandwich the inorganic layers, n the number of PbX_6 layers between the R ligands, A is the small A-site cation that can fit within the cuboctahedral voids of the inorganic layers (usually Cs, FA, or MA), and X is a halide. The bulky organic cations used to form the RP phase in MHPs are typically alkyl chains or phenyl groups. Two of the most common R-site cations are phenylethylammonium (PEA), as shown in Figure 7b, and butylammonium (BA). The former is used for the entirety of this work and coupled with PbBr2 compound.

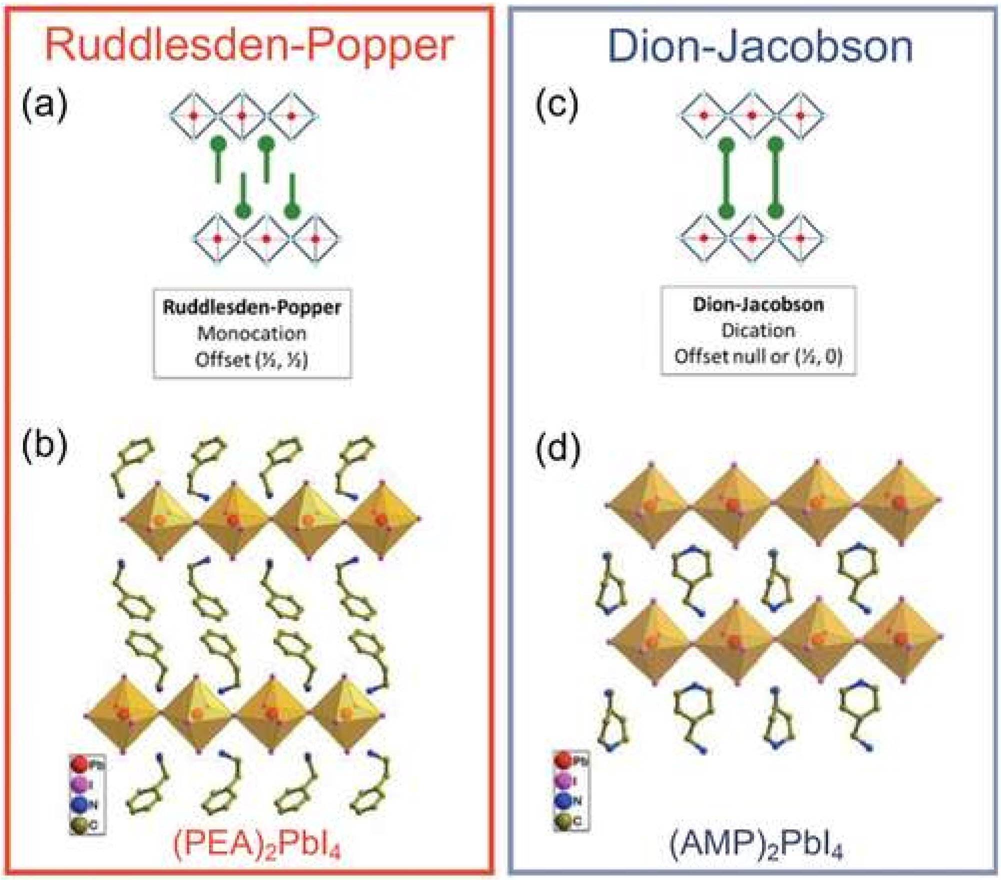

Figure 7 2D perovskites in the a,b) Ruddlesden–Popper and c,d) Dion–Jacobson phases. a,c) A structural comparison of the two phases[96]. b,d) Examples of RP and DJ perovskites, in which the R-site cation is PEA (phenethylamine, $C_6H_5C_2H_4NH_3^+$) (b) for the RP phase, and AMP (4- (aminomethyl)piperidinium) (d) for the DJ phase[97]. Adapted from [59]

Another low-dimensional halide perovskite phase that has been gaining attention is the Dion–Jacobson (DJ) family of perovskites[97]. The key difference between the RP and DJ perovskites is that the DJ perovskites only have one layer of organic cations between the inorganic layers (whereas the RP perovskites have two long organic ligands between the inorganic layers), as illustrated in Figure 7a versus Figure 7c[98]. Furthermore, to maintain charge neutrality, the long-chain cation in DJ perovskites needs to be divalent, whereas in RP perovskites the long-chain cation is monovalent. DJ perovskites can form a stack with either a perfect alignment or a minor displacement depending on the steric demands of the spacer cation The general formula of DJ perovskites is $RA_{n-1}Pb_nX_{3n+1}$. The most common long-chain R cations used in the DJ perovskites are 4-(aminomethyl)piperidinum (AMP or 4AMP; illustrated in Figure 7d), 3AMP, 1,4-phenylendimethanammonium (PDMA), and others[99]. These low-dimensional perovskites can offer several advantages over their 3D counterparts, in terms of improved environmental stability, increased exciton binding energy, and tunability in the band gap, but fully harnessing these advantages to achieve more efficient and stable solar cells and LEDs requires an understanding of how dimensionality affects these properties, the trade off with other optoelectronic properties (e.g., mobility), and how the materials can be grown with controlled preferred orientation. Compared to the RP phase, the DJ phase of MHPs is reported to have a shorter interlayer distance a. As an example, $(3AMP)MA_{n-1}Pb_nI_{3n+1})$ is reported to have a reduced distance $a \approx 4.0$ Å compared to ≈8.0 Å for the RP perovskite $(BA)_2PbI_4$ ($n = 1$)[100].

In 2D metal halide perovskites (MHPs), the structural order significantly impacts mobility and exciton binding energy, as evidenced by various examples presented in Figure 8. For low-dimensional perovskites, the crystallographic orientation is critical, as it governs the diffusion and drift lengths of charge carriers within the plane connecting the two electrodes[101]. In particular, charge movement in 2D MHPs is restricted between layers, owing to the lower band dispersion between layers rather than within the planes of the inorganic layers[102]. It is therefore essential to control the preferred orientation, for example, to achieve efficient charge-carrier extraction in photovoltaics. Tsai et al. [103]developed a hot casting deposition method for tuning the preferred orientation of Ruddlesden–Popper perovskites with $n = 4$ ($BA_2MA_3Pb_4I_{13}$), such that films with a (101) preferred orientation (vertically-aligned inorganic layers) gave 12.5%-efficient photovoltaic devices. Importantly, ageing tests showed that encapsulated and unencapsulated Ruddlesden–Popper perovskites demonstrated improved stability over their 3D counterparts, showing the advantage of the RP phase. Another method to grow vertically oriented 2D perovskites, developed by Chen et al., was achieved by the nucleation and growth of a 2D $BA_2MA_3Pb_4I_{13}$ perovskite from the liquid–gas interface to form a solid top-layer with strong vertical orientation. Grazing-incidence wide-angle x-ray scattering (GIWAXS) measurement results showed different degrees of preferential vertical orientation, where the film highly oriented shows the highest power conversion efficiency[104].

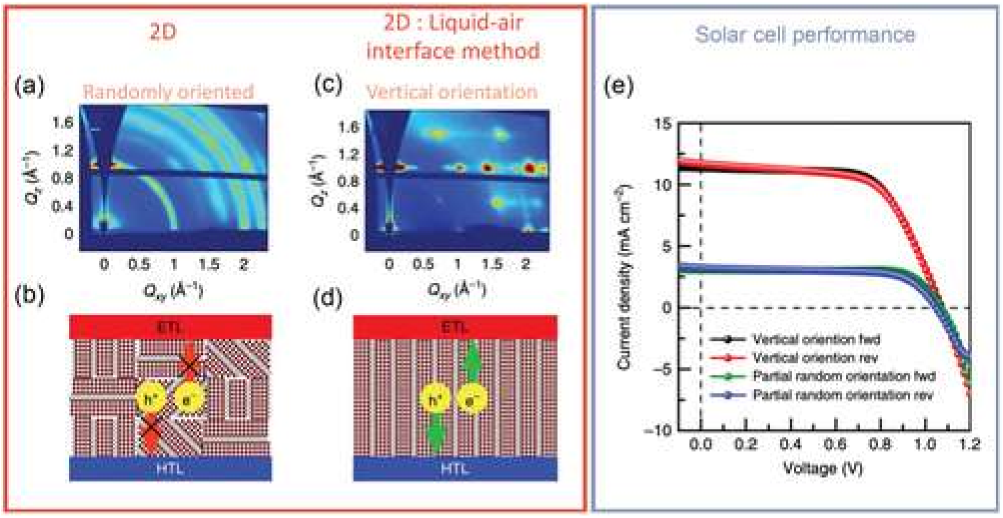

Figure 8 The importance of controlling preferred orientation in solar cells based on RP perovskites [104]. a) grazing incidence wide-angle x-ray scattering (GIWAXS) measurements of 2D perovskite that nucleates in the solvent or solvent/substrate interface and the b) proposed random orientation of the perovskite grains. c) GIWAXS measurements of a 2D perovskite that nucleates from the liquid–air interface, and d) the proposed vertical orientation of the perovskite grains. e) Comparison of the photovoltaic performance of the 2D perovskites with a random versus vertical preferred orientation. Adapted from [59]

Stability

Replacing 3D perovskites with 2D counterparts has resulted in improved moisture stability, attributed to the hydrophobic side chains of the long-chain organic cations. For example, Smith et al. used PEA as a moisture barrier for 2D-RP MHP layers, obtaining films that did not decompose over the entire 46-day stability test in ambient air with 52% relative humidity. $MAPbI_3$, by contrast, started degrading to PbI_2 within 4 days under the same conditions [105].

PEA_2PbBr_4 also showed signal stability under X-ray irradiation with tests run over three years: recorded decrease was <10%[106]. Liao et al. [107]also achieved improved stability over $MAPbI_3$ by using a low-dimensional BA-Cs based RP MHP (where BA is *n*-butylammonium, $C_4H_9NH_3^+$). In general, perovskites incorporating PEA or BA cations demonstrate enhanced anisotropic absorption and emission, along with improved chemical stability. While these alkylammonium organic cations serve as moisture barriers, they do not possess specific functionalities that directly enhance optoelectronic properties, except indirectly by altering the crystal structure or, in some cases, modifying exciton binding energy, as previously reported. The enhancements in environmental stability can be leveraged either by utilizing 2D or quasi-2D MHPs with controlled preferred orientation as the active layer in devices, or by coating 3D perovskites with 2D or quasi-2D perovskites to shield the underlying 3D perovskite from moisture-induced degradation.

DJ perovskites have also been shown to be more stable than 3D $MAPbI_3$ perovskites. In particular, the stability of DJ perovskites is enhanced by the long-chain R cations being hydrogen bonded on both sides to inorganic layers. Conversely, in RP perovskites the R cation is only hydrogen bonded to the inorganic lattice on one side.

Enhanced structural stability is directly correlated to device stability achievement. Shang et al. [108]performed density functional theory (DFT) calculations to compare DJ and RP perovskites. 1,4-bis(aminomethyl)benzene (BAB) molecules were used as the bridging ligands for the DJ perovskite, and the typical PEA ligand was used for the RP phase. Firstly, it was found that the distance between the PbI_6 octahedra was shorter for the DJ perovskite (1.15 nm) compared to the RP perovskite (1.65 nm). The binding energy of the long-chain R cation with the inorganic layer was calculated (note: this is not the same as the exciton binding energy), and these results are shown in fig. 9. Results reveal that the binding energies of DJ and RP perovskites are overall comparable. However, a crucial distinction exists in their dissociation energies: the dissociation energy of RP perovskite is half that of DJ perovskite. This difference arises from the weak van der Waals interactions between the long-chain organic ligands in RP perovskites, whereas DJ perovskites feature interlayer ligands that are more strongly bonded to the inorganic lattice via hydrogen bonds. This can be used to assess higher levels of DJ perovskite stability[109], [110], [111], [112].

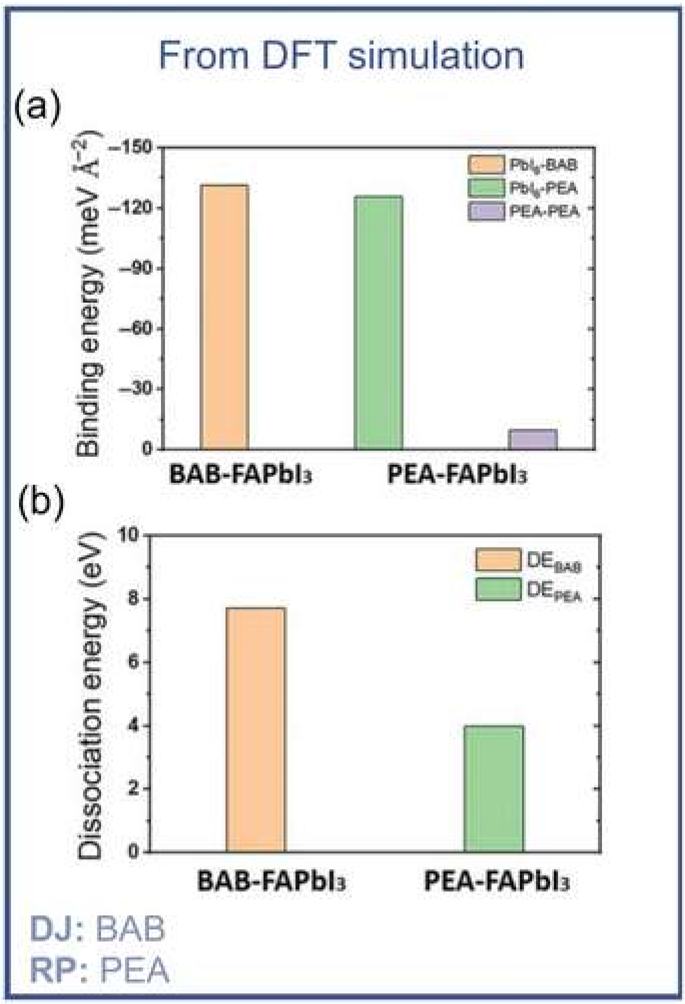

Figure 9 DFT simulations to compare between a Dion–Jacobson (DJ) phase and a Ruddlesden–Popper (RP) 2D perovskite [108]. a) Calculated binding energies between PbI_6-BAB (1,4-bis(aminomethyl)benzene), PbI_6-PEA (phenylethylamine), and PEA-PEA, and the b) calculated molecule dissociation energy of the perovskites based on BAB (DJ phase) and PEA (RP phase). Adapted from [59]

Optoelectronic Properties- Excitons

In addition to free electrons and holes, band-edge excitations can give rise to bound electron-hole pairs that are electrically neutral and which function as quasi-particles -namely, excitons[113]. These structures are exhibited to be prevalent in low-dimensional perovskites. In photovoltaics and other devices generating current from photon absorption (e.g., photodetectors or radiation detectors), excitons need to be dissociated into free carriers in order to extract the electrons and holes in separate electrodes[114], [115]. By contrast, LEDs require electrons and holes to recombine radiatively, and often the injected electrons and holes would first form an exciton [116]. A key parameter is the exciton binding energy E_b, which represents the difference between the excitonic state energy and the material's electronic band gap. When E_b is comparable to or less than kT, excitons can easily dissociate into free carriers due to thermal energy, as seen in 3D MHP and various inorganic materials like silicon at room temperature. While a low E_b is advantageous for photovoltaics, efficient LEDs require enhanced electron-hole confinement. In contrast, materials with high E_b necessitate structures, such as heterojunctions, to facilitate exciton dissociation for photovoltaic applications[117], [118], [119]. Accounting for the E_b of the active material is therefore critical in designing the optimal device structure for desired applications.

Going further, excitons can be classified as low E_b Wannier–Mott excitons (or free excitons, which are free to move in the crystal) and high E_b (typically 100 to 1000 meV) Frenkel excitons (which are confined within a unit cell). Wannier–Mott excitons can be described with a hydrogen model, and the E_b can be calculated from

$$E_b = Ry \frac{\mu_e}{\epsilon_{eff} n^2}$$

in which μ_{ex} is the exciton reduced mass ($1/\mu_{ex} = 1/m_h + 1/m_e$), n is the principal quantum number (i.e., 1st excitonic level, 2nd excitonic level, etc.), m_h the hole effective mass relative to the free electron mass m_0, m_e the electron effective mass relative to the free electron mass m_0, ε_{eff} the effective dielectric constant, and R_y the hydrogen Rydberg constant (13.6 eV).

In MHPs, Pb and I are heavy elements, which contribute to large dielectric constants of ≈30 (static) and ≈5 (high frequency)[120]. Although this would lead to lower E_b values if Wannier–Mott excitons were present, high dielectric constants do not guarantee that Frenkel excitons do not occur instead. Furthermore, lowering the dimensionality of the perovskites through the formation of RP or DJ phases, or through quantum confinement in perovskite nanoplatelets, leads to higher E_b values.

Given their high exciton binding energies, many studies on 2D MHPs are headed towards an understanding of exciton characteristics to optimize properties for various applications, such as photovoltaics (PVs) and LEDs. As an example, Li et al.[118]investigated the exciton anisotropy to understand the behavior of excitons in 2D $(BA)_2PbI_4$ RP perovskites through polarization-resolved reflection, and PL and photoconductivity measurements. These studies revealed anisotropy in both free and self-trapped excitons within the system. Notably, they observed that free and self-trapped excitons exhibited opposite polarization-dependent behavior in photoluminescence (PL) and photoconductivity measurements, attributed to differing optical selection rules for each type of exciton. These findings could be primary steps in the development of polarization-resolved optoelectronic devices.

Further investigations have focused on the role of charge-transfer excitons in 2D metal halide perovskites (MHPs). These excitons form in the interlayer between adjacent materials with varying electronegativity and local energy levels, also referred to as interlayer excitons. Investigating these excitons is crucial for understanding and enhancing charge transfer between molecules and different heterostructures, which is particularly important for improving the performance of solar cells and LEDs. Zhang et al. [121]proposed two methods to show the presence of charge-transfer excitons and interface excitons in a heterostructure of two 2D perovskites (PEA_2PbI_4 and PEA_2SnI_4). One method was by mixing two precursor solutions, and the other was introducing a new mechanical “hand-finger pressing method”. They show that charge transfer excitons are formed at the PEA_2PbI_4/PEA_2SnI_4 interface and led to a broad, sub-bandgap peak in the photoluminescence spectrum. Transient absorption spectroscopy measurements showed that the charge transfer excitons are rapidly formed within 3ps and become metastable states. Furthermore, these charge transfer excitons can give rise to sub-bandgap photocurrent and are also formed following charge injection, making them important considerations when optimizing the performance of PVs and LEDs.

Quantum Confinement

The higher exciton binding energies of 2D MHPs compared to 3D MHPs comes from quantum confinement effects, which also affect the band gap as reported in fig. 10. In 2D MHPs, the long-chain R group has a low dielectric constant of ≈2.4, while the inorganic lead-halide octahedra layer has a higher dielectric constant of over 6. The array of inorganic layers sandwiched between organic ligands therefore creates a periodic array of barriers (from the organic ligands) and quantum wells within the inorganic layers. This gives rise to quantum confinement[122], [123], [124]. The exciton binding energy of the low-dimensional perovskite ($E_{b,n}$) can be calculated from:

$$E_{b,n} = \left(\frac{2}{\alpha - 1}\right)^2 E_b$$

Here, α is the dimensionality (3 for 3D; 2 for 2D) and E_b is the exciton binding energy for the bulk 3D, non-confined perovskite. It can be noted that a 2D perovskite would have an exciton binding energy four times that of a 3D perovskite. However, in most cases, the exciton binding energy of 2D MHPs is larger than this, usually ranging from 190 to 400 meV for pure 2D MHPs. Furthermore, the exciton binding energy values of quasi-2D perovskites vary with the number of *n*-layers, as well as the length of the organic cation used, with typical values of approximately 80 meV. This is due to the dielectric confinement effect and occurs when the dielectric constant of the inorganic layer is larger than the dielectric constants of the neighboring organic layer, as occurs in the case of 2D and quasi-2D perovskites. In the inorganic layer, the electrostatic forces between electrons and holes are increased because the electric field lines between the charges extend into the organic layers, where they are less effectively screened, resulting in stronger attraction between the carriers. Larger differences in dielectric constant result in increased exciton binding energy, as well as increases in the electronic band gap owing to larger changes in the energy levels as the electrostatic forces change. Figure 10 illustrates the effect of structural dimensionality, quantum confinement and a combination of quantum and dielectric confinement on the E_b value for the (decyl-$NH_3)_2PbI_4$ perovskite.

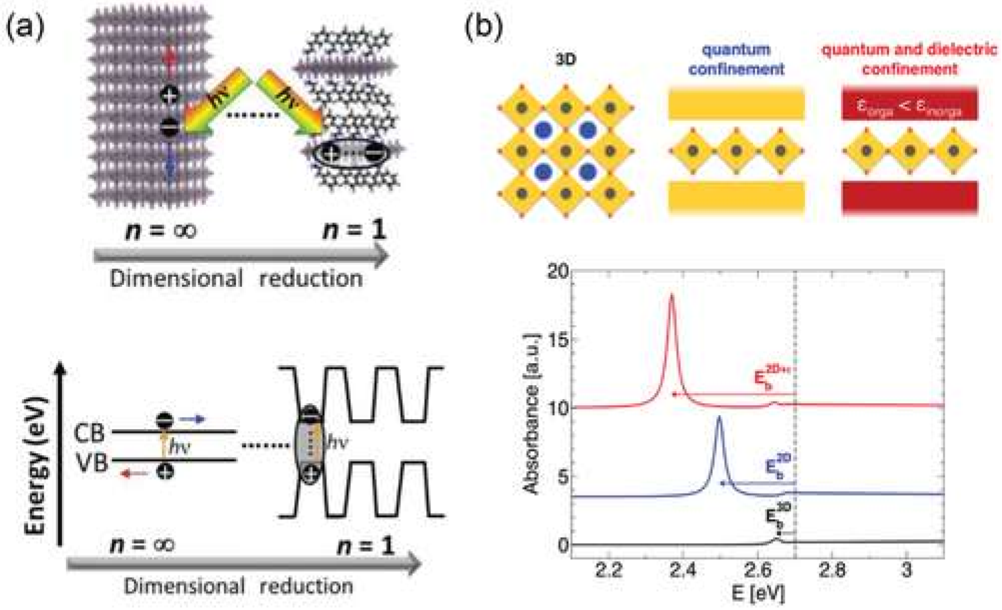

Figure 10 The role of dimensionality on confinement effects. a) How dimensionality (different n values) affects the generation and recombination of charge carriers and the corresponding energy bands scheme for n = ∞ (3D perovskites) and n = 1 (2D perovskites) to illustrate the effect of quantum confinement in the dissociation (3D) or binding (2D) of the electron hole pair. b) Schematic of the hypothetical 3D (decyl-NH_3)$_2$$PbI_4$ perovskite (black), 2D perovskite with only quantum confinement (blue) and 2D perovskite with quantum dielectric confinement (red) with its corresponding optical absorption calculated using a k.p/BSE approach [125]. Adapted from [59]

Strategies to Overcome High Exciton Binding Energies

Charge transport mechanism and properties are strongly affected by the presence of excitonic levels. If the binding energy is high (>50 meV), the exciton may become localized to a unit cell, thus becoming a Frenkel exciton. However, investigations into Ruddlesden–Popper perovskites have mostly concluded that the excitons have Wannier–Mott character, owing to the Bohr radii extending over several unit cells; as excitons could also exist in the organic ligands, these are likely exhibiting Frenkel character. It has been shown that organic-inorganic hybrid systems can form Frenkel–Wannier hybrid excitons due to the coupling between the Wannier excitons in the inorganic layer and the Frenkel excitons in the surrounding organic layers. These hybrid excitons have in fact been proposed to occur in lead-based 2D perovskites[126], [127], [128].

An additional approach to mitigate the effects of Frenkel excitons in 2D perovskites is to modify the electronic structure by introducing functional organic molecules with strong electron-donating or -accepting properties. Gelvez-Rueda et al. demonstrated effective charge separation in quantum- and dielectrically-confined 2D perovskite materials by incorporating a highly electron-accepting perylene diimide chromophore on the surface of a bi-layered lead bromide-based perovskite *nanoplatelet*.[129], [130], [131]This strategy offers a promising method for achieving efficient formation of mobile free charge carriers, with carrier lifetimes extended to tens of microseconds—two orders of magnitude longer than in the absence of the organic moiety.

Band Gap

RP and DJ perovskites provide the benefit of band gap tunability not only through compositional changes but also by adjusting structural dimensionality. Quantum confinement effects cause 2D metal halide perovskites (MHPs) to have larger optical band gaps than 3D MHPs, as discussed earlier. Moreover, the band gap of a single-layered perovskite (n = 1) can be tailored by modifying the interlayer spacing and structural distortion within the perovskite layer[60], [95], [101], [102]. Modifications of the organic molecular cation RRR provide a way to adjust the interlayer spacing, where increasing the cation length results in wider band gaps. For this reason, DJ perovskites, with their naturally lower interlayer spacing, exhibit narrower band gaps than RP phases. [100]. In iodide-based RP perovskites, the band gap can be modulated from 1.59 to 2.36 eV by controlling the number of inorganic layers between the organic ligands (i.e., the *n* value), as shown in figure 11[132], [133]. For example, Cho et al. [125]show a blue-shift of the band gap of PEA-MA RP perovskites when the ratio of PEA:MA increases and the parameter *n* decreases. Similar results have been obtained with BA-MA RP perovskites, as well as with DJ perovskites. Moreover, theoretical studies by ab initio molecular dynamics (AIMD) have allowed calculations of the dynamic electronic structures in 2D perovskites[100].

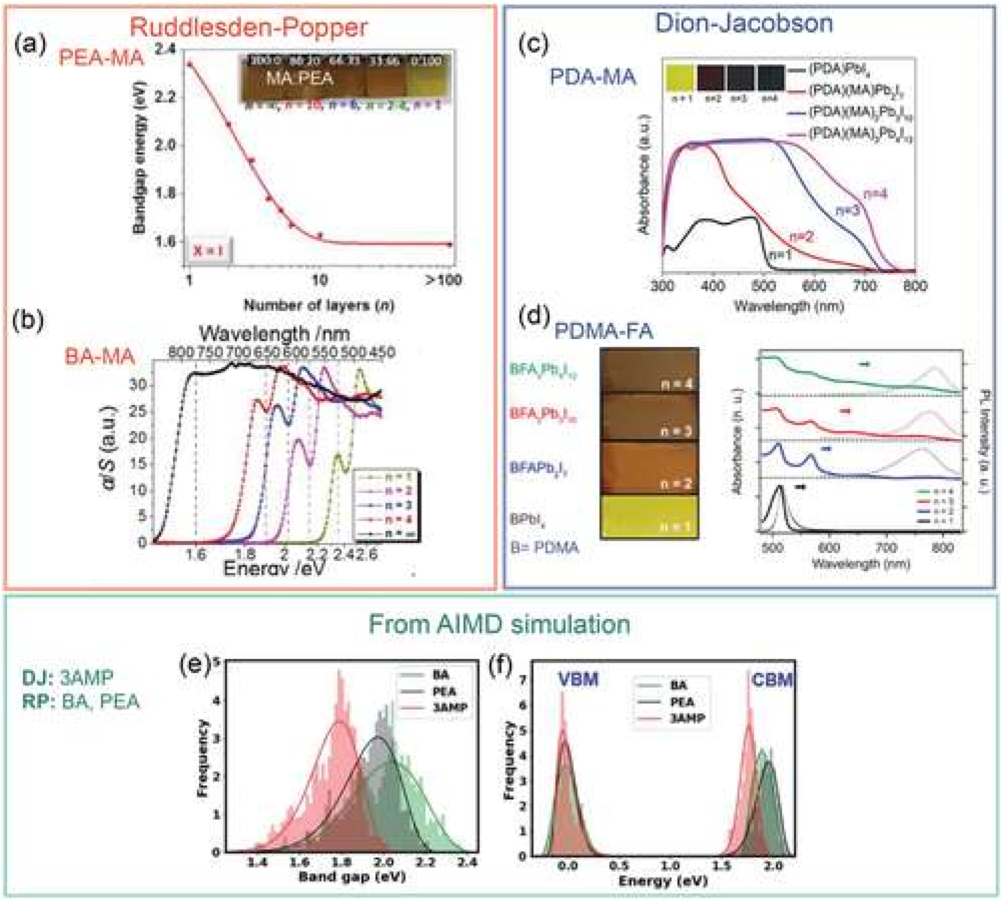

Figure 11 Effect of dimensionality, n, on the band gap of RP and DJ perovskites. a) $(PEA)_2(MA)_{n-1}Pb_nI_{3n+1}$ and b) $(BA)_2(MA)_{n-1}Pb_nI_{3n+1}$. Note that in part (b), the band gap was determined from diffuse reflectance measurements converted with the Kubelka–Munk function, in which $\alpha/S = (1 - R)^2/(2R)$. Effect of dimensionality on the band gap of DJ perovskites (c) $(PDA)(MA)_{n-1}Pb_nI_{3n+1}$ and (d) $(PDMA)(FA)_{n-1}Pb_nI_{3n+1}$. All inset panels of (a,c,d) show photographs of films for the different n values. e,f) Theoretical comparison of band gaps through ab initio molecular dynamics (AIMD) calculations of the dynamic electronic structures of the 2D-perovskites RP: $(BA)_2PbI_4$, $(PEA)_2PbI_4$, and DJ: $(3AMP)PbI_4$. e) The histogram distribution of band gaps along the AIMD trajectories, and f) the thermal broadening in the VBM and CBM states. Adapted from [59], [60], [102], [110], [111], [125]

These studies show that the DJ phase (3AMP) exhibits a lower band gap than the RP phase, along with a narrower distribution in the valence and conduction band maxima (VBM and CBM). This narrower distribution in band-edge positions results from reduced thermal broadening, attributed to a higher equatorial Pb-I-Pb angle in the DJ phase, which reduces distortion in the PbI6 octahedra and causes a red shift in the electronic band gap. Reduced distortion also minimizes thermal motion, as demonstrated by comparing thermal broadening in the VBM and CBM between the RP and DJ phases.

Application in photovoltaics

In photovoltaics, the power conversion efficiency of RP perovskites has increased from 4.74% in 2014 to 22% in 2023[132], [134], [135], [136], [137], [138], [139], [140]. This fast improvement gains have been attributed to efforts in optimizing the band gap, controlling preferred orientations, engineering the composition and making optimal use of mixed phases[141], [142].

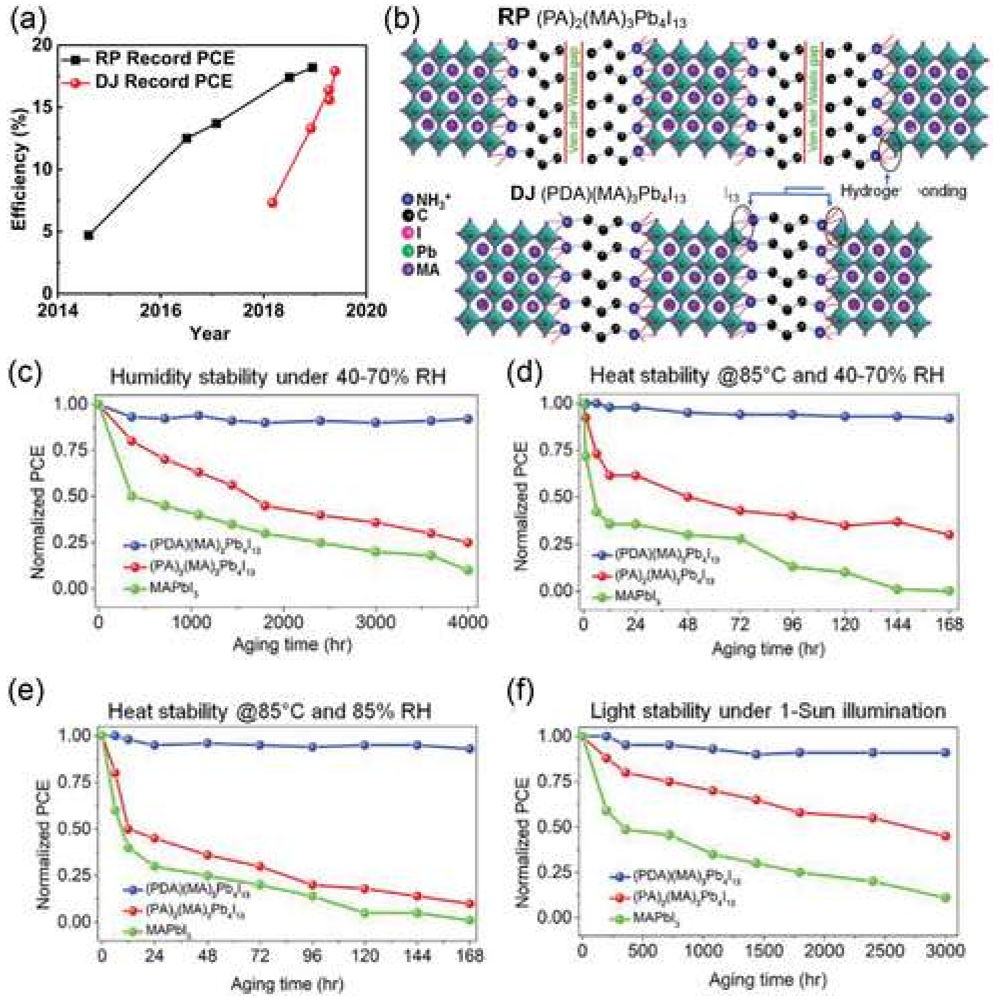

Figure 12 Comparison of Ruddlesden–Popper (RP) versus Dion–Jacobson (DJ) perovskites in solar cells and their power conversion efficiency (PCE). a) Evolution of the record PCE for layered RP and DJ perovskite solar cells. b) Schematic illustration of the RP $(PA)_2(MA)_3Pb_4I_{13}$ (n = 4), and DJ $(PDA)(MA)_3Pb_4I_{13}$ (n = 4) perovskites. The performance of these perovskites in solar cells is given in (c–f). Stability test of RP, DJ, and 3D $MAPbI_3$ perovskite-based devices in c) ambient air, d) under damp heat stress (85 °C, 40–70% RH), e) under damp heat stress (85 °C, 85% RH), f) under 1-sun illumination[99]. Adapted from [59]

Additionally, DJ perovskites have recently garnered attention for photovoltaic applications because of their enhanced phase stability and superior electronic properties compared to RP perovskites.

Although the record efficiency values of RP and DJ perovskites are comparable, the DJ-phase shows a sharper increase, as illustrated in Figure 12. Additionally, Ahmad et al.[99] found that while RP perovskites (PA-MA, n = 4) showed enhanced environmental, thermal, and photostability over 3D MAPbI3 perovskites in solar cells, DJ perovskites (PDA-MA, n = 4) demonstrated even greater stability improvements.

1.2.5 STATE OF THE ART OF PEROVSKITE-BASED RADIATION DETECTORS

In the following, we present recent advancements in radiation detection with perovskite-based devices. As target of this work is *direct* detection, no scintillation counterparts will be taken into consideration. It is nevertheless important to highlight that 2D perovskites have been widely employed in scintillating detectors for alpha and beta particles, X- and gamma-rays, neutrons and protons. The obtained results are extensively reviewed in [143], [144].

This section is divided into single-crystals and thin film detectors: reason is to be found in different performance and applicability. It will become clear that SCs offer high energy resolution and ultra-fast recording up to single pulses. Conversely, thin films advantage flexibility and large area as their appealing features as they combine optimal outcomes and versatility, as they can be employed for personal monitoring in both medical and space-related applications.

1.2.5.1 Perovskite Single Crystals

NEUTRONS

Gao *et al.*[145]report a novel approach to direct fast-neutron detection using 2D Dion–Jacobson perovskite semiconductor $BDAPbBr_4$. As 2D perovskites that contain long-chain organic amine with high hydrogen content are more suitable for neutron detection than their 3D counterparts, they select $BDAPbBr_4$ as the candidate semiconductor, where BDA (butane-1,4-diammonium) links two adjacent inorganic Pb-Br layers to form strong interlayer forces. Devices are in the form of polished single crystals of thicknesses around 1.5 mm and sandwiched between Au electrodes.

They report resistivity values of 2.38×10^{12} Ω cm and μτ product for holes that is 3.3×10^{-4} $cm^2 V^{-1}$.

Results under neutrons are obtained both in counting and in integration modes; a direct comparison with anthracene -as representative scintillator- and SiC as typical semiconductor is presented.

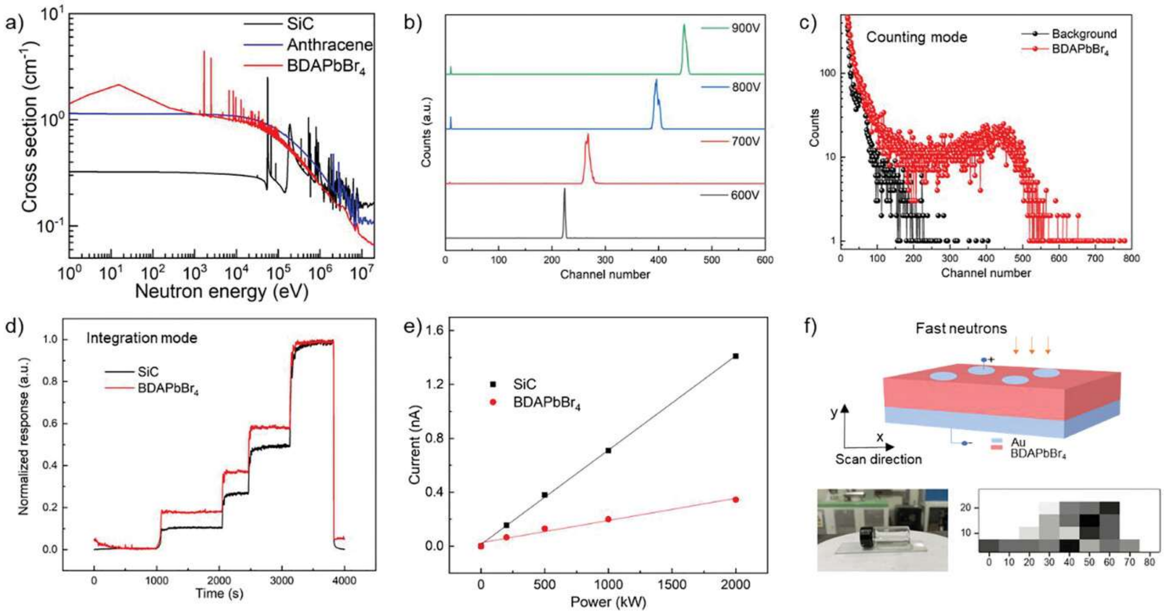

Figure 13 a) Macroscopic cross-section of BDAPbBr$_4$ toward neutrons. SiC semiconductor and Anthracene scintillator are also listed for comparison. b) Pulse-height spectra toward ^{241}Am α-particles. c) Measured pulse height spectra (counting mode) toward fast-neutrons from Am-Be source. d) Measured response current of SiC and BDAPbBr$_4$ in integration mode toward fast-neutron from Am-Be source. e) The derived response current under different powers of Am-Be source. f) The fast-neutron imaging result by BDAPbBr$_4$ detector, and the fast-neutrons were provided by deuterium-deuterium fusion reaction.

PROTONS

After the publication of the work about alpha-particles spectroscopy with Cs-based perovskite single crystals [146], proton detection has gathered interest and research efforts, as it requires the combination of high performance and radiation-hard devices. Huang *et al. [147]* report MHP direct 3 MeV proton detector based on 3D MAPbBr3 single crystal of dimensions 6x6x3 mm^3.

Results show high sensitivity at low bias ((1.540 ± 0.008) × 10^{-10} C Gy^{-1} at -10V applied bias), high signal stability and radiation hardness to incredibly high absorbed doses (45kGy).

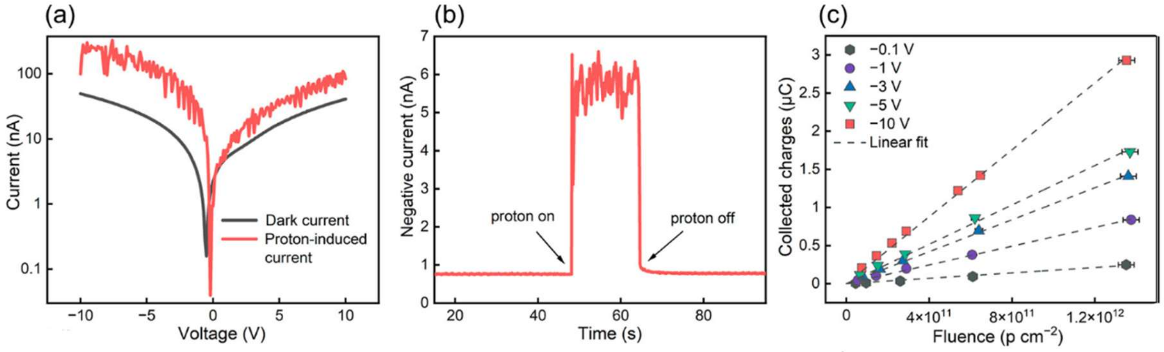

Figure 14 (a) Proton-induced current and dark current of the detector. (b) Time-resolved proton-induced current at −0.1 V. (c) Relationship between the collected charges and fluence at various bias voltages.

X-RAYS

The application of perovskite-devices for radiation detection has been primary subject of interest. Their response to high-energy photons led straightforwardly to the investigation of their radiation-detection capabilities. In this field, 2D perovskite have been widely explored: first evidence of PEA-based single crystals is found in the work of Li *et al [148],* which reports (F-PEA)$_2$PbI$_4$ single crystal detector with a sensitivity of 3402 μC Gy^{-1}air cm^{-2} to 120 keV$_p$ hard X-rays, lowest detectable X-ray dose rate of 23 nGy$_{air}$ s^{-1} . Current state of the art is devoted to devices engineering towards high sensitivities to be combined with low toxicity, that is crucial requirement for medical imaging and human-related applications. In this sense, Liang *et al [149]* report a mixed 2D Pb–Ge system that combines improvements in X-rays response and structural stability. Specifically, the detectors exhibit a record high sensitivity of 13488 μC Gy^{1-} cm^{-2}, a low detection limit of 8.23 nGy s^{-1}, as well as a high spatial resolution of 8.56 lp/mm^{-1} in X-ray imaging.

GAMMA RAYS

Extensive studies have been conducted in the past that assess the feasibility of detecting gamma rays through direct perovskite single crystals. On top of them, plenty of works have been published on FAPbI$_3$ and CsPbBr$_3$ which reported energy resolution down to 1.4% for 662-keV γ-rays from ^{137}Cs source [150], [151], [152]. Latest efforts are directed towards quality improvements in the form of resolution and stability. We report recent results on ligand engineering as a powerful tool for performance enhancement of MHPs as gamma ray detectors.

Yuan *et al. [153]* demonstrated MAPbBr3 single crystal γ-ray detectors with remarkable improvement in ER, achieving an impressive 3.9% for 511 keV γ-rays at room temperature, which is among the best performances reported for perovskite γ-ray detectors. The ^{22}Na γ-ray spectrum of these detectors clearly resolved the photoelectric peak, Pb escape peak, and Compton edge. Additionally, the stability of the γ-ray energy spectrum was maintained over 300 minutes of continuous operation under a continuous electric field, demonstrating superior long-term stability.

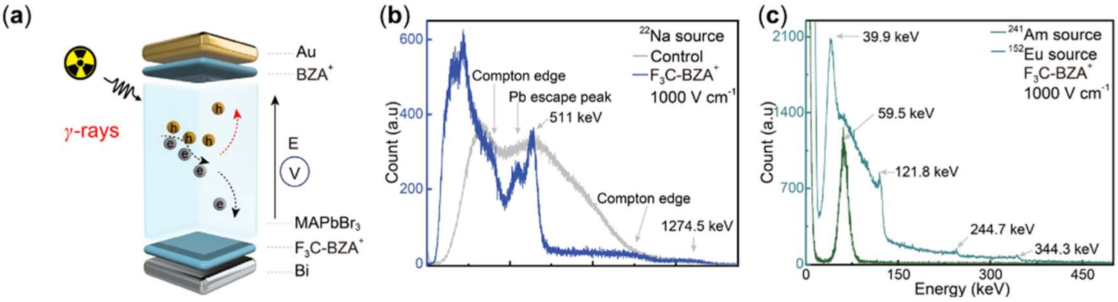

Figure 15 Architecture and γ-ray spectrum analysis for MAPbBr 3 detectors. a) Schematic diagram of the detector structure. b) The γ-ray spectrum of the control and F 3C-BZA + -treated detectors under ^{22}Na sources with an electric field of 1,000 V cm $^{-1}$. c) The γ-ray spectrum of the F 3C-BZA+ -treated detectors under 241Am and152 Eu radiation sources with an electric field of 1,000 V cm $^{-1}$. Adapted from [153]

1.2.5.2 Thin Film devices

X-RAYS

Given the aforementioned characteristics of perovskite-based devices, the dominant application of direct X-ray detection currently lies in photoconductive flat-panel imagers[154]. These devices utilize perovskite thin films deposited over large-area substrates, integrated with multielectrode arrays. Significant progress has been made in optimizing the selection of active materials and device architectures. Initial studies on perovskite thin films for radiation detection focused on micrometer-thick layers of 3D MAPI and MAPbBr3, which achieved sensitivities on the order of 10 µC Gy^{-1air} cm^{-2}[155], [156]. More recently, the incorporation of FAPbBr3 has improved both the stability and performance of 3D perovskites[157]. However, stability challenges persist, which are being addressed through the use of 2D/3D hybrid structures or pure 2D perovskites that also exhibit very low dark current[158]. Additionally, advancements in printable electronics have enabled the development of high-sensitivity detectors with exceptional spatial resolution, including flexible radiation detection systems[159].

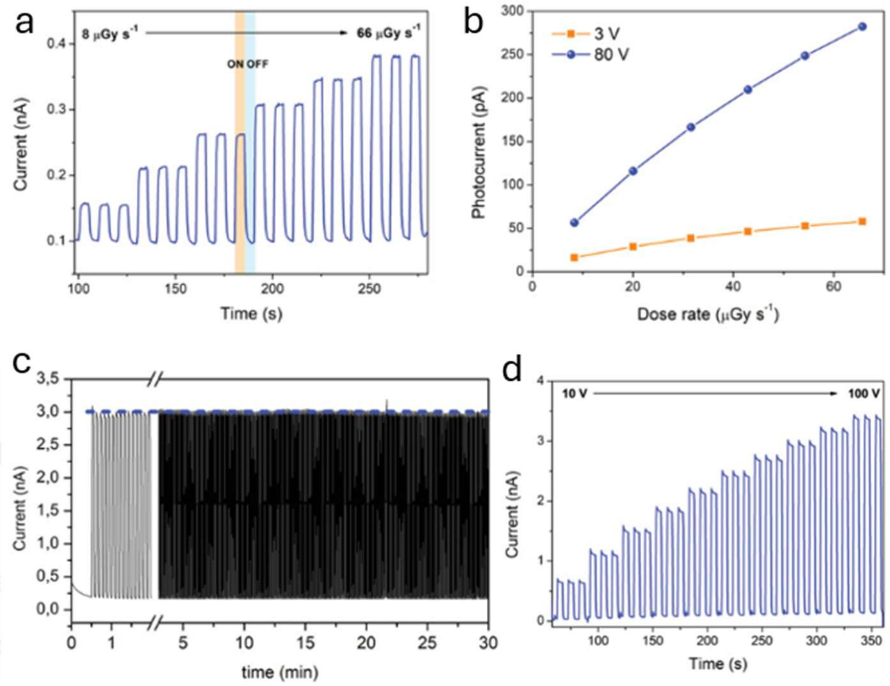

Figure 16 a) Dynamic X-rays response under X-rays with 150 kVp accelerating voltage (80 V bias). b) X-ray induced PC as a function of the dose rate at 3 V (orange) and 80 V (blue) applied bias. c) Stability of the dynamic response to X-rays at a constant 80 V applied bias after 80 days of aging. The dose rate and the total dose received are 4.2 mGy s^{-1} and 3.8 Gy respectively, over 300 pulses. d) Dynamic X-rays response at 150 kVp and bias increasing from 10 to 100 V. Each step corresponds to a 10 V bias increase.

We here report the work of Ledee *et al.[160]* on MHP thin films which presents solid-state ionizing radiation direct detectors based on the 2D layered hybrid perovskite PEA_2PbBr_4 (PEA = $C_6H_5C_2H_4NH_3^+$) -we choose the same material as active layer for the devices presented in this work as high-energy radiation detectors. These films are deposited from solution using scalable techniques and directly integrated onto a pre-patterned flexible substrate in the form of micro-crystalline films displaying crystal-like behavior, as evidenced by the ultra-fast (sub-microsecond) and good detection performances under UV light. The effective detection of X-rays (up to 150 kVp) is demonstrated with sensitivity values up to 806 μC Gy^{-1} cm^{-2} and Limit of Detection of 42 nGy s^{-1}, thus combining the excellent performance for two relevant figures of merit for solid-state detectors. Additionally, the tested devices exhibit exceptionally stable response under constant irradiation and bias, assessing the material robustness and the intimate electrical contact with the electrodes.

PROTONS

Critical aspect of proton detection is the need of proton beam monitoring in terms of space and energy resolution. Towards this direction, preliminary work has been conducted by Basiricò *et al [161] ,* which report the firs flexible proton beam direct detector based on mixed 3D–2D perovskite films deposited by solution onto thin plastic foils. The 3D–2D mixture ($MAPbBr_3$ (3D) and $(PEA)_2PbBr_4$ (2D) tuned in proportions) allows to obtain micrometer-thick and highly uniform films that constitute the detector's active layer. The devices demonstrate excellent flexibility with stable electric transport properties down to a bending radius of 3.1 mm. The detector is characterized under a 5 MeV proton beam with fluxes in the range [4.5 × 10^5 – 1.4 × 10^9] H$^+$ cm^{-2} s^{-1}, exhibiting a stable response to repetitive irradiation cycles with sensitivity up to (290 ± 40) nC Gy^{-1}mm^{-3} and a limit of detection down to (72±2) μGy s^{-1}. The detector radiation tolerance is also assessed up to a total of 1.7 × 10^{12} protons impinging on the beam spot area, with a maximum variation of the detector's response of 14%.

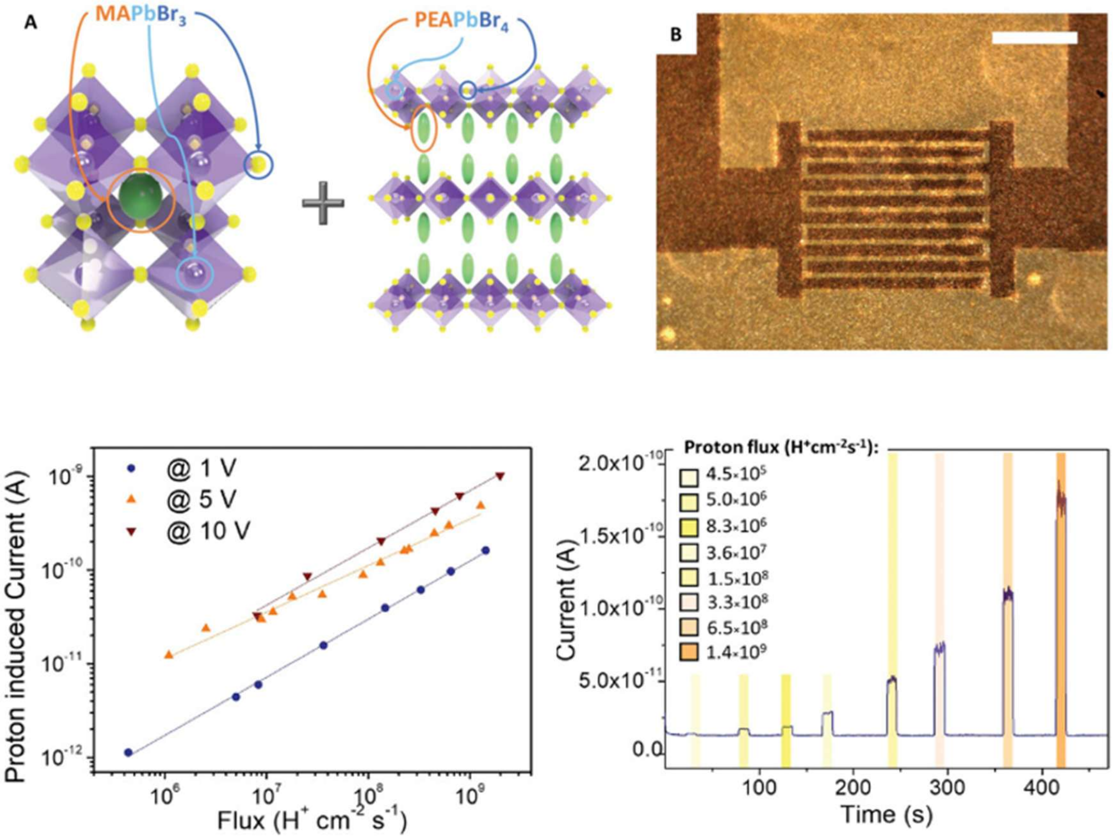

Figure 17 A) Schematics of $MAPbBr_3$ (3D) and $(PEA)_2PbBr_4$ (2D) perovskite composing the 3D–2D perovskite film under study. B) Optical microscope image of the detector's active layer. Scale bar: 500 μm. Below: Proton induced current as function of applied bias and flux (left); dynamic current response in function of time for the detector biased at 1 V and irradiated with 10 s proton beam shots (right). The colored boxes indicate the increasing proton fluxes employed, in the range [4.5 × 10^5–1.4 × 10^9] H$^+$ cm^{-2} s^{-1}

1.3 CORE OF THE WORK

This brief section covers the targets and objectives of the entire work, that is perovskite-based direct radiation detectors in the form of thin films for clinical relevance and applications.

Prior to delving into technical features, the choice of active material has been crucial for desired outcomes. In here, we employ 2D-perovskite PEA_2PbBr_4 (PEA= $C_6H_5CH_2CH_2NH_3^+$) in the form of thin films to be deposited on flexible substrates. Bias is applied through interdigitated metal contacts that form single pixels to be used as one or connected in parallel depending on target application. The reason is to be found in the outstanding features listed below; a complete scheme of the intended devices is reported in fig. 18.

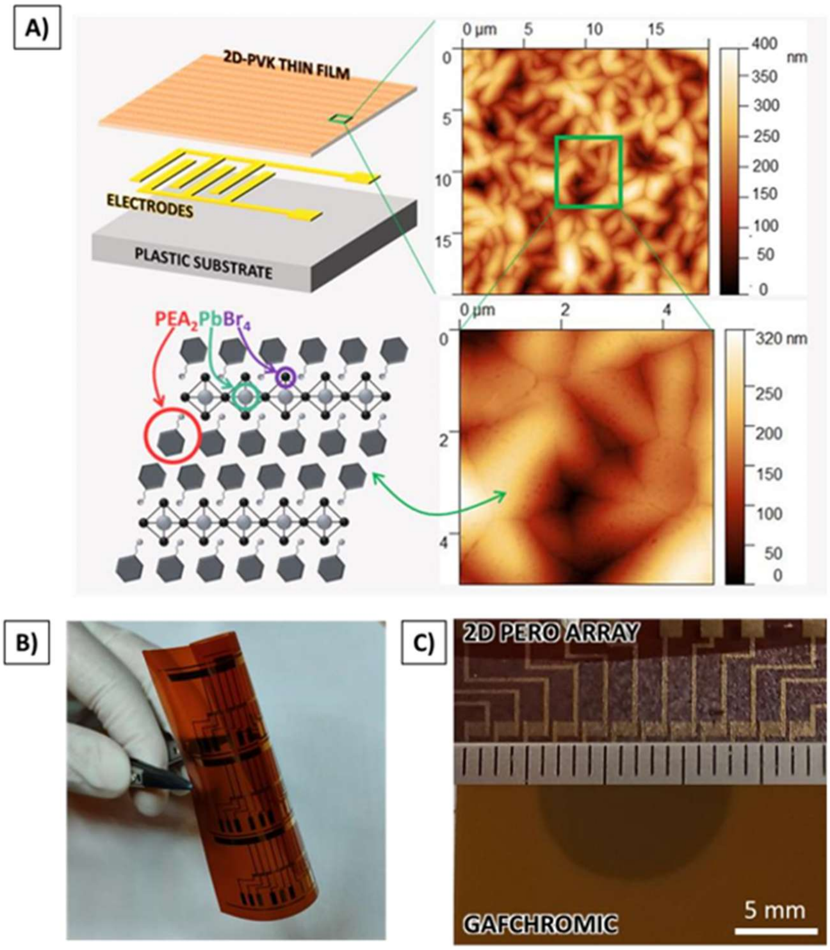

Figure 18 2D perovskite structure and implementation onto flexible substrate. A) reports basic device architecture, perovskite molecular structure and surface topography images obtained with Atomic Force Microscopy to assess microcystallinity. In B), multielectrode arrays on flexible polymide substrates are shown and compared with a radiochromic sheet from proton beam therapy.

- Extremely long-term stability: PEA_2PbBr_4 thin films have demonstrated stable dynamic response under X-ray irradiation up to 720 days after the samples were fabricated. Moreover, they require no hard conditions to be considered for storage, as no detrimental effects from external environment are observed to reduce the samples performance. The reason behind the choice of Bromine rather than Iodine as halide is to be found in their different size: iodide ions are larger and more reactive compared to bromide ions, making perovskites with iodide more prone to degradation when exposed to moisture, oxygen, or light. The weaker Pb–I bonds in PEA_2PbI_4 can break down more easily, leading to faster degradation. Moreover, iodide-based perovskite has demonstrated higher hygroscopic levels, meaning they are prone to faster degradation.

- Extremely low dark current: PEA_2PbBr_4 features resistivity values of the order of 10^16 Ohm m. This translates to thin film devices dark current that is measured to be <10pA with 4kV/mm applied electric field. These values grant high signal-to-noise ratio, that is primary requirement in matter of high-energy radiation detection.

- Easy processability: thin films are processed through solution and grant cost-effective, large area devices. Perovskite solution can be deposited on desired substrates with different techniques: this allows for scalability of devices, that is to be coupled with specific readout electronics that allows for parallel measurement of multipixel arrays. On top of that, interdigitated pixels are crucial for improving spatial resolution, as their features such as channel length and finger width can be tuned according to need.

- Devices flexibility: the possibility to choose flexible foils as substrates for perovskite deposition meets the need for wearable dosimeters to be actually conformable to the anatomic conditions of patients in clinical trials. In here, plastic substrates are chosen as main substrate: flexibility tests have been conducted that demonstrate PEA_2PbBr_4 response under X-rays with bending radii down to 3mm.

As reported in Sec.1.2.5, PEA_2PbBr_4-based devices have been tested over the last few years and their results reported high sensitivity under X-rays and promising outcomes under charged particles.

This work is intended to explore new radiation sources and related applications and tries to exploit the power of PEA_2PbBr_4 as all-around direct radiation detector. For this reason, time and resources have been spent towards the characterization and deep understanding of this material optoelectronic properties. Lastly, with the rapid growth of space exploration and the increasing frequency of space missions, the need for advanced personal dosimetry for astronauts has become more critical than ever. Astronauts are exposed to a variety of high-energy radiation sources, including cosmic rays and solar particles, which pose significant health risks during long-duration missions. Traditional radiation detection technologies, while effective on Earth, face limitations in the extreme conditions of space, such as weight constraints, durability, and sensitivity to high-energy particles.

In response to this pressing challenge, a collaboration with the Italian Space Agency (ASI) has led to the development of an innovative personal dosimeter prototype designed specifically for use in space environments. The prototype is slated for inclusion in a scheduled launch to the International Space Station (ISS) in March 2025.

2. METHODS

This entire chapter gathers materials, procedures and analytical techinquest employed for the fabrication and functioning assessment of thin film devices based on 2D perovskite PEA_2PbBr_4.

The outline of the first section follows the chronological order of events, from the choice of the substrate to working devices fabrication. Patterning technologies and material processing are highlighted with specific parameters used in the form of laboratory protocols: reproducibility is crucial for technological transfer to effective applications in real conditions (sec. 2.2).

Note: core of the work is the fabrication of devices in the form of photoconductor for direct radiation detection. This structure consists of co-planar interdigitated metal electrodes on specific substrates onto which one deposits a thin film of chosen active material as reported in Sec 1.3. Therefore, we here focus on this target structure; Appendix 2 briefly summarizes crystal growth of 2D perovskite for comparison purposes.

The second part is then dedicated to characterization techinques and integrated measurements setups. A brief description of large-scale apparatuses of dedicated facilities is also presented for the clarity of reading: primary tests have been conducted in medical facilities, results reported in sec. 3.3.

2.1 FABRICATION OF DEVICES

Optimal outcomes for working photoconductor devices require accurate choice of materials and techniques that guarantee large-area scalability, cost-effective procedures and high performance. In this sense, chosen architecture account for the following elements: substrates with low roughness, high stability and mechanical flexibility; limited spatial dimensionality of the electrical contacts and a charge-collecting active layer.

We start with explaining the needs and requirements to be fulfilled by the substrates and go deep into micropatterning with photolithography; last subsection is focused on perovskite synthesis and optimization.

2.1.1 DEVICE ARCHITECTURE

A complete scheme of a ready-to-use device is reported below.

The proposed devices consist in a flexible substrate onto which metal contacts are patterned in the form of interdigitated pixels. This structure enables high spatial resolution and combines excellent performance with low applied bias. The fine spacing between the fingers can be scaled down to as little as 5 μm (see figure 19).

Previous investigations have led to the choice of Kapton as primary candidate due to its high resistance to temperature and chemical treatments [162], [163], [164]. For this reason, we employ it as main substrate for radiation detection applications. Nevertheless, PEN and PET are also present in this work as they have constituted the standard for radiation measurements conducted before 2022.

Perovskite active layers are produced through spin-coating a solution onto the already patterned substrate, resulting in microcrystalline thin films of thicknesses of up to 2 μm. This thickness enables substantial absorption of ionizing radiation while preserving flexibility features.

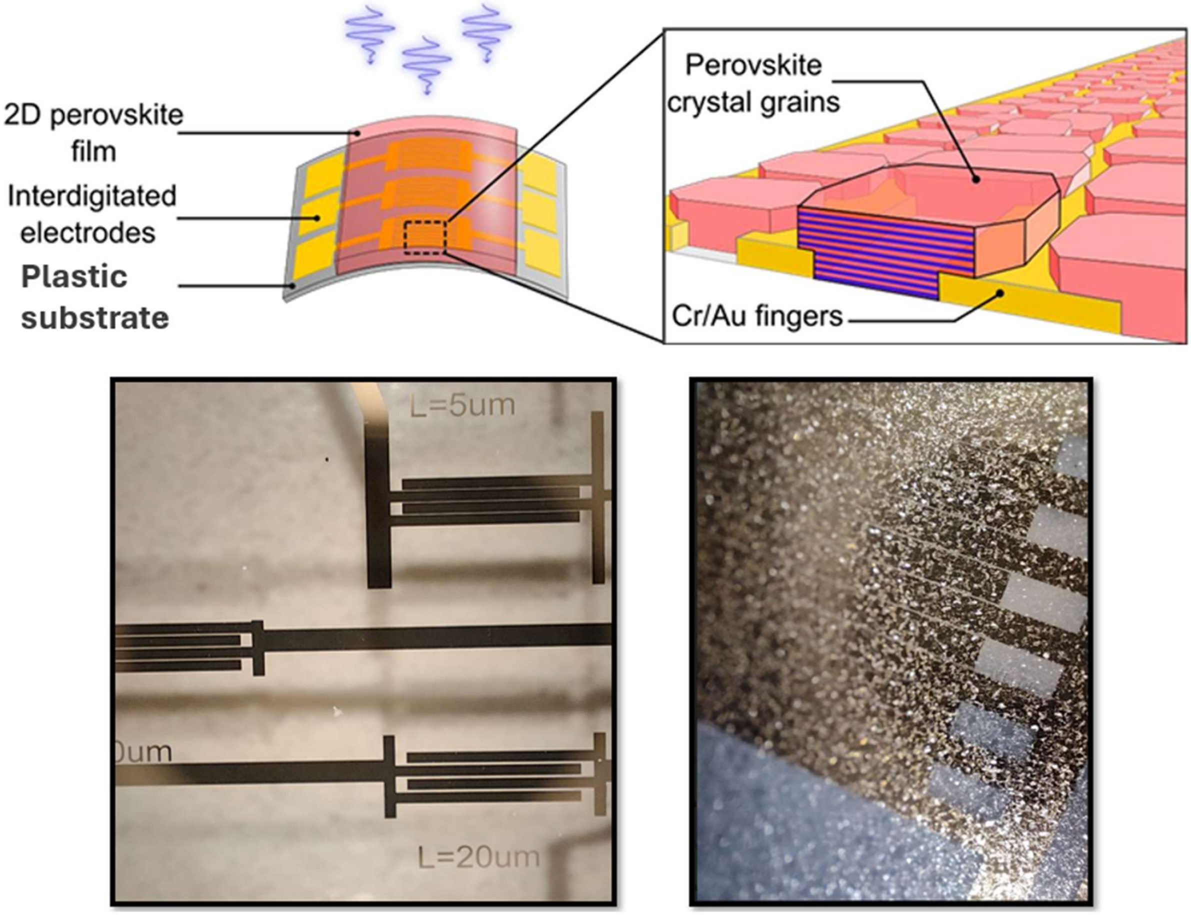

Figure 19 Scheme of device basic device used in this fork for direct detection of ionizing radiation. The electric field is applied through inderdigitated pixels made of Cr/Au and deposited onto flexible substrates. The 2D perovskite film is deposited via spincoating and exposed to radiation in order for generated charge carriers to be collected at the electrodes. High resolution in channel length down to 5 μm allows for low required bias to operate. Perovskite deposition through spincoating leads to nanocrystalline thin films of thickness in the range 0.5-2 μm.

2.1.1.1 Substrate preparation

Prior to the choice of materials to be employed as substrates, considerations are required in matter of target application and interface effects. For instance, flexibility is key for wearable electronic systems: this implies the only possible option is thin plastic foils.

Plenty of research literature exists on the impact of the effects at the interface on stability and performance: physical interactions occurring between substrate, metal and active material can be detrimental to the device operations. Furthermore, substrates need to undergo chemical processes that employ aggressive solvents and treatments, these damaging it irretrievably. As an example, we report a study on the effect of substrate choice on perovskite crystallization [165], [166].

Silicon and glass have always been a reference in matter of substrate flatness and resistance to harsh conditions; for this reason they can be used as a standard for testing active material performance. However, flexibility is priority for personal dosimetry. For this reason, we chose PEN ($(C_{14}H_{10}O_4)n$), PET($(C_{10}H_8O_4)n$) and Kapton ($(C_{22}H_{10}N_2O_5)n$).

These substrates offer high chemical resistance and do not show degradation with increasing temperature: precisely, Kapton is reported to whitstand every organic solvent, to exhibit a unique tensile strength (140MPa at 200°C) and operate at a broad temperature range up to 400°C. These features allow it to be considered a standard in matter of space-related applications.

The fabrication procedure starts with selection of substrates thicknesses and shaping through laser cutter. Laser speed and intensity vary as function of material and thickness. Parameters are reported in Table 2.

Substrate	Laser speed	Power	Thickness
PET	25mm/s	5%	125 µm
PEN	25mm/s	5%	125 µm
Kapton	20mm/s	10-20%	300 µm

Table 2 Specific parameters of Laser-cutter employed for the preparation of substrates of target dimension and thickness.

Substrates cleaning procedure accounts for sonication in organic and inorganic solvents (here, Acetone, IPA, DI water) and oxygen plasma treatment, the latter being used as cleaning process as well as a surface passivation method that leads to hydrophilicity [167].

2.1.1.2 Laser Lithography

High resolution metallic contacts are typically obtained through deposition methods on samples onto which a physical mask is laid that shadows its design on the sample itself, allowing for metals to deposit on target areas only. Although this technique being widely employed and extended to ultra-high quality and precision down to hundreds of nanometers in resolution[168], it lacks tunability of parameters and design variability, thus limiting specific applications.

The finest way to transfer desired patterns up to the micro-scale onto specific films or substrates accounts for light-driven mechanisms that expose specific materials in target areas. Photolithography is here employed in the fabrication of interdigitated structures whose channel distance L is minimized to the microscale, with resolution of 1µm. Thus, performance can be increased by orders of magnitude without widening spatial dimensions (for explanation and modelling, see Sec. 1.3).

Figure below sketches the entire photolithography process, the steps of which are here described in detail according to employed proceedings for better yield and quality. Notably, tuning of laboratory-related and environmental parameters is crucial for optimal outcomes. Provided the substrate choice and treatments discussed previously, essential component is a **photoresist**: this is a radiation-sensitive material that, when exposed to -mainly UV- light, undergoes a chemical change that allows selected areas to be removed or retained during subsequent processing steps. Depending on the exact chemical composition, light exposure hardens (*negative)* or weakens (*positive)* photoresist target area: undesired regions can therefore be easily removed through chemical etching.

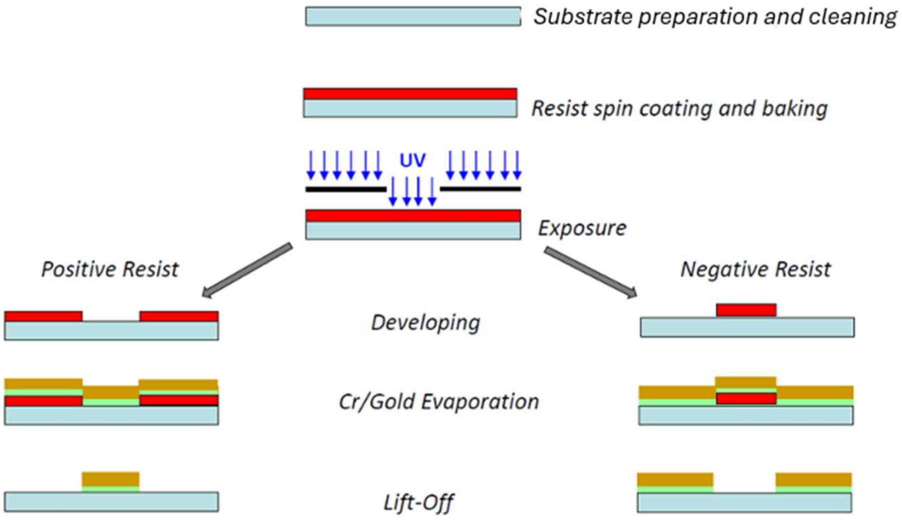

Figure 20 Photolithography for metal contact patterning. Scheme step by step for the preparation of patterned Cr/Au metal contact on glass substrates. The process starts with the substrate preparation and the deposition of the photoresist. The sample is exposed to UV light through a mask placed between the UV source and the sample. The developing step removes the resist exposed (not exposed in the case of negative photoresist) leavening it instead in the region where the UV light was blocked by the mask. After the metal evaporation the lift-off removes the excess photoresist leaving a patterned metal film on the substrate.

Additional considerations regard deposition methods. It is important to say that plenty of techniques such as blade coating or chemical vapour deposition have been explored and are still employed in many fields. We refer to [169] and [170] as review papers that outline features, differences and advantages.

As one of the largest employed solution-based methods for lab-scale thin film deposition, practical approach of this work is **spincoating** technique; its basic working principle sketched in figure 21. It requires a motor system with a rotating platform that allows the chosen substrate to be attached mechanically or through vacuum generation underneath (in this second case, a vacuum pump is required) and to spin at high frequency (up to 10krpm). A solution containing the material to be deposited is poured via syringe onto the substrate and it starts spreading due to centrifugal force as rotation of the platform begins. The high rotational speed grants uniformity of film growth and low thickness as the solvent evaporates and/or chemical reactions occur at the interface; excess liquid drops.

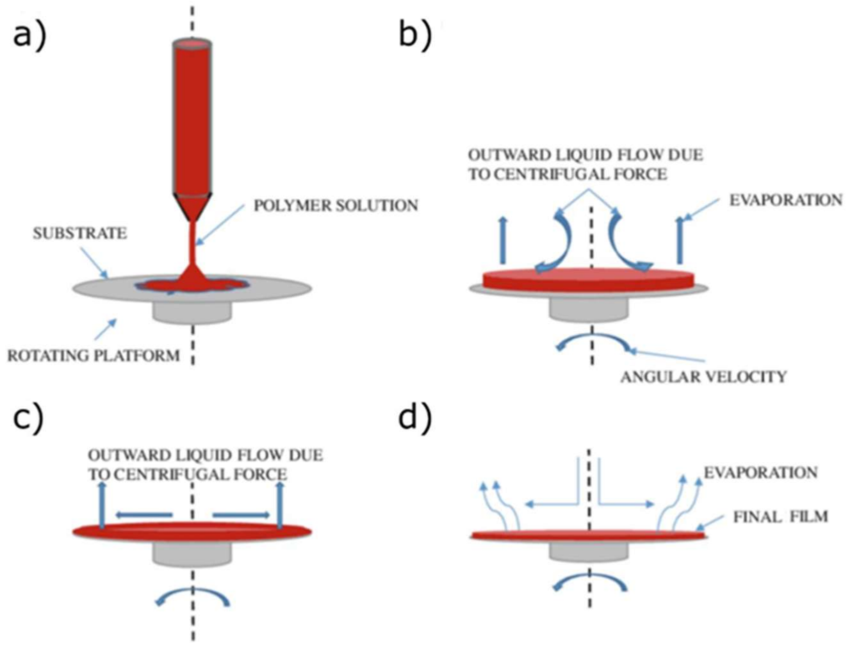

Figure 21 Brief scheme of the spin-coating technique for thin film deposition. a) The solution or ink is placed on top of the substrate. b) The spin-coater rotating platform starts to rotate, and the solution is spread evenly on the substrate by the centrifugal force. c) The excess material gets ejected from the substrate by the centrifugal force and the liquid continues to spread until all the substrate is covered. d) The evaporation of the solvent leads to the final film formation[171].

Lastly, annealing procedure at high temperature is typically required in order to let the sample dry completely. Notably, a number of parameters is to be taken into account. For instance, hydrophilicity -this comes back to plasma treatment of the substrate- promotes adhesion; type and viscosity of the solvent affect thin film quality as well as rotation frequency and time.

Although no exact mathematical model exists to predict film thickness, a proportionality holds between it and selected frequency:

$$h \propto 1/((\omega)1/2).$$

This simplified expression is consistent in specific cases only and for limited and material-dependent thickness ranges. A formal derivation and useful insights are gathered in [172].

2.1.1.3 Metal contacts

When choosing metals for contact deposition in electronic devices, key factors include the metal's purity, work function, and overall cost. The work function is especially critical, as it determines how well the metal aligns with the semiconductor's energy levels, influencing whether the contact behaves as ohmic or forms a Schottky barrier, which can drastically affect device performance. Gold, due to its high work function and excellent conductivity, is commonly used, particularly for p-type semiconductors. In here, we evaporate chromium-gold contacts of 5 and 40nm in thickness, respectively. It is worth mentioning that gold has recently demonstrated to migrate over time and under radiation environment in perovskite materials. This is thought to be related to the formation of reactive polyiodide/bromide melts which aggressively target gold ions leading to the formation of Au-aggregates. For this reason, efforts are put towards its replacement with other metals.

Thermal evaporation is here chosen for metal contacts deposition. It relies on a high vacuum system connected to a electrical current generator that heats up the target metal until sublimation is reached: hot atoms and molecules lose their kinetic energy when the substrate is contacted and the film formation starts.

Metal holder accounts for a three-slot structure connected to a high current generator that allows for three different metals to be deposited one after another. Desired targets are inserted in conductive, spiral-shaped tungsten crucibles engineered to transfer heat with the highest efficiency. A large sample holder is placed above the crucibles (distance between 30 and 50cm) with the samples to be coated facing the metals; next to it, a calibrated quartz balance connected to a dedicated software monitors evaporation rate and film thickness in real time[1]. The high vacuum system is composed of a primary rotary pump and a turbo-molecular pumps that guarantee pressure values below $2x10^{-6}$ mBar inside a bell-shaped vacuum chamber: the lower the vacuum pressure, the better the deposited film quality. Once low pressure is reached, current injection can be controlled manually and slowly increased according to desired evaporation rate. A mechanical shutter is also provided inside the chamber that can be opened and closed from the outside depending on need. For instance, it can prevent the samples to overheat through direct irradiation from heated metal.

Note: evaporation rate is key parameter for high quality film. As it gives insight on film growth, it is recommended to be kept as constant as possible. It is also important to consider that metal evaporation is NOT uniform in space, as the particle density lowers with distance from vertical axis. This implies that values from the microbalance are to be scaled with a form factor that is dimension- and time-dependent.

2.1.1.4 Perovskite deposition

Major advantage of hybrid metal halide perovskite materials is the possibility of having them solution-processed[173], [174], [175]. The most effective way of obtaining microcrystalline thin films consists in producing perovskite solution from related chemical precursors (in here, $PbBr_2$ and $PEABr_2$ dissolved in DMF) and making it evaporate on target substrate -in this work we will focus on spincoating of perovskite as well.

Practically, solution is spincoated on target substrate and the obtained film is softly annealed in order to promote defect-free crystallisation as desired. Alternatively, the use of *antisolvent* can be considered to make crystallisation happen faster: these substances decrease the solubility of solute, causing it to precipitate out of solution rather than dissolve. Further insights in [176], [177].

Perovskite treatments require strict conditions for optimal crystallization: for this reason, nitrogen atmosphere is mandatory as non-inert gases would be detrimental to material surface[178]. Notably, solution concentration and spin-coating parameters are to be tuned for film quality and thickness control. Studies on flexibility have shown that threshold is to be set at 5um: thicker films report evidence of cracks after bending [106].

---

[1] *From the variation of the vibration frequency of the quartz resonator is possible to calculate the evaporation rate expressed in nm s-1 and from this, the total material thickness deposited onto the substrate.*

2.2.1 PROTOCOLS

LITHOGRAPHY

Substrates treatment

- Plastic sheets or foils of different thicknesses to be cut to desired area (from 4 to 100cm^2).
- Sonication in Acetone, IPA and DI water, 5 minutes per step; then blow dried with N2 gas.
- Plasma treatment with Oxygen gas. PIE Scientific TERGEO plus Plasma cleaner, 7sccm, pulse ratio 255, 50W, 1min.

Pre-patterning

- Substrate to be fixed into the spin coater holder through vacuum -larger, flexible foils can be stuck on wider glass slide before it to be inserted onto the holder.
- Yellow environmental light required: no white light is recommended when handling photoresist materials.
- Spin coating of Microposit S1818 positive Photoresist; 2000rpm, 1min dwell time; poured dose: 100µl/cm^2 -expected thickness in the range 1/2µm.
- Annealing at 110°C, 1 min.

Patterning

- Software-driven optical alignment of the sample inside the patterning machine with definition of corners and/or reference points; MicroWriter ML3 Durham Magneto Optics employed; 375nm UV laser.
- Upload of the desired file (.ciff) with the design to be patterned.
- Definition of resolution (down to 1µm) and quality of the real-time focus correction (Best) -the higher the required performance, the longer the exposure process (>2h for large substrates).
- Definition of desired laser intensity. The exact determination of it requires a priori procedure that is a dose rate focus test. Refer to the user guide. In this work, values in the range between 450-500mJ/cm^2 have been selected.

Post-exposure

- At finished exposure, sample is chemically treated in order to have the weakened photoresist removed
- Development in MF319 Dev. for 50s followed by a cleaning in DI H_2O for the same amount of time
- Sample is blow-dried with N2 gas
- Post-development optical verification with microwriter microscope to check for flaws and/or issues. *Commonly observed: i) not well-defined edges (annealing time and temperature above recommended values, lower intensity, diluted developer, shorter developing time) and ii) over-exposure with wider pattern creation (higher intensity, longer developing time).*

Finally, metal contacts can be deposited on the sample.

METAL CONTACTS

Technical notes:

- starting conditions require the chamber being vented to be freely opened; if the pumps are on, make sure the related valves are closed before venting, as contact of it with air at standard pressure is to be prevented.
- Make sure that no current is flowing: power needs to be set to zero before the glass bell is removed.

Preliminary

- Check pump valves to be closed
- Vent the chamber opening the dedicated valve
- Insert crucibles in needed number in their exact place and direction (follow the signs reported in the setup)
- If off, turn on the current generator and verify that current passes through the crucibles as expected: select the target crucible channel and slightly increase the delivered power until a signal appears in the amperometer screen

Metals preparation

- Weight desired amount of metal -for previously mentioned values, we recommend 18/20mg Cr, 350mg Au- and cut it in form of tiny segments of 6/8mm in length.
- Place the segments in their dedicated crucible basket. Repeat the procedure of checking current flow.

Samples preparation

- Stick the samples to the holder with magnets or tape -glues prevent vacuum levels to decrease fast as they trap gas molecules: use it scarcely.
- Place the holder face down in its dedicated spot and verify its alignment

Vacuum

- Close the chamber and its venting valve, then verify the shutter is free to move
- Turn on primary pump and Pirani pressure sensor
- Wait until pressure is below 1mTor, then turn on the turbomolecular pump and wait for it to run at full regime
- Close the valve of primary pump and open electrovalve, then turn Pirani off
- Turn Penning sensor on and wait until desired vacuum level is reached

Optimal values in the range 1/5e-6 mBar

Evaporation

- Set material density in the software and start a slow ramp in current up to desired evaporation rate
- Keep to slowly increase the current to maintain a costant rate until target thickness is reached
- Use the shutter to cover from overheating, reduce current and wait until pressure levels come back to reasonably low values
- Repeat for metal n.2
- Close the electrovalve and open chamber

Lift-off

- Put the coated samples in acetone for 3 to 4h to remove excessive photoresist
- Sonicate the samples in Acetone, IPA and DI water for 2min per step, then blow-dry.

PEROVSKITE THIN FILMS DEPOSITION

The procedure below is performed in N2 environment, in order to prevent oxidation or contamination issues.

Preparation of solution

- For 1M solution of PEA_2PbBr_4, exact quantities are the following:
- 917.5mg PbBr2
- 1018.2mg PEABr
- 2.5ml DMF
- Stirring is required overnight to allow the precursors to dissolve property

Perovskite spincoating

- Solution is poured onto the substrate (1µl/mm^2)
- Spincoating procedure accounts for a two-step process, that is 800rpm/5s and 2000rpm/55s

Annealing

- Samples are put at 70°C for 10min
- Samples are stored in N2 environment in order for residual solvents to evaporate

2.2 CHARACTERIZATION TECHNIQUES

2.2.1 OPTOELECTRONIC PROPERTIES

2.2.1.1 Dark Current and Light Response

Primary feature of interest of 2D perovskite is their outstanding performance thanks to a high signal-to-noise ratio, that is consequence of an extremely low dark current. Resistivity analyses are of fundamental importance for devices characterisation: for this reason, a dedicated probe-station with integrated Faraday shielding is required that prevents external light from reaching the sample and external noise sources to disturb the collected signal. We here employ micrometer-sized tungsten tips as contacts and an optical microscope for perfect alignment. A custom-made UV-LED system (λ = 385nm, max power 1mW) is also integrated and calibrated with a silicon photodiode for measuring electrical response under light in the form of photocurrent.

In order to measure the samples' dark current, bias is applied through the tips with a source-measure unit and the signal is recorded in real time. As previously mentioned, the extremely low dark current makes it mandatory to use high-resistance measurement system: here, a Keithley 6517A Electrometer is employed that allows for current signals down to 10fA to be collected. Applied bias ranges between -15V and 15V for standard dark current analyses at room temperature; time between each collected point is to be set at values > 15s, as this is the standard time to wait for the output signal to stabilise and relax capacitance-related effects after a change in bias is made.

Note that PEA thin films are demonstrated to resist to high applied electric field, with limit values in the range of 5kV/mm. High-bias techniques are here employed to infer material optoelectronic properties and to assess its stability under high energy radiation with high applied electric field.

2.2.1.2 Time-Response setup

This measurement is performed with a fast excitation source -PicoQuant picosecond laser diode- with narrow emission at 375 nm and 40 ps pulse duration with adjustable power through the Taiko PDL M1 driver. Using built-in bunch mode, an arbitrary long laser burst with 50% duty cycle can be obtained. In this operation mode, the laser shoots 40 ps pulses at 10MHz. A longer wavelength square wave is used to modulate the power of the LASER creating separate bunch of pulses. The light-induced current signal is converted to voltage using a current amplifier FEMTO DHPCA-100 (bandwidth 1.8 MHz), then the output signal is acquired with a Rohde & Schwarz RTB 2004 oscilloscope. Through the amplifier it is possible to apply up to 10V bias to the sample. A picture of the set up used is reported in Figure 22. Two mirrors are used to control the position of the beam, a lens is used to focus the beam spot on the sample surface. The sample is positioned in a metal box, thus providing both protection and shielding with the electrical connections. The time response is evaluated by calculating the time difference between the moments in which the response is 10 % and 90 % of the total photocurrent signal in the rising or falling dynamics.

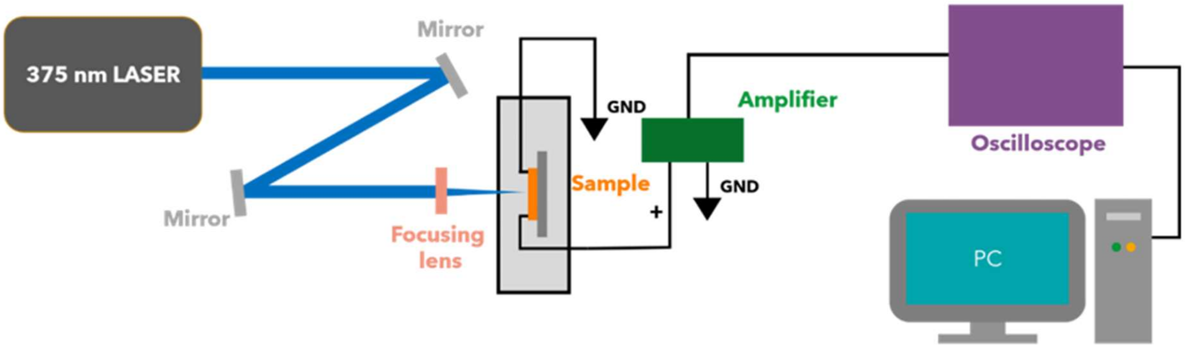

Figure 22 Transient photocurrent setup. A ps 375 nm LASER source is positioned on an optical board. Two mirrors are used to modify the direction of the beam. A focusing lens before the sample focuses the beam spot on the sample. The sample is positioned inside a faraday cage and connected to a current/voltage transimpedance amplifier used to amplify the signal. An oscilloscope measures the voltage pulse and acquires the data.

2.2.1.3 Photoluminescence

Photoluminescence is the emission of light from a material after it absorbs photons. When a material is excited by an external light source, typically with a higher energy than the material's band gap (such as ultraviolet or visible light), electrons in the material are promoted from the valence band to the conduction band, creating electron-hole pairs (excitons). As these excited electrons relax back to their lower energy states, they release energy in the form of emitted light, which is the photoluminescence signal. The wavelength of the emitted light provides information about the material's band structure, defects, impurities, and overall electronic properties.

For the purpose of this work, the main experiment conducted is photoluminescence at room-temperature, from which the energy of the photon emissions can be measured. Experimental setups are encapsulated in a light-tight box during measurements; laser alignment is obtained through specific optical lenses and dedicated filters.

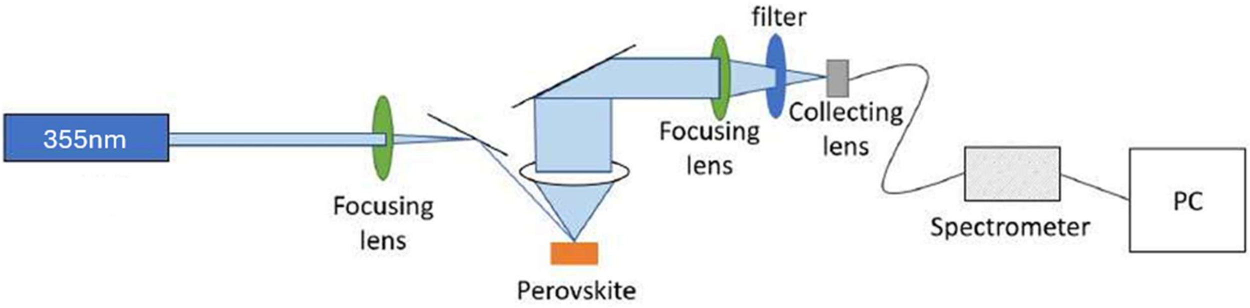

Figure 23 Illustration of the PL experimental setup, using a 355 nm wavelength YAG laser with various focusing lenses, a longpass filter to block the direct laser beam and a collecting lens with a built-in collimator. The spectrometer used was Ocean Optics QE65000 and spectra were collected using SpectraSuite.

Room temperature PL is carried out at the university of Surrey using a Nd:YAG excitation laser of 355 nm wavelength and 20 mW power, with the experimental setup shown in Figure 23. The spectrometer used is Ocean Optics QE65000 and spectra are acquired using SpectraSuite.

Integration times are varied slightly for each sample, but generally integration times of up to around 100 ms is enough to observe a strong signal.

2.2.2 ATOMIC FORCE MICROSCOPY

Atomic Force Microscopy (AFM) is a high-resolution scanning technique used to image surfaces at the nanometer scale by measuring the forces between a sharp probe and the sample. The AFM operates by moving a tiny, sharp tip attached to a cantilever across the surface of a sample. As the tip scans the surface, it experiences forces such as van der Waals forces, electrostatic forces, or repulsive contact forces depending on the distance from the sample. These forces cause the cantilever to deflect, and this deflection is measured using a laser that reflects off the cantilever into a photodetector. By monitoring these deflections, AFM generates detailed 3D images of the surface topography with atomic or near-atomic resolution.

In this work, we employ non-contact AFM for both surface and photovoltage mapping of perovskite thin films. This means no mechanical interaction between tip and sample occurs: only Van der Waals and Coulombic forces actually contribute to cantilever bending, thus preventing the samples from disruptures or damages.

For this purpose, the employed AFM is Park NX10.

2.2.2.1 Surface Topography

The basic operation principle of a standard AFM system with optical feedback involves scanning an AFM probe with a sharp AFM tip over a sample surface in a raster pattern as reported in fig. 24.

The AFM tip is usually made of silicon or silicon nitride and is integrated near the free end of a flexible AFM cantilever. A piezoelectric ceramic scanner controls the lateral and the vertical position of the AFM probe relative to the surface. When the tip is approached to the sample at distances down to 0.1-20 nm, information on the sample properties can be studied from the interactions between the tip and the sample surface, inducing the deflection of the AFM cantilever. Such a process is tracked by a laser beam reflected from the back site of the cantilever and directed into a position sensitive photodetector (PSPD). A PSPD is a photodiode divided into four quadrants: from the measurement of the laser intensity variations on the different sections it is possible to extract the amount of vertical and lateral deflection of the cantilever. As the AFM tip moves over features of different heights, the deflection of the AFM cantilever changes according to the different local interactions. A feedback loop controls the vertical extension of the vertical scanner to maintain near-constant constant interaction force. The coordinates that the AFM tip tracks during the scan are combined to generate a three-dimensional topographic image of the surface. According to the tip-sample distance r, the interaction between the tip and the sample can be either repulsive or attractive, enabling two different AFM operation modes: in here, non-contact mode is reviewed only.

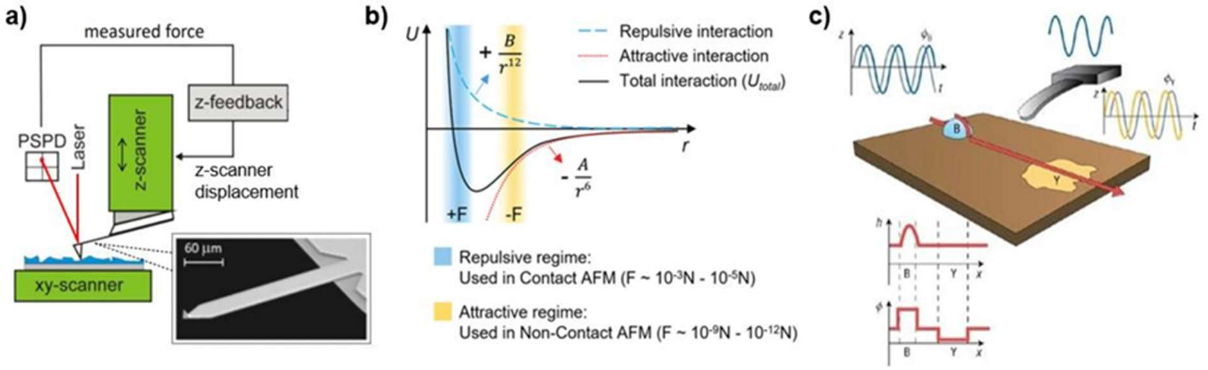

Figure 24 Atomic force microscopy. a) Schematic representation of the AFM components. The scanning electron microscope image of an AFM probe is reported as inset, showing the AFM cantilever and tip. b) Lennard-Jones potential approximating the tip-sample interaction energy. According to the tip-sample distance, AFM can be operated in contact or non-contact mode. c) Non-contact AFM operation. Variations in the sample topography (blue region) are measured by changes in both the cantilever oscillation amplitude and phase, while only phase traces are sensitive to compositional changes (yellow region).

The AFM probe cantilever is oscillated by a piezoelectric actuator at or near its fundamental resonance frequency, usually several tens to several hundred kilohertz. The AFM probe is subsequently brought closer to the sample, maintaining a separation of several nanometers from the surface. The resulting attractive interaction forces damp the cantilever oscillation amplitude and modify its phase. The feedback loop acts to maintain a constant AFM cantilever oscillation amplitude and hence a constant interaction force. The advantage of non-contact mode is that it offers the lowest possible interaction between the tip and the sample surface. Small interaction forces help preserve AFM tip sharpness and achieve high resolution. The oscillation phase is affected by variation in the dissipated energy on the sample surface, thus non-contact mode AFM is sensitive to the sample composition.

2.2.2.2 Kelvin-Probe Force Microscopy

Kelvin Probe Force Microscopy (KPFM) is a variation of Atomic Force Microscopy (AFM) that measures the surface potential and work function of materials with nanometer-scale resolution. In KPFM, a conductive AFM probe scans the surface in non-contact mode, and an electrical bias is applied between the tip and the sample. By detecting the electrostatic forces and nullifying the potential difference via a feedback loop, KPFM maps the local contact potential difference (LCPD) across the surface. This technique provides valuable information about electronic properties, including variations in work function and charge distribution, making it essential for characterizing semiconductors, thin films, and nanostructures.

In here, this technique is exploited for the analysis of light-induced photovoltage on 2D perovskite films. An integrated optic system is aligned with AFM active operating area: this allows for simultaneous illumination and mapping. A scheme of the integrated setup is reported in figure 25; illumination is performed through a 375nm picosecond laser and modulated via dedicated laser driver.

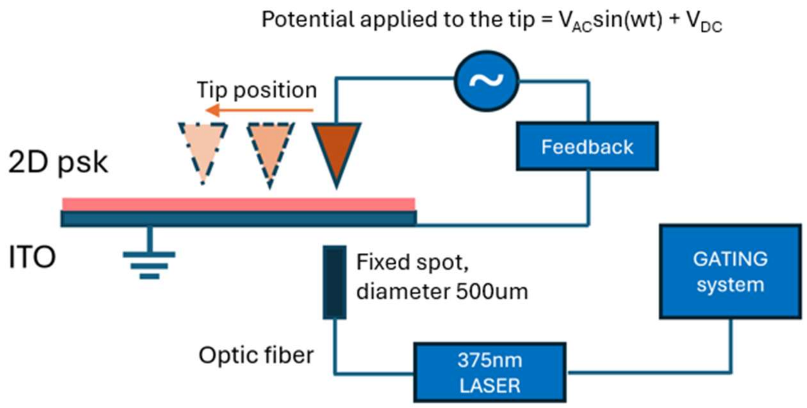

Figure 25 Scheme of the experimental setup employed for photovoltage analyses on 2D perovskite films through KPFM. The material is spincoated onto ITO substrate connected to ground. A feedback circuit allows for KPFM measurements through the application of a bias to the tip that nullifies the potential difference generated by the non-contact interaction between the surface and the tip itself. The illuminating laser is focused though an optical system that grants laser spot of 500um in diameter. The tip is moved far from the spot up to 8mm in distance and a gating system allows KPFM mapping in light and dark.

2.2.3 HIGH ENERGY RADIATION EXPOSURE

As primary target of this work is radiation detection through 2D perovskite devices, we here highlight the main features and experimental setup of the employed radiation sources, which range from standard laboratory-scale X-ray tubes to high energy proton facilities from radiotherapy centres. The exact set of measurements and experimental conditions will be discussed in greater detail in section 3.2.

2.2.3.1 X-ray tube

In X-ray photocurrent experiments, commonly used to evaluate the performance of X-ray direct detectors, the current response of a device under an X-ray beam is measured to extract key performance metrics like sensitivity and limit of detection (LoD). As reported in sec 1.1.3.1, Fluence, Activity and Dose are fundamental parameters to understand the outcomes of these experiments.

In here, X-ray tubes are employed as main radiation source. A radiation X-ray tube consists in a vacuum device with a cathode (negative) and anode (positive). The cathode, typically made of tungsten, is heated to emit electrons via the thermionic effect, which are then directed towards the anode through the application of high voltages (tens to hundreds of kV). There, they collide and lose energy, producing bremsstrahlung radiation (broad-spectrum X-rays). If the electron energy is high enough, characteristic X-rays are emitted as electrons from inner shells of the target material are ejected and replaced by outer electrons. The spectrum consists of continuous bremsstrahlung and sharp characteristic peaks, depending on the target material. Beryllium windows allow X-rays to exit while minimizing absorption, and the target is cooled to maximize heat dissipation from electron-target interactions.

- Experimental system, University of Bologna: Hamamatsu Microfocus L12161-07 X-ray source. It is a tungsten target X-ray rube with operating voltage up to 150 kVp and tube current between 10 to 500 μA. The tube has a 0.2 μm Be window and an X-ray beam aperture of 43°. The X-ray tube is air cooled with an external power supply that can be controlled with a PC via RS-232C interface. The simulated spectrum of the Hamamatsu tube at the two operating voltages used (40 and 150 kV) is obtained with the SpecCalk simulation software; exact dose calibration is performed through commercial detector Barracuda (RTI Group, Sweden) inserted inside the same boxes used for the samples.

- Experimental system, University of Surrey: Amptek Mini-X2 gold target X-ray tube. The X-ray tube is controlled using the Amptek Mini-X2 Controller software with a voltage range of 10 kV- 50 kV and current range of 5 µA- 200 µA. The irradiated sample is fixed to a PCB with a bias applied and current measured using a Keithley 487 source meter.

These systems allow for dose rates in the range 100-5000µGy/s. The former is also provided a shutter to be controlled remotely for ON/OFF measurements as reported in the sketch below (fig. 26).

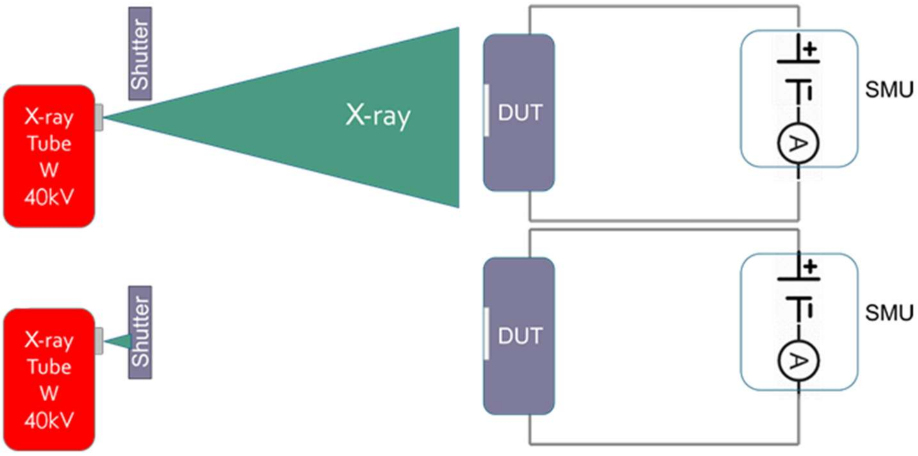

Figure 26 X-ray photocurrent experiment. The system is composed by the X-ray source, a lead shutter, the device under test and a source meter unit (SMU) electrically connected to the sample. The sample is placed inside a metal box with an aluminium window for light protection. The shutter is controlled to modulate the photon flux impinging on the sample. Top scheme reports the configuration with the shutter open, bottom refers to shutter closed blocking the X-rays.

2.2.3.2 Alpha particles detection

As this work accounts for both alpha-particle spectroscopy and real-time direct detection in the form of generated photocurrent, the two different experimental systems are here described in detail.

Spectroscopy measurements have been performed in the laboratories of the University of Surrey.

2.2.3.2.1 Real-time detection of alpha particles

Devices' response under alpha particles is here monitored through the integration of a dedicated measurement system that accounts for

- a shielding metallic box, that grants no light can get to the sample

- a source holder, whose distance from sample can be tuned mechanically from 2 to 50mm. No internal manipulation is required as the up/down movement is obtained through a calibrated screw system that allows for resolution down to 0.25mm.
- a device under test (DUT) to be connected to high-performance source-measure unit.

The alpha source here employed is ^{221}Ra, 0.5 μCi; bias is applied to the sample with Keithley 6517A Electrometer.

Measurements are performed in current mode and results are obtained in the form of photocurrent as function of distance from source. Notably, exact dose-rate is to be estimated a priori, as it requires the convolution of both the decrease in particles' energy and number. Moreover, exact energy loss is to be predicted via SRIM simulation software [179].

2.2.3.2.2 Alpha pulse-height spectroscopy

To perform alpha pulse measurements, the samples were exposed to a single alpha ^{241}Am source of activity 1.85 MBq. For acquiring alpha spectra, the signal output from the sample is connected to a charge sensitive preamplifier (Kromek eV-550) and an analog shaping amplifier (ORTEC 571) which allows for shaping times between 0.5 and 10μs. The latter is then connected to a multichannel analyser which digitizes the shaped signals and classifies them based on energy, storing the results in a histogram. The alpha spectrum is displayed as peaks corresponding to the energy of the detected alpha particles. A precise scheme of the employed setup is reported below. Alpha spectra are acquired using Maestro software, with acquisition times of typically 30 seconds. Amplification gain is set according to noise level through the shaping amplifier; shaping time is chosen to be 10μs as the rise time of perovskite devices is expected to be slower compared to it due to low charge carriers' mobility.

An analog system is also implemented for direct comparison, which accounts for digital shaping amplifier (Amptek PX4) and dedicated Amptek ADMCA software.

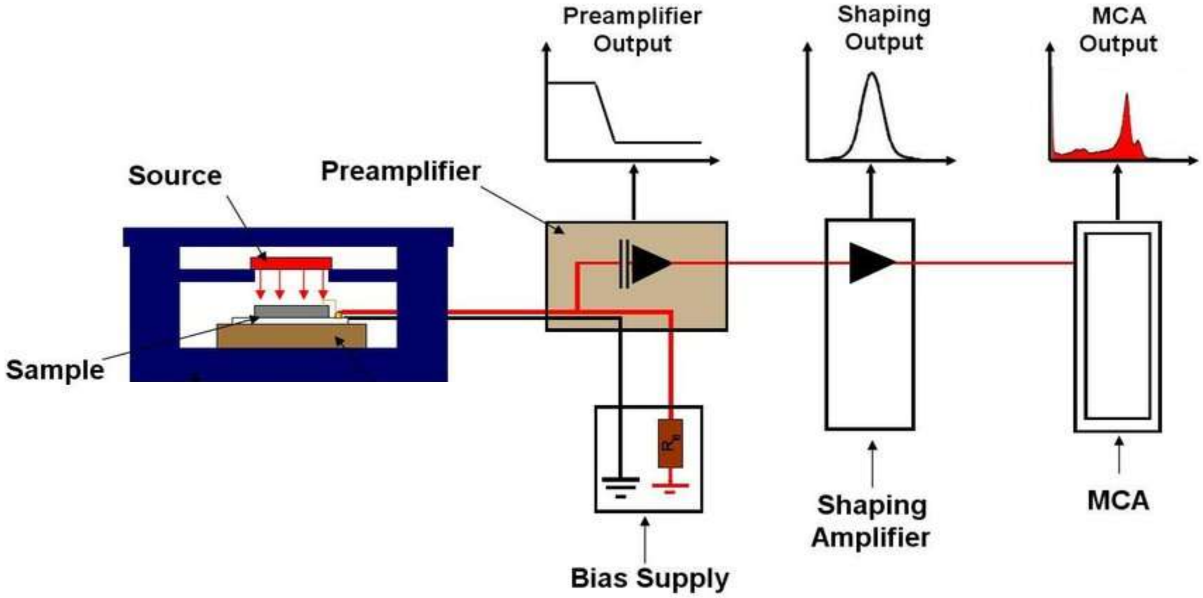

Figure 27 An alpha spectroscopy setup includes a detector that captures alpha particles and sends weak signals to a preamplifier, which boosts them. A shaping amplifier then optimizes the signal shape and reduces noise. Finally, a multichannel analyzer (MCA) digitizes the signals and sorts them by energy, generating a spectrum for identifying alpha-emitting isotopes. M. Veale, University of Surrey.

2.2.3.3 Characterization of Y-rays from radiotracers

To assess the capability of the 2D-perovskite detector to effectively detect gamma rays emitted by medically relevant radiotracers[2](^{18}F and ^{99m}Tc) a custom experimental setup is developed and shown below. This is equipped with a 3D-printed frame that holds in place a stepper motor and the sample box; the motor is guided by an Arduino UNO board and an A4988 stepper motor driver. The ^{18}F radioactive drug is contained into a vial kept by a printed support connected to the motor axis. The Arduino is programmed to send a PWM signal to the driver; based on the pulse sequence the driver sends a specific current sequence to the motor coils. The motor moves the source by 180°, in the OFF state the source is > 15 cm from the sample. A thick Pb cylinder is used to screen the sample from the radiation when the state is in the OFF position, while in the ON position the motor moves the gamma source on top of the sample. The detector response is measured for different sources activity values through a SMU connected to the sample box.

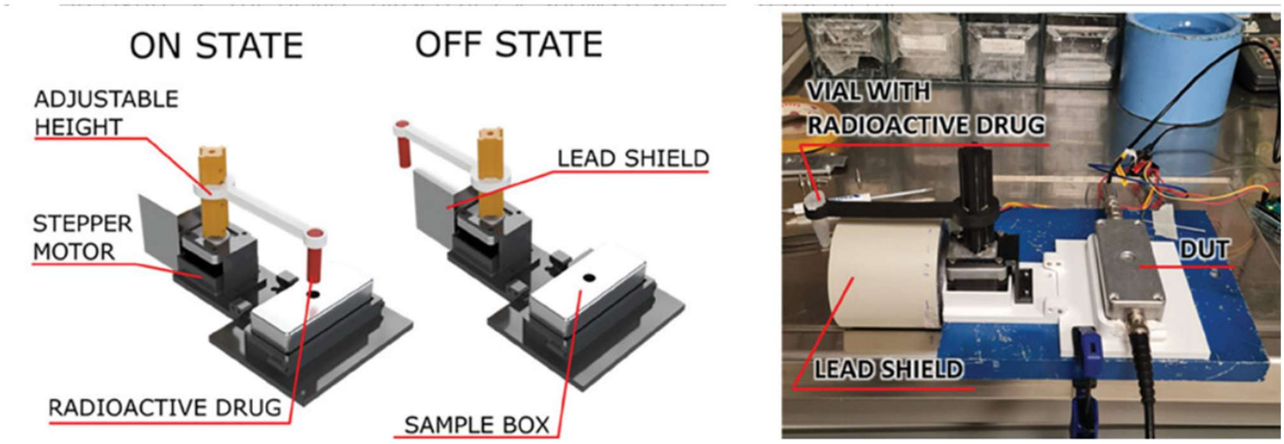

Figure 28 Shutter for high energy gamma rays. Left) Scheme of the shutter system employed for the sensors characterization under high energy gamma ray emitted by radioactive drugs. A stepper motor is controlled by an Arduino UNO board. 3D printed holders keep the moto and sample box in place. The radioactive drug is contained in a vial hold by a custom support connected to the motor axis. A thick Pb cylinder is used to screen the sample from the radiation when the state is in the off position. In the on position the motor moves the gamma source on top of the sample. Right) Picture of the setup used at the IRCCS in Reggio Emilia.

2.2.3.4 High-energy Proton Facilities

Test at high proton energies-TIFPA

Measurements under highly energetic protons have been carried out at the Trento Proton Therapy facility, which primarily provides a cyclotron that serves two medical treatment rooms both equipped with rotating gantries dedicated to patient treatments[180]. The facility is also equipped with an experimental area where the beam line is split in two branches, both dedicated to a large spectrum of scientific applications, including medical physics, detector testing, radiation hardness measurements, space research and radiobiology. The main beam line is split into two additional sub-branches at 0◦ and 30◦ with respect to its initial direction by a dipole magnet (Fig. 29). This allows the simultaneous setup of two different experiments if necessary, but the beam cannot be transported along the two branches at the same time. We refer to the 0◦ and to the 30◦ lines as the "Biology" and "Physics" beam line, respectively (Fig.

---

[2] The experiments were carried out at the IRCCS in Reggio Emilia. The setup was fabricated by Verdi M.

29B), since they are intended for different purposes and thus are be implemented with different hardware.

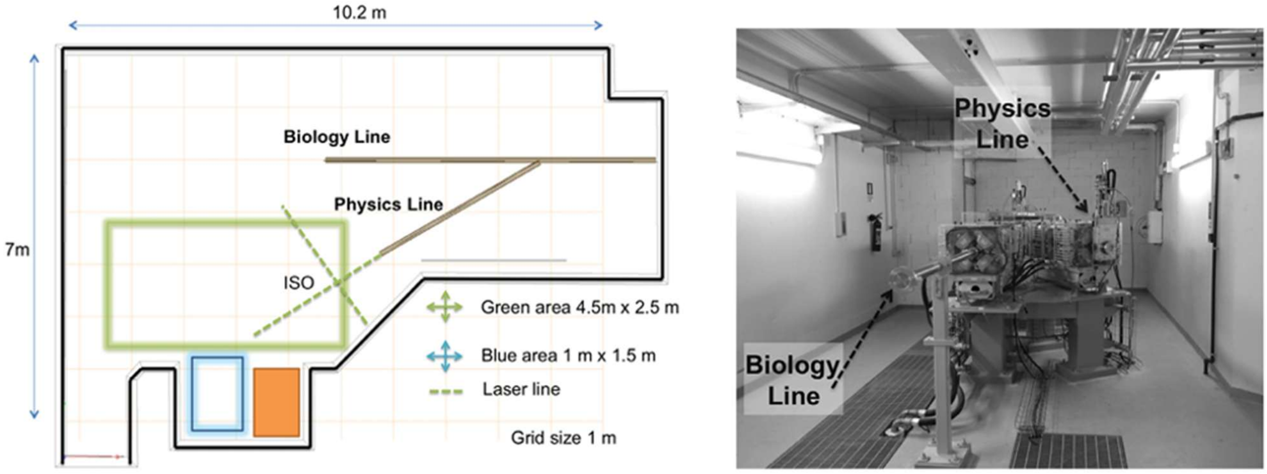

Figure 29 Picture (lower panel) and a schematic view (higher panel) of the experimental room at the Trento Protontherapy centre. The biology (0◦ branch) and physics (30◦ branch) beamlines are indicated. In the map the space available for experimental setup at the Physics line is indicated (green area), together with an additional area for equipment storage inside the cave during irradiation (blue area)[180].

Precisely, as the physics line is the main source of protons for this work, its features are reported in figure 30. Proton energy and beam profile range between 70-228MeV and 16.7/8.8 cm FWHM at the lowest and highest energy respectively. Exact measurements have been performed through the use of dedicated detectors; interested readers are referred to[181]. A tissue-equivalent human phantom is also provided that allows for measurements that resemble clinical trials. Flux and exposure time, reported in Figure 30, are controlled via dedicated software, through which it is possible to control the total delivered dose and the number of incident protons at the isocenter.

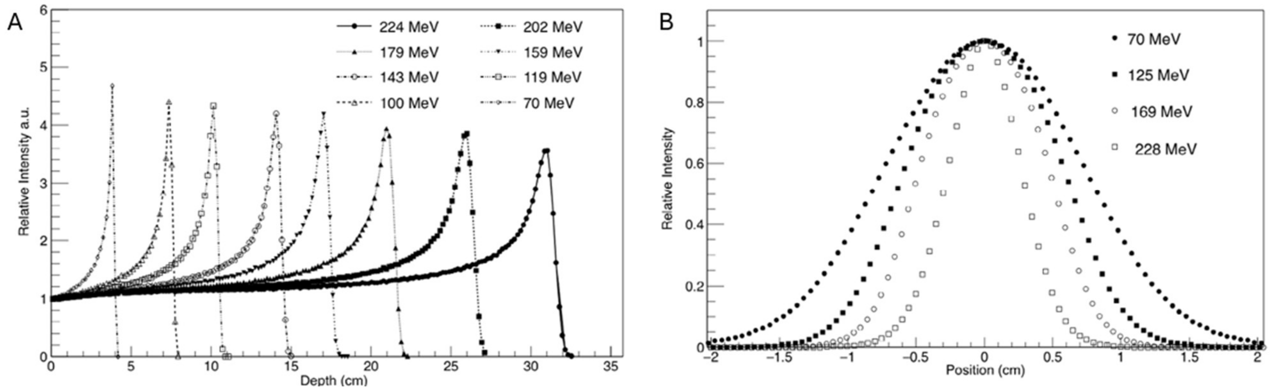

Figure 30 A) Bragg curves measured at different energies with the Giraffe detector placed at the Isocenter position. Thanks to a previous calibration of the detector, the depth plotted on the X-axis is expressed as water-equivalent. B) Beam spot profiles measured at different energies with the Lynx detector placed at the Isocenter position[181]

Low-energy proton beam monitoring

The detectors were irradiated using a 5 MeV proton beam provided by the 3 MV Tandetron accelerator of the LABEC (**La**boratorio di tecniche nucleari per l'**A**mbiente e i **Be**ni **C**ulturali) ion beam center (INFN Firenze, Italy). The beam was extracted into ambient pressure through a 200 nm thick Si_3N_4 membrane; the sample was typically mounted at a distance of 8 mm from the extraction window. Proton beam currents used in this work were typically in the 1 – 100 pA range. The weak intensity of the extracted beam was monitored and quantitatively measured using a rotating chopper, placed between the silicon nitride window and the sample, that intercepts the beam; the chopper was a graphite vane covered with a thin nickel evaporation, and the Ni X-ray yield was used as an indirect measurement of the beam current.

To determine the actual energy of the protons impinging onto the semiconducting layer, the energy lost by the protons passing through the several layers interposed between the beam and the sensor, namely, 200 nm of Si_3N_4 for the beam extraction window, 8 mm of mixed air-He (50%–50%) atmosphere in the gap between the extraction window and the metal box, 13 μm of Al for the entrance window of the box, where the sensor was enclosed, and 36 mm of air inside the box, has to be calculated. After passing through these layers, protons lose ≈ 575 keV, as calculated with the SRIM Monte Carlo code.

3. RESULTS

This chapter fundamentally gathers the obtained outcomes of direct radiation detection through co-planar devices based on 2D-PSK PEA_2PbBr_4 thin films. As this work has comprised extensive studies on material properties prior to target applications, the first section is dedicated to the analysis of the abovementioned devices as basic photodetectors.

This work contributes to the extensive characterization of simple 2D-PSK-based structures, which have garnered significant interest in recent years. Primarily, these devices are shown to exhibit exceptionally low dark current, high responsivity to UV light and X-rays, rapid time-response, and impressive long-term stability, as highlighted in numerous recent studies. These properties are thus covered quickly in sec. 3.1.1, with major focus on the effectiveness of thin films extension to radiation detection. It is important to notice that thin films offer high flexibility, that is key feature in matter of wearable electronics. Results as function of bending radius under radiation are reported in the works[75], [182], [183] . While investigating response under UV-laser, a critical light-driven effect emerged that will be elaborated in sec. 3.1.2.

Rather than being chronologically exposed, this list is intended to report tests and experiments that have led to medically relevant applications -which have been published in high-quality journals- and future prospects towards space-grade personal dosimetry.

Sec. 3.1.3 covers devices response under alpha particles from specific sources in both current- and pulse-modes. Goal is to be found in the demonstration of thin films' spectroscopy properties, which are reported to exhibit counting down to single pulses. Prior to results on thin films, a direct comparison with 2D-psk single crystal is provided. Experiments regarding spectroscopic properties of perovskite thin films have been performed at the University of Surrey and still ongoing.

Moving forward, sec. 3.2.1 reports results under high energy protons from linear accelerators of medical centre, with energies of 70/200MeV. Although preliminary, these outcomes pave the way for deeper understanding of material response under charged particles and provide insights on specific applications in matter of radiation hard, wearable detectors. These are found to be enveloped further in that section, which is focused on medical application of 2D-PSK thin films. Specifically, sec. 3.2.2 presents published results on real-time proton beam monitoring (5MeV) through the implementation of microelectrode arrays. In there, highlights are put on the possibility of having longitudinal profiling without the need for post-processing or analyses prior to treatment. Following, sec. 3.2.3 is focused on wearable perovskite films for on-line monitoring of radiotracers in nuclear medicine. The detectors have been optimized in channel length and active area to work at low bias for the detection of gamma rays emitted by clinically relevant radiotracers at the IRCCS of Reggio Emilia, with the aim to monitor the intravenous injection of radiopharmaceutical drugs.

Lastly, section 3.3 is intended to present preliminary analyses and tests on-earth for the IRIS project, that accounts for wearable personal dosimeters to be sent to outer space onboard the ISS. As launch is planned for Mar 2025, no data from space missions are available as for now. Nevertheless, the entire process of fabrication and characterization of sensors is provided, together with a-priori simulations for devices materials and structure assessments. IRIS dosimeters couple 2D perovskites with organic semiconductor thin films made of TIPS:Pn. A brief overview of these materials and their features is thus provided in Appendix 1.

3.1 OPTOELECTRONIC CHARACTERIZATION OF 2D-PSK DEVICES

Prior to the application of perovskite thin films for radiation detection, investigations on devices performance as state-of-the-art photodetector are mandatory for quality assessments and consistency with declared figures of merit such as dark current and responsivity.

For this reason, we employ standard single pixels for optoelectronic analyses, which is made according to sec. 2.1 and whose features are reported below. This helps in defining whether if changes in fabrication parameters have led to different response outcomes and it provides clear evidence of devices reproducibility.

Surface topography techniques are useful tool for thin films analyses in terms of quality and uniformity assessments. PEA_2PbBr_4 thin films fabricated according to sec. 2.1 exhibit crystal grains in the form of flakes that measure up to 15 µm, as shown in figure 31. Measurements are performed through atomic force microscopy.

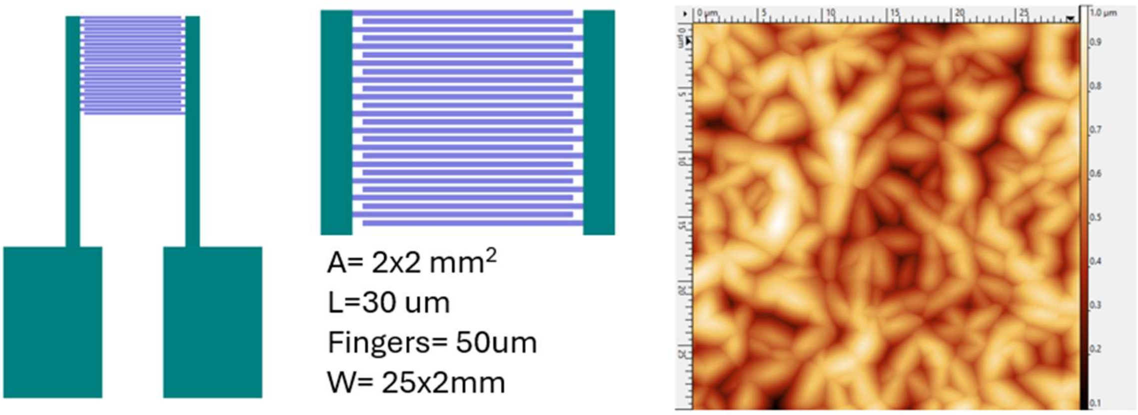

Figure 31 On the left, the standard single pixel structure and spatial dimensions are reported: these are standard electrical Cr/Au contacts evaporated on the desired substrate and over which perovskite thin films are deposited. The right panel reports a surface topography map (30x30 µm^2) of a spin-coated PEA_2PbBr_4 thin film, obtained with Atomic Force Microscopy.

3.1.1 RESPONSE UNDER UV LIGHT

Prior to electronic tests, the investigation of photocurrent spectra in PEA_2PbBr_4 perovskite thin films is essential for overall response analyses. As reported in chapter 1.2, these low-dimensional perovskites exhibit strong excitonic effects and tuneable electronic properties, making them promising candidates for next-generation photodetectors and solar cells. Optoelectronic characterization of these devices typically begins with the use of ultraviolet (UV) light, as this higher-energy radiation can efficiently probe the wide-bandgap structure of the material. UV light excites electrons across the bandgap, enabling a more precise analysis of the material's photoresponse and carrier dynamics. Additionally, UV excitation allows for the identification of surface and near-surface phenomena, where defect states or excitonic behavior may strongly influence device performance. This preliminary step is crucial for establishing a baseline understanding of the material's efficiency and stability before exploring broader spectral ranges.

Figure 32 reports a photocurrent spectrum of a PEA_2PbBr_4 thin film illuminated from the top, together with Tauc plot and linear fit used for the extraction of the band gap value, which is reported to be 2.90eV. Notably, it exhibits excitonic peak and band onset as expected[1]. The narrow transition peaked at 410 nm is attributed to the 1s Rydberg series Wannier-Mott exciton transition [184]. It is worth mentioning that in the UV range, 2D perovskites have a very high absorption coefficient (α_λ) in the range of 0.03-0.05 nm^{-1} at 300 - 400 nm wavelength. According to the Lambert Beer model the light intensity (I) through a medium follows the relation:

$$I = I_0 e^{-(\alpha_\lambda \mathrm{d})}$$

Where I_0 is the impinging light intensity on the sample and d is the thickness. Therefore, in a few hundred of nanometres, the perovskites absorb almost all the incoming radiation. Remarkably, the obtained signal was good revealing the presence of charge collection in the out-of-plane direction since the electrodes are positioned at the bottom and the film thickness is around 2 μm.

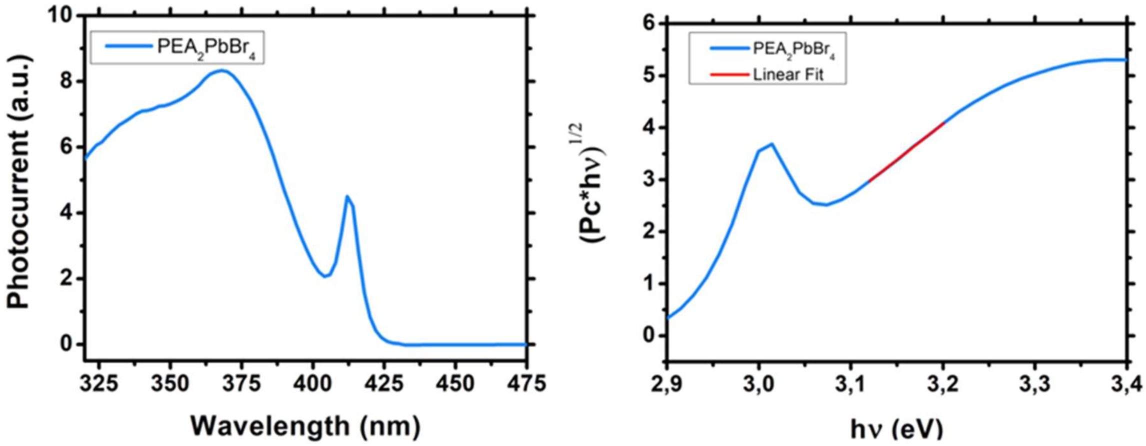

Figure 32 PEA2PbBr4 optoelectronic properties. Photocurrent spectra of a PEA_2PbBr_4 thin film illuminated from the top on the left panel; Tauc plot and linear fit used for the extraction of the band gap value, which is reported to be 2.9eV[106].

Devices dark current and basic photoresponse are performed in dark environment with dedicated probestation tips that provide low-noise connections; instruments that allow for high-impedance measurements are mandatory as source-measure units. Light source is placed on top of the sample, thus illuminating the film on the side farther from electrical contacts. As this seems contradictory with the theoretical estimation of penetration depth of UV photons into perovskite materials, further explanation and insights are discussed in 3.1.2.

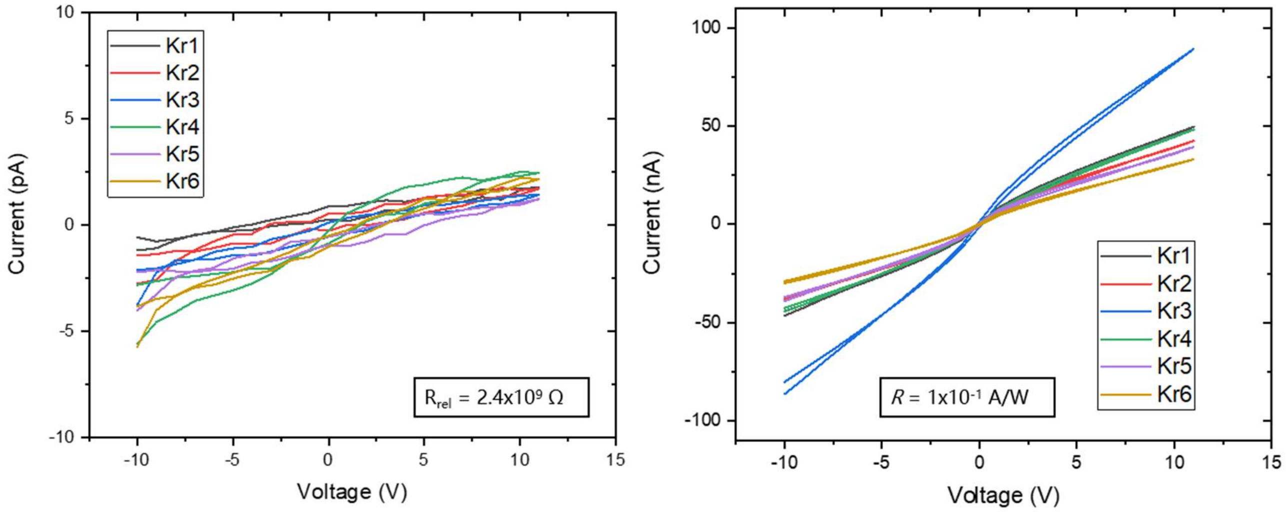

Figure 33 Dark current and response under UV LED (380nm) of six thin film devices on deposited on Kapton substrate. Results show reproducibility of high-performing samples with currents down to 10^{-13}A at low applied bias and light-to-dark ratio of 10^5, with responsivity of 100mA/W.

Dark current values are reported to be lower that 5pA at 10V applied bias, which corresponds to 300V/mm electric field; light response is demonstrated to be up to 5 orders of magnitude larger (figure 33). As changes in pixel size notably affect current outcomes, a relative resistance is used as a figure of merit that allows for direct comparison of material performance in different devices. We express it as

$$R_{REL} = R_{MEAS}\, W/L$$

In which W and L are single-pixel perimeter and channel length respectively; R_{MEAS} is the measured resistance in the form of dV/dI.

Responsivity is evaluated from:

$$Responsivity(R) = I_{pc} / P_{incident}$$

where:

- I_{pc} is the photocurrent (in amperes, A) generated by the photodetector in response to incident light,
- $P_{incident}$ is the incident optical power (in watts, W).

We obtain average values of $R_{REL} = (2.4 \pm 0.2) x 10^9\ \Omega$ *and* $R = 0.103 \pm 0.004$ *A/W,* which are comparable with state-of-the-art resistance values of 2D perovskites films [185]and responsivity values from perovskite-based planar photodetectors[186].

Time response has been evaluated through the use of a picosecond UV laser, wavelength 375nm, which was set in burst mode -train of picosecond pulses, duty cycle 30%. Plenty of works report ultrafast response of 2D perovskites under UV light, that is, photocurrent transient times are typically in the range between 0.1 and 2μs [187], [188], as reported in figure 34.

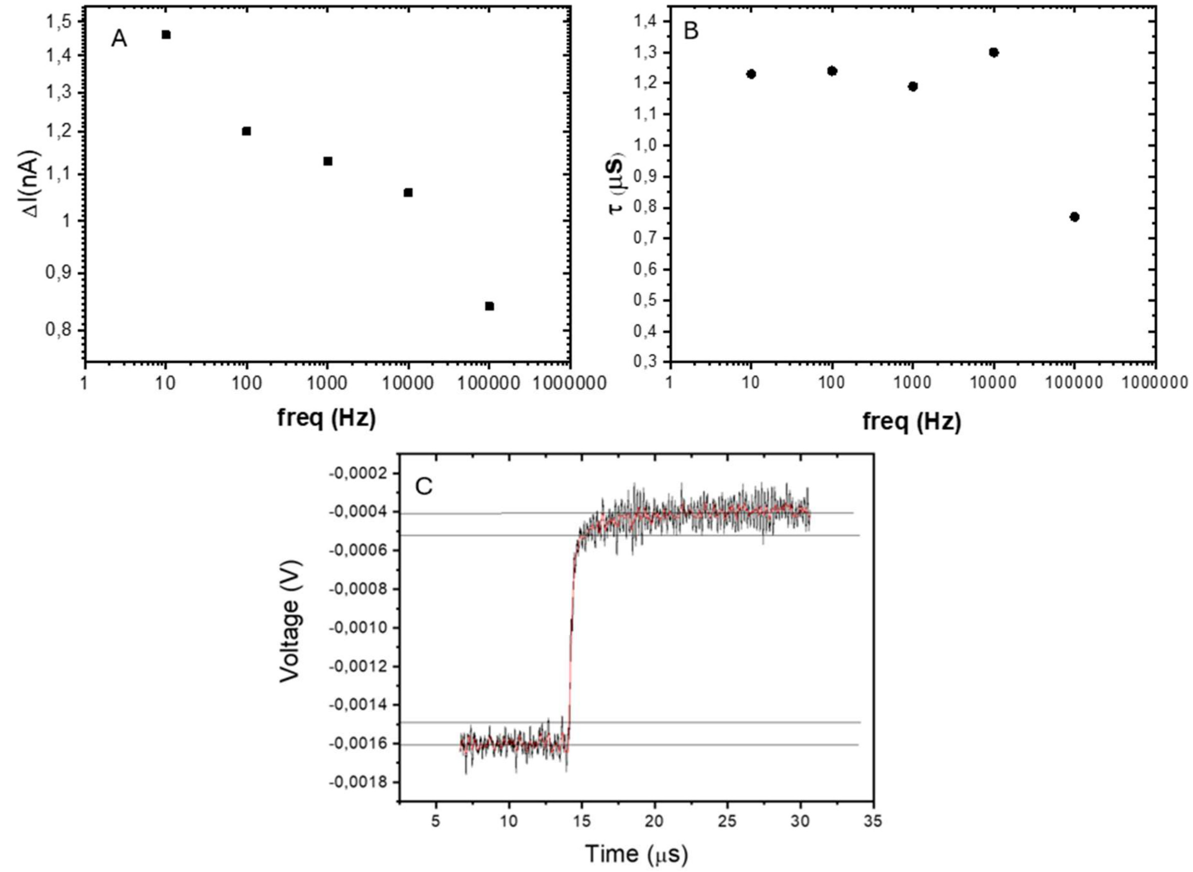

Figure 34 Response of a thin film device under 375 nm picosecond laser. A) photocurrent values are demonstrated to decrease as function of frequency. No plateau is observed at low values. B) Time response of the device under illumination in the form of rise-time, with a close-up shown in C). The samples exhibit time response in the microsecond range as reported in literature[189]; this lowers for high frequency values.

Exact time-response is extracted from rise and fall dynamics of generated photocurrent, that is converted into voltage signals through a dedicated current amplifier and read with a high-performance oscilloscope. Precise value is obtained considering the timing between 10 and 90% of the abovementioned signal. Moreover, photocurrent and time-response are investigated as function of frequency. As expected, transient time and photocurrent generation decrease as the laser frequency increases. For the fall-time response, almost constant values of 1.2±0.2 μs are measured below 20kHz, which is higher compared to [160] . Nevertheless, no plateau is observed for the photocurrent below 1kHz, as one would expect according to photodetector theory and recent publications on perovskite devices [190], [191], [192], [193], [194].

3.1.2 LONG-RANGE SIGNAL RECORDING

As previously mentioned, absorption of UV light by perovskite materials is reported to be in the first 200nm from incident surface[195] [196]. While in single crystals or in general top-bottom configurations -that is active material sandwiched between metal electrodes- the electric field lines cross the entire bulk, co-planar devices are demonstrated to exhibit electric field lines that emerge no more than 50nm above the metal contacts depending on active material. Considering film thicknesses of 2 µm, it is worth noting that there must be physical phenomena that carry out the generation of charge carriers inside the materials. In this direction, plenty of studies have reported *photon recycling* as major source of energy in the form of re-emitted photons that cause charge carriers to be generated. A simplified scheme of this effect is reported in fig. 35.

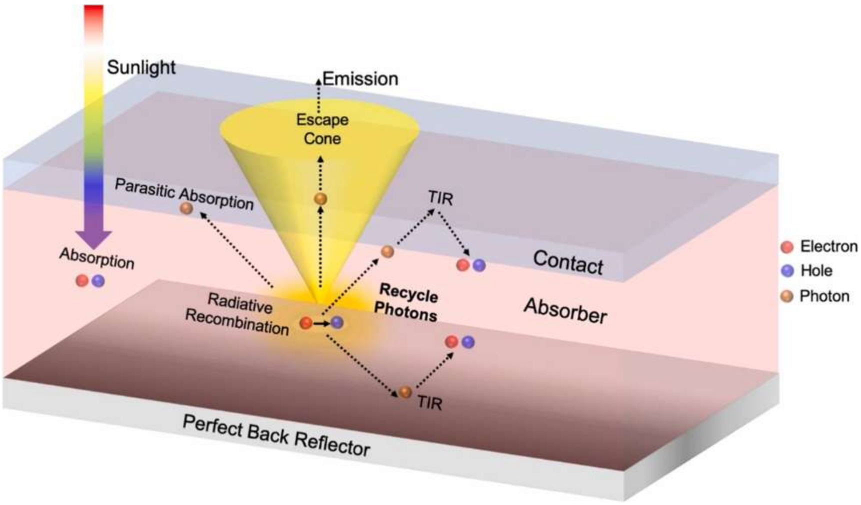

Figure 35 Schematic design of photon recycling under thermal equilibrium in a semiconductor slab. Following radiative recombination, photon recycling may occur due to direct reabsorption or photons emitted outside the escape cone due total internal reflection (TIR). Re-emitted photons may lie within the escape cone leaving the slab without further recycling. Re-emitted photons could also be absorbed parasitically into another layer without generating any electron-hole pair. Adapted from [197].

Photon recycling in perovskite materials refers to the reabsorption of photons emitted via radiative recombination, generating additional electron-hole pairs. This process enhances the effective carrier lifetime and improves optoelectronic performance in devices like solar cells and LEDs. In perovskites, particularly lead halide varieties, photon recycling occurs due to high photoluminescence quantum yield (PLQY), where a significant fraction of recombination events results in photon emission. These photons can be reabsorbed, creating new charge carriers and contributing to longer photon diffusion lengths. In solar cells, photon recycling enhances the open-circuit voltage (V_{OC}) and overall efficiency by reducing recombination losses and enabling multiple carrier generation cycles. It allows the material to approach the theoretical Shockley-Queisser efficiency limit [198]. In light-emitting diodes (LEDs), recycling boosts internal quantum efficiency (IQE), resulting in brighter light emission.

Photon recycling is particularly effective in perovskites with a high absorption coefficient and strong overlap between the absorption and emission spectra. Materials like PEA_2PbBr_4, with strong excitonic binding and high radiative recombination rates, are well-suited for this process. However, challenges like photon escape and competition from non-radiative recombination can limit its full potential, emphasizing the need for optimal material quality and device design.

In practical terms, photon recycling in perovskite solar cells and LEDs are typically observed over distances on the order of 5-20 micrometers. Variations are determined by the interplay of photon reabsorption, radiative recombination, and optical confinement in the device.

Deeper analyses have been performed that demonstrate photocurrent generation for illumination that is farther from the applied electric field than the abovementioned distances. This has been preliminary observed using a collimated 375nm laser beam (33 μW optical power, 500 μm spot diameter) targeting a thin film deposited on an interdigitated pixel from the top, with moving front edge up to 5 mm distance from the pixel edge. Setup and results are reported in figure 36: photocurrent is shown to decrease as function of distance as expected, but still it remains high in value up to 200pA at 20V applied bias with spot distance from pixel set at 4mm.

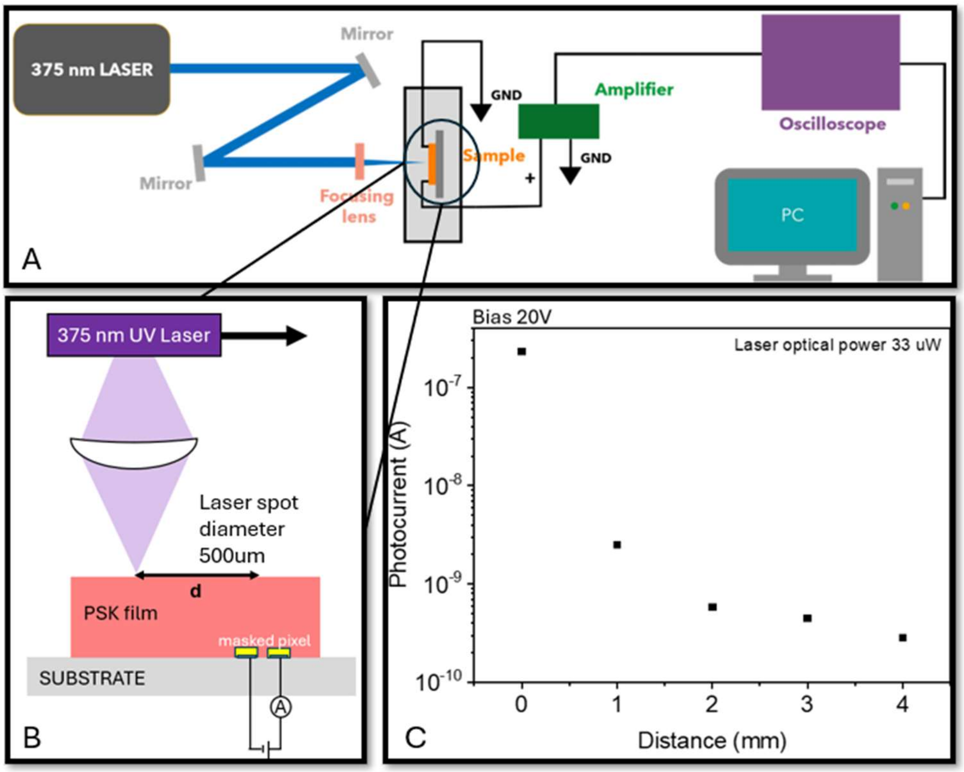

Figure 36 Scheme of experimental setup and obtained result of a thin film device's response under UV laser as function of distance from the applied electric field. In A) a simple optical configuration is proposed that allows for the laser beam to be collimated into a 500 μm spot, which can then be moved while keeping the device steady. As reported in C), photocurrent generation and recording occurs even for illumination distance that exceed theoretical predictions of photon recycling -20 μm.

This has led to further considerations and investigation under different experimental conditions. In order to prove that this phenomenon actually consists in the generation of charge carriers inside the electric field, we employed Kelvin Probe Force Microscopy in order to verify the generation of photovoltage in target region by illuminating the film up to 8mm far from AFM tip. The employed setup is reported in chapter 2; 2D perovskite is spin-coated onto ITO substrate for simpler analysis. Illumination is performed from the bottom through the abovementioned 375nm picosecond laser at 1mW optical power -an optic system composed of fiber optic and dedicated collimator allow for a 500 μm spot to be obtained. The reason is to be found in the need for no reflection or dispersion of light to contribute to the overall signal. Measurement is performed in the form of KPFM mapping of 3x3 μm^2 area in dark and light conditions (top panel, figure 37); the internal AFM gating system allows for sampling to be performed in dual mode, that consists in backward scanning in dark and forward scanning under UV exposure. This results in two different KPFM maps whose digitalization and subtraction lead to a final photovoltage map. The latter is post-processed in the form a histogram (bottom panel of fig. 37, inset *a*) whose peak actually corresponds to the desired photovoltage value.

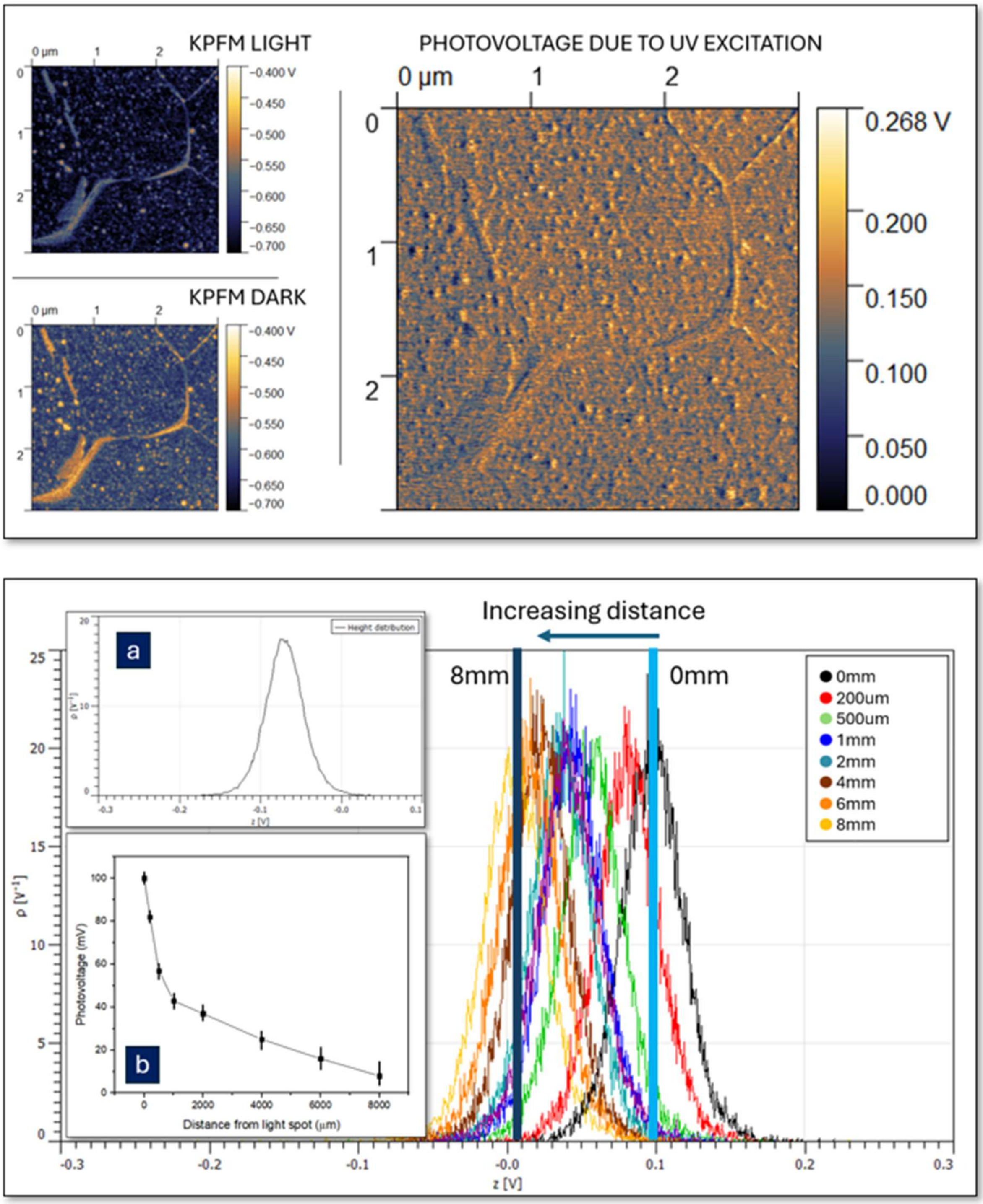

Figure 37 Photovoltage analyses through KPFM technique on PEA$_2$PbBr$_4$ thin film illuminated with 380nm. In order to extract the photovoltage, two different maps are obtained that measure the local KPFM in dark environment and under illumination. Image processing and statistical data analysis allow for a histogram to be generated that represents the actual photovoltage pointwise -exact representation is reported in inset a. This procedure is repeated as the laser spot is moved far from the collection area: unexpectedly, a photovoltage is recorded under illumination up to 8mm distance from the illuminated spot (bottom panel, with peaks as function of distance in inset b) which means that charge carriers are generated far from the applied electric field.

This procedure is repeated for 8 different distances and the obtained values of photovoltage extracted accordingly (bottom panel of fig. 37, inset *b*) and compared to the zeroth value of it, that is photovoltage generated *inside* the illumination spot.

We prove that photovoltage is generated in PEA_2PbBr_4 thin film at distances up to 8mm, with a decrease in value that results to be 10% of zeroth value, which is reported to be 100 mV.

Although preliminary, these results make us speculate about the possibility of light to travel inside the material due to internal reflection that generate photon waveguides. This implies the need to reconsider perovskite-related performance values such as sensitivity and responsivity, as the active area that contributes to signal is to be extended to the entirety of the material rather than the one effectively confined in the electric field.

Finally, it should be stressed that these optoelectronic properties of 2D perovskite films are fundamental for radiation detection. The connection between the strong UV response of 2D perovskite films and their potential for radiation detection lies in their **wide bandgap**, **efficient charge transport**, and **fast response time**, while their high atomic number (Z) enhances interaction with ionizing radiation. The abovementioned analyses are thus intended to extend the high-performance of pixelated devices towards the use of them as proper dosimeters. This is given by the possibility to have these structures scaled to large areas with extremely high resolution in terms of pixel size and lateral dimensions. On top of that, thin plastic substrates imply flexibility and transparency to high-energy radiation, which is of high importance for clinically relevant applications.

To summarise, sec. 3.1.1 provides numbers and data regarding the extremely low dark current of 2D perovskite films on interdigitated pixels: this means the material is highly resistant to high applied electric field, which can be useful to enhance charge collection efficiency. Moreover, the fast response reported in figure 34 is key feature for precise and accurate radiation detection. Lastly, the contribution of the overall film to the measured signal is significant for higher quality, more efficient outcomes.

The features of interest for each kind of application will be further discussed in the appropriate section (see, for instance, the introduction to sec. 3.2.2 for proton beam monitoring).

3.1.3 DIRECT X-RAY DETECTION

To confirm the potential of PEA_2PbBr_4 perovskite thin films in radiation detection, sensitivity measurements were performed under controlled X-ray exposure. The unique 2D layered structure of PEA_2PbBr_4, combined with its high absorption coefficient for high-energy photons, makes it a promising candidate for efficient X-ray detection. Absorbed x-ray photons can generate electron-hole pairs within the perovskite material, that are drifted by the applied external electric field and collected at the metal electrodes. The resulting X-ray photocurrent can be measured to assess the film's responsivity and detection efficiency. By evaluating the photocurrent under various X-ray intensities, we succeeded in determining the film's signal-to-noise ratio, linearity with dose rate, and stability under prolonged X-ray exposure, which are key parameters for its use in X-ray imaging or radiation sensing applications.

PEA_2PbBr_4 thin films response and features under X-rays have been deeply investigated in previous works: tuning pixel size and material properties have led to sensitivity values in the range of 10^2 μC/Gy/cm^2 under X-rays of 150kVp, 4kV/mm applied electric field, dose rates in the range 8-100μGy/s.

We employ X-rays as a standard characterization technique for our thin films to assess their responsivity and consistency with state of the art in matter of sensitivity and signal-to-noise ratio. Figure 38 reports analyses of standard single pixels under 50kVp X-rays for different dose rates, ranging from 50μGy up to 900μGy. Applied bias is set at 130V, which corresponds to 4kV/mm electric field: this provides dark current values of less than 10pA. A direct comparison is also provided with two devices whose active films of different thicknesses have been fabricated with standard spincoating (thickness = 2 μm) and with anti-solvent technique (5 μm) respectively: sensitivity outcomes show almost identical behaviour between the two, thus demonstrating that thin films response to X-ray is mostly dependent on the electrode sizes and distance rather than thickness, as the electric field lines of interdigitated contacts do not penetrate deep into the bulk of the material.

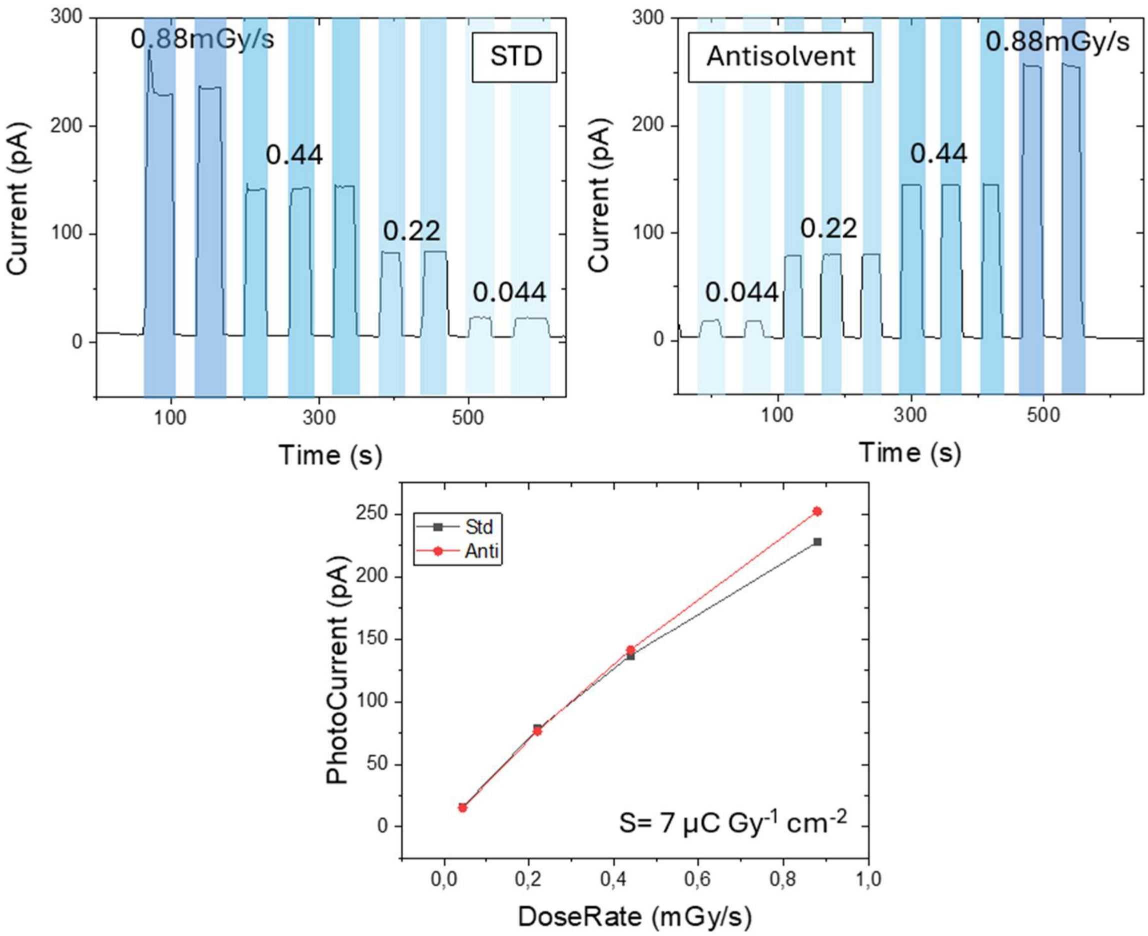

Figure 38 Performance under 50kVp X-ray photons of perovskite thin films, fabricated with two different recipes that provide up to 200% difference in thickness (2 and 5μm respectively for the top left -standard- and the top right-antisolvent technique). Tests are performed at 130V applied bias, identical dose rates and exposure times. Sensitivity is extracted accordingly, which results in being almost identical for the two structures

The plot of photocurrent as function of dose rate provides insights on the linearity with dose rate of these devices, which is confirmed in the mid-region as reported in [160]. The dependence of sensitivity with dose rate, particulary evident at low dose rates, is a common phenomenon in perovskite radiation detectors and it is still under study.

Sensitivity values are measured to be ~ 7±2 μC/Gy/cm^2, which is in the range of values of 2D RP perovskite films [199], [200], [201]. Since sensitivity calculations depend on the defined active area, it's important to clarify that for single-pixel measurements, the active area is considered as the entire pixel size. This approach tends to overestimate the actual sensitive region, making direct comparisons with single crystals inaccurate.

Additionally, a different set of measurements is performed on the standard device after 500 days from fabrication. This is intended to assess the major features of interest of these thin-film structures, such as stability over time and under high-flux exposure and low limit of detection. Figure 39 reports single-pixel response using a tungsten X-ray tube which allows for higher range of energies to be employed. Specifically, figure 39A shows results obtained at 40kVp and 150kVp for three different applied bias (10, 50 and 100V): these values confirm the linearity with dose and demonstrate the dependence of sensitivity on applied bias and on the dose rate, as mentioned above and in previous studies[160]Perovskite stability over time -that is device ageing- is presented in figure 39B, in which the single-pixel response after 500 days from fabrication is compared to the one of a pristine device. Although a degradation can be observed, this can be quantified to be less than 20% in photocurrent. It is worth noting that no degradation in dark current is observed as the values remain in the range of a few pA at 100V applied bias, which is of great importance for long-term analyses. Figures 39C and 39D detail the extremely low limit of detection and the robustness of response to high-flux photons of thin film devices respectively. Due to the low dark current, the LoD is estimated through the fit of the photocurrent curve as function of dose rate and it is evaluated to be 1.0±0.2 μGy/s; this value is to be tuned according to the non-linear behaviour at extremely low doses, which provides values of the LoD which are reported to be down to 50nGy/s[160] .

In 39D, the sample is irradiated for 30 minutes (10s on/10s off peaks) at 150kVp, 15mGy/s dose rate (27Gy total) and no significant variation is recorded in its response after stability adjustments (few on-off cycles). We speculate that stability issues can be attributed to four main reasons: defect passivation, charge trapping and detrapping, structural and ionic rearrangement, radiation-induced activation or conditioning[202]. These effects and the way to mitigate them are now under investigation.

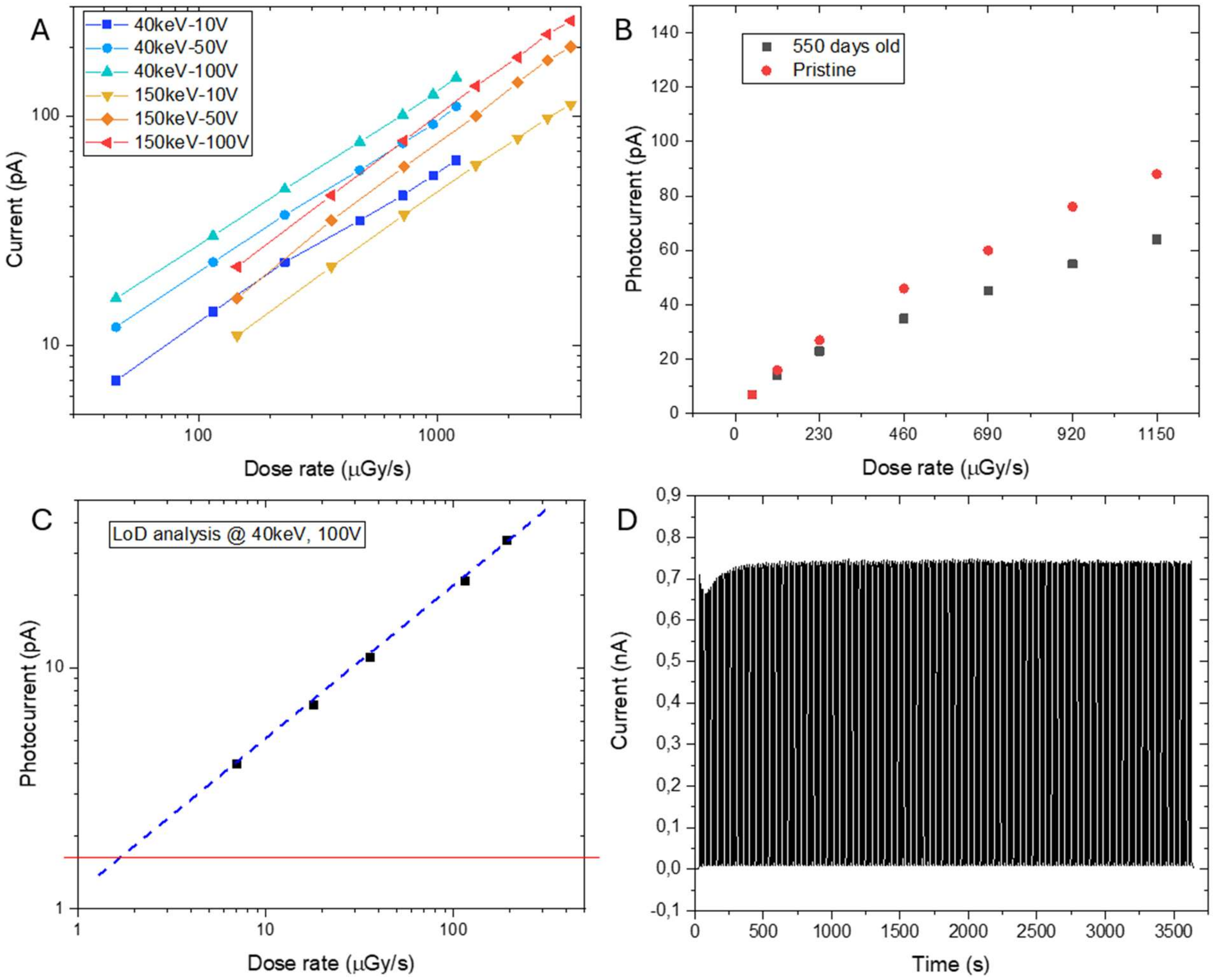

Figure 39 A) Signal response of 2D-perovskite thin-film device under X-rays for different applied bias (10,50,100V) and two different accelerating voltages (40keV and 150keV) while varying the dose rate from 0.03 to 4 mGy/s. B) Ageing test which relates pristine device to a 550-days-old one. Measurement performed using 40kVp, 10V applied bias for different dose rates. After 550 days the sample exhibits a decrease in response which is less than 20%. C) Evaluation of the limit of detection of 2D-perovskite device, which is estimated to be <1μGy/s. The red line refers to the dark current at 100V applied bias. D) Response stability under high-flux irradiation (27Gy, 15mGy/s dose rate). The measurement is performed through on-off cycles of 10s each.

3.1.4 ALPHA PARTICLE SPECTROSCOPY

Nuclear science accounts for alpha particle spectroscopy as a powerful analytical tool that allows for precise identification and quantification of alpha-emitting radionuclides. Being helium nuclei flow with weak penetrability and strong ionization property, the monitoring of these fluxes is crucial for safety, radiological protection and environmental contamination issues. Traditional methods rely on room temperature semiconductor detectors based on CdZnTe or HgI_2, which achieve resolutions in the range 1.5/2.5% FWHM with intrinsic detection efficiency between 30 and 60% depending on material and thickness; recorded sensitivities up to 10^{-2} cps/Bq allow for the detection of low-level alpha fluxes. High-cost diamond-based devices guarantee resolutions < 0.3%.

Recent studies have explored perovskite structures as valid alternative to the costly, standard RTSDs owing to their unique high stopping power and high charge carrier mobility. Tunability and versatility of these materials coupled with their easy and low-cost fabrication methods have contributed to the realization of alpha-particle spectroscopy devices. As mentioned in sec. 1.2.5, the first result in this field reports a CsPbBr3 single crystal with low and stable dark current that resolves alpha and gamma peaks of ^{241}Am isotope[146]. Latest advancements account for organic metal halide perovskite single crystals, including 3D perovskite $MAPbBr_3$, $MAPbI_3$ and FAPbBr, 2D perovskite $(BA)_2PbBr_4$ (BA: butylammonium) and $(BDA)CsPb_2Br_7$ (BDA: 1,4-butanediamine), and other mixed perovskite-related structures[203]. On top of that, remarkable scintillation properties of 2D and 0D perovskite structures have been exploited for alpha particle detection[204].

We here report the first evidence of spectroscopic properties of PEA_2PbBr_4 thin films, which are demonstrated to resolve alpha particles from ^{241}Am source down to single pulses. Before that, an extensive study on single crystals has been conducted to assess the feasibility of this experiment.

We start with a simple analysis on thin film response in the form of induced current under alpha fluxes at different bias as reported in figure 40, discriminating the effect of substrate that is actually generating low-intensity signals. For this measurement, we employ ^{221}Ra source, 5uCi intensity, which is placed at 1cm distance from sample and a dedicated setup described in sec. 2.2 that allows for automatic signal recording while opening and closing the particles' flux through a mechanical shutter controlled remotely. On/off time is set to be 15s; 30s interval is chosen between changes in the applied bias. For the exact estimation of the rate of incident particles, the source is assumed to be point-like: at 1cm distance, the number of particles reaching the surface of the sample per second is evaluated to be ~300/s. This demonstrates that PEA_2PbBr_4 thin films can effectively detect low flux of charged particles, opening the possibility to spectroscopic grade, energy sensitive, detection.

It is important to keep in mind that alpha particles are not entirely absorbed by the film, as their penetration depth on PEA_2PbBr_4 is reported to be in the 5/15 μm range [205]. Incomplete absorption implies partial energy loss inside the film, which means the substrate is actually absorbing major part of radiation. This being noted, accurate analyses require the effect of air to be taken into account [206].

As discussed previously, prior to analyses on thin films, the spectroscopic power of PEA_2PbBr_4 is assessed for single crystal devices. The samples are fabricated from solution through slow-evaporation method and are provided two different contact structures for better comparison: we here proposed a top-bottom configuration and a co-planar interdigitated pixel that is thermally evaporated on the surface of the crystal. Further details on crystal growth are reported in Appendix 2.

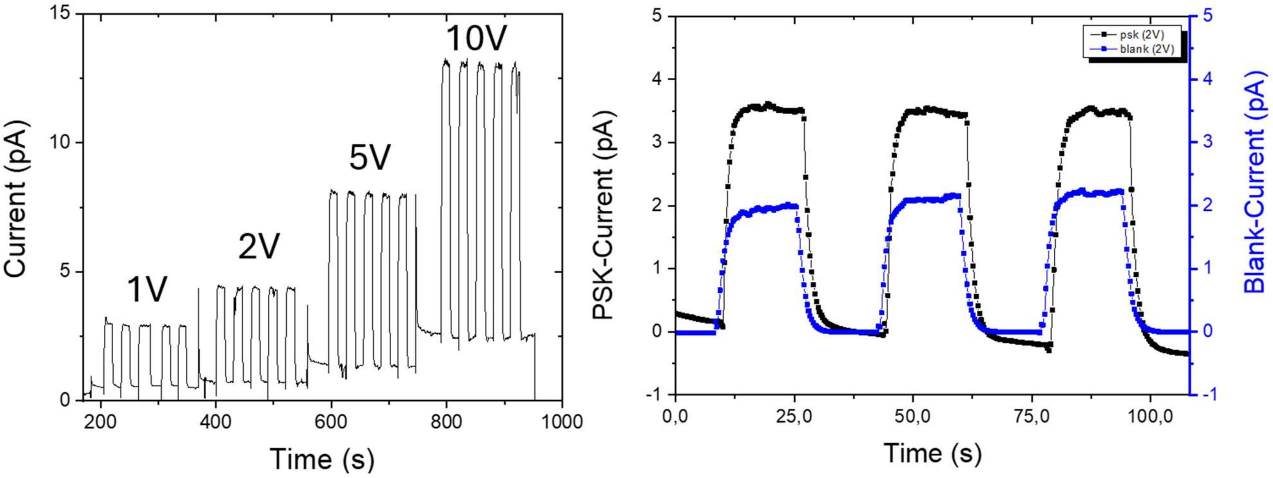

Figure 40 Direct detection of alpha particles from ^{221}Ra source performed through PEA$_2$PbBr$_4$ thin film device. The sample's extremely low dark current makes it possible to record signals down to 3p A at low applied bias. Notably, a comparison is reported that makes clear evidence of a contribution from the substrate to the overall signal, which is still not as intense as the one obtained with perovskite active layers.

Primary investigations require an integrated readout system that is designed to measure down to single pulses at low noise. For these tests, a more intense source is chosen that is ^{241}Am, 1.8MBq activity. An analog shaping amplifier is integrated that allows for shaping times down to 0.5 μs. As discussed in the Methods section 2.2, the shaping time determines the time duration that the charge is collected from the detector to be processed for analysis. If the shaping time is too short then not all of the signal pulses will be collected, and if the shaping time is too long then noise will enter the processing stage and will affect the analysis. In samples with lower mobility, longer shaping times are required.

The two single-crystal different samples are tested at 10μs shaping time and for different applied bias. In fact, from voltage-dependent analyses it is possible to extract mobility-lifetime product, which is key metric for determining devices quality and performance. The first thing to consider is the way noise affects the signal outputs: for this reason, accurate investigations require the need for discrimination between noise, signal from alpha source, additional contributions from emitted gamma rays. In figure 41 we report results obtained for both the top-bottom and the co-planar configurations. Figure 41 is intended to demonstrate that no signal is recorded other than the one from alpha particles reaching the sample. A 1mm paper thick is used to screen alpha particles at high bias for comparison. Furthermore, Figure 41B gathers results with applied bias ranging from 0 to 200V. As one would expect, top-bottom data exhibit higher count rate, which is due to the particles penetrating the bulk and being collected for the entirety of the crystal itself. Conversely, interdigitated electrodes collect only from the first layers deep in the material.

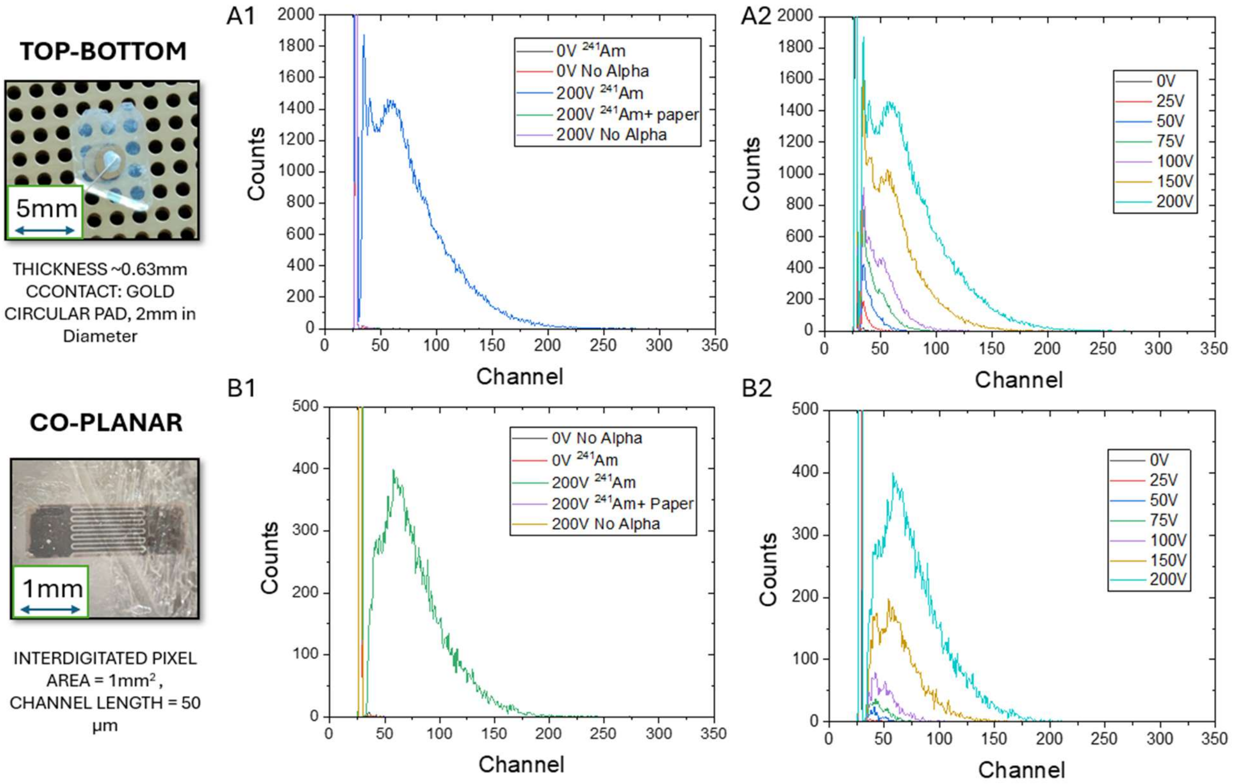

Figure 41 Alpha measurements on PEA_2PbBr_4 single crystals with electrical contacts in Top-Bottom (A) and co-planar configuration (B). A,B1 demonstrate the validity of our assumption of measuring actual alpha pulses: no source leads to no signal, paper tissue blocking the alphas also leads to no signal. A,B2 show signal dependence on the applied bias. 3x difference recorded in the n.o. counts.

The estimation of mobility-lifetime product requires higher bias values: the behaviour of the channel peak as function of applied voltage can be expressed by the Hecht law, that relates the charge collection efficiency to the distance *d* travelled by the charge carriers and the electric field *V/d*. It is expressed as:

$$CCE = \frac{\mu\tau V}{d^2}\left(1 - e^{-\frac{d^2}{\mu\tau V}}\right).$$

Notably, saturation is expected for high applied bias. Furthermore, the sign of the applied bias makes it possible to distinguish between mobility-lifetime product of electrons and holes accordingly. In here, as positive bias is applied at the top electrode, we discuss of features of holes only. It is worth mentioning that this exact model is to be applied carefully when it comes to more comple structures: a modified equation is reported in [207] that also takes surface recombination[208] and detector structure[209]

As no exact peak can be extracted from the plots above, a first approximation is required that considers the max channel number instead of the peak maximum. Therefore, adequate normalization is required for accurate fit.

In this direction, the same spectrum of Figure 41B2 is collected for the top-bottom configuration for higher values of the applied voltage up to 1kV and reported in Figure 42. Analyses through Hecht model led to a μτ product for holes of (1.03 x10^{-6} cm^2/V), which is not far from values reported in literature obtained through different techniques (e.g. time of flight experiments).

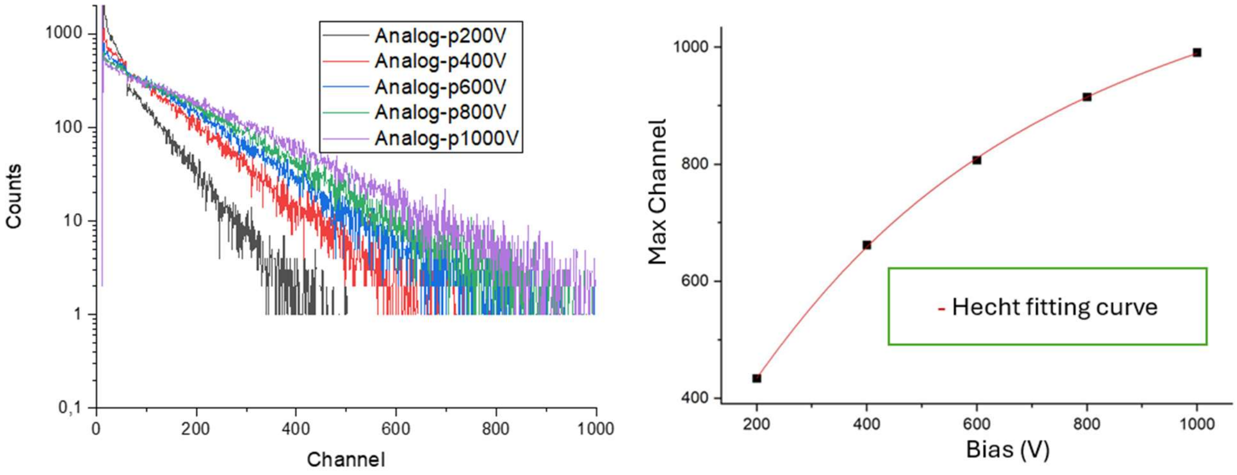

Figure 42 Response of Single crystal device under alpha source in pulse mode as function of bias. High electric field is applied up to 1kV in order for a saturation behaviour to be observed. A fitting procedure through Hecht model leads to mobility lifetime product of 1.03x10^{-6}cm^2/V, which is similar to values reported in literature.

Analyses on thin films require more effort and improvement in shielding of the entire apparatus. Provided the extremely low dark current of PEA$_2$PbBr$_4$ devices, the first thing to be investigated is the observation of single pulses by using an oscilloscope.

Figure 43 report the first evidence of single pulses from 2D perovskite thin films for different applied bias.

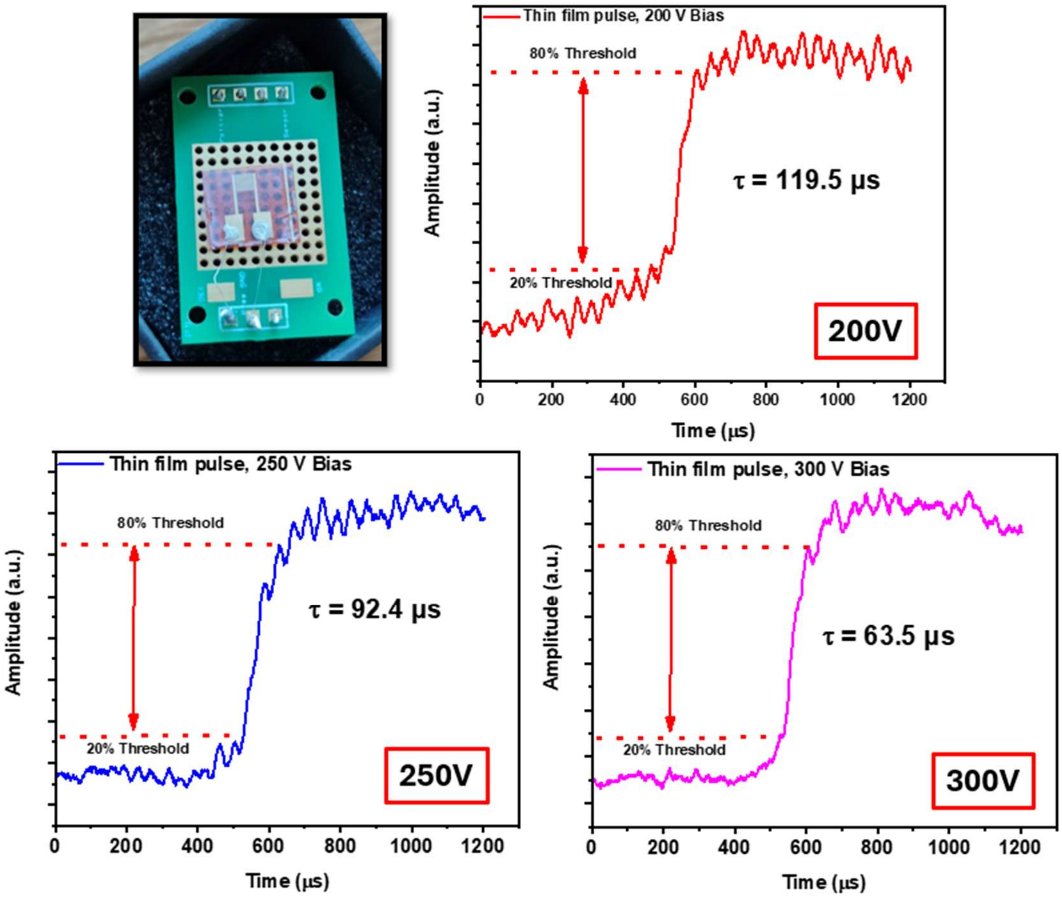

Figure 43 Pre-amplified ^{241}Am single pulses obtained through PEA$_2$PbBr$_4$ thin films. The rise-time is demonstrated to be slow due to the low mobility of 2D perovskites. As the bias is increased, the rise-time is reported to decrease down to <100 μs.

As expected from the relatively low mobility values of charge carriers in thin films, the rise time of these pulses is slower compared to state-of-the-art devices ($CsPbBr_3$, [210]) and measured to be up to 120μs at 200V applied bias. As the bias is increased, the rise-time is reported to decrease down to 63.5 μs at 300V applied bias. This helps in forecasting interesting outcomes through the implementation of a higher shaping-time system.

This being observed, we collect spectra with the same experimental setup, that allows for analog pulses with shaping time of 10μs to be recorded. As per the previous considerations, preliminary analyses are required that show no signal coming from the film without source nor when alpha particles are prevented from reaching the film surface. Figure 44 thus shows the effect of alpha particles on MCA output, with clear evidence of signal collection only with particles reaching the surface. Moreover, a bias dependence of the max channel is also observed up to 300V applied voltage.

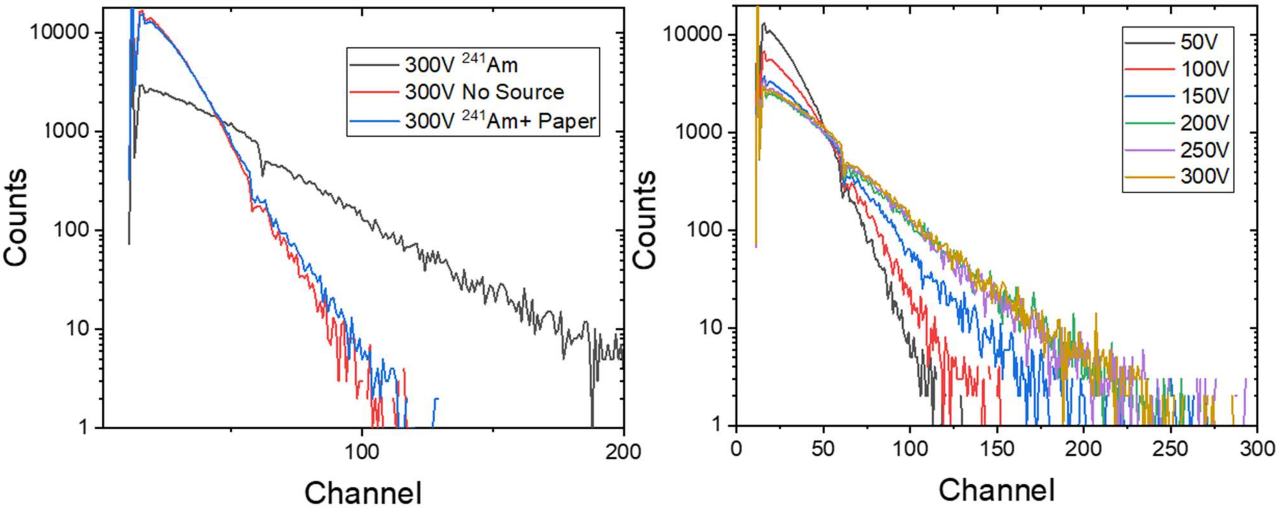

Figure 44 Preliminary results and assessments that demonstrate the spectroscopic power of perovskite thin films. On the left, a simple signal comparison is reported that shows a huge variation in the shape and intensity when the sample is exposed to alpha particles; N stands for No Source, while PT refers to the alpha particles being blocked by 1mm paper tissue. On the right, we report a response as function of bias, which results in the consistent behaviour of saturation at higher values of the applied electric field. Max applied bias is 300V, which corresponds to 10kV/mm electric field.

Notably, shifting in the max channel seems to occur as the bias increases up to saturation values. Nevertheless, the higher count rate and the incredibly long rise-time of the measured pulses imply that longer shaping times are required for clearer and more defined peaks. Preliminary and promising results have been obtained with the use of a digital shaping amplifier that allows for peak times up to 100μs. This leads to gaussian shaped peaks as reported in figure 45; post-processing evaluations allow for mobility-lifetime products to be extracted: the obtained value for a thin film is $1x10^6m^2/V$, which is not far from the values extracted from the single crystal.

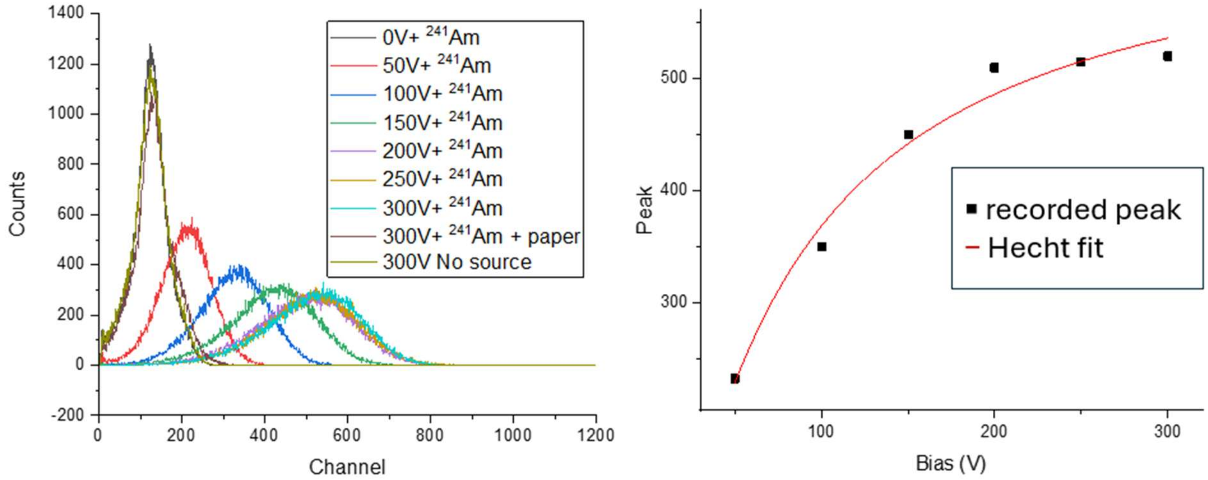

Figure 45 Preliminary analyses on thin film device using a digital shaping amplifier, shaping time set to be >40μs. Similarly with what observed with the analog shaping amplifier, no signal is recorded when alpha particles are prevented from reaching the surface or removed from the dedicated source holder (PT- and N- respectively). From the Hecht plot, a mobility-lifetime product is extracted that is 1x10^{-6}cm^{2}/V, which is not far from the values extracted from the single crystal.

As a final remark, it is necessary to clarify that further investigation is being undertaken with the digital shaping amplifier in order to ensure that these gaussian-shaped peaks are actually originated by the shaping and are not artefacts nor noise-amplification effects. Lastly, an exact modelling of the electric field lines from interdigitated contacts is required for quantitative analyses on μτ products.

3.2 CLINICALLY RELEVANT RADIATION DETECTORS

Radiation systems have constituted a paradigm change in cancer therapy. The advent of sophysticated technology has given the oncologysts tools and methods to actually select planning target volumes (PTV) for precise, personalized treatments with minimized damage of the nearby healthy tissues.

Fundamental task for ensuring effective results is the determination of region of interest and actual dose to be delivered to. The most recent computer-based techniques allow for real-time imaging of the tumor and surrounding anatomy immediately prior to treatment delivery. Furthermore, coupling them with molecular and metabolic imaging analyses enables clinicians to account for changes in position and determination of possible radiation-resistant regions. Thus, case-specific operation procedures can be instituted. Dose distribution studies are core for successful radiation therapies (RTs). Monitoring radiation spatial distribution and its interaction with tissues is mandatory for optimal outcomes. Current clinically relevant state-of-the-art technologies employ ionization chambers (ICs), film dosimetry or electronic portal imaging devices (EPIDs) prior to treatment for dose evaluations. During tumor irradiation, real-time imaging techniques (such as Ionizing Radiation Acoustic Imaging) allow for adaptive feedback through radiation distribution mapping. Major issue is the a-priori determination of delivered dose, with lack of reliable in-situ analyses and no real-time monitor. On top of that, the rise of targeted radionuclide therapies has rendered the need for wearable, high precision dosimetry compelling, capable to follow the patient for several hours after completion of treatment.

As recent discoveries in the field of metal halide perovskites for radiation detection have led to significant performance improvement, we believe 2D PEA_2PbBr_4 can be promising for a wide range of clinically relevant applications as it is proven to be sensitive to a large spectrum of high energy radiation. In this direction, the following presents preliminary tests and extensive studies conducted on perovskite thin film response in medical applications.

Primarily, basic analyses are reported for highly energetic protons (70/200MeV) being operated in dedicated medical facility (Trento, TIFPA) under therapeutical conditions.

Then, we describe in detail the application of flexible multielectrode arrays as innovative medical tools for online proton beam transversal monitoring and real-time gamma-ray detection from radiotracers. These works mark fundamental milestones in personal dosimetry, earning recognition through publication in prestigious journals [4], [5].

3.2.1 HIGH ENERGY PROTONS

Proton therapy, an advanced form of radiation treatment, offers highly targeted cancer therapy by delivering protons directly to tumours while minimizing damage to surrounding healthy tissues. This is due to the physics of interaction with protons and matter as reported in sec.1: the linear energy transfer of heavility charged particles reaches its maximum at a specific confined penetration depth, which is easily estimated from target density and energy of the incoming beam. As this technique becomes more widespread, the demand for accurate, real-time monitoring of radiation exposure has grown. Traditional dosimeters, often rigid and bulky, are not well-suited for conforming to the complex contours of the body or tracking dynamic patient movements during treatment. This limitation creates a clear need for flexible dosimeters that can be seamlessly integrated into wearable devices or placed on irregular surfaces to ensure precise dose measurements.

In here, we propose a dual set of measurements of 2D perovskite thin films as direct proton detectors, capable of collecting electronic signals from particles of energies in the range 70/200MeV.

To assess the clinical relevance of the proposed detectors, we make use of an anthropomorphic phantom composed of tissue equivalent materials that allow for consistent results to be collected as it was routine therapy. The sample is placed inside it and centered on the beam spot, whose incident distance from sample is 155mm. Simulations using SRIM code allow for the exact estimation of energy loss inside the phantom and thus the corresponding energy of protons reaching the sample surface. For this first experiment we employ protons with initial energy of 200MeV, which lose 82MeV while passing through the phantom, thus leading to measuring the signal produced by 118MeV protons.

The primary set of measurements consists in verifying response and dose linearity, with sample biased at 5V and proton flux regulated as for exact delivered dose in clinical trials (2.5e10 H+ = 1Gy, FWHM= 8mm) for different dose rates. These are set according to the tube current: 1, 2 and 5nA, which correspond to [5, 8.5 and 19] $x10^8$ protons per second.

Experimental setup and outcomes are reported in figure 46. The signal produced by 118MeV protons at 20mGy/s dose rate reaches average values of 40pA, thus confirming the detection power of thin film devices. For increasing dose rate, the signal increases accordingly, with average values up to 110pA at 76mGy/s. Linearity with dose is also confirmed by plotting the proton induced charges as function of dose. Notably, dose rate dependence occurs, which manifest lower proton induced charges for higher dose rates. We speculate this is to be attributed to trap levels inside the material that are activated at lower dose rates, thus contributing to the overall increase in the induced charges. Further details on that can be found in the review work of Karsh *et al. [211]*

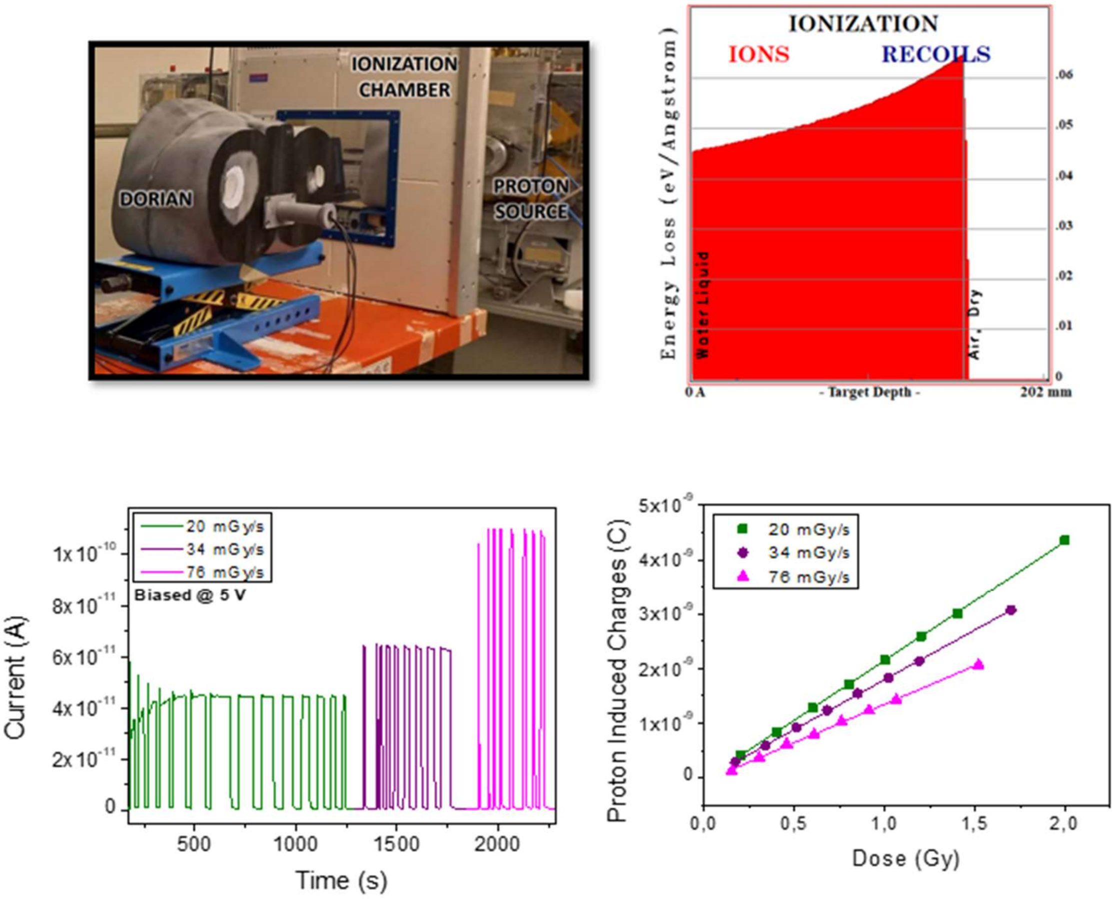

Figure 46 Measurements under high energy protons inside an anthropomorphic phantom which is designed to simulate human tissue. A) Experimental setup. The sample is positioned inside the phantom, 15.5mm from incident surface. B) SRIM simulation that allows for an estimation of proton energy when reaching the sample, which is reported to be 118MeV. C) Response of 2D psk under 118MeV protons at 5V applied bias as function of dose rate. D) Plot of linear dependence of proton induced current on the absorbed dose.

Secondly, a set of experiments are conducted that allow for longitudinal beam profiling. The former idea is to map pointwise the energy loss of incident protons in order to reproduce the Bragg curve. With that intent, solid water slabs (RW3) of different dimensions are interposed between the source and the sample (figure 47B). As this material is tissue equivalent (density 1,045g/cm^3, mean excitation energy 69.8 eV), standard conditions are set so that irradiation is at 4Gy fixed dose (measured at incidence), proton energy 70MeV, proton flux 9.7e17H+/s. Primary measurements are performed to obtain an energy dependent response as function of dose as reported in figure 47A -118MeV from previous measurements inside the phantom as comparison. Solid water slabs are used to reduce the energy of incident protons, which are effectively estimated from SRIM simulations according to the slabs thickness. Precisely, 60 and 48MeV are obtained through the use of 0.5 and 1.5 cm of solid water respectively. For fixed dose rates of 40mGy/s, higher energies correspond to lower proton induced charges at same absorbed dose of 4Gy. As expected, the differential energy loss at higher energies is lower than for less energetic particles, thus resulting in lower proton induced charges.

Moreover, a Bragg-like behaviour is observed as reported in figure 47C. With increasing thickness of the solid water slabs, the energy loss inside the sample increases up to a peak at 3.4 cm, which not far from theoretical estimations of LET inside human tissues (3.6 to 4cm for 70MeV protons, as reported in ICRU Report 49)[212].

Finally, stability tests are conducted for radiation hardness verifications. The sample is exposed to high flux 200MeV protons up to 20Gy total absorbed dose. Analyses on pre- and post- irradiation dark currents demonstrate the radiation hard feature of PEA_2PbBr_4, thus making it promising candidate as personal dosimeter for cancer treatments.

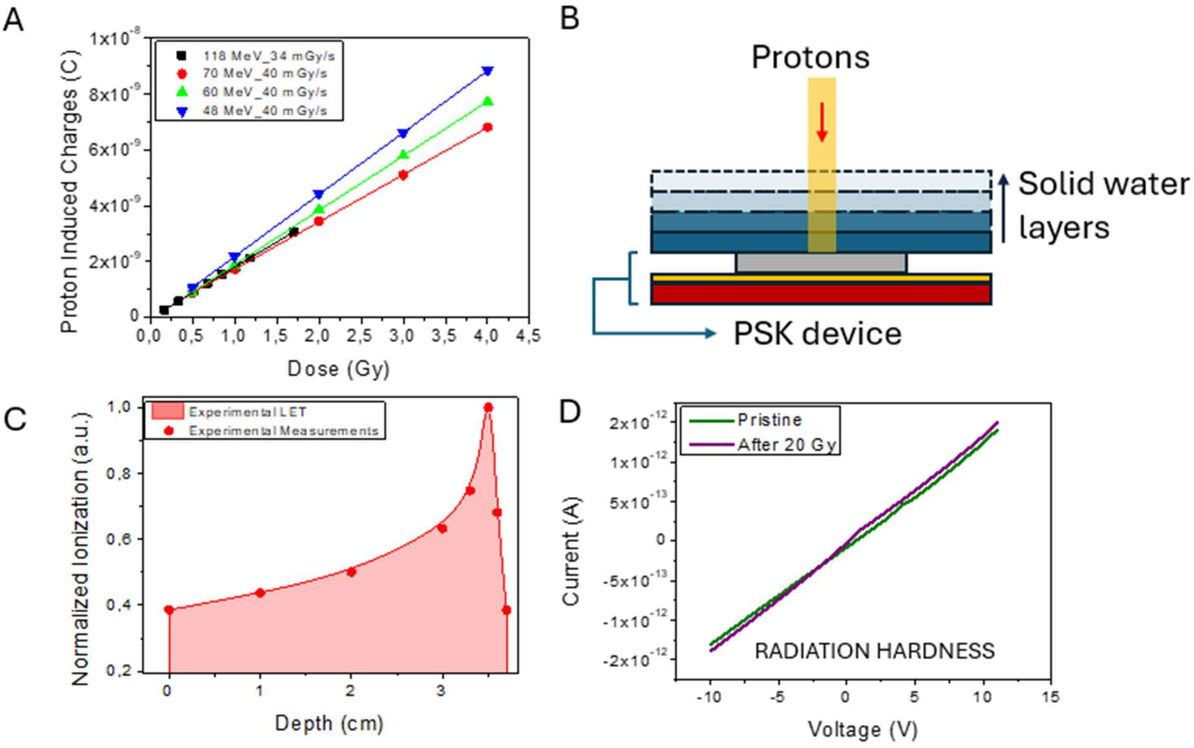

Figure 47 A) Energy dependence of the proton induced charges for the same absorbed dose; values obtained considering tuneable solid water thickness: the proton energy is fixed at 70MeV and 0.5 and 1.5cm thick slabs are placed in between the source and the sample to obtain 60 and 48MeV respectively. B) scheme of the measurement setup. C) Bragg curve reproduced increasing the thickness of solid water up to 4cm, which is demonstrated to completely stop 70MeV protons. D) Radiation hardness test on perovskite thin film. No significant change is observed in the dark current after 20Gy, 200MeV energy exposure.

3.2.2 PROTON BEAM MONITORING

As discussed previously, real-time and non-destructive monitoring of ionizing radiation beams is essential in various applications, particularly in medical radiation therapy. Accurate, real-time beam characterization ensures the precise delivery of radiation to the target, safeguarding surrounding healthy tissues.

The reason behind the choice of 2D perovskite PEA_2PbBr_4 based devices is founded in the requirements they meet in matter of high-energy beam profiling:

- **High sensitivity**, crucial for detecting low radiation doses and ensuring accurate dose measurements within the 2.5% uncertainty margin required in clinical settings.

- **Low noise levels** to maintain a high signal-to-noise ratio, with dark current being less than 1% of the signal to enable accurate detection of the radiation beam, even at low doses.

- **Fast response time** (<1 ms) is vital for capturing rapid beam dynamics, such as movements in the transverse plane that can exceed 100 mm/ms, necessitating detectors with readout frequencies of several kHz.

- **Beam transparency** is crucial for non-invasive monitoring, as it ensures the detector does not perturb the beam while providing real-time spatial and intensity distribution mapping.

- **Radiation tolerance** guarantees long-term stability in harsh environments.

- **Large area coverage** (>100 cm^2) is necessary to map the beam over substantial surfaces.

Traditional detection technologies like diode arrays, scintillating detectors, and ionization chambers meet some of these demands but often fall short in combining all desired features. Notably, radiochromic films provide excellent spatial resolution (0.1–0.2 mm) but lack real-time measurement capabilities due to the need for post-exposure processing and they can’t be used twice, thus limiting the applicability and resulting in costly and time-consuming procedures.

In here we report a novel radiation detector based on PEA_2PbBr_4 micrometer-thin film that allows for real-time monitoring of 5MeV proton beam through direct radiation detection in the form of output current signals. The active material is deposited on a multielectrode array patterned on Kapton substrate, which guarantees flexibility and conformability to anatomic/experimental profiles.

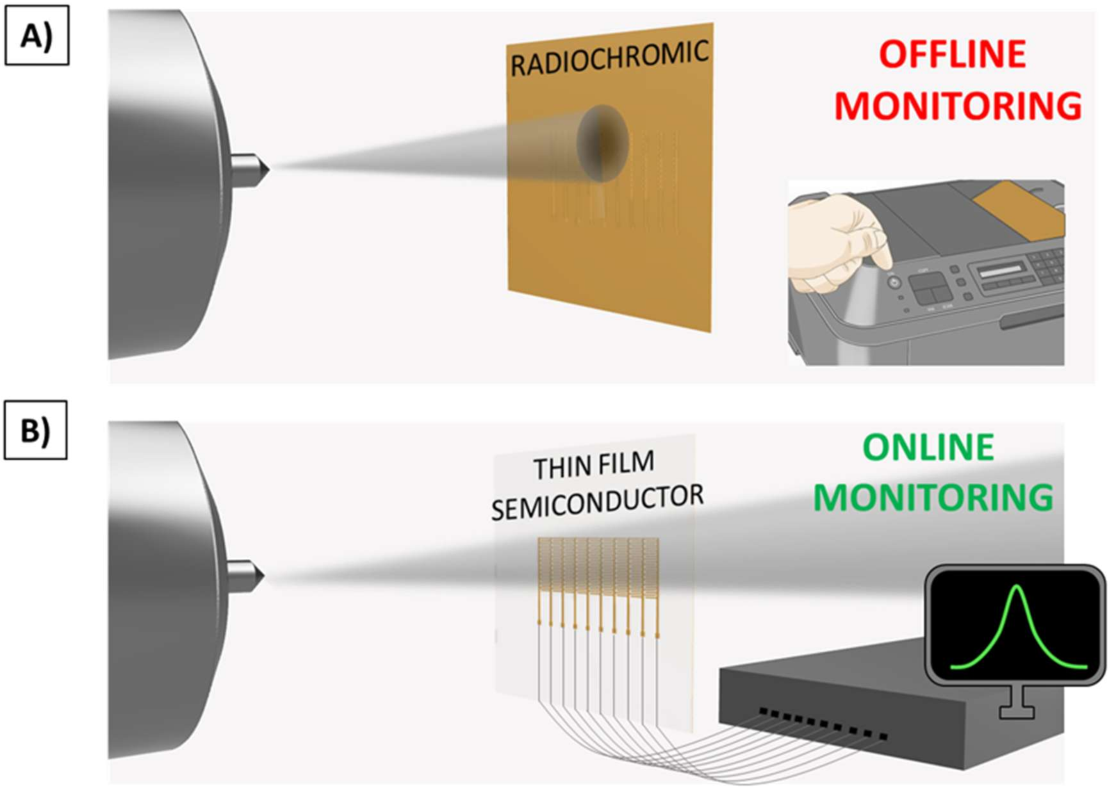

Figure 48 Sketch of radiation transversal beam monitoring acquired by A) commercial radiochromic film and B) semiconductor thin film-based detector array. The first approach requires an off-line analysis, while employing solid state detectors allows real-time and online monitoring by the acquisition of the electrical signal instantaneously generated by the absorption of radiation.

This device is demonstrated to stand tens of subsequent irradiation cycles (operating consecutively for over one hour), showing negligible degradation of the collected signal. A sketch of the proposed device is reported in Figure 48, together with a simple comparison with state-of-the-art radiochromic films working principle.

Prior to the acquisition with multiple pixels, a standard single pixel is characterized and its response reported under 5MeV protons. Irradiation is tested using a 5 MeV beam extracted into ambient pressure, provided by the 3 MV Tandetron accelerator of the LABEC ion beam center (Laboratory of Nuclear Techniques for the Environment and Cultural Heritage, INFN Firenze, Italy) [213].

Figure 49A shows the typical Current-Voltage curve of the device, which is consistent with sec. 3.1. In B, an example of the current signal induced in the device due to the absorption of energy from a 5 MeV proton beam is reported. Here the device has been exposed to a 20 s irradiation cycle while it was kept at a bias voltage of 5 V (i.e., 0.2 V μm^{-1}), the proton flux set at $(9.0 \pm 0.2)\cdot 10^{8}$ H^{+} s^{-1} cm^{-2}. The absorption of energy from the protons provokes a steep increase in the current and the number of charges induced by the radiation can be calculated as the integral of the curve (i.e., the pink shadow highlighted in Figure 48B). We calculated the rise and falling time as the time for reaching 90% of the signal starting from 10% (i.e., the opposite for the falling time). Notably, the response times of the detector are $\tau_{rise} = (1.5 \pm 0.1)$ s and $\tau_{fall} = (2.4 \pm 0.2)$ s respectively. As shown in Figure 49C, the induced charges are proportional to the total number of protons impinging on the detector, showing a sensitivity of $(4.25 \pm 0.02)\cdot 10^{-18}$ C H^{+-1} (i.e., the slope of the curve). In this graph, each point represents the integral of the proton-induced current at different times. In Figure 49D, the charges induced by protons and collected at the electrodes under three different polarization conditions (i.e., 0.03 V, 0.2, and 0.3 V μm^{-1}) are reported as a function of the total number of impinging protons. The sensitivity value increases with the bias because of the improvement of collection efficiency with larger electric fields: $(1.66 \pm 0.05) \cdot 10^{-18}$, $(4.25 \pm 0.02) \cdot 10^{-18}$, and $(6.43 \pm 0.07) \cdot 10^{-18}$ C H^{+-1} for 0.03, 0.2, and 0.3 V μm^{-1}, respectively. As expected, the electrical noise increases at higher bias and consequently, the signal-to-noise ratio lowers for larger bias voltage conditions.

By defining the Lowest Detectable Dose (LoD) of the detector as the intensity of radiation which induces a signal three times higher than the electrical noise, and under the assumption that noise is dominated by dark current shot noise and, the LoDs in the three bias conditions are $(10.9 \pm 0.4) \cdot 10^{6}$ H^{+}, $(6.1 \pm 0.3) \cdot 10^{6}$ H^{+}, and $(2.3 \pm 0.1) \cdot 10^{6}$ H^{+} for 0.3, 0.2, and 0.03 V μm^{-1} respectively. In order to keep a high sensitivity and a low LoD, all the measurements reported in this work have been carried out at 5 V bias voltage (i.e., 0.2 V μm^{-1}).

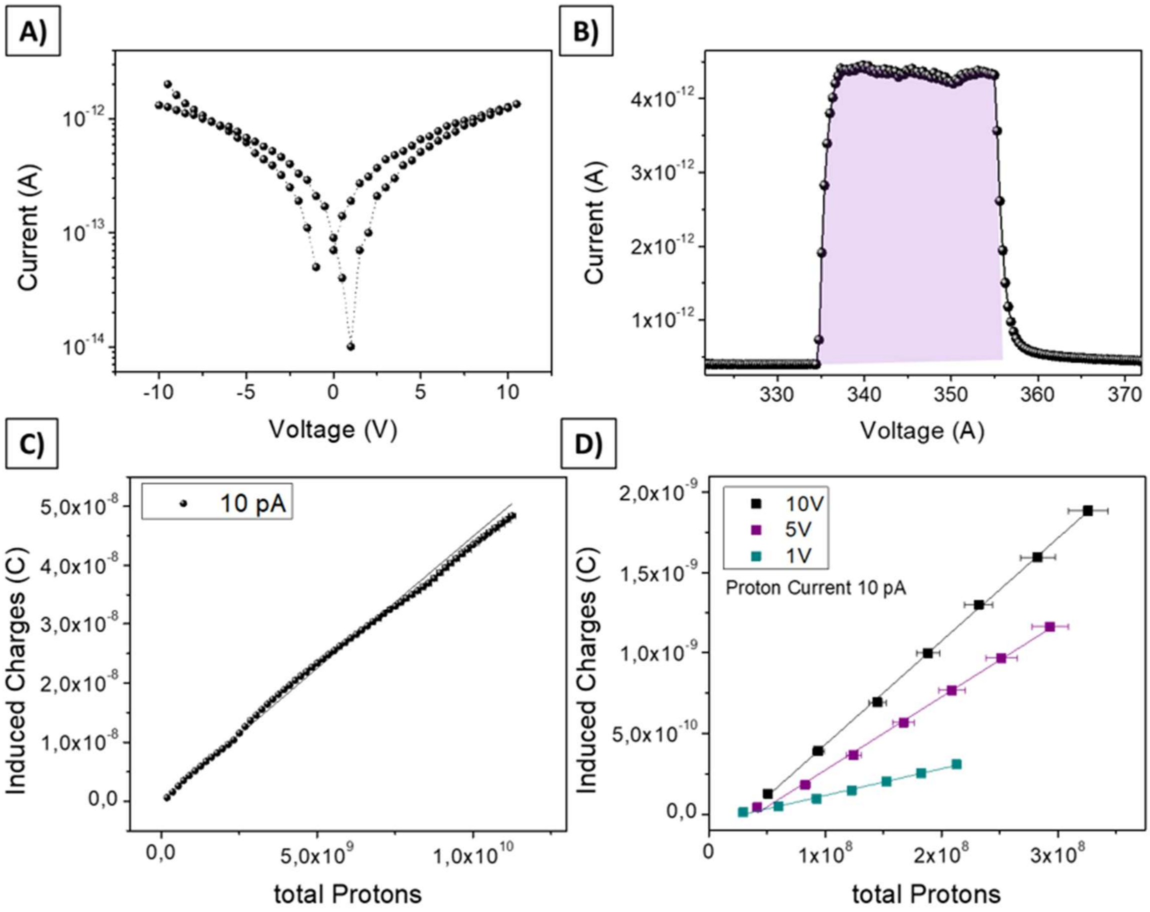

Figure 49 A) Current–Voltage curve of the 2D perovskite thin film-based detector. B) Dynamic response of the detector polarized at 5 V (0.2 V μm^{-1}) and irradiated by 5 MeV proton beams at $(9.0 \pm 0.2) \cdot 10^{8}$ H^{+} s^{-1} cm^{-2} (10 pA) of intensity. The absorption of energy from the proton beam provokes the increase of the current flowing in the device channel and the integral of the curve (pink shadow) indicates the proton-induced charges collected at the electrodes. The two arrows indicate the rise time ($\tau_{rise} = (1.5 \pm 0.1)$ s) and the falling time ($\tau_{fall} = (2.4 \pm 0.2)$ s) calculated as the time for reaching the 90% of the signal starting from the 10% (i.e., the opposite for the falling time). C) Dose Linearity curve obtained by integrating at different instant times the peak reported in B). The plot confirms a very good linearity ($R^2 = 0.996$) over more than two orders of magnitude of total proton number impinging onto the device. D) Dose linearity acquired polarizing the device with three different biases (voltages 1, 5, and 10V) which correspond to different electric fields 0.03, 0.2, and 0.3 V μm^{-1}. The plot shows that the collected induced charges increase following the increase in the electric field (i.e., bias applied at the electrodes).

The achieved sensitivity $S = (4.25 \pm 0.02) \times 10^{-18}$ C H^{+-1} surpasses prior results with a 2D/3D mixed perovskite under similar architectures ($S = (1.12 \pm 0.01) \times 10^{-18}$ C H^{+-1}). This value is also two orders of magnitude higher than the sensitivity of organic-based planar photoconductors biased below 0.03 V/µm ($S = 6.4 \times 10^{-20}$ C H^{+-1}). Furthermore, it is comparable to a $MAPbBr_3$ single crystal photoconductor irradiated with 3 MeV protons ($S = 2.19 \times 10^{-18}$ C H^{+-1}) and it exceeds $CsPbCl_3$ thin-film devices irradiated with 100–228 MeV protons, even when accounting for differences in linear energy transfer (LET) values.

The first attempt on proton beam monitoring is performed through the use of a specific single pixel (channel length L = 30 µm, width W = 30 mm and the entire pixel area is 0.5×5 mm^2) by moving it across the beam spot from one side to the other using a step motor (step size = 0.5 mm), as reported in Figure 50A. In 50B and 50C the beam profile are extracted for two different proton fluxes (i.e., $(9.0 \pm 0.2) \cdot 10^8$ H^+ s^{-1} cm^{-2} and $(1.2 \pm 0.1) \cdot 10^{10}$ H^+ s^{-1} cm^{-2}). For each position, the sample is irradiated for 10 s and the charges induced by protons is extracted following the procedure described above. The dynamic response of the 2D PVK-based detector is reported in the top panels. The signals are acquired keeping the devices polarized at 5 V (0.2 V µm^{-1}).

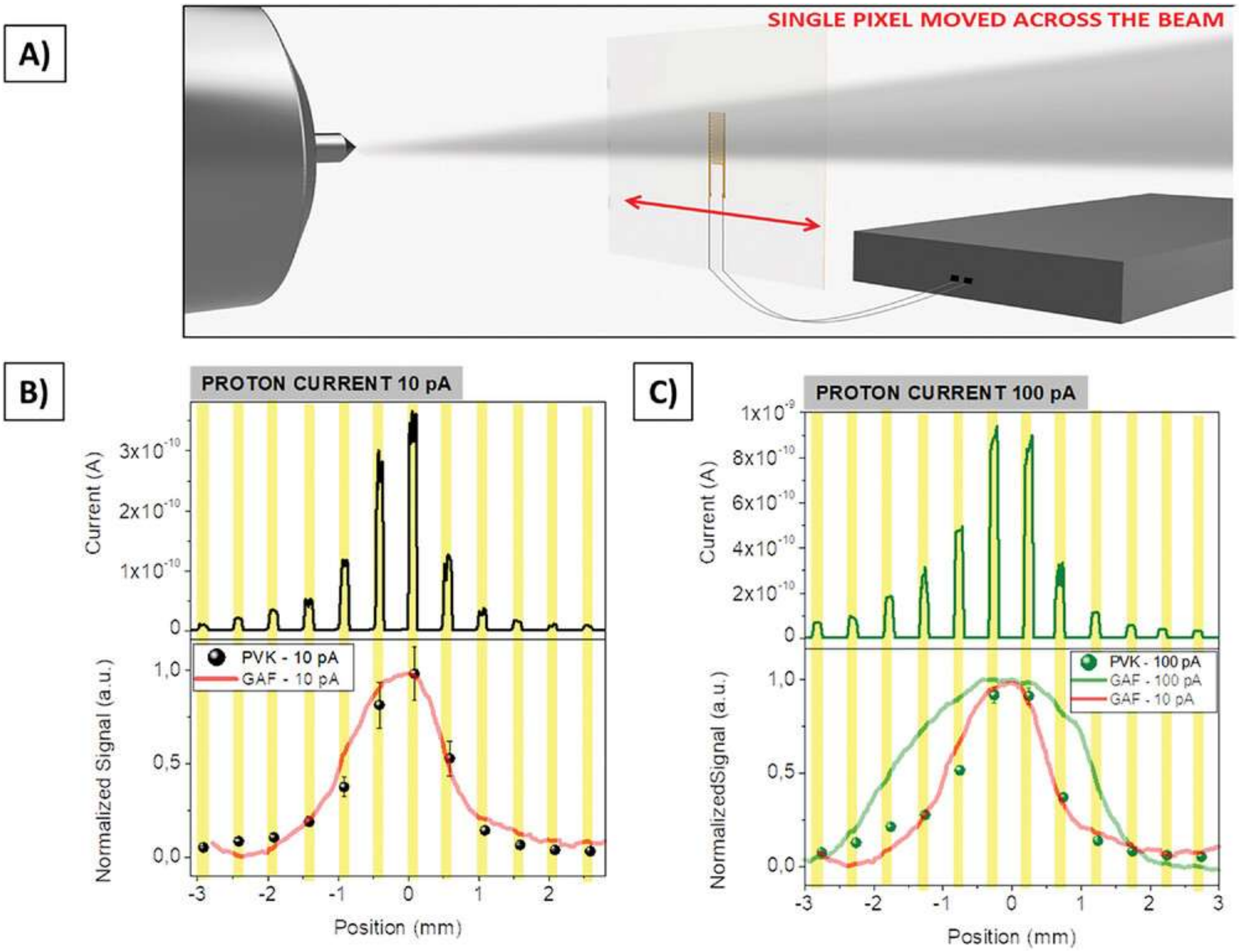

Figure 50 A) A perovskite single pixel has been moved transversally in front of the extracted 5 MeV proton beam using a stepper motor (step size 0.5 mm). In each position, the response of the detector under two different proton currents has been acquired. Dynamic response (top) and normalized signal (bottom) recorded for the proton beam at 10 pA B) and 100 pA C). The symbols represent the proton-induced charges recorded at each position by the perovskite based-detector while the lines correspond to the signal recorded by a commercial radiochromic foil in the same irradiation conditions (GAFCHROMIC – HD V2).

In the bottom panels, the spheres represent the normalized signal induced at each position by the protons while the solid lines show the beam profile, extracted after off-line reading, by a radiochromic sheet GAFCHROMIC – HD V2 exposed to the same beam conditions of the perovskite detectors. At the lowest proton flux there is a good agreement between the 2D perovskite-based detector and the radiochromic sheet indicating a successful reconstruction of the beam profile. At higher fluxes, the experimental points provided by the perovskite-based detector still match the profile acquired by the radiochromic at lower fluxes, while the new profile extracted by the radiochromic foil is much broader. It is worth noting that, after 10s of exposure at high proton flux, the radiochromic foil clearly shows a saturation effect leading to a distortion of the beam shape while the 2D PSK- based detector maintains its full detection properties and provides a reliable performance.

Finally, Figure 51 reports the proof of principle of the scalability of flexible 2D perovskite-based detectors as large-area beam monitoring tools. We fabricated multi-pixels arrays to be employed for the in-line and real-time ionizing radiation beam monitoring. Tests have been performed under X-rays produced by a W-target X-ray tube (40 kVp, 500 μA, 8 mGy s^{-1}). As mentioned earlier, the hybrid 2D perovskite's low density and chemical composition contribute to minimal interference with the primary beam. However, this also results in a low attenuation fraction of high-energy ionizing radiation, reflected in the measured X-ray sensitivity value of $S_A = 123 \pm 2$ nC Gy^{-1} cm^{-2}. Besides, to demonstrate the mechanical flexibility of the here presented detecting system, different tests under X-rays are performed while the 2D perovskite-based detector is kept bent at different curvature radii down to $R_C = 2$ mm. These measurements demonstrate that the detecting response of the device decreased at 90% of the initial value acquired in the flat conditions but the original photocurrent is recovered once the device is placed back in the flat condition, indicating a reversible and not-permanent effect induced by the mechanical stress (see SI of [4]).

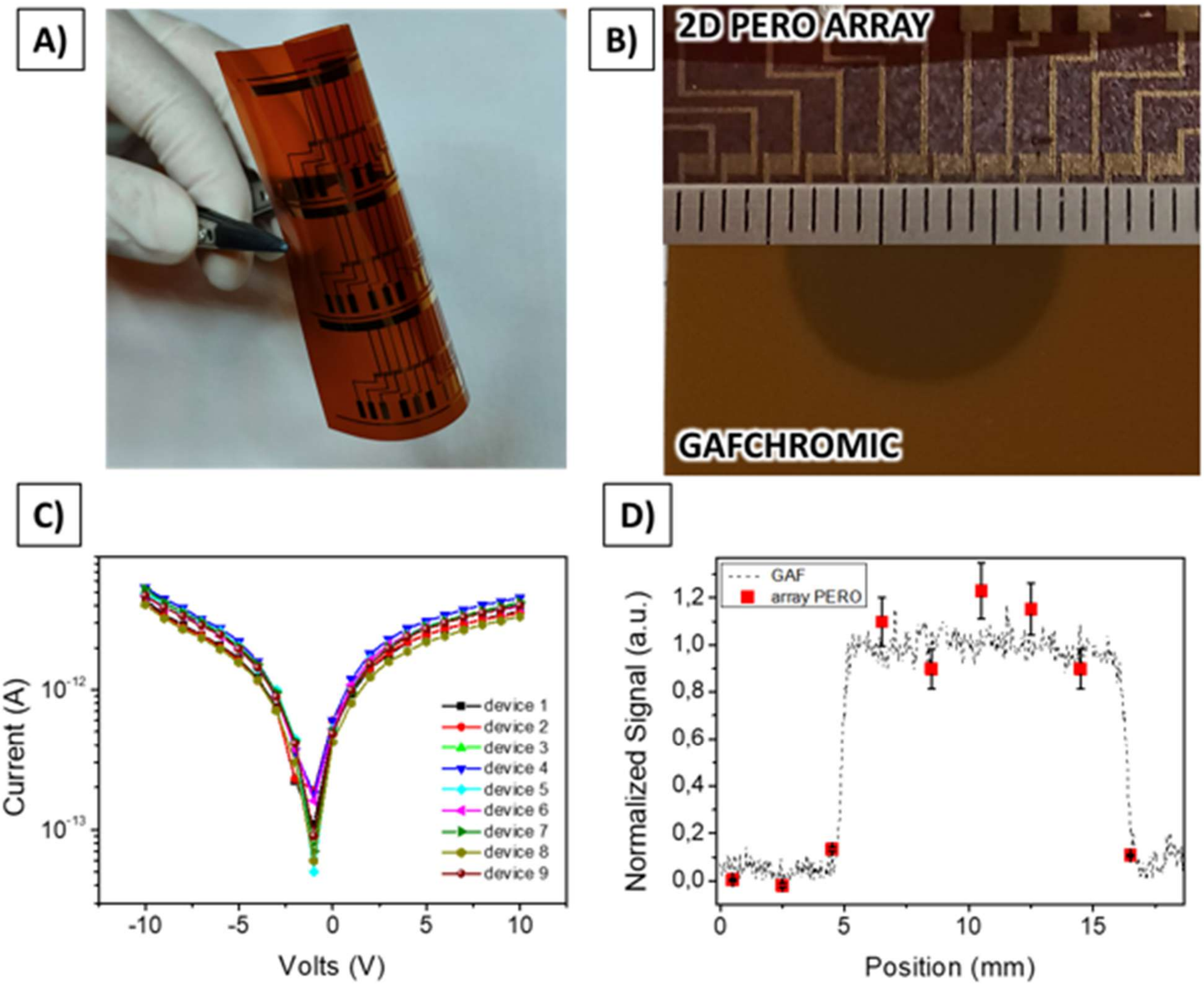

Figure 51 A) Scalability of 2D perovskites-based detectors as pixelated and flexible beam monitoring devices. The planar perovskite photoconductor has been deposited as active layer for a 12-pixel linear array fabricated onto a polyimide substrate. Here, a picture of three arrays fabricated in one single run is reported to demonstrate the scalability of the process. B) Linear 2D perovskite-based array (top) and GAFCHROMIC sheet (XR-QA2) (bottom) reporting a circular spot produced by an X-ray beam (40 kVp, 500 μA, W-target tube, 8 mGy s^{-1}). C) IV curves of the pixels contained in the array necessary to map the beam spot. D) Normalized signal induced by the X-rays provided by GAFCHROMIC (XR-QA2) (line) and 2D perovskite array (symbol) show a good overlapping.

Figure 51A shows three 12-pixel arrays printed in one single run on a flexible polyimide substrate. Each pixel presents a co-planar configuration similar to the one reported above, but with different dimensions resolution (L = 30 μm, W = 11 mm, pixel area is 1 × 1 mm^2, pitch = 2 mm). Multiple arrays can be printed in one single run maintaining a very good yield (i.e., ≥90%) and demonstrating the easy scalability of the process even in a lab-scale facility. In Figure 51B the picture of one single array is reported on top. On the bottom of the figure a radiochromic sheet (GAFCHROMIC XR-QA2) simultaneously exposed to the same X-ray beam spot is shown. Figure 51C reports the dark Current-Voltage curves for 9 pixels from which we extracted the mean value of the electrical conductivity 6.3 ± 0.8 pS cm^{-1}. The variation of the pixel response is within 10%, demonstrating the excellent uniformity of the detecting performances achieved by the devices. Figure 51D reports the actual experimental mapping of the X-ray beam spot. For this test, both the 2D-perovskite array and the radiochromic foil have been placed in front of the X-ray tube aperture. The 2D perovskite-based array has been connected to a custom multiplexing system for the readout. The red symbols represent the experimental points obtained by extracting and normalizing the photocurrent ΔI induced in 9 pixels of the array in different positions ($\Delta I = I_{X\text{-}Ray} - I_{dark}$). The dashed line represents the profile of the spot acquired by the radiochromic sheet. It is noteworthy that we intentionally chose an X-ray beam flux that would not induce saturation effects in the radiochromic foil, that we use here as a gold standard to validate the performance of the 2D-perovskite array.

The two curves are in excellent agreement, confirming a successful and reliable real-time and in-line transversal mapping of the X-ray beam.

3.2.3 GAMMA DETECTION FROM RADIOTRACERS

Nuclear medicine plays a vital role in cancer diagnosis and treatment, particularly through the use of radiopharmaceuticals in techniques like PET imaging and radionuclide therapies. However, extravasation—when administered radioactivity leaks outside the venous system—can compromise both diagnostic accuracy and patient safety. This can lead to complications, such as inaccurate imaging and tissue damage due to excessive radiation doses in unintended areas.

Wearable, real-time dosimeters are needed to monitor extravasation events and prevent potential tissue damage during procedures. Current systems using scintillators are rigid and expensive, with limitations in spatial resolution. Provided the abovementioned results that demonstrate the possibility to have 2D perovskite-based devices fabricated to be scalable to large-area and flexible, we report tests and analyses on multipixel devices that enable online and real-time detection of gamma rays from radiotracers used in nuclear medicine. These perovskite-based thin films provide an innovative approach for wearable radiation detectors that can improve patient safety and treatment personalization by offering high sensitivity, portability, and scalability.

In the field of targeted radionuclide therapy (TRT), the most common radiotracer for PET imaging systems is ^{18}F, which is a positron emitter with a half-life of 109.7 min. The emitted positron annihilates with a nearby electron emitting two 511 keV photons in opposite directions.

In here we report the use of ^{18}F radiotracer solution to validate thin-film perovskite-based detector performance for the real-time monitoring of extravasation event occurring during radiopharmaceutical injection. The device is composed of 4 pixels with active area of 2mm^2 and channel length L=10 μm.

To assess the capability of the detector to effectively detect gamma rays emitted by the radiotracer we developed a custom experimental setup shown in Figure 52. This is equipped with a 3D-printed frame that holds in place a stepper motor and the sample box. The ^{18}F radioactive drug is contained into a vial kept by a printed support connected to the motor axis. A thick Pb cylinder is used to screen the sample from the radiation when the state is in the OFF position, while in the ON position the motor moves the gamma source on top of the sample. Three radiotracer solutions with different activities between 1800 and 94 MBq are prepared and their produced signal measured with a calibrated commercial detector (ISOMED 2000, Nuclear

System)[214]. The shutter was set with a period of 20s with duty cycle of 50%. Every three peaks the source is changed while the shutter in the OFF state. The dynamic response is reported in Figure 52C. The device, biased at 2 V, shows a steep increase of the photocurrent in the ON state, followed by a decrease to the pristine dark current value in the OFF state. Although the first three peaks are not properly stable, the remaining peaks even at low activity are repeatable. We speculate that the instability measured at high activities can be attributed to a polarization effect, reported in literature for perovskite-based X-ray detectors under high fluxes. The amplitude of the response well-scales with the activity, as evidenced in the plot of Figure 52D.

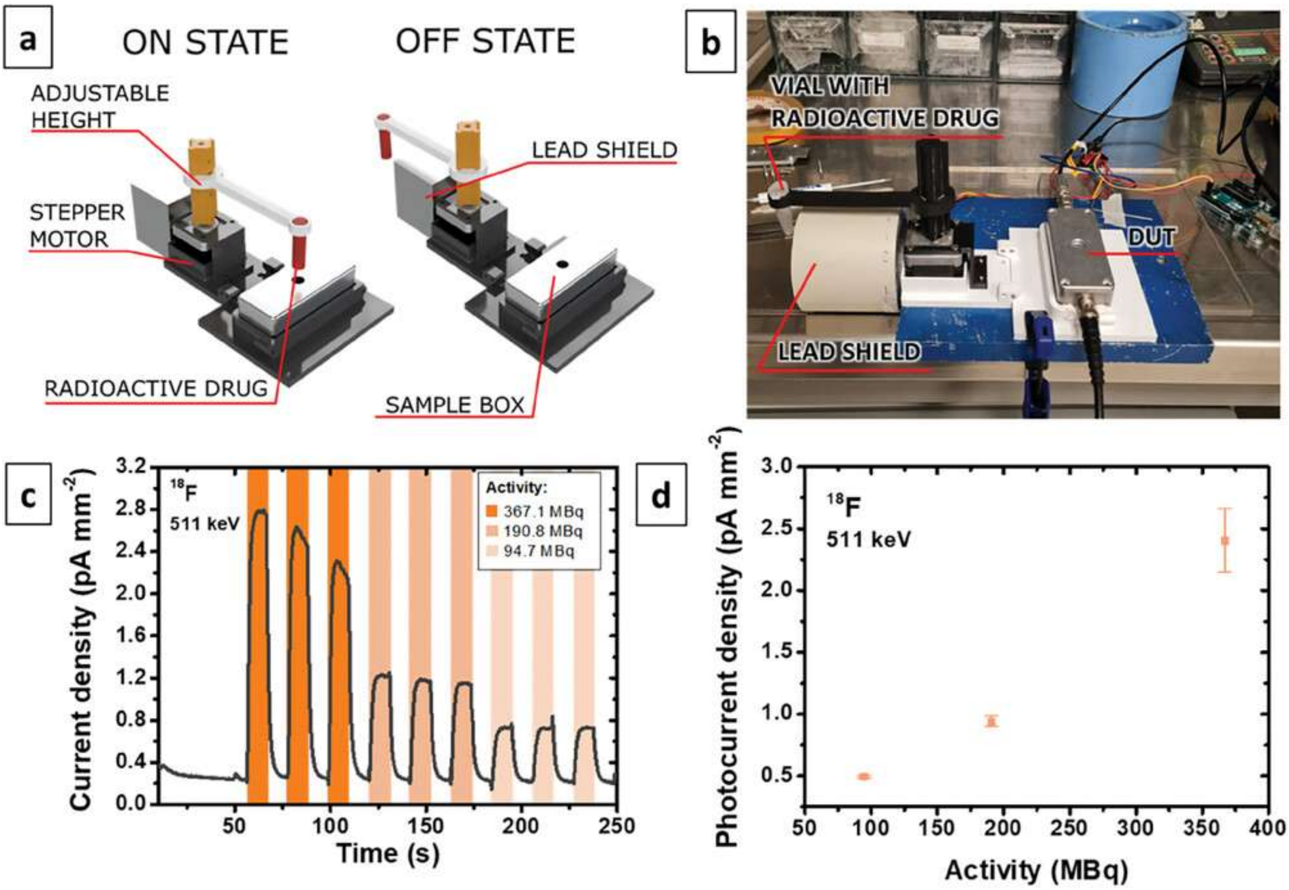

Figure 52 a) Schematics and picture (b) of the shutter system employed for the sensors characterization under high energy gamma ray emitted by radioactive drugs. A stepper motor is controlled by an Arduino UNO board. 3D printed holders keep the moto and sample box in place. The radioactive drug is contained in a vial hold by a custom support connected to the motor axis. c) Dynamic response at 2 V of PEA_2PbBr_4 detector. The data were collected using three ^{18}F with decreasing activity with a source to sample distance of 8 mm. d) Photocurrent density as a function of the source activity. Data has been calculated as the average of the three signals reported in c) collected for each activity value and the associated error bar as the standard deviation.

Furthermore, the decay of ^{18}F is monitored with each of the 4 pixels, provided that they respond equally as exposed to the same irradiation conditions (328 MBq and biased at 5 V). The higher bias is chosen in order to achieve signal outcomes larger in amplitude. The device is set under gamma rays emitted by the radiotracer for 4h and signal decay is monitored through the integration of a portable battery that allows for safe measurements to be run in protected environments. As reported in Figure 53B, the 4 pixels show very similar response, with an exponential decay following the natural radioactive decay of fluorine, starting from an activity of 1.8 GBq.

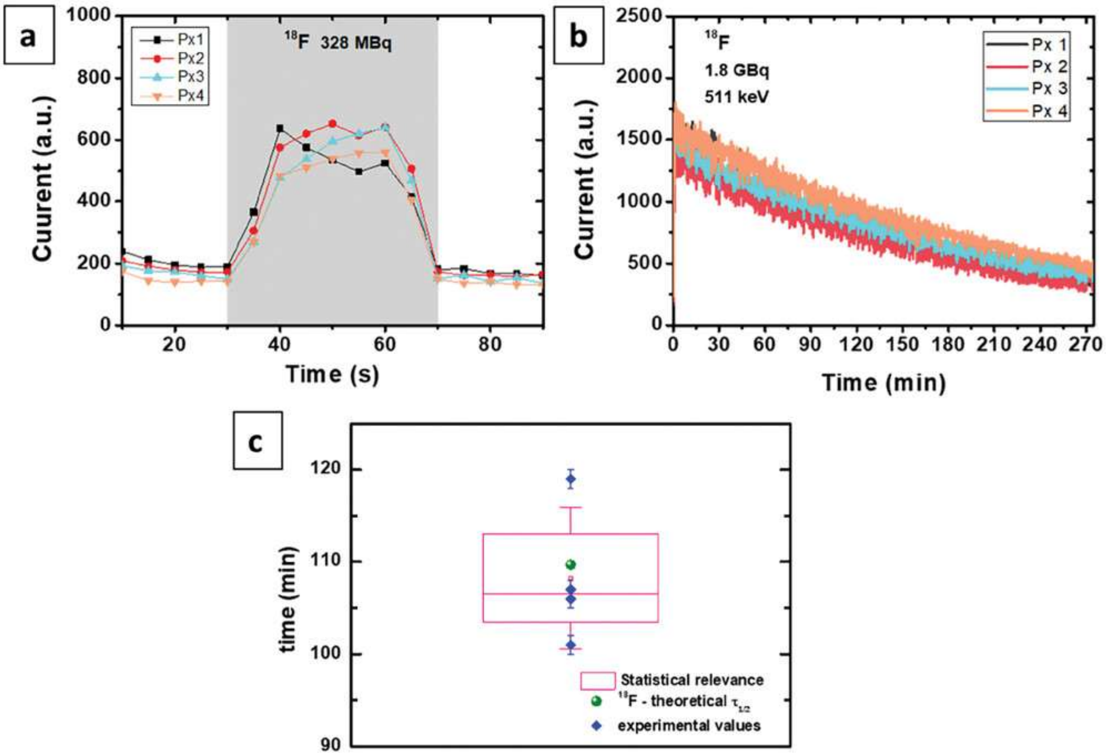

Figure 53 ^{18}*F decay. a) Photocurrent signals of the 4 pixels biased at 5 V, exposed to* ^{18}*F at 328 MBq. b) Current signal from 4 different detector pixels positioned underneath a* ^{18}*F source for more than 4 h. c)* ^{18}*F half-life measurement.*

To validate the detector for its actual application as radiation monitor for nuclear medicine treatments, we setup an experiment mimicking an extravasation event after the radiotracer injection procedure. Figure 54 shows the experimental configuration employed for this test. A phantom with plastic tubing was used to simulate the blood vessels in the patient's arm. The radioactive drug, with a blue dye added in the solution to make the flow easily visible, was injected in the phantom vein by a lead-shielded syringe. The activity used for the experiment was estimated based on assessments of the extravasation areas identified in the cohort of patients enrolled in the study approved by the Ethics Committee (Registration number 448/2021/SPER/IRCCSE). The main vein was simulated by an almost straight plastic tube, while the extravasation region, close to the detector, was simulated by a plastic tube rolled up. The experimental sequence is reported in Figure 54:

1. Injection (grey). The radiotracer is injected in the main vein, and it flows to the opposite direction of the injection point (toward the heart, in the real case). In the picture (Figure 54B), an intense blue color is visible.

2. Extravasation (yellow). A valve is opened causing a partial flow of radiotracer in the secondary tube accumulating above the detector.

3. Release of the accumulated radiotracer (orange). A valve at the end of the system is opened causing the radiotracer accumulated over the detector to flow away.

4. Flushing (cyano). At the end, physiological solution is released inside the tube cleaning all the system from the radioactive drug.

Figure 54C reports the recorded signal, the colored regions corresponding to the different steps in the injection procedure. The detector reliably monitored the whole process. A small increase in the current is measured soon after the injection of the radiotracer in the main vein. When the valve is opened leading the extravasation, a higher increase in the sensor current is observed. The current starts to decrease immediately when the accumulated radiotracer is released from the extravasation region. A low current signal still remains until the physiological solution reaches the extravasation region and cleans the tube from the ^{18}F atoms. After few seconds the signal returns to the baseline level. The detector demonstrates to be able of measuring the low amplitude of the signal emitted by a radiotracer, thanks to the unique dark current stability of 2D perovskite.

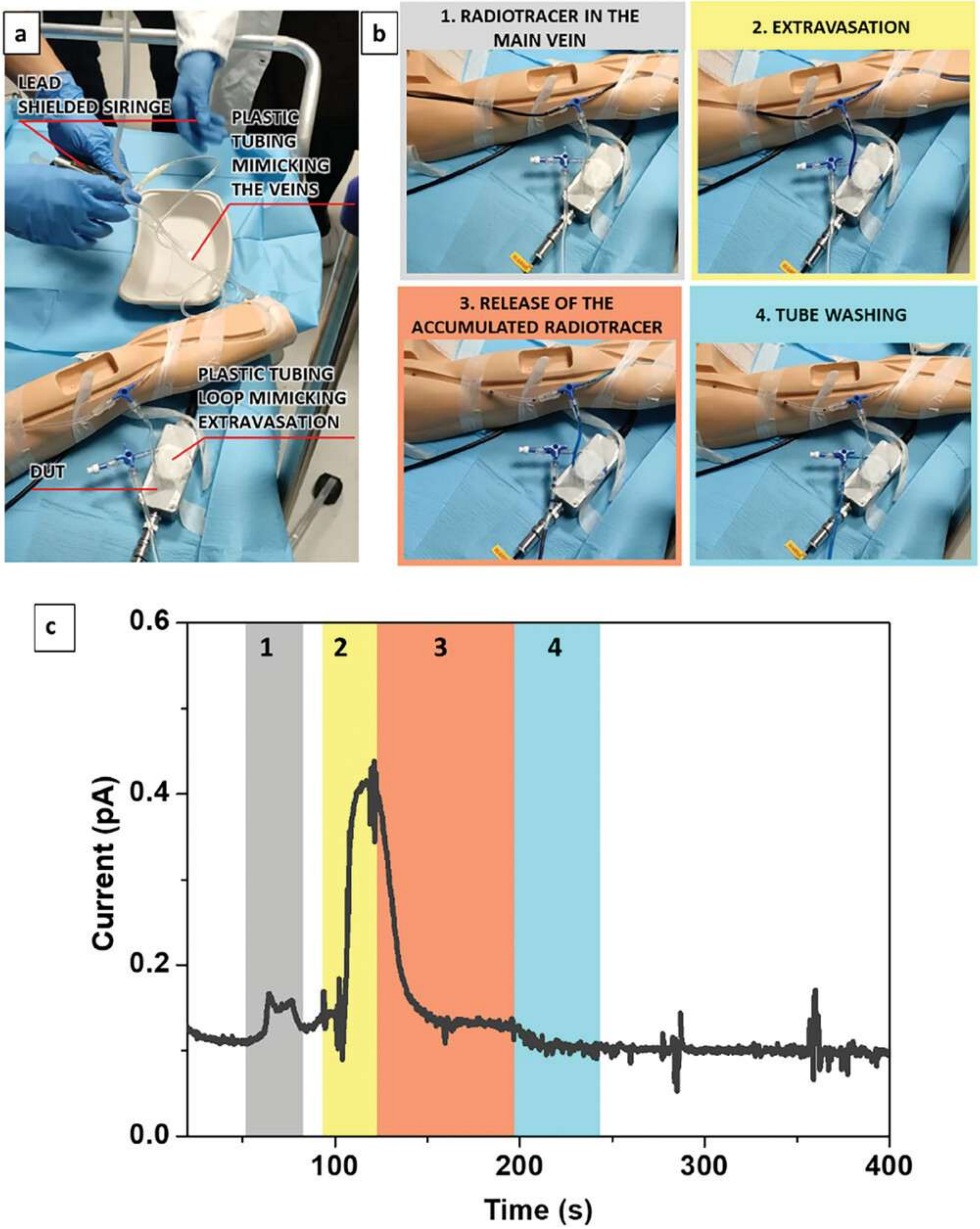

Figure 54 Monitoring radiotracer extravasation. a) Picture of the whole experimental setup used to mimic the extravasation event. b) Different steps in the injection procedures: 1. the blue colored radiotracer solution is injected in the plastic main tube simulating the vein. 2. The valve controlling the extravasation is opened and the radiotracer starts to flow in the secondary line rolled up and placed over the sample box simulating the accumulation of radiotracer in an unwanted region of the body. 3. After a while the extravasation line is opened, and the radiotracer starts to flow away from the detector (blue color is less intense). 4. Physiological solution is injected in the system flushing away the remaining radiotracer. c) Detector current signal, acquired at 2 V, during the whole injection procedure described above. The colored region refers to different test steps according to b).

3.3 SPACE APPLICATIONS: SPACE-CREW PERSONAL DOSIMETRY

In view of the previous discussion on 2D perovskite features in matter of high energy radiation detection, the following provides a comprehensive overview of the IRIS project (Large area, wearable Ionizing Radiation dosimeters for real-tIme crew perSonal monitoring), which is designed to to enable real-time monitoring of high energy radiation in space environment. Extensive studies have been conducted to optimize the device according to the radiation environment of outer space. Deep analyses have also been performed to scale it to the international space station (ISS), Columbus modulus, as this will be the sector of operation of Crew 10, in charge of the tests in space.

3.1 BRIEF INTRODUCTION

As exploration and targeted efforts are aimed at sustained human presence in outer space, it is essential to deeply consider radiation exposure and its associated risks. During missions, astronauts are immersed in a chronic, low dose-rate ionizing radiation field, primarily originated from outside the solar system (galactic cosmic rays, GCR) and from sporadic, much higher dose rate Solar Particle Events (SPEs). These fields, during the future Mars mission, may exceed established radiation limits (values related to sex and age as reported in NASA STD Vol.1) [215], [216].

Effective risk assessment requires continuous monitoring of the incoming radiation in the space habitat, including the secondary radiation resulting from the interaction of the primary field with spacecrafts. Accurate absorbed dose evaluation demands for both discrimination of radiation nature and energy [217]. Current state-of-the-art of radiation-linked operations integrate forecasting, mission time scheduling (Space Permissible Exposure Limits) and exposure control at specific locations via radiation detection. Regarding the latter, various devices are implemented that allow for both environmental and personal monitoring [218]. The first systems [219] employ, for example, Timepix technology for time-resolved analyses. Among the several personal monitoring systems, we mention the NASA active dosimeter Crew Active Dosimeters (CAD) that exploit floating gate MOSFETs surrounded by conducting walls to create ionization chambers [218]. Main features of CADs include low weight, low size, high battery lifespan and time-resolved data of the total absorbed dose, regardless of the nature of the incoming radiation. Limitations of this equipment reckon the read frequency longer than 10 minutes and the need to set a threshold in dose; furthermore, these devices exhibit high background noise.

We here propose a self-sustained device (IRIS) that integrates a set of flexible dosimeters to monitor the radiation fluxes the space crew is exposed to. It implements flexible, thin film dosimeters made of PEA_2PbBr_4 and TIPS:Pe Organic Semiconductor onto a portable, wearable self-powered readout electronics that measures the photocurrent signals at low applied bias, thus allowing for fast read frequency and direct outcomes transmitted to an onboard computer. Its architecture allows for energy discrimination and tracking of events occurrences. Furthermore, an integrated memory guarantees data recording in working conditions in and outside the spacecraft.

Organic semiconductors, overviewed in Appendix 1, have been increasingly recognized for their potential as direct radiation detectors due to their ability to efficiently convert high-energy radiation, into an electrical signal. When exposed to ionizing radiation they generate electron-hole pairs within its structure. These charge carriers are then collected and measured at low bias. Their high photoconductive gain -that is an effective multiplication of charge carriers inside the structure- enhances the material's sensitivity, enabling it to detect even low levels of radiation[220]. The produced signal is in the form of an integrated photocurrent, the level of which increases with increasing absorbed dose. Response of OSCs under heavily charged particles is reported in [221].

Stability over time of the two classes of materials have been assessed in the past; recent works on perovskite crystals proof their hardness in space environment [222], [223], [224].

The IRIS ground tests have been carried out in the last two years, and the flight-model will be part of the equipment to be included in the space mission of next year inside the ISS, Columbus modulus, and will undergo 7 days of continuous testing in different crew operating conditions. It is envisaged the possibility to have a detailed comparison of the IRIS outcomes with the LIDAL measurements [225], another detector which measures the radiation field in real time in the ISS [226].

The target of the IRIS project is two-fold. Firstly, from a fundamental research perspective, it aims to thoroughly investigate the performance and resilience of the materials used in dosimeters when exposed to the harsh conditions of the space environment. This involves studying how these materials respond to low-dose, low dose rates, high-energy radiation, extreme temperatures, and other space-specific factors. Secondly, the project seeks to develop low-cost, large area, flexible fully operational dosimeters tailored to provide real-time analysis of radiation exposure levels during space missions.

3.3.1 SIMULATIONS OF RADIATION ENVIRONMENT

Prior to dosimeter realization, crucial task is to determine the target space environment to be monitored.

Columbus is a science laboratory that is part of the International Space Station (ISS) and is the largest single contribution to the ISS made by the European Space Agency (ESA). The experimental sector is a cylindrical module, made from stainless steel, kevlar and hardened aluminum, with two end cones. It is 4.48 m in external diameter and 6.87 m in overall length, excluding the projecting external experiment racks. A Monte Carlo study with the radiation transport code PHITS (v 3.22) [227] is used to characterize the expected radiation environment inside it and, more specifically, to initially verify the extent of photon and electron production as by-products of fragmentation processes for ions interacting with the space station. A software replica of the Columbus space habitat, modelled as an aluminium module, with an astronaut inside, modelled as a spherical tissue phantom, has been implemented and exposed to an isotropic flux of protons/ions (see Fig. 55, top panel). The fluxes of particles and X-rays at the interface between the air (inside the module) and the phantom surface has been then analysed.

To a first approximation, the SPE scenario was tested with representative beams of monoenergetic protons, in the energy range 10-500 MeV. Below 10 MeV, indeed, no primary protons or secondary products can reach the phantom.

GCR representative ions (protons, alpha particles, C-ions and Fe-ions) were also simulated at the characteristic energy of 1 GeV/u.

Results, in terms of X-ray fluxes per incident particle at the air-phantom interface, are shown in the bottom panel of Fig. 55 for the SPE (on the left) and the GCR (on the right) scenarios. As one can see, the energy range of secondary X-rays is 80 KeV – 3 MeV for the case of a SPE and 70 keV – 300 MeV for GCR.

A full characterization of the expected radiation environment inside the Columbus module, to be adapted to different external radiation sources, is in progress.

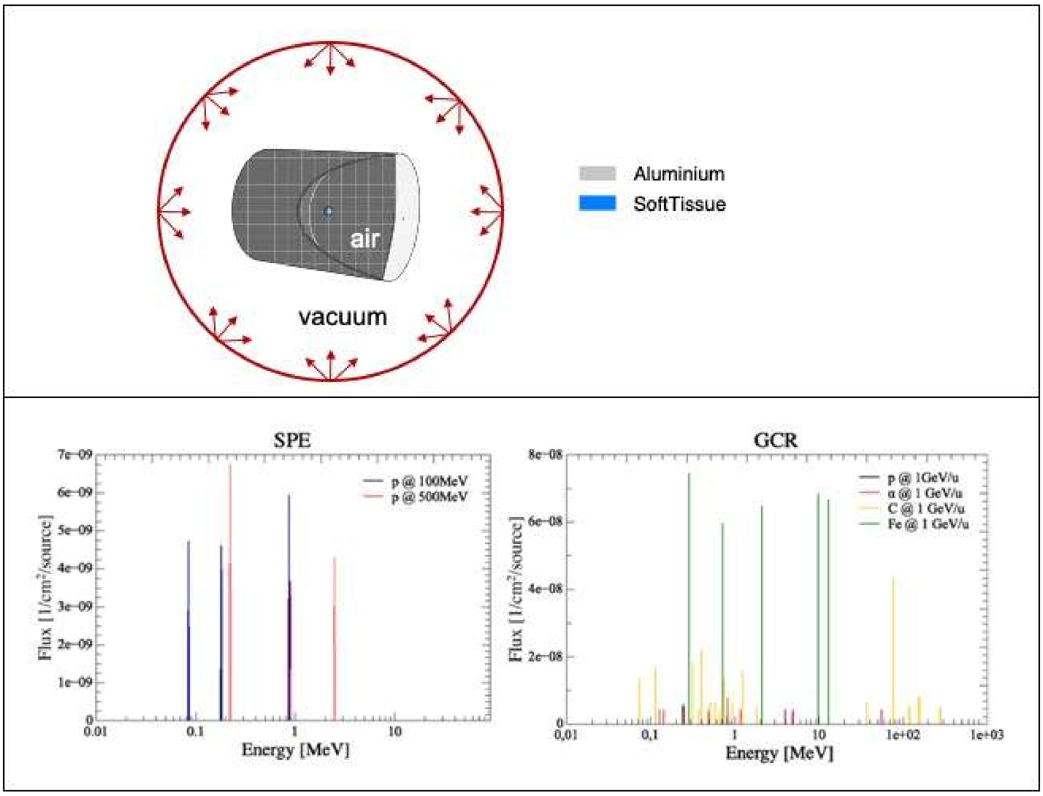

Figure 55 Top panel: 3D-view of the PHITS simulation setup: the Columbus habitat, modelled as an aluminium module filled with air, and a tissue spherical phantom, representative of an astronaut, inside. Bottom panel: Fluxes of X-rays per incident particle at the interface between the air and the phantom surface, obtained by PHITS simulation of a SPE (left) and a GCR (right) scenario. Courtesy of A.Mentana, G.Baiocco, L.Narici.

This being provided, intensive efforts have been dedicated to the simulation of dosimeters materials and architecture to obtain an optimal configuration for better resolution and eventual discrimination of particles' nature. As the device accounts for two pairs of dosimeters for both better resolution and particles featuring, we made use of SRIM analyses to determine required materials and thicknesses of the components. Figure 56 reports a sketch (top panel) of the chosen sensor's structure, which is described in detail in sec. 3.3.2. Below, a SRIM simulation with 5MeV and 20MeV protons incident to the dosimeter, with dedicated ionization plots that gather the energy loss inside the dosimeter as function of position. Tuning the parameters such as material density and thickness helps in determining the ranges of recorded energy from each device.

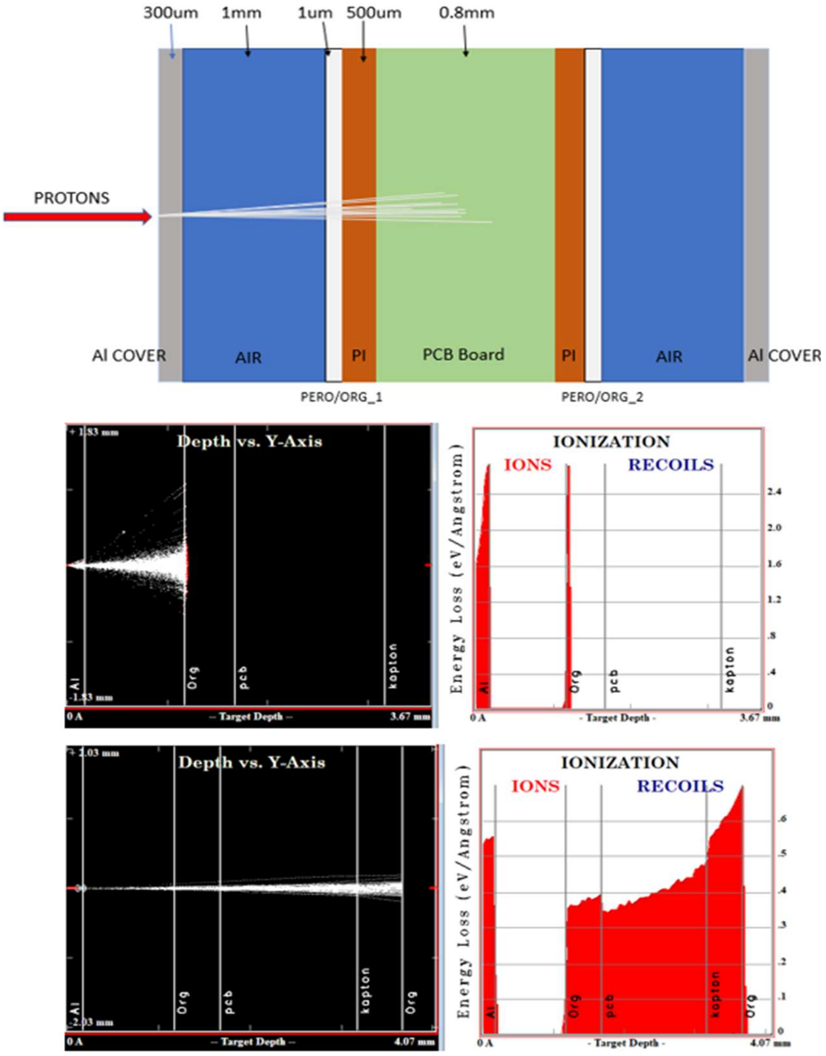

Figure 56 A) IRIS dosimeter scheme with chosen materials and relative thicknesses. Symmetric devices provide different signals that can be then analysed for clear discrimination as function of the different energy loss through the interposed layers. B) SRIM simulation of incident 5MeV and 20MeV protons, used to investigate the ranges of efficiency of the chosen structure. Notably, 5MeV protons can't be detected by the device that is farther from the source; similarly, the dosimeter detects 20MeV protons differently between the front and back films.

3.3.2 IRIS DOSIMETER: STRUCTURE AND METHODS

IRIS complete architecture is sketched in figure 57. IRIS external and internal parts are made of aluminium, electrical contacts obtained using space-grade H20E conducting paste (Epoxy Technology).

IRIS core is composed of a multichannel electronic readout system connected to an internal data storage that allows for parallel, real-time reading of electronic signals produced by direct detection of the absorbed ionizing radiation in the form of photocurrent (provider: KAYSER ITALIA SRL).

Additionally, a dedicated external and space-grade powerbank is intended to provide battery life for long acquisitions.

Dosimetry is performed through a double 4-pixel architecture reported in fig. 57B, the active materials being 2D-PSK (PEA_2PbBr_4) and TIPS:Pn in the form of thin films of thicknesses around 1 μm and 500nm and spin-coated onto Kapton and PEN flexible substrates respectively. Bias is applied independently, and it is set to be 4.5V for PSKs, 1V for OSCs. The designed front-back architecture guarantees higher level of discrimination of radiation nature and energy. Exact data collection process accounts for specific working principles for the two different materials. The pulse-like nature of signals from PSK pixels permits the setting of a current threshold below which no data is recorded, thus lowering battery consumption. The threshold is set at 10pA; when higher signals happen to be detected irrespective of which pixel did record it, acquisition starts for the four of them with tuneable sub-second sampling time. OSCs account for a system that constantly reports the measured current with tuneable sampling time down to 20s.

The IRIS device has successfully completed the acceptance test campaign (including functional, EMC/EMI, touch temperature, interface with ISS laptop tests) to achieve the flight readiness for its use onboard the ISS.

Ground calibration and tests conducted in dedicated labs include radiation measurements under X-rays (Tungsten tube, dose rates from 10μGy/s to 1mGy/s, energy ranges 40-150keV, exposure beam-on times varied from 1 to 10s) and alpha particles (^{221}Ra, 5μCi; ^{241}Am, 0.5μCi, 30 minutes continuous measurement). Exposure campaigns aimed to assess coherent sampling of the electronic readout and related parameters to be set (sampling time, threshold), linearity with dose rate of PSK pixels under photons, integration over time of Alpha-induced photocurrent signal of OSCs.

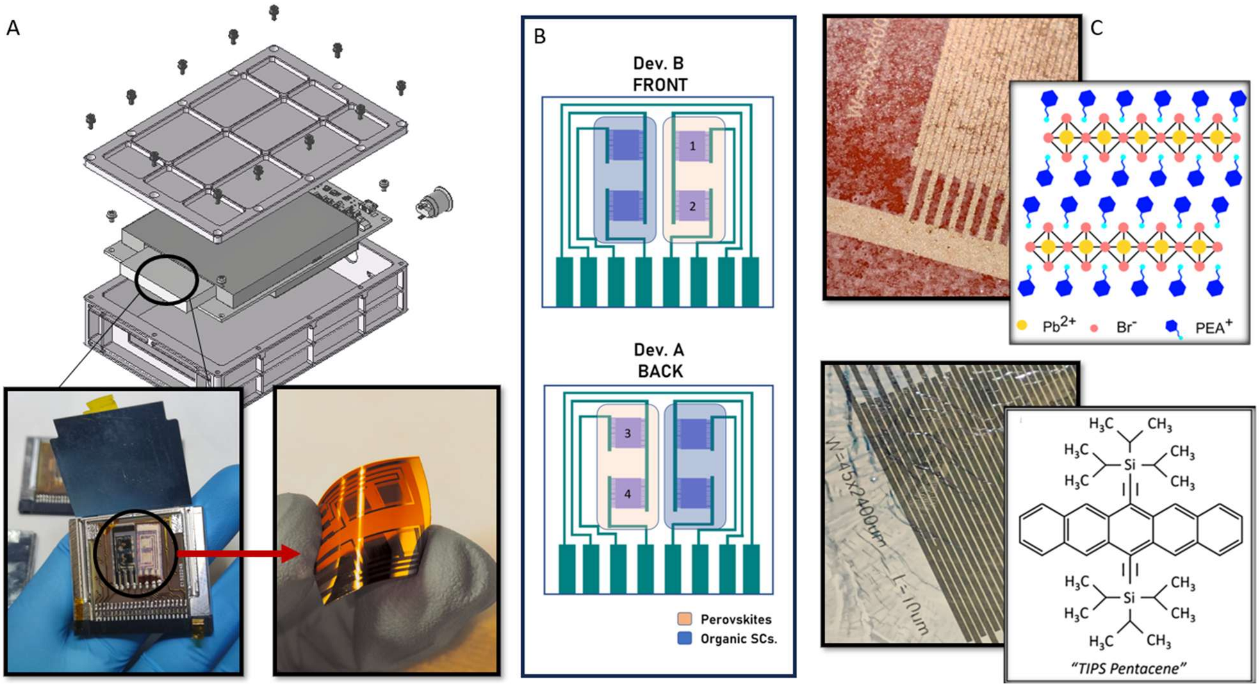

Figure 57 Complete scheme of IRIS design and components. A) Sketch of IRIS structure with close-up on one of the two integrated dosimeters connected to a dedicated electronic readout system encapsulated in an aluminium shield. Active materials are deposited on ultra-flexible space-grade plastic substrates. B) Scheme of dosimeters composition. Two symmetrical devices separated by a plastic PCB with patterned electrical contacts on both sides, composed of two PSK-based and two OSC-based pixels. C) Actual picture of the interdigitated pixels with deposited films and insets of target molecular structure and chemical formula of the employed active materials

3.3.3 PRELIMINARY RESULTS

We here report preliminary results with IRIS flight model obtained in laboratory-scale radiation facilities.

Measurements aimed to validate IRIS functioning under high energy photons or particle beams in term of dosimeters response, accuracy of readout system, practical usability and handling. Tuning of parameters allowed for low-dose analyses for Limit of Detection (LOD) estimations for X-rays and charge accumulation analyses of organic pixels under alpha particles. Furthermore, experimental tests under high energy proton beam will be carried out before space-launch as additional references for post-processing.

Figure 58 displays recorded signals under X-rays for PSK-based pixels of target dosimeters and response of a single OSC pixel after alpha particle exposure. Results show clear difference in pixels position with respect to source: as the Pvk1 and Pvk2 pixels are closer to source, their response is greater compared to their symmetric conterparts. B) exposes perovskite signals for different beam aperture times (1,2,5,10s ON-time reported); sampling time set to be 600ms, beam parameters 150kVp, incident -to IRIS box, not to dosimeter- dose rate 6mGy/s, distance of IRIS from source 30cm. In C), generated current as function of dose rate is recorded to demonstrate scaling of signal and low-dose detection down to incident 100μGy/s. Linearity of single pixels with respect to dose rate is reported in D).

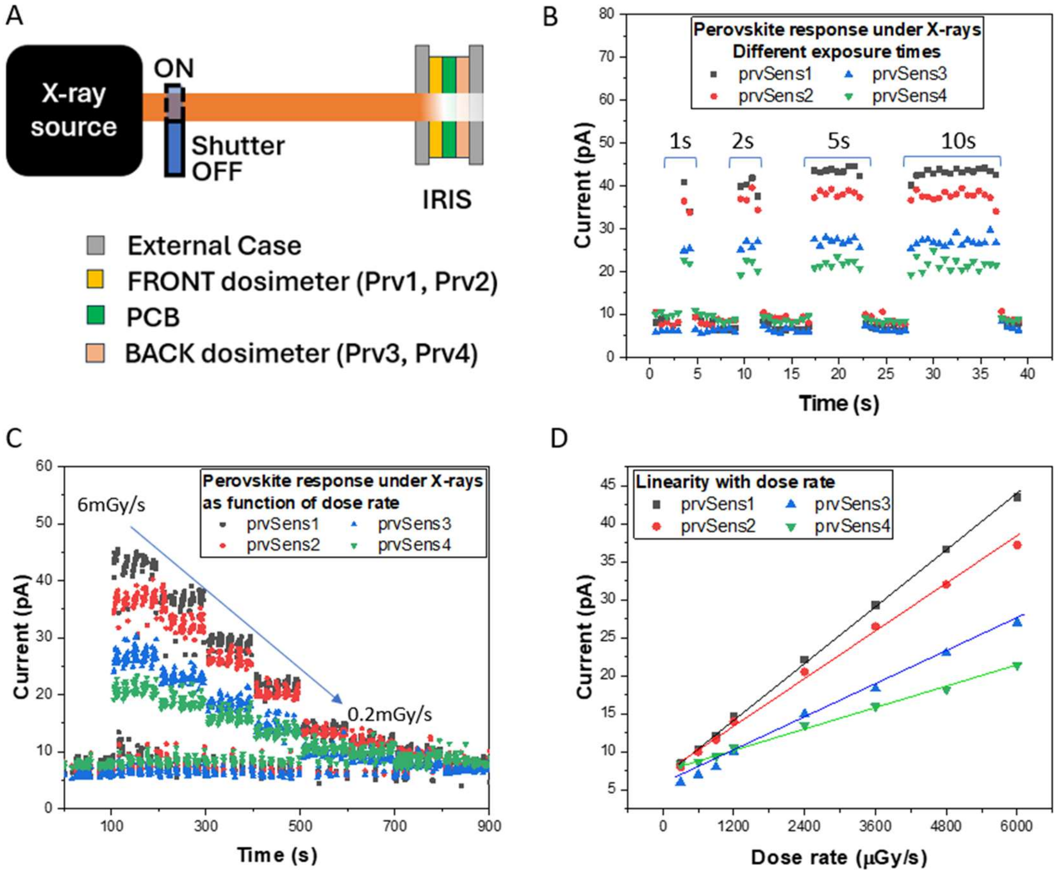

Figure 58 A) Simplified scheme of IRIS device under X-rays; the tests are performed to assess perovskite response under high-energy photons inside IRIS. Labels namely front and back configurations are required for clearer discrimination in matter of signal recording. In B, the pixels response as function of ON-OFF beam-times. As sampling time is set at 600ms, each point corresponds to a collected outcome. Notably, pixels 1 and 2 exhibit higher signals as they are closer to X-ray source. C shows a decrease in response with decreasing dose rate down to 0.2mGy/s; low-noise of the Ground Model covers signal produced from lower dose rates. In D, a test of linearity with dose rate is reported for consistency with previous measurements.

Finally, 5.5MeV alpha particles from ^{221}Ra source have been used in place of heavily charged ions or protons to demonstrate OSCs working principle as in Figure 59; the source is inserted directly on target pixel as no alpha would penetrate IRIS box nor the opposite pixel. For these measurements, 1) the sample is relaxed for 12h, recorded current signal at 1min sampling time; 2) alpha flux is opened, sampling time decreased to 20s, total exposure time set to be 20min; 3) post-exposure relaxation for 30min.

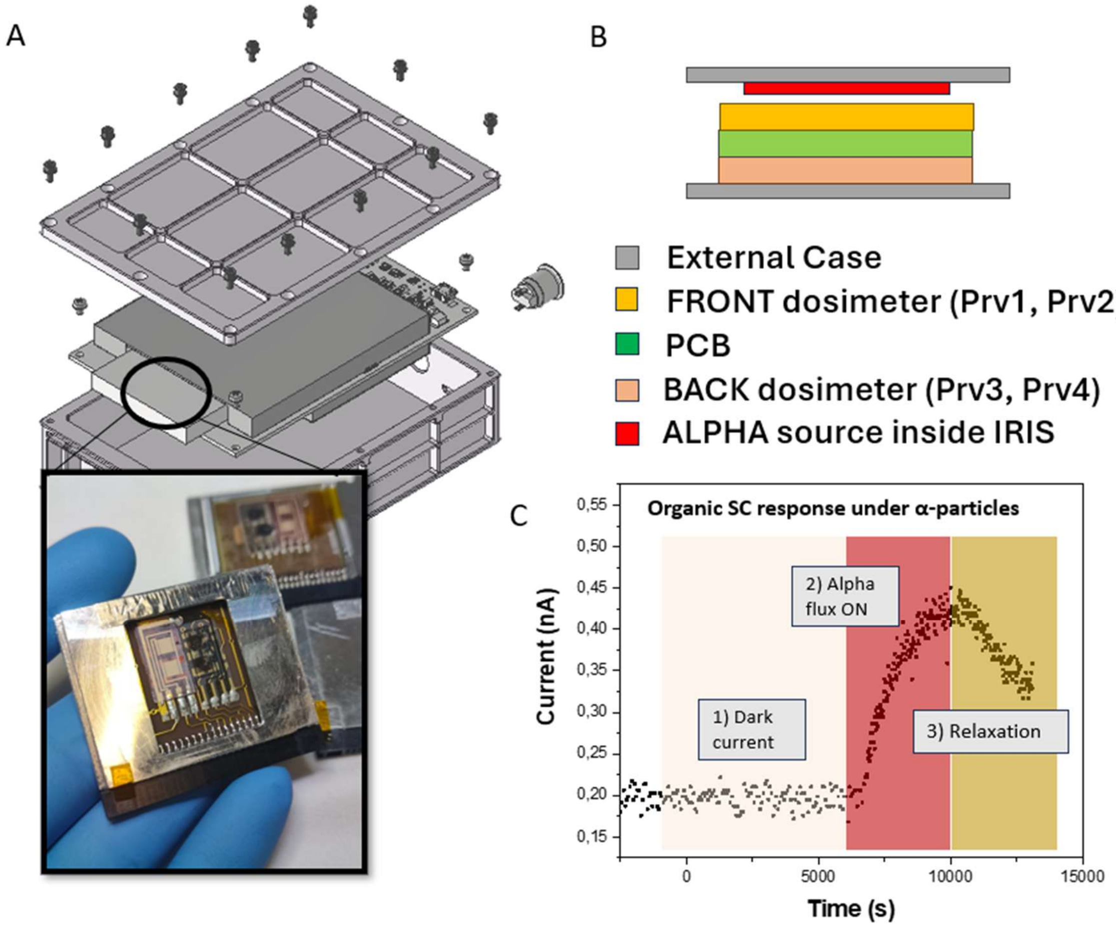

Figure 59 Structure of IRIS dosimeter employed for characterization under alpha particles of organic SC pixels. As no modifications could be imparted to the GM, we employed a dosimeter with an exposed region into which an alpha-source (^{241}Am) could be inserted, as reported in the sketch B). In C, a complete characterization of the exposed pixel is presented for three main conditions: the sample is left 12h in dark in order to prevent bias drifts; alpha source is then allowed emit towards the pixel, thus making it integrate the photocurrent as expected for 30 min; finally, relaxation is recorded for 30 min in order to demonstrate the integrative property of OSCs.

Although preliminary, these results clearly highlight the power of 2D perovskites and TIPS:Pe as active materials for radiation detection as they feature extremely low dark current, high stability and robust response. IRIS portability and real-time reading is key for radiation environment monitoring and astronauts' safety as it provides insights on type and intensity of the impinging radiation source.

DISCUSSION AND CONCLUSIONS

This contribution can be considered as one among the ocean of works that demonstrate how promising are 2D perovskites in matter of radiation detection performance and related transfer to medical applications. We here provide a short summary of the obtained outcomes, starting with the reasons behind the choice of material and going forward with discussion of achievements and observations that require further analyses.

In principle, 2D layered RP PEA_2PbBr_4 perovskite is selected as active material because of its extremely low dark current, which is mainly due to the intrinsically high band gap and defect tolerance. As reported in sec 3.1, these materials can stand incredibly high applied bias. In the form of thin films on interdigitated pixels, this becomes high stability under even higher values of electric fields while maintaining dark currents below 10pA. As high energy radiation detection -which can be in the form of low fluxes- requires a combination of high responsivity and signal-to-noise ratio, we do believe PEA_2PbBr_4 can be great candidate for the latter to be accomplished at least. Moreover, these films have demonstrated to be stable up to a year after fabrication. This is to be integrated with considerations regarding the possibility of having these materials processed towards flexible, large area devices. This is key in enabling clinically relevant real-time monitoring of ionizing radiation for nuclear medicine and human safety in radiation environments.

Photolithography is here used to achieve high resolution interdigitated pixels on flexible PET, PEN and Kapton substrates, with spacing between fingers down to 5μm. The tunability of pixels size and shape allows for direct applications with high spatial accuracy and precision.

As in sec. 3.1, material properties and potential applications are still under investigation. We here report the first evidence of the spectroscopic power of these thin film devices which can resolve alpha particles from ^{241}Am source down to single pulses. Although preliminary, these results show rise pulses with rise-time values that scale with bias. Further analyses will be carried out to extract pulse spectra from digital shaping amplifier with increased shaping time: as the mobility of 2D perovskite is low compared to their 3D counterparts, longer values of τ are required to achieve higher resolution. Modelling the exact electric field inside the interdigitated pixels is next step for an accurate evaluation of mobility-lifetime product. All this can be of high relevance in forecasting device architectures for neutron detection.

Analyses under laser illumination have demonstrated that a signal is produced in the form of both photocurrent and photovoltage even with light spots at distances up to 8mm from the applied electric field. This has been observed at significantly less distances in the study of perovskite LEDs [228]. In here, a signal is produced with values of photovoltage that reduce to 10% of their original amplitude at 8mm distance. The meaning of this is two-fold: from one side, we speculate that the layered structure of the material coupled with its microcrystallinity allows for waveguides to form beneath the layers, thus leading to photons travelling through the films and producing electron-hole pairs. Deeper analyses will be carried out to investigate the nature of charge carriers' generation through fluorescence microscopy and time-of-flight measurements. On the other hand, as the contribution of the overall material becomes significantly relevant in matter of devices sensitivity, we plan on quantifying this contribution in both thin films and single crystals, as this would provide clear insight on the actual performance of perovskite materials.

PEA_2PbBr_4 thin films are here reported to be incredibly useful for high energy radiation detection. Provided their outstanding performance in detecting X-rays, the results from this work assess their potential as both proton-beam and gamma-rays detectors for medical applications ranging from profile monitoring to targeted radionuclide therapy (TRT). Our devices are demonstrated to detect protons up to 118MeV in energy while exhibiting linearity with dose rate and precise longitudinal energy-loss monitoring. The tests have been conducted inside a human phantom to address proton-therapy as main target of these detectors' primary applications. Furthermore, radiation hardness is also verified for 20Gy continuous irradiation from 200MeV protons. This is crucial to the extension of these devices to actually applicable dosimeters. Finally, transversal real-time monitoring of the proton beam is to be considered of high future impact in matter of speeding up treatments and enhancing precision in the selection of the planning target volume (PTV) to be irradiated. Considerations regarding the dose rate dependence of the response and related calibration curves are still ongoing.

Thin film devices have also been employed for gamma ray detection from pharmaceutical radiotracers. Signals have been recorded as function of activity and compared with medical treatment: the devices provided actual real-time monitoring of injection, extravasation and release of the radiative solution throughout the entire process. Notably, as these experiments account for multielectrode arrays to be employed, they can be coupled with dedicated portable electronics which limit radiation hazard of clinicians and provide higher space resolution during treatment.

Finally, with the advent of space missions of high duration, targeted efforts are now directed towards personal crew dosimetry. IRIS project takes the lead in this direction, proposing preliminary tests on flexible devices onboard a mini, wearable laboratory to be mounted onboard the ISS. This is intended as a prototype of personal dosimeter to be explored in performance and applicability in target environment and extreme conditions: the data collected from ISS launch, scheduled March 2025, will provide insights on material stability and feasibility of detecting low-flux high energy radiation. As this implements state-of-the-art materials, we expect its outcomes to be of high relevance towards the fabrication of high-performance devices and technological transfer to everyday life applications.

APPENDIX 1. ORGANIC SEMICONDUCTING MATERIALS

Over the past decade, organic semiconductors have gained significant attention as a promising class of materials for ionizing radiation detection. Their unique properties offer advantages over traditional inorganic detectors, particularly for applications in medical dosimetry. The potential to fabricate these detectors on flexible, polymeric substrates at low temperatures and through solution-based processes offers a low-cost pathway to large-area, pixelated architectures. Such configurations are critical for real-time, high-resolution applications in radiotherapy and proton therapy, where accurate, scalable, and non-intrusive dosimeters are essential.

One of the most important attributes of organic semiconductors in radiation detection is their tissue equivalency. With low atomic numbers and density, these materials absorb radiation similarly to human tissue, allowing them to mimic energy deposition more closely than inorganic counterparts. This similarity reduces the need for complex calibration procedures and enables direct placement between the radiation source and the patient, preserving the integrity of the radiation beam. Such properties are particularly advantageous in medical contexts, where precise dosimetry is critical for effective treatment delivery[229].

Despite these benefits, a significant challenge lies in their relatively low quantum efficiency for ionizing radiation detection. The commonly adopted strategy to overcome this limitation involves enhancing the photoconductive gain (PG) effect. By carefully tuning electrically active trap states—localized states that can hold charges temporarily within the semiconductor—the photocurrent generated from radiation exposure can be significantly amplified [230]. These trap states, however, do not exhibit sharp energy levels but rather a broad distribution (often Gaussian or exponential), arising from grain boundaries, defects, and material interfaces. Managing and characterizing these traps are crucial for optimizing detector performance, as they directly influence the PG and, consequently, the sensitivity of the detector.

For effective electrical conductivity in a material, a critical requirement is the presence of delocalized electrons capable of absorbing energy from an external field. Organic semiconductors (OSCs), which are primarily carbon-based, achieve this delocalization via π-conjugation networks that connect molecular subunits within the solid. The electronic configuration of carbon ($1s^2 2s^2 2p^2$) reveals that two p-orbital electrons remain available after the s-orbitals are fully occupied, leading to hybridization with neighboring atoms as per valence shell electron pair repulsion theory (VSEPR). In a typical double-bonded carbon system, each carbon atom engages in sp^2 hybridization, creating three coplanar σ-bonds and one perpendicular π-bond with the unhybridized 2p orbital. As π-conjugation extends across a network of carbon atoms, the overlapping 2p orbitals form a delocalized molecular orbital, resulting in closely spaced energy levels.

These energy levels effectively create a band structure analogous to that of inorganic semiconductors, with the highest occupied molecular orbital (HOMO) and the lowest unoccupied molecular orbital (LUMO) acting as the organic analogs of the valence and conduction bands, respectively. However, OSCs differ from inorganic semiconductors in several crucial ways. The primary photoexcited state in OSCs manifests as a bound electron–hole pair (exciton), rather than as free carriers, due to weaker π-orbital interactions.

Consequently, charge transport in OSCs does not follow a typical band transport model; instead, it relies on a hopping mechanism due to the limited π-orbital overlap.

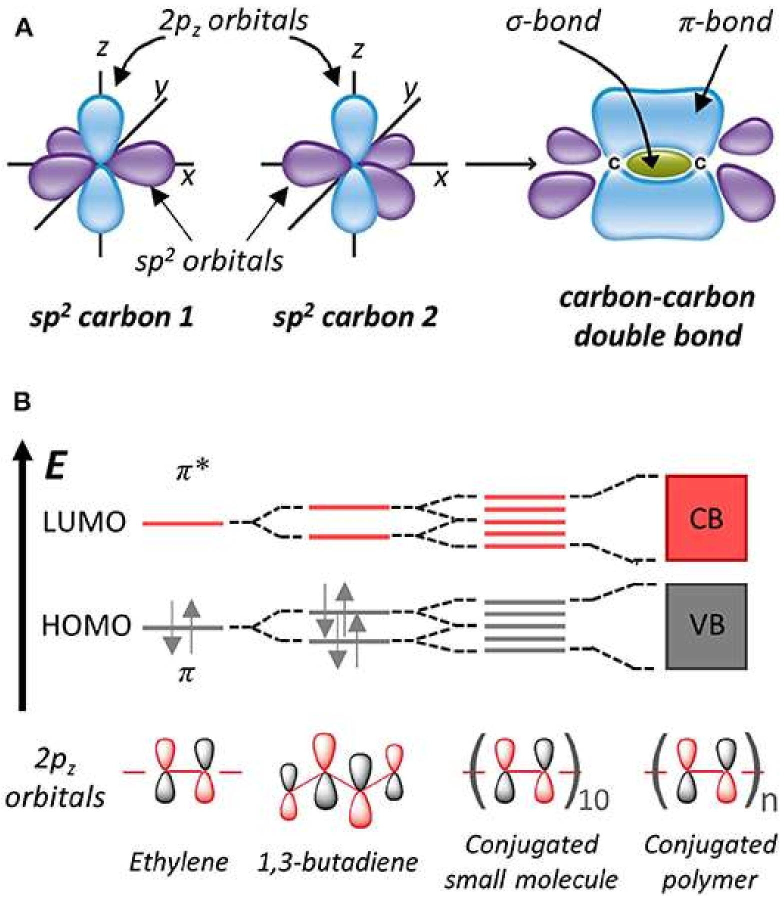

Figure 60 (A) A schematic illustration of hybridized sp^2 and unhybridized 2p$_z$ orbitals combining to form a σ-bond and a π-bond in a carbon–carbon double bond. (B) An extension of molecular orbitals to long conjugated oligomers and polymers indicating the origin of band structures (VB, valence band; CB, conduction band) in organic semiconductors[231].

These characteristics significantly influence the application of OSCs in ionizing radiation detection, whether in indirect detection (high-energy particles interact with a scintillator, producing optical photons that photoexcite the OSC) or direct detection (where high-energy particles interact directly with the OSC substrate).

As an example of organic semiconductor thin films for radiation detection we report the work of Fratelli *et al.* [232] which demonstrated proton direct detection capability of organic thin film (150 nm thick) of microcrystalline bis(triisopropylgermylethynyl)-pentacene (hereafter TIPGe-Pn), deposited by drop casting onto two interdigitated gold electrodes in coplanar architecture. During the irradiation, the sensors were polarized at low voltages (<1 V) to collect the charges generated by anelastic interactions of protons with the electrons of the semiconducting layer. The detector performance was tested under consecutive ON/OFF cycles of exposure to 5-MeV proton beam, tuning the fluence of particles impinging onto the devices in the range between 3.5×10^9 H$^+$ cm^{-2} and 8.7×10^{11} H$^+$ cm^{-2}. Sensitivity of these devices were extracted to be ~5pC Gy^{-1} and Limit of Detection (LOD) of (30 ± 6) cGy s^{-1}.

APPENDIX 2. 2D PEROVSKITE SINGLE CRYSTALS GROWTH

The crystal growth of 2D perovskite single crystals, especially through solution-processable methods, provides finely tunable control over structural and optoelectronic properties, essential for applications in photodetectors and solar cells. Among these methods, slow cooling crystallization, inverse temperature crystallization (ITC), and controlled evaporation temperature (CET) techniques are particularly effective in producing high-quality, large-area crystals with minimal defects.

In the slow cooling method, precursors are dissolved at elevated temperatures, then cooled gradually to promote uniform crystal growth with control over size and thickness. ITC leverages reduced solubility at high temperatures to initiate rapid crystallization, facilitating single-crystal growth with relatively simple equipment. The CET method, on the other hand, carefully controls the evaporation of solvent to achieve a gradual increase in solute concentration, which drives steady nucleation and growth once critical saturation is reached.

As the solvent evaporates, the solution gradually reaches and maintains a saturated state, enabling continuous crystallization, a principle Raghavan et al. [233]employed to grow RP phase $(BA)_2(MA)_{n-1}Pb_nI_{3n+1}$ crystals (for n = 1, 2, and 3) via slow evaporation at constant temperature (SECT), yielding millimeter-sized crystals with high crystallinity and spectral uniformity. Similarly, Liu's group [234][235] refined the controlled evaporation method to grow large $(PEA)_2PbBr_4$ crystals at room temperature. By regulating solvent evaporation rate at a fixed temperature of 23 ± 0.5°C, they achieved centimeter-sized crystals ($\approx 27 \times 11$ mm^2) in a DMF-based precursor solution over 20 days.

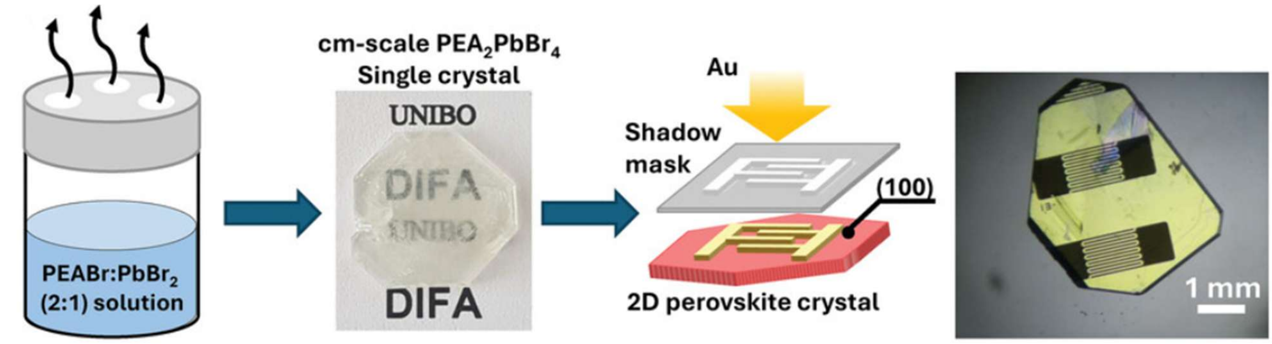

Figure 61 Schematic diagram of the growth process of the controlled-evaporation method of $(PEA)_2PbBr_4$ single crystals (left) Photograph of a transparent, ~27 × 11 mm^2 $(PEA)_2PbBr_4$ single crystal made by the controlled-evaporation method (right). Adapted from[233], [236]

This last method has been employed in here for the fabrication of PEA_2PbBr_4 single crystals of various sizes, with thicknesses ranging between 0.5 and 0.7mm. Photoluminescence tests have been performed at the university of Surrey using a 355nm UV YAG laser. The obtained spectra are reported in fig. 62 for different illumination spots and completed with an absorption spectrum.

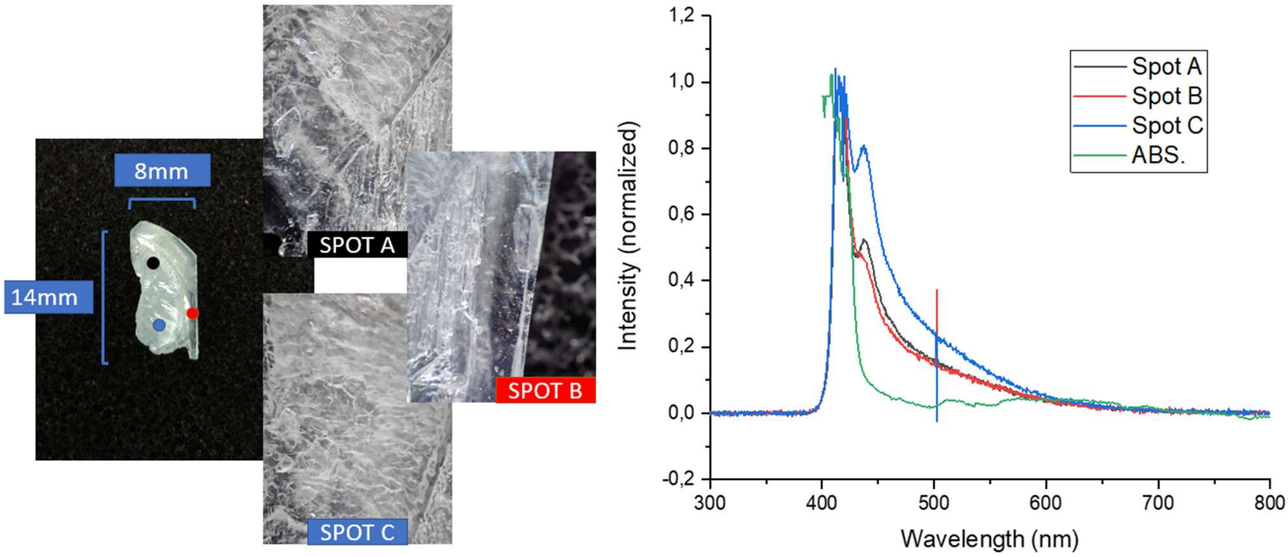

Figure 62   2D perovskite single crystal fabricated through CET method. PL spectra are extracted through illumination with a 355nm YAG laser targeting different crystal spots. A peak is recorded at 410nm and compared with its absorption spectrum, which is consistent with the 2.90eV bandgap reported in sec. 3.1.

In order to have a direct comparison with thin films, five different crystals have been obtained and divided according to the type of metal contacts configurations. Specifically, one group is provided top-bottom contact configuration, with gold pads of 2mm in diameter; the second is instead evaporated interdigitated pixels with 50um in channel length. In principle, this allows to distinguish between bulk and surface effects, on top of providing clear insights on the penetration depth of alpha particles in the material.

REFERENCES

[1] S. Kahmann *et al.*, “Photophysics of Two-Dimensional Perovskites—Learning from Metal Halide Substitution,” *Adv Funct Mater*, vol. 31, no. 46, 2021, doi: 10.1002/adfm.202103778.

[2] J. Jakůbek, “Semiconductor Pixel detectors and their applications in life sciences,” *Journal of Instrumentation*, vol. 4, no. 3, 2009, doi: 10.1088/1748-0221/4/03/P03013.

[3] G. Kakavelakis, M. Gedda, A. Panagiotopoulos, E. Kymakis, T. D. Anthopoulos, and K. Petridis, “Metal Halide Perovskites for High-Energy Radiation Detection,” 2020. doi: 10.1002/advs.202002098.

[4] I. Fratelli *et al.*, “Real-Time Radiation Beam Monitoring by Flexible Perovskite Thin Film Arrays,” *Advanced Science*, Aug. 2024, doi: 10.1002/advs.202401124.

[5] L. Basiricò *et al.*, “Wearable Perovskite Films for On-Line Monitoring of Radiotracers in Nuclear Medicine,” *Adv Mater Technol*, Aug. 2024, doi: 10.1002/admt.202401111.

[6] M. Rizzi, M. D’Aloia, and B. Castagnolo, “Semiconductor detectors and principles of radiation-matter interaction,” *Journal of Applied Sciences*, vol. 10, no. 23, 2010, doi: 10.3923/jas.2010.3141.3155.

[7] A. Del Guerra and D. Panetta, “Radiation measurement,” in *Modern Applications*, vol. 2, 2022. doi: 10.1515/9783110742701-001.

[8] S. Matsuhashi and N. S. Ishioka, “Medical Utilization of Radiation,” 2018, pp. 293–335. doi: 10.1007/978-981-10-7350-2_17.

[9] A. V. Wegst, “ Radiation Detection and Measurement , by G. F. Knoll ,” *Med Phys*, vol. 7, no. 4, 1980, doi: 10.1118/1.594739.

[10] J. D. COCKCROFT, “Experimental Nuclear Physics,” *Nature*, vol. 175, no. 4445, 1955, doi: 10.1038/175053a0.

[11] B. Gottschalk, “Physics of Proton Interactions in Matter,” in *Proton Therapy Physics*, 2016. doi: 10.1201/b22053-3.

[12] M. L. Maiello, “Physics & Engineering of Radiation Detection,” *Health Phys*, vol. 94, no. 2, 2008, doi: 10.1097/01.hp.0000295554.27735.22.

[13] G. F. Knoll and H. W. Kraner, “Radiation Detection and Measurement,” 1981. doi: 10.1109/PROC.1981.12016.

[14] H. Bichsel and H. Schindler, “The Interaction of Radiation with Matter,” in *Particle Physics Reference Library*, Cham: Springer International Publishing, 2020, pp. 5–44. doi: 10.1007/978-3-030-35318-6_2.

[15] J. H. H. S. M. S. J. C. J. S. C. R. S. D. S. Z. and K. O. M.J. Berger, “NIST Standard Reference Database 8 (XGAM),” *NIST,PML,RADIATIONPHYISCSDIVISION*.

[16] D. W. Aitken, B. L. Beron, G. Yenicay, and H. R. Zulliger, “The fluorescent response of NaI(Tl), CsI(Tl), CsI(Na) and CaF2(Eu) to x-rays and low energy gamma rays,” *IEEE Trans Nucl Sci*, vol. NS-14, no. 1, 1967, doi: 10.1109/TNS.1967.4324457.

[17] R. F. Barth, J. A. Coderre, M. G. H. Vicente, and T. E. Blue, “Boron neutron capture therapy of cancer: Current status and future prospects,” 2005. doi: 10.1158/1078-0432.CCR-05-0035.

[18] "Scintillation Detectors," in *Essentials of Nuclear Medicine Physics, Instrumentation, and Radiation Biology: Fourth Edition*, 2021. doi: 10.1002/9781119621027.ch5.

[19] S. N. Ahmed, "Gas-filled detectors," in *Physics and Engineering of Radiation Detection*, 2015. doi: 10.1016/b978-0-12-801363-2.00003-6.

[20] M. S. Rahman *et al.*, "Measurements of scintillation light yield non-proportionality in NaI(Tl) detector," *Journal of Nuclear Engineering and Radiation Science*, vol. 7, no. 4, 2021, doi: 10.1115/1.4050932.

[21] M. Moszyński, J. Zalipska, M. Balcerzyk, M. Kapusta, W. Mengesha, and J. D. Valentine, "Intrinsic energy resolution of NaI(Tl)1," *Nucl Instrum Methods Phys Res A*, vol. 484, no. 1–3, 2002, doi: 10.1016/S0168-9002(01)01964-7.

[22] M. Laval *et al.*, "Barium fluoride - Inorganic scintillator for subnanosecond timing," *Nuclear Instruments and Methods In Physics Research*, vol. 206, no. 1–2, 1983, doi: 10.1016/0167-5087(83)91254-1.

[23] O. D. I. Moseley, T. A. S. Doherty, R. Parmee, M. Anaya, and S. D. Stranks, "Halide perovskites scintillators: unique promise and current limitations," 2021. doi: 10.1039/d1tc01595h.

[24] A. Jana *et al.*, "Perovskite: Scintillators, direct detectors, and X-ray imagers," 2022. doi: 10.1016/j.mattod.2022.04.009.

[25] Y. Zhou, J. Chen, O. M. Bakr, and O. F. Mohammed, "Metal Halide Perovskites for X-ray Imaging Scintillators and Detectors," 2021. doi: 10.1021/acsenergylett.0c02430.

[26] Q. Chen *et al.*, "All-inorganic perovskite nanocrystal scintillators," *Nature*, vol. 561, no. 7721, 2018, doi: 10.1038/s41586-018-0451-1.

[27] M. Z. Kabir and S. Kasap, "Photoconductors for X-Ray Image Detectors," 2017, pp. 1–1. doi: 10.1007/978-3-319-48933-9_45.

[28] W. Zhao and J. A. Rowlands, "X-ray imaging using amorphous selenium: Feasibility of a flat panel self-scanned detector for digital radiology," *Med Phys*, vol. 22, no. 10, 1995, doi: 10.1118/1.597628.

[29] X. Li, A. E. Chavarria, S. Bogdanovich, C. Galbiati, A. Piers, and B. Polischuk, "Measurement of the ionization response of amorphous selenium with 122 keV γ rays," *Journal of Instrumentation*, vol. 16, no. 6, 2021, doi: 10.1088/1748-0221/16/06/P06018.

[30] S. Abbaszadeh and C. S. Levin, "Direct conversion semiconductor detectors for radiation imaging," in *Semiconductor Radiation Detectors: Technology and Applications*, 2017. doi: 10.1201/9781315200729.

[31] M. Z. Kabir and S. O. Kasap, "Charge collection and absorption-limited sensitivity of x-ray photoconductors: Applications to a-Se and HgI2," *Appl Phys Lett*, vol. 80, no. 9, 2002, doi: 10.1063/1.1454213.

[32] M. Z. Kabir, S. O. Kasap, W. Zhao, and J. A. Rowlands, "Direct conversion X-ray sensors: Sensitivity, DQE and MTF," in *IEE Proceedings: Circuits, Devices and Systems*, 2003. doi: 10.1049/ip-cds:20030663.

[33] S. Tie *et al.*, "Robust Fabrication of Hybrid Lead-Free Perovskite Pellets for Stable X-ray Detectors with Low Detection Limit," *Advanced Materials*, vol. 32, no. 31, 2020, doi: 10.1002/adma.202001981.

[34] A. Burdyko, M. Caccia, A. Giaz, R. Santoro, and G. Tomaciello, “Design and commissioning of a Silicon Photomultiplier-based dosimeter for Low Dose Rate (LDR) oncological brachytherapy,” *Journal of Instrumentation*, vol. 19, no. 3, 2024, doi: 10.1088/1748-0221/19/03/C03025.

[35] C. C. Bueno *et al.*, “Performance Characterization of Dosimeters Based on Radiation-Hard Silicon Diodes in Gamma Radiation Processing,” *Frontiers in Sensors*, vol. 3, 2022, doi: 10.3389/fsens.2022.770482.

[36] J. B. Chung *et al.*, “Dosimetrie characteristics of standard and micro MOSFET dosimeters as in-vivo dosimeter for clinical electron beam,” *Journal of the Korean Physical Society*, vol. 55, no. 6, 2009, doi: 10.3938/jkps.55.2566.

[37] J. H. Koivisto, J. E. Wolff, T. Kiljunen, D. Schulze, and M. Kortesniemi, “Characterization of MOSFET dosimeters for low-dose measurements in maxillofacial anthropomorphic phantoms,” *J Appl Clin Med Phys*, vol. 16, no. 4, 2015, doi: 10.1120/jacmp.v16i4.5433.

[38] S. F. Kry *et al.*, “AAPM TG 191: Clinical use of luminescent dosimeters: TLDs and OSLDs,” *Med Phys*, vol. 47, no. 2, 2020, doi: 10.1002/mp.13839.

[39] E. Damulira, M. N. S. Yusoff, A. F. Omar, and N. H. M. Taib, “A review: Photonic devices used for dosimetry in medical radiation,” 2019. doi: 10.3390/s19102226.

[40] P. Casolaro, “Radiochromic films for the two-dimensional dose distribution assessment,” 2021. doi: 10.3390/app11052132.

[41] I. Méndez, J. J. Rovira-Escutia, and B. Casar, “A protocol for accurate radiochromic film dosimetry using Radiochromic.com,” *Radiol Oncol*, vol. 55, no. 3, 2021, doi: 10.2478/raon-2021-0034.

[42] G. Bassi *et al.*, “Calibration of diamond detectors for dosimetry in beam-loss monitoring,” *Nucl Instrum Methods Phys Res A*, vol. 1004, 2021, doi: 10.1016/j.nima.2021.165383.

[43] C. Talamonti, K. Kanxheri, S. Pallotta, and L. Servoli, “Diamond Detectors for Radiotherapy X-Ray Small Beam Dosimetry,” 2021. doi: 10.3389/fphy.2021.632299.

[44] B. Lee *et al.*, “Feasibility of ultra-thin fiber-optic dosimeters for radiotherapy dosimetry,” *Sensors (Switzerland)*, vol. 15, no. 11, 2015, doi: 10.3390/s151129003.

[45] N. Lynch, T. Monajemi, and J. L. Robar, “Characterization of novel 3D printed plastic scintillation dosimeters,” *Biomed Phys Eng Express*, vol. 6, no. 5, 2020, doi: 10.1088/2057-1976/aba880.

[46] U. O’Connor *et al.*, “Recommendations for the use of active personal dosemeters (APDs) in interventional workplaces in hospitals,” 2021. doi: 10.1016/j.ejmp.2021.05.015.

[47] F. Araki, T. Ohno, and S. Umeno, “Ionization chamber dosimetry based on 60Co absorbed dose to water calibration for diagnostic kilovoltage x-ray beams,” *Phys Med Biol*, vol. 63, no. 18, 2018, doi: 10.1088/1361-6560/aad9c0.

[48] K. Lin *et al.*, “Perovskite light-emitting diodes with external quantum efficiency exceeding 20 per cent,” *Nature*, vol. 562, no. 7726, 2018, doi: 10.1038/s41586-018-0575-3.

[49] N. Suresh Kumar and K. Chandra Babu Naidu, “A review on perovskite solar cells (PSCs), materials and applications,” *Journal of Materiomics*, vol. 7, no. 5, 2021, doi: 10.1016/j.jmat.2021.04.002.

[50] Z. K. Tan *et al.*, “Bright light-emitting diodes based on organometal halide perovskite,” *Nat Nanotechnol*, vol. 9, no. 9, 2014, doi: 10.1038/nnano.2014.149.

[51] H. Wang *et al.*, “A Review of Perovskite-Based Photodetectors and Their Applications,” 2022. doi: 10.3390/nano12244390.

[52] B. W. Wessels, “Lead halide perovskites for radiation detectors: Perspectives,” *J Appl Phys*, vol. 134, no. 13, 2023, doi: 10.1063/5.0141594.

[53] G. Meng, Y. Ye, L. Fan, S. Wang, V. Gnatyuk, and X. Fang, “Recent Progress of Halide Perovskite Radiation Detector Materials,” 2020. doi: 10.15541/jim20190394.

[54] F. Liu *et al.*, “Recent Progress in Halide Perovskite Radiation Detectors for Gamma-Ray Spectroscopy,” 2022. doi: 10.1021/acsenergylett.2c00031.

[55] Y. He, I. Hadar, and M. G. Kanatzidis, “Detecting ionizing radiation using halide perovskite semiconductors processed through solution and alternative methods,” Jan. 01, 2022, *Nature Research*. doi: 10.1038/s41566-021-00909-5.

[56] S. H. Bennett, “Charge Transport of Lead Halide Perovskites for Solid State Radiation Detectors written by.”

[57] H. Zhang, M. K. Nazeeruddin, and W. C. H. Choy, “Perovskite Photovoltaics: The Significant Role of Ligands in Film Formation, Passivation, and Stability,” 2019. doi: 10.1002/adma.201805702.

[58] M. Petrović, K. Rogdakis, and E. Kymakis, “Beneficial impact of materials with reduced dimensionality on the stability of perovskite-based photovoltaics,” *JPhys Energy*, vol. 1, no. 4, 2019, doi: 10.1088/2515-7655/ab3585.

[59] R. L. Z. Hoye, J. Hidalgo, R. A. Jagt, J. P. Correa-Baena, T. Fix, and J. L. MacManus-Driscoll, “The Role of Dimensionality on the Optoelectronic Properties of Oxide and Halide Perovskites, and their Halide Derivatives,” 2022. doi: 10.1002/aenm.202100499.

[60] W. Ware, T. Wright, A. Davita, E. Danilov, and B. Gautam, “Impact of dimensionality on optoelectronic properties of hybrid perovskites,” *International Journal of Photoenergy*, vol. 2021, 2021, doi: 10.1155/2021/8822703.

[61] E. A. Katz, “Perovskite: Name Puzzle and German-Russian Odyssey of Discovery,” 2020. doi: 10.1002/hlca.202000061.

[62] C. Li, X. Lu, W. Ding, L. Feng, Y. Gao, and Z. Guo, “Formability of ABX 3 (X = F, Cl, Br, I) halide perovskites,” *Acta Crystallogr B*, vol. 64, no. 6, 2008, doi: 10.1107/S0108768108032734.

[63] A. E. Fedorovskiy, N. A. Drigo, and M. K. Nazeeruddin, “The Role of Goldschmidt’s Tolerance Factor in the Formation of A2BX6 Double Halide Perovskites and its Optimal Range,” *Small Methods*, vol. 4, no. 5, 2020, doi: 10.1002/smtd.201900426.

[64] Z. Li, M. Yang, J. S. Park, S. H. Wei, J. J. Berry, and K. Zhu, “Stabilizing Perovskite Structures by Tuning Tolerance Factor: Formation of Formamidinium and Cesium Lead Iodide Solid-State Alloys,” *Chemistry of Materials*, vol. 28, no. 1, 2016, doi: 10.1021/acs.chemmater.5b04107.

[65] C. C. Stoumpos and M. G. Kanatzidis, “The Renaissance of Halide Perovskites and Their Evolution as Emerging Semiconductors,” *Acc Chem Res*, vol. 48, no. 10, pp. 2791–2802, Oct. 2015, doi: 10.1021/acs.accounts.5b00229.

[66] T. Oku, “Crystal structures of perovskite halide compounds used for solar cells,” 2020. doi: 10.1515/rams-2020-0015.

[67] J. J. Yoo *et al.*, “Efficient perovskite solar cells via improved carrier management,” *Nature*, vol. 590, no. 7847, 2021, doi: 10.1038/s41586-021-03285-w.

[68] D. Shi *et al.*, “Low trap-state density and long carrier diffusion in organolead trihalide perovskite single crystals,” *Science (1979)*, vol. 347, no. 6221, 2015, doi: 10.1126/science.aaa2725.

[69] C. M. Wolff, P. Caprioglio, M. Stolterfoht, and D. Neher, “Nonradiative Recombination in Perovskite Solar Cells: The Role of Interfaces,” *Advanced Materials*, vol. 31, no. 52, 2019, doi: 10.1002/adma.201902762.

[70] X. Zhang, M. E. Turiansky, J. X. Shen, and C. G. Van De Walle, “Defect tolerance in halide perovskites: A first-principles perspective,” *J Appl Phys*, vol. 131, no. 9, 2022, doi: 10.1063/5.0083686.

[71] E. L. Unger, L. Kegelmann, K. Suchan, D. Sörell, L. Korte, and S. Albrecht, “Roadmap and roadblocks for the band gap tunability of metal halide perovskites,” *J Mater Chem A Mater*, vol. 5, no. 23, 2017, doi: 10.1039/c7ta00404d.

[72] S. Wieghold and L. Nienhausi, “Engineering 3D perovskites for photon interconversion applications,” *PLoS One*, vol. 15, no. 3, 2020, doi: 10.1371/journal.pone.0230299.

[73] H. Zhang, T. Ji, J. He, L. Shi, G. Li, and Y. Cui, “Fast-Response Vertical-Structure Two-Dimensional Perovskite Photodetector,” *Laser and Optoelectronics Progress*, vol. 61, no. 5, 2024, doi: 10.3788/LOP230924.

[74] N. Leupold and F. Panzer, “Recent Advances and Perspectives on Powder-Based Halide Perovskite Film Processing,” *Adv Funct Mater*, vol. 31, no. 14, 2021, doi: 10.1002/adfm.202007350.

[75] X. Zhang *et al.*, “Review on flexible perovskite photodetector: processing and applications,” 2023. doi: 10.1007/s11465-023-0749-z.

[76] J. Y. Huang, Y. W. Yang, W. H. Hsu, E. W. Chang, M. H. Chen, and Y. R. Wu, “Influences of dielectric constant and scan rate on hysteresis effect in perovskite solar cell with simulation and experimental analyses,” *Sci Rep*, vol. 12, no. 1, 2022, doi: 10.1038/s41598-022-11899-x.

[77] H. Su *et al.*, “Surface Energy Engineering of Buried Interface for Highly Stable Perovskite Solar Cells with Efficiency Over 25%,” *Advanced Materials*, vol. 36, no. 2, 2024, doi: 10.1002/adma.202306724.

[78] N. K. Elangovan, R. Kannadasan, B. B. Beenarani, M. H. Alsharif, M. K. Kim, and Z. Hasan Inamul, “Recent developments in perovskite materials, fabrication techniques, band gap engineering, and the stability of perovskite solar cells,” *Energy Reports*, vol. 11, 2024, doi: 10.1016/j.egyr.2023.12.068.

[79] A. A. Goje *et al.*, “Review of flexible perovskite solar cells for indoor and outdoor applications,” *Mater Renew Sustain Energy*, vol. 13, no. 1, 2024, doi: 10.1007/s40243-024-00257-8.

[80] J. A. Castañeda *et al.*, “Efficient Biexciton Interaction in Perovskite Quantum Dots under Weak and Strong Confinement,” *ACS Nano*, vol. 10, no. 9, 2016, doi: 10.1021/acsnano.6b03908.

[81] R. Su *et al.*, “Dielectric screening in perovskite photovoltaics,” *Nat Commun*, vol. 12, no. 1, 2021, doi: 10.1038/s41467-021-22783-z.

[82] X. Wu, M. T. Trinh, and X. Y. Zhu, “Excitonic Many-Body Interactions in Two-Dimensional Lead Iodide Perovskite Quantum Wells,” *Journal of Physical Chemistry C*, vol. 119, no. 26, 2015, doi: 10.1021/acs.jpcc.5b00148.

[83] K. R. Hansen *et al.*, “Low Exciton Binding Energies and Localized Exciton–Polaron States in 2D Tin Halide Perovskites,” *Adv Opt Mater*, vol. 10, no. 9, 2022, doi: 10.1002/adom.202102698.

[84] M. Baranowski and P. Plochocka, “Excitons in Metal-Halide Perovskites,” 2020. doi: 10.1002/aenm.201903659.

[85] A. Forde, S. Tretiak, and A. J. Neukirch, “Dielectric Screening and Charge-Transfer in 2D Lead-Halide Perovskites for Reduced Exciton Binding Energies,” *Nano Lett*, vol. 23, no. 24, 2023, doi: 10.1021/acs.nanolett.3c03320.

[86] P. C. Sercel, J. L. Lyons, D. Wickramaratne, R. Vaxenburg, N. Bernstein, and A. L. Efros, “Exciton Fine Structure in Perovskite Nanocrystals,” *Nano Lett*, vol. 19, no. 6, 2019, doi: 10.1021/acs.nanolett.9b01467.

[87] T. Ishihara, “Optical properties of PbI-based perovskite structures,” *J Lumin*, vol. 60–61, no. C, 1994, doi: 10.1016/0022-2313(94)90145-7.

[88] S. J. Yang *et al.*, “Two-Factor Phase Separations in Mixed-Halide Quasi-2D Perovskite LEDs: Dimensionality and Halide Segregations,” *ACS Energy Lett*, vol. 8, no. 9, 2023, doi: 10.1021/acsenergylett.3c01009.

[89] D. Zhang *et al.*, “Comprehensive Passivation for High-Performance Quasi-2D Perovskite LEDs,” *Small*, vol. 19, no. 11, 2023, doi: 10.1002/smll.202206927.

[90] G. Wu, R. Liang, Z. Zhang, M. Ge, G. Xing, and G. Sun, “2D Hybrid Halide Perovskites: Structure, Properties, and Applications in Solar Cells,” 2021. doi: 10.1002/smll.202103514.

[91] J. Di, J. Chang, and S. Liu, “Recent progress of two-dimensional lead halide perovskite single crystals: Crystal growth, physical properties, and device applications,” 2020. doi: 10.1002/eom2.12036.

[92] T. L. Leung, I. Ahmad, A. A. Syed, A. M. C. Ng, J. Popović, and A. B. Djurišić, “Stability of 2D and quasi-2D perovskite materials and devices,” *Commun Mater*, vol. 3, no. 1, 2022, doi: 10.1038/s43246-022-00285-9.

[93] G. Grancini and M. K. Nazeeruddin, “Dimensional tailoring of hybrid perovskites for photovoltaics,” 2019. doi: 10.1038/s41578-018-0065-0.

[94] Q. Ou *et al.*, “Band structure engineering in metal halide perovskite nanostructures for optoelectronic applications,” *Nano Materials Science*, vol. 1, no. 4, 2019, doi: 10.1016/j.nanoms.2019.10.004.

[95] S. K. Sharma *et al.*, “Reversible Dimensionality Tuning of Hybrid Perovskites with Humidity: Visualization and Application to Stable Solar Cells,” *Chemistry of Materials*, vol. 31, no. 9, 2019, doi: 10.1021/acs.chemmater.8b04115.

[96] M.-H. Tremblay, J. Bacsa, B. Zhao, F. Pulvirenti, S. Barlow, and S. R. Marder, “Structures of $(4\text{-Y-}C_6H_4CH_2NH_3)_2PbI_4$ {Y = H, F, Cl, Br, I}: Tuning of Hybrid Organic Inorganic Perovskite Structures from Ruddlesden–Popper to Dion–Jacobson Limits,” *Chemistry of Materials*, vol. 31, no. 16, pp. 6145–6153, Aug. 2019, doi: 10.1021/acs.chemmater.9b01564.

[97] I.-H. Park *et al.*, "Ferroelectricity and Rashba Effect in a Two-Dimensional Dion-Jacobson Hybrid Organic–Inorganic Perovskite," *J Am Chem Soc*, vol. 141, no. 40, pp. 15972–15976, Oct. 2019, doi: 10.1021/jacs.9b07776.

[98] F. Zhang, H. Lu, J. Tong, J. J. Berry, M. C. Beard, and K. Zhu, "Advances in two-dimensional organic–inorganic hybrid perovskites," *Energy Environ Sci*, vol. 13, no. 4, pp. 1154–1186, 2020, doi: 10.1039/C9EE03757H.

[99] P. Huang, S. Kazim, M. Wang, and S. Ahmad, "Toward Phase Stability: Dion–Jacobson Layered Perovskite for Solar Cells," *ACS Energy Lett*, vol. 4, no. 12, pp. 2960–2974, Dec. 2019, doi: 10.1021/acsenergylett.9b02063.

[100] D. Ghosh *et al.*, "Charge carrier dynamics in two-dimensional hybrid perovskites: Dion–Jacobson *vs.* Ruddlesden–Popper phases," *J Mater Chem A Mater*, vol. 8, no. 42, pp. 22009–22022, 2020, doi: 10.1039/D0TA07205B.

[101] Z. Xiao, W. Meng, J. Wang, D. B. Mitzi, and Y. Yan, "Searching for promising new perovskite-based photovoltaic absorbers: the importance of electronic dimensionality," *Mater Horiz*, vol. 4, no. 2, pp. 206–216, 2017, doi: 10.1039/C6MH00519E.

[102] L. Etgar, "The merit of perovskite's dimensionality; can this replace the 3D halide perovskite?," *Energy Environ Sci*, vol. 11, no. 2, pp. 234–242, 2018, doi: 10.1039/C7EE03397D.

[103] H. Tsai *et al.*, "High-efficiency two-dimensional Ruddlesden–Popper perovskite solar cells," *Nature*, vol. 536, no. 7616, pp. 312–316, Aug. 2016, doi: 10.1038/nature18306.

[104] A. Z. Chen *et al.*, "Origin of vertical orientation in two-dimensional metal halide perovskites and its effect on photovoltaic performance," *Nat Commun*, vol. 9, no. 1, p. 1336, Apr. 2018, doi: 10.1038/s41467-018-03757-0.

[105] I. C. Smith, E. T. Hoke, D. Solis-Ibarra, M. D. McGehee, and H. I. Karunadasa, "A Layered Hybrid Perovskite Solar-Cell Absorber with Enhanced Moisture Stability," *Angewandte Chemie*, vol. 126, no. 42, pp. 11414–11417, Oct. 2014, doi: 10.1002/ange.201406466.

[106] P. Da:, M. Verdi, M. Cicoli, B. Fraboni, and A. Ciavatti, "HYBRID LEAD-HALIDE PEROVSKITES AS NOVEL MATERIALS FOR THIN FILM DIRECT AND FLEXIBLE IONIZING RADIATION DETECTORS Coordinatore Dottorato Supervisore Co-Supervisore."

[107] J.-F. Liao, H.-S. Rao, B.-X. Chen, D.-B. Kuang, and C.-Y. Su, "Dimension engineering on cesium lead iodide for efficient and stable perovskite solar cells," *J Mater Chem A Mater*, vol. 5, no. 5, pp. 2066–2072, 2017, doi: 10.1039/C6TA09582H.

[108] Y. Shang *et al.*, "Highly stable hybrid perovskite light-emitting diodes based on Dion-Jacobson structure," *Sci Adv*, vol. 5, no. 8, Aug. 2019, doi: 10.1126/sciadv.aaw8072.

[109] S. R. Kumavat, G. Sachdeva, Y. Sonvane, and S. K. Gupta, "Structural and compositional properties of 2D CH3NH3PbI3 hybrid halide perovskite: a DFT study," *RSC Adv*, vol. 12, no. 40, 2022, doi: 10.1039/d2ra02874c.

[110] L. Mao *et al.*, "Hybrid Dion-Jacobson 2D Lead Iodide Perovskites," *J Am Chem Soc*, vol. 140, no. 10, 2018, doi: 10.1021/jacs.8b00542.

[111] C. C. Stoumpos *et al.*, "Ruddlesden-Popper Hybrid Lead Iodide Perovskite 2D Homologous Semiconductors," *Chemistry of Materials*, vol. 28, no. 8, 2016, doi: 10.1021/acs.chemmater.6b00847.

[112] X. Liu *et al.*, “Shallow defects levels and extract detrapped charges to stabilize highly efficient and hysteresis-free perovskite photovoltaic devices,” *Nano Energy*, vol. 71, 2020, doi: 10.1016/j.nanoen.2020.104556.

[113] D. Marongiu, M. Saba, F. Quochi, A. Mura, and G. Bongiovanni, “The role of excitons in 3D and 2D lead halide perovskites,” 2019. doi: 10.1039/c9tc04292j.

[114] C. M. Mauck and W. A. Tisdale, “Excitons in 2D Organic–Inorganic Halide Perovskites,” 2019. doi: 10.1016/j.trechm.2019.04.003.

[115] W. Tao, C. Zhang, Q. Zhou, Y. Zhao, and H. Zhu, “Momentarily trapped exciton polaron in two-dimensional lead halide perovskites,” *Nat Commun*, vol. 12, no. 1, 2021, doi: 10.1038/s41467-021-21721-3.

[116] C. G. Bailey *et al.*, “Influence of Organic Spacer Cation on Dark Excitons in 2D Perovskites,” *Adv Funct Mater*, vol. 34, no. 6, 2024, doi: 10.1002/adfm.202308095.

[117] J. C. Blancon *et al.*, “Scaling law for excitons in 2D perovskite quantum wells,” *Nat Commun*, vol. 9, no. 1, 2018, doi: 10.1038/s41467-018-04659-x.

[118] J. Li, J. Ma, X. Cheng, Z. Liu, Y. Chen, and D. Li, “Anisotropy of Excitons in Two-Dimensional Perovskite Crystals,” *ACS Nano*, vol. 14, no. 2, 2020, doi: 10.1021/acsnano.9b08975.

[119] M. Seitz *et al.*, “Exciton diffusion in two-dimensional metal-halide perovskites,” *Nat Commun*, vol. 11, no. 1, 2020, doi: 10.1038/s41467-020-15882-w.

[120] Z. Yang *et al.*, “Unraveling the Exciton Binding Energy and the Dielectric Constant in Single-Crystal Methylammonium Lead Triiodide Perovskite,” *J Phys Chem Lett*, vol. 8, no. 8, pp. 1851–1855, Apr. 2017, doi: 10.1021/acs.jpclett.7b00524.

[121] J. Zhang, X. Zhu, M. Wang, and B. Hu, “Establishing charge-transfer excitons in 2D perovskite heterostructures,” *Nat Commun*, vol. 11, no. 1, p. 2618, May 2020, doi: 10.1038/s41467-020-16415-1.

[122] L. Y. Huang and W. R. L. Lambrecht, “Electronic band structure, phonons, and exciton binding energies of halide perovskites CsSnCl3, CsSnBr3, and CsSnI3,” *Phys Rev B Condens Matter Mater Phys*, vol. 88, no. 16, 2013, doi: 10.1103/PhysRevB.88.165203.

[123] A. M. Askar and K. Shankar, “Exciton binding energy in organic-inorganic tri-halide perovskites,” 2016. doi: 10.1166/jnn.2016.12936.

[124] J. V. Passarelli *et al.*, “Tunable exciton binding energy in 2D hybrid layered perovskites through donor–acceptor interactions within the organic layer,” *Nat Chem*, vol. 12, no. 8, 2020, doi: 10.1038/s41557-020-0488-2.

[125] J. Cho, J. T. DuBose, and P. V. Kamat, “Charge Carrier Recombination Dynamics of Two-Dimensional Lead Halide Perovskites,” *J Phys Chem Lett*, vol. 11, no. 7, pp. 2570–2576, Apr. 2020, doi: 10.1021/acs.jpclett.0c00392.

[126] D. Garrot *et al.*, “Exciton-Exciton Annihilation in Two-dimensional Halide Perovskites,” 2019. doi: 10.29363/nanoge.ngfm.2019.246.

[127] A. Burgos-Caminal, E. Socie, M. E. F. Bouduban, and J.-E. Moser, “Exciton-Carrier Dynamics in 2D Perovskites,” *J. Phys. Chem. Lett.*, vol. 11, no. 18, 2020.

[128] G. Delport *et al.*, "Exciton-exciton annihilation in two-dimensional halide perovskites at room temperature," *Journal of Physical Chemistry Letters*, vol. 10, no. 17, 2019, doi: 10.1021/acs.jpclett.9b01595.

[129] M. C. Gélvez-Rueda, W. T. M. Van Gompel, R. Herckens, L. Lutsen, D. Vanderzande, and F. C. Grozema, "Inducing Charge Separation in Solid-State Two-Dimensional Hybrid Perovskites through the Incorporation of Organic Charge-Transfer Complexes," *Journal of Physical Chemistry Letters*, vol. 11, no. 3, 2020, doi: 10.1021/acs.jpclett.9b03746.

[130] D. Bartesaghi *et al.*, "Charge Carrier Dynamics in Cs2AgBiBr6 Double Perovskite," *Journal of Physical Chemistry C*, vol. 122, no. 9, 2018, doi: 10.1021/acs.jpcc.8b00572.

[131] M. C. Gélvez-Rueda, M. B. Fridriksson, R. K. Dubey, W. F. Jager, W. van der Stam, and F. C. Grozema, "Overcoming the exciton binding energy in two-dimensional perovskite nanoplatelets by attachment of conjugated organic chromophores," *Nat Commun*, vol. 11, no. 1, 2020, doi: 10.1038/s41467-020-15869-7.

[132] S. Ahmad *et al.*, "Dion-Jacobson Phase 2D Layered Perovskites for Solar Cells with Ultrahigh Stability," *Joule*, vol. 3, no. 3, pp. 794–806, Mar. 2019, doi: 10.1016/j.joule.2018.11.026.

[133] Y. Li *et al.*, "Bifunctional Organic Spacers for Formamidinium-Based Hybrid Dion–Jacobson Two-Dimensional Perovskite Solar Cells," *Nano Lett*, vol. 19, no. 1, pp. 150–157, Jan. 2019, doi: 10.1021/acs.nanolett.8b03552.

[134] Z. Xu *et al.*, "CsPbI3-Based Phase-Stable 2D Ruddlesden-Popper Perovskites for Efficient Solar Cells," *Nano Lett*, vol. 22, no. 7, 2022, doi: 10.1021/acs.nanolett.2c00002.

[135] M. Shao *et al.*, "Over 21% Efficiency Stable 2D Perovskite Solar Cells," *Advanced Materials*, vol. 34, no. 1, 2022, doi: 10.1002/adma.202107211.

[136] R. Liu, X. Hu, M. Xu, H. Ren, and H. Yu, "Layered Low-Dimensional Ruddlesden-Popper and Dion-Jacobson Perovskites: From Material Properties to Photovoltaic Device Performance," 2023. doi: 10.1002/cssc.202300736.

[137] Z. Liu, L. Wang, H. Zhao, Y. Wei, X. Xie, and P. Chen, "High-performance Ruddlesden-Popper two-dimensional perovskite solar cells using integrated electron transport materials of tin oxide and indacenodithiophene," *Mater Adv*, vol. 4, no. 16, 2023, doi: 10.1039/d3ma00221g.

[138] Q. Fu, M. Chen, Q. Li, H. Liu, R. Wang, and Y. Liu, "Selenophene-Based 2D Ruddlesden-Popper Perovskite Solar Cells with an Efficiency Exceeding 19%," *J Am Chem Soc*, vol. 145, no. 39, 2023, doi: 10.1021/jacs.3c08604.

[139] Y. Zhang *et al.*, "Highly Efficient and Stable FA-Based Quasi-2D Ruddlesden–Popper Perovskite Solar Cells by the Incorporation of β-Fluorophenylethanamine Cations," *Advanced Materials*, vol. 35, no. 17, 2023, doi: 10.1002/adma.202210836.

[140] M. Chen *et al.*, "Crystal Growth Regulation of Ruddlesden–Popper Perovskites via Self-Assembly of Semiconductor Spacers for Efficient Solar Cells," *Angewandte Chemie - International Edition*, vol. 63, no. 3, 2024, doi: 10.1002/anie.202315943.

[141] C. M. M. Soe *et al.*, "Understanding Film Formation Morphology and Orientation in High Member 2D Ruddlesden–Popper Perovskites for High-Efficiency Solar Cells," *Adv Energy Mater*, vol. 8, no. 1, 2018, doi: 10.1002/aenm.201700979.

[142] C. M. M. Soe *et al.*, “New Type of 2D Perovskites with Alternating Cations in the Interlayer Space, (C(NH2)3)(CH3NH3)nPbnI3n+1: Structure, Properties, and Photovoltaic Performance,” *J Am Chem Soc*, vol. 139, no. 45, 2017, doi: 10.1021/jacs.7b09096.

[143] W. Yan, B. Li, B. Duan, Y. Song, G. Song, and J. Ma, “Research Progress of Performance of Two-dimensional Organic-inorganic Perovskite Scintillator,” *Faguang Xuebao/Chinese Journal of Luminescence*, vol. 45, no. 1, 2024, doi: 10.37188/CJL.20230270.

[144] J. Ghosh, S. Parveen, P. J. Sellin, and P. K. Giri, “Recent Advances and Opportunities in Low-Dimensional Layered Perovskites for Emergent Applications beyond Photovoltaics,” 2023. doi: 10.1002/admt.202300400.

[145] Y. Gao, P. Wan, T. Jin, H. Hu, L. Liu, and G. Niu, “Direct Fast-Neutron Detection by 2D Perovskite Semiconductor,” *Small*, vol. 19, no. 40, Oct. 2023, doi: 10.1002/smll.202301530.

[146] Y. He *et al.*, “Perovskite CsPbBr 3 single crystal detector for alpha-particle spectroscopy,” *Nucl Instrum Methods Phys Res A*, vol. 922, 2019, doi: 10.1016/j.nima.2019.01.008.

[147] H. Huang *et al.*, “Radiation-Tolerant Proton Detector Based on the MAPbBr $_3$ Single Crystal,” *ACS Appl Electron Mater*, vol. 5, no. 1, pp. 381–387, Jan. 2023, doi: 10.1021/acsaelm.2c01406.

[148] H. Li *et al.*, “Sensitive and Stable 2D Perovskite Single-Crystal X-ray Detectors Enabled by a Supramolecular Anchor,” *Advanced Materials*, vol. 32, no. 40, Oct. 2020, doi: 10.1002/adma.202003790.

[149] Y. Liang *et al.*, “Interlamellar-Spacing Engineering of Stable and Toxicity-Reduced 2D Perovskite Single Crystal for High-Resolution X-ray Imaging,” *Nano Lett*, vol. 24, no. 27, pp. 8436–8444, Jul. 2024, doi: 10.1021/acs.nanolett.4c02507.

[150] Y. He *et al.*, “CsPbBr3 perovskite detectors with 1.4% energy resolution for high-energy γ-rays,” *Nat Photonics*, vol. 15, no. 1, pp. 36–42, Jan. 2021, doi: 10.1038/s41566-020-00727-1.

[151] H. Wei and J. Huang, “Halide lead perovskites for ionizing radiation detection,” *Nat Commun*, vol. 10, no. 1, p. 1066, Mar. 2019, doi: 10.1038/s41467-019-08981-w.

[152] S. Yakunin *et al.*, “Detection of gamma photons using solution-grown single crystals of hybrid lead halide perovskites,” *Nat Photonics*, vol. 10, no. 9, pp. 585–589, Sep. 2016, doi: 10.1038/nphoton.2016.139.

[153] M. Yuan *et al.*, “Interface Energy-Level Reorganization for Efficient Perovskite γ-Ray Detectors,” *Angewandte Chemie International Edition*, Sep. 2024, doi: 10.1002/anie.202412685.

[154] M. Xia *et al.*, “Compact and Large-Area Perovskite Films Achieved via Soft-Pressing and Multi-Functional Polymerizable Binder for Flat-Panel X-Ray Imager,” *Adv Funct Mater*, vol. 32, no. 16, Apr. 2022, doi: 10.1002/adfm.202110729.

[155] L. Basiricò, S. P. Senanayak, A. Ciavatti, M. Abdi-Jalebi, B. Fraboni, and H. Sirringhaus, “Detection of X-Rays by Solution-Processed Cesium-Containing Mixed Triple Cation Perovskite Thin Films,” *Adv Funct Mater*, vol. 29, no. 34, Aug. 2019, doi: 10.1002/adfm.201902346.

[156] S. Demchyshyn *et al.*, “Designing Ultraflexible Perovskite X-Ray Detectors through Interface Engineering,” *Advanced Science*, vol. 7, no. 24, Dec. 2020, doi: 10.1002/advs.202002586.

[157] M. Girolami *et al.*, “Metal-Halide Perovskite Submicrometer-Thick Films for Ultra-Stable Self-Powered Direct X-Ray Detectors,” *Nanomicro Lett*, vol. 16, no. 1, p. 182, Dec. 2024, doi: 10.1007/s40820-024-01393-6.

[158] P. Jin *et al.*, “Realizing nearly-zero dark current and ultrahigh signal-to-noise ratio perovskite X-ray detector and image array by dark-current-shunting strategy,” *Nat Commun*, vol. 14, no. 1, p. 626, Feb. 2023, doi: 10.1038/s41467-023-36313-6.

[159] H. Mescher *et al.*, “Origami-inspired perovskite X-ray detector by printing and folding,” *npj Flexible Electronics*, vol. 7, no. 1, p. 9, Feb. 2023, doi: 10.1038/s41528-023-00240-9.

[160] F. Lédée, A. Ciavatti, M. Verdi, L. Basiricò, and B. Fraboni, “Ultra-Stable and Robust Response to X-Rays in 2D Layered Perovskite Micro-Crystalline Films Directly Deposited on Flexible Substrate,” *Adv Opt Mater*, vol. 10, no. 1, Jan. 2022, doi: 10.1002/adom.202101145.

[161] L. Basiricò *et al.*, “Mixed 3D–2D Perovskite Flexible Films for the Direct Detection of 5 MeV Protons,” *Advanced Science*, vol. 10, no. 1, 2023, doi: 10.1002/advs.202204815.

[162] E. A. Plis, D. P. Engelhart, R. Cooper, W. R. Johnston, D. Ferguson, and R. Hoffmann, “Review of radiation-induced effects in polyimide,” 2019. doi: 10.3390/app9101999.

[163] L. Zhao and P. E. Phelan, “Thermal contact conductance across filled polyimide films at cryogenic temperatures,” *Cryogenics (Guildf)*, vol. 39, no. 10, 1999, doi: 10.1016/S0011-2275(99)00095-8.

[164] N. Lacerda Silva, L. M. Gonçalves, and H. Carvalho, “Deposition of conductive materials on textile and polymeric flexible substrates,” *Journal of Materials Science: Materials in Electronics*, vol. 24, no. 2, 2013, doi: 10.1007/s10854-012-0781-y.

[165] M. De Bastiani, V. D’Innocenzo, S. D. Stranks, H. J. Snaith, and A. Petrozza, “Role of the crystallization substrate on the photoluminescence properties of organolead mixed halides perovskites,” *APL Mater*, vol. 2, no. 8, 2014, doi: 10.1063/1.4889845.

[166] T. Abzieher *et al.*, “From Groundwork to Efficient Solar Cells: On the Importance of the Substrate Material in Co-Evaporated Perovskite Solar Cells,” *Adv Funct Mater*, vol. 31, no. 42, 2021, doi: 10.1002/adfm.202104482.

[167] K. Duangkanya, A. Kopwitthaya, S. Chanhorm, and Y. Infahsaeng, “Oxygen plasma treatment time induced hydrophilicity of polydimethylsiloxane (PDMS) thin films for liquid lenses application,” in *Materials Today: Proceedings*, 2022. doi: 10.1016/j.matpr.2022.06.121.

[168] T. Pucher, P. Bastante, E. Sánchez Viso, and A. Castellanos-Gomez, “Low-Cost Shadow Mask Fabrication for Nanoelectronics,” *Nanomanufacturing*, vol. 3, no. 3, 2023, doi: 10.3390/nanomanufacturing3030022.

[169] M. N. Chaudhari, “Thin film Deposition Methods: A Critical Review,” *Int J Res Appl Sci Eng Technol*, vol. 9, no. VI, 2021, doi: 10.22214/ijraset.2021.36154.

[170] K. Reichelt and X. Jiang, “The preparation of thin films by physical vapour deposition methods,” 1990. doi: 10.1016/0040-6090(90)90277-K.

[171] R. Das and A. Chanda, “Fabrication and properties of spin-coated polymer films,” in *Nano-Size Polymers: Preparation, Properties, Applications*, 2016. doi: 10.1007/978-3-319-39715-3_10.

[172] A. G. Emslie, F. T. Bonner, and L. G. Peck, “Flow of a viscous liquid on a rotating disk,” *J Appl Phys*, vol. 29, no. 5, 1958, doi: 10.1063/1.1723300.

[173] L. Yang, J. Wang, and W. W. F. Leung, “Lead Iodide Thin Film Crystallization Control for High-Performance and Stable Solution-Processed Perovskite Solar Cells,” *ACS Appl Mater Interfaces*, vol. 7, no. 27, 2015, doi: 10.1021/acsami.5b01049.

[174] F. Yang *et al.*, “Upscaling Solution-Processed Perovskite Photovoltaics,” 2021. doi: 10.1002/aenm.202101973.

[175] Z. Saki, M. M. Byranvand, N. Taghavinia, M. Kedia, and M. Saliba, “Solution-processed perovskite thin-films: The journey from lab: The large-scale solar cells,” 2021. doi: 10.1039/d1ee02018h.

[176] S. Chen *et al.*, “Crystallization in one-step solution deposition of perovskite films: Upward or downward?,” *Sci Adv*, vol. 7, no. 4, 2021, doi: 10.1126/sciadv.abb2412.

[177] J. R. Bautista-Quijano, O. Telschow, F. Paulus, and Y. Vaynzof, “Solvent-antisolvent interactions in metal halide perovskites,” *Chemical Communications*, vol. 59, no. 71, 2023, doi: 10.1039/d3cc02090h.

[178] D. Bryant *et al.*, “Light and oxygen induced degradation limits the operational stability of methylammonium lead triiodide perovskite solar cells,” *Energy Environ Sci*, vol. 9, no. 5, 2016, doi: 10.1039/c6ee00409a.

[179] K. N. Yu, C. W. Y. Yip, D. Nikezic, J. P. Y. Ho, and V. S. Y. Koo, “Comparison among alpha-particle energy losses in air obtained from data of SRIM, ICRU and experiments,” *Applied Radiation and Isotopes*, vol. 59, no. 5–6, 2003, doi: 10.1016/S0969-8043(03)00201-X.

[180] F. Tommasino *et al.*, “A new facility for proton radiobiology at the Trento proton therapy centre: Design and implementation,” *Physica Medica*, vol. 58, 2019, doi: 10.1016/j.ejmp.2019.02.001.

[181] F. Tommasino *et al.*, “Proton beam characterization in the experimental room of the Trento Proton Therapy facility,” *Nucl Instrum Methods Phys Res A*, vol. 869, 2017, doi: 10.1016/j.nima.2017.06.017.

[182] Y. Wu, J. Feng, Z. Yang, Y. Liu, and S. Liu, “Halide Perovskite: A Promising Candidate for Next-Generation X-Ray Detectors,” 2023. doi: 10.1002/advs.202205536.

[183] T. Wang, D. Zheng, K. Vegso, N. Mrkyvkova, P. Siffalovic, and T. Pauporté, “High-Resolution and Stable Ruddlesden–Popper Quasi-2D Perovskite Flexible Photodetectors Arrays for Potential Applications as Optical Image Sensor,” *Adv Funct Mater*, vol. 33, no. 43, 2023, doi: 10.1002/adfm.202304659.

[184] T. E. Czerny, Q. Shen, J. Konieczny, M. A. Schroer, M. Winterer, and F. Muckel, “Efficient Narrowband Photoconductivity of the Excitonic Resonance in Two-Dimensional Ruddlesden-Popper Perovskites Due to Exciton Polarons,” *Journal of Physical Chemistry Letters*, vol. 14, no. 20, 2023, doi: 10.1021/acs.jpclett.3c00710.

[185] Y. Miao *et al.*, “Gradient 2D–3D Ruddlesden-Popper perovskite film for high-performance self-powered photodetectors,” *Nano Energy*, vol. 113, 2023, doi: 10.1016/j.nanoen.2023.108605.

[186] P. Mai, J. Houel, N. Dreveton, B. Mahler, and A. Gassenq, “High-Responsivity Planar Photodetector Based on Methylammonium Lead Bromide Perovskite Thin Film,” *Photonics*, vol. 10, no. 9, 2023, doi: 10.3390/photonics10091043.

[187] G. Ghosh, A. Dutta, A. Ghosh, S. Ghosh, and A. Patra, “Ultrafast Carrier Dynamics in 2D CdSe Nanoplatelets-CsPbX3 Composites: Influence of the Halide Composition,” *Journal of Physical Chemistry C*, vol. 124, no. 18, 2020, doi: 10.1021/acs.jpcc.0c03206.

[188] M. Rahil, R. M. Ansari, S. Ahmad, and S. S. Islam, “Nanostructured Ruddlesden-Popper-Layered Lead Bromide Perovskites with Stable and Selected Wavelength for Photodetection Applications,” *ACS Appl Nano Mater*, vol. 6, no. 7, 2023, doi: 10.1021/acsanm.2c05092.

[189] Z. Xu *et al.*, “Highly Sensitive and Ultrafast Responding Array Photodetector Based on a Newly Tailored 2D Lead Iodide Perovskite Crystal,” *Adv Opt Mater*, vol. 7, no. 11, 2019, doi: 10.1002/adom.201900308.

[190] T. A. Qasuria *et al.*, “Stable perovskite based photodetector in impedance and capacitance mode,” *Results Phys*, vol. 15, 2019, doi: 10.1016/j.rinp.2019.102699.

[191] C. H. Kang *et al.*, “High-speed colour-converting photodetector with all-inorganic CsPbBr3 perovskite nanocrystals for ultraviolet light communication,” *Light Sci Appl*, vol. 8, no. 1, 2019, doi: 10.1038/s41377-019-0204-4.

[192] L. Salamandra *et al.*, “Perovskite photo-detectors (PVSK-PDs) for visible light communication,” *Org Electron*, vol. 69, 2019, doi: 10.1016/j.orgel.2019.03.008.

[193] J. Wan *et al.*, “2D Ruddlesden–Popper Polycrystalline PerovskitePyro-Phototronic Photodetectors,” *Small*, vol. 19, no. 38, 2023, doi: 10.1002/smll.202207185.

[194] S. Soriano-Díaz, O. E. Solis, D. Ramírez-Muñoz, P. P. Boix, J. P. Martínez-Pastor, and I. Suárez, “Frequency Response of MAPbI3 Perovskites for Photodetection Application,” *Adv Electron Mater*, vol. 10, no. 7, 2024, doi: 10.1002/aelm.202300833.

[195] F. Corsini and G. Griffini, “Recent progress in encapsulation strategies to enhance the stability of organometal halide perovskite solar cells,” 2020. doi: 10.1088/2515-7655/ab8774.

[196] B. Dryzhakov, B. J. Lawrie, J. Z. Celio, M. Wang, M. Koehler, and B. Hu, “Dual Emission Bands of a 2D Perovskite Single Crystal with Charge Transfer State Characteristics,” *ACS Nano*, vol. 17, no. 13, 2023, doi: 10.1021/acsnano.3c00496.

[197] W. Raja *et al.*, “Photon recycling in perovskite solar cells and its impact on device design,” 2021. doi: 10.1515/nanoph-2021-0067.

[198] K. Wang *et al.*, “Overcoming Shockley-Queisser limit using halide perovskite platform?,” 2022. doi: 10.1016/j.joule.2022.01.009.

[199] H. Tsai, J. Tisdale, S. Shrestha, F. Liu, and W. Nie, “Emerging Lead-Halide Perovskite Semiconductor for Solid-State Detectors,” in *Advanced X-ray Detector Technologies: Design and Applications*, 2022. doi: 10.1007/978-3-030-64279-2_2.

[200] H. Tsai *et al.*, “A sensitive and robust thin-film x-ray detector using 2D layered perovskite diodes,” *Sci Adv*, vol. 6, no. 15, 2020, doi: 10.1126/sciadv.aay0815.

[201] W. Wei *et al.*, “Monolithic integration of hybrid perovskite single crystals with heterogenous substrate for highly sensitive X-ray imaging,” *Nat Photonics*, vol. 11, no. 5, pp. 315–321, May 2017, doi: 10.1038/nphoton.2017.43.

[202] M. Nur-E-Alam *et al.*, “Current scenario and future trends on stability issues of perovskite solar cells: A mini review,” *Curr Opin Colloid Interface Sci*, vol. 76, p. 101895, Apr. 2025, doi: 10.1016/j.cocis.2025.101895.

[203] X. Liu *et al.*, “Solution-Grown Formamidinium Hybrid Perovskite (FAPbBr3) Single Crystals for α-Particle and γ-Ray Detection at Room Temperature,” *ACS Appl Mater Interfaces*, vol. 13, no. 13, 2021, doi: 10.1021/acsami.1c00174.

[204] S. Chhangani, M. Kumar, R. M. Sahani, A. Bera, and A. Pandya, “Lead Halide perovskite based plastic scintillators for alpha particle detection,” *Mater Today Commun*, vol. 33, 2022, doi: 10.1016/j.mtcomm.2022.104303.

[205] F. Liu *et al.*, “Halide perovskites and perovskite related materials for particle radiation detection,” 2022. doi: 10.1039/d2nr01292h.

[206] U. Fano, “Penetration of Protons, Alpha Particles, and Mesons,” *Annu Rev Nucl Sci*, vol. 13, no. 1, 1963, doi: 10.1146/annurev.ns.13.120163.000245.

[207] J. Androulakis *et al.*, “Dimensional Reduction: A Design Tool for New Radiation Detection Materials,” *Advanced Materials*, vol. 23, no. 36, pp. 4163–4167, Sep. 2011, doi: 10.1002/adma.201102450.

[208] Y. Fang, Q. Dong, Y. Shao, Y. Yuan, and J. Huang, “Highly narrowband perovskite single-crystal photodetectors enabled by surface-charge recombination,” *Nat Photonics*, vol. 9, no. 10, pp. 679–686, Oct. 2015, doi: 10.1038/nphoton.2015.156.

[209] R. Wu *et al.*, “The Modified Hecht Equation for Pixel Detectors: A Methodological Approach to Evaluating Mobility-Lifetime Products,” *IEEE Trans Nucl Sci*, vol. 71, no. 3, pp. 352–359, Mar. 2024, doi: 10.1109/TNS.2024.3355242.

[210] X. Zhang *et al.*, “High energy resolution CsPbBr3 alpha particle detector with a full-customized readout application specific integrated circuit,” *Nat Commun*, vol. 15, no. 1, p. 6333, Jul. 2024, doi: 10.1038/s41467-024-50746-7.

[211] L. Karsch *et al.*, “Dose rate dependence for different dosimeters and detectors: TLD, OSL, EBT films, and diamond detectors,” *Med Phys*, vol. 39, no. 5, 2012, doi: 10.1118/1.3700400.

[212] J. Deasy, “ICRU Report 49, Stopping Powers and Ranges for Protons and Alph Particles,” *Med Phys*, vol. 21, no. 5, 1994, doi: 10.1118/1.597176.

[213] M. Chiari *et al.*, “LABEC, the INFN ion beam laboratory of nuclear techniques for environment and cultural heritage,” *Eur Phys J Plus*, vol. 136, no. 4, 2021, doi: 10.1140/epjp/s13360-021-01411-1.

[214] M. Bauwens *et al.*, “A comparison of four radionuclide dose calibrators using various radionuclides and measurement geometries clinically used in nuclear medicine,” *Physica Medica*, vol. 60, 2019, doi: 10.1016/j.ejmp.2019.03.012.

[215] J. Chancellor, G. Scott, and J. Sutton, “Space Radiation: The Number One Risk to Astronaut Health beyond Low Earth Orbit,” *Life*, vol. 4, no. 3, pp. 491–510, Sep. 2014, doi: 10.3390/life4030491.

[216] A. Fogtman *et al.*, “Towards sustainable human space exploration—priorities for radiation research to quantify and mitigate radiation risks,” *NPJ Microgravity*, vol. 9, no. 1, p. 8, Jan. 2023, doi: 10.1038/s41526-023-00262-7.

[217] J. C. Chancellor *et al.*, “Limitations in predicting the space radiation health risk for exploration astronauts,” *NPJ Microgravity*, vol. 4, no. 1, p. 8, Apr. 2018, doi: 10.1038/s41526-018-0043-2.

[218] R. Gaza *et al.*, “The importance of time-resolved personal Dosimetry in space: The ISS Crew Active Dosimeter,” *Life Sci Space Res (Amst)*, vol. 39, pp. 95–105, Nov. 2023, doi: 10.1016/j.lssr.2023.08.004.

[219] L. Narici and T. Berger, “Radiation in human space exploration: Detectors and measurements, today and tomorrow,” *Life Sci Space Res (Amst)*, vol. 39, pp. 1–2, Nov. 2023, doi: 10.1016/j.lssr.2023.10.002.

[220] I. Fratelli *et al.*, “Trap States Ruling Photoconductive Gain in Tissue-Equivalent, Printed Organic X-Ray Detectors,” *Adv Mater Technol*, vol. 8, no. 3, Feb. 2023, doi: 10.1002/admt.202200769.

[221] I. Fratelli *et al.*, “Direct detection of 5-MeV protons by flexible organic thin-film devices,” *Sci Adv*, vol. 7, no. 16, Apr. 2021, doi: 10.1126/sciadv.abf4462.

[222] W. Delmas *et al.*, “Evaluation of Hybrid Perovskite Prototypes After 10-Month Space Flight on the International Space Station,” *Adv Energy Mater*, vol. 13, no. 19, 2023, doi: 10.1002/aenm.202203920.

[223] L. Li, J. Liu, M. Zeng, and L. Fu, “Space-confined growth of metal halide perovskite crystal films,” 2021. doi: 10.1007/s12274-020-3050-z.

[224] V. Romano, A. Agresti, R. Verduci, and G. D’Angelo, “Advances in Perovskites for Photovoltaic Applications in Space,” 2022. doi: 10.1021/acsenergylett.2c01099.

[225] L. Narici, T. Berger, D. Matthiä, and G. Reitz, “Radiation Measurements Performed with Active Detectors Relevant for Human Space Exploration,” *Front Oncol*, vol. 5, Dec. 2015, doi: 10.3389/fonc.2015.00273.

[226] L. Di Fino *et al.*, “Radiation measurements in the International Space Station, Columbus module, in 2020–2022 with the LIDAL detector,” *Life Sci Space Res (Amst)*, vol. 39, pp. 26–42, Nov. 2023, doi: 10.1016/j.lssr.2023.03.007.

[227] T. Sato *et al.*, “Features of Particle and Heavy Ion Transport code System (PHITS) version 3.02,” *J Nucl Sci Technol*, vol. 55, no. 6, 2018, doi: 10.1080/00223131.2017.1419890.

[228] X. Fu *et al.*, “Directional Polarized Light Emission from Thin-Film Light-Emitting Diodes,” *Advanced Materials*, vol. 33, no. 9, 2021, doi: 10.1002/adma.202006801.

[229] I. Fratelli *et al.*, “Trap States Ruling Photoconductive Gain in Tissue-Equivalent, Printed Organic X-Ray Detectors,” *Adv Mater Technol*, vol. 8, no. 3, Feb. 2023, doi: 10.1002/admt.202200769.

[230] H. F. Haneef, A. M. Zeidell, and O. D. Jurchescu, “Charge carrier traps in organic semiconductors: a review on the underlying physics and impact on electronic devices,” *J Mater Chem C Mater*, vol. 8, no. 3, pp. 759–787, 2020, doi: 10.1039/C9TC05695E.

[231] M. J. Griffith, S. Cottam, J. Stamenkovic, J. A. Posar, and M. Petasecca, “Printable Organic Semiconductors for Radiation Detection: From Fundamentals to Fabrication and Functionality,” *Front Phys*, vol. 8, Mar. 2020, doi: 10.3389/fphy.2020.00022.

[232] I. Fratelli *et al.*, “Direct detection of 5-MeV protons by flexible organic thin-film devices,” *Sci Adv*, vol. 7, no. 16, Apr. 2021, doi: 10.1126/sciadv.abf4462.

[233] C. M. Raghavan *et al.*, “Low-Threshold Lasing from 2D Homologous Organic–Inorganic Hybrid Ruddlesden–Popper Perovskite Single Crystals,” *Nano Lett*, vol. 18, no. 5, pp. 3221–3228, May 2018, doi: 10.1021/acs.nanolett.8b00990.

[234] J. Di, J. Chang, and S. (Frank) Liu, “Recent progress of two-dimensional lead halide perovskite single crystals: Crystal growth, physical properties, and device applications,” *EcoMat*, vol. 2, no. 3, Sep. 2020, doi: 10.1002/eom2.12036.

[235] Y. Zhang *et al.*, “Two-dimensional $(PEA)_2PbBr_4$ perovskite single crystals for a high performance UV-detector,” *J Mater Chem C Mater*, vol. 7, no. 6, pp. 1584–1591, 2019, doi: 10.1039/C8TC06129G.

[236] A. Ciavatti *et al.*, “Radiation Hardness and Defects Activity in PEA_2PbBr_4 Single Crystals,” *Adv Funct Mater*, Sep. 2024, doi: 10.1002/adfm.202405291.

RINGRAZIAMENTI

Per quanto insignificanti rispetto a quanto ho ricevuto, inondo questa pagina di grazie alle persone - davvero tante, sono grato anche di questo- che hanno contribuito, direttamente e indirettamente, alla stesura di questo lavoro.

Ringrazio la prof.ssa Fraboni per la supervisione, il supporto, le chiacchiere gentili, il continuo offrire possibilità e spunti professionali. Ringrazio Andrea per la presenza costante ed estremamente competente in ogni singolo momento: fonte inesauribile di entusiasmo per la ricerca e di ispirazione. Ringrazio Laura ed Ilaria per l'attenzione e la cura con cui mi hanno coinvolto e guidato, con grande esperienza e precisione. Ringrazio Tobias per l'affiancamento e per il suo essere riferimento e stimolo. Ringrazio infine il prof. Sellin per avermi ospitato e seguito nel mio periodo all'estero; con lui anche Jayana, Joydip e John-William, il confronto coi quali è stato fondamentale.

Ringrazio uno ad uno i colleghi, dottorandi presenti e d'una volta, senza i quali avrei fatto poco o niente: Matteo, Filippo, Luca, Giovanni, Camilla, Sara, Giulia, Luca, Elisabetta, Francesco, Alberto, Chenhong, Aleksandra, Cesare.

Ringrazio i miei genitori, Anselmo ed Angela, ai quali dovrei dedicare un'intera pagina tanta è stata la pazienza con cui m'han accompagnato ad essere ciò che sono.

Ringrazio Carlo e Silvia perché sì, perché poverini non han scelto d'essere i miei fratelli.

Ringrazio Lia, che si meriterebbe una statua invece che dieci parole.

Ringrazio le bestiacce che mi son vicine da ormai quindici anni: Alessandro, Alfredo, Enrico, Giacomo, Guglielmo, Matteo, Nicola, Alan, Pier, Rafael.

Ringrazio chiunque si senta escluso da questa lista: grazie di cuore.